

Dissertation

**Predicting photoemission:
From the single-particle interpretation to
the many-electron picture**

Matthias Dauth



UNIVERSITÄT
BAYREUTH

Von der Universität Bayreuth
zur Erlangung des akademischen Grades eines
Doktors der Naturwissenschaften (Dr. rer. nat.)
genehmigte Abhandlung

Predicting photoemission:

From the single-particle interpretation to the many-electron picture

Matthias Dauth

aus Bayreuth

1. Gutachter: Prof. Dr. Stephan Kümmel
2. Gutachter: Prof. Dr. Vollrath Martin Axt
3. Gutachter: Prof. Dr. Jaakko Akola

Tag der Einreichung: 26.07.2016

Tag des Kolloquiums: 11.11.2016

Abstract

Quantum-mechanical systems of practical relevance often comprise hundreds or even thousands of electrons. To describe their electronic structure in a rigorous way, the calculation and storage of correlated many-electron wavefunctions are necessary. Even with the most efficient methods this is far beyond the capacity of the presently available computational power and will probably ever be. Therefore, a commonly pursued strategy is to accommodate many-electron physics in manageable single-particle theories as well as possible. In recent years, the debate about the credibility of the single-particle interpretation of the electronic structure, particularly in terms of molecular orbitals, has been fueled by intriguing results of orbital imaging techniques. Angle-resolved photoemission spectroscopy (ARPES) experiments on organic semiconductor molecules, for instance, have revealed tomographic images that can be interpreted as showing molecular orbitals. Yet, this interpretation rests upon a simple model of the photoemission process, which assumes, for example, that the emitted electron can be described by a plane wave. Triggered by the issues associated with orbital imaging, this thesis aims to shed light on essential aspects of the theoretical description of ARPES and photoemission in general. These aspects can roughly be subsumed under the following topics: (i) the description of the electronic structure of the probed molecule as regards simulating photoemission spectra within a Fermi's golden rule formalism, (ii) a fully dynamical simulation of the photoemission process focusing on a proper description of the emitted electron, and (iii) the satisfaction of an exact constraint within many-body perturbation-theory approaches for establishing highly accurate ionization-potential predictions.

A major part of (i) is concerned with the credibility of the molecular-orbital concept. From a rigorous theory of photoemission it becomes evident that imaging experiments do not show molecular orbitals but Dyson orbitals. In contrast to molecular orbitals, Dyson orbitals are exact quasiparticle states that can be derived from many-electron wavefunctions. Under the premise of employing a high quality single-particle theory, molecular orbitals can be granted a physically meaningful interpretation as approximations to Dyson orbitals. Particularly the freedom of the prominent self-interaction error within density-functional theory (DFT) approaches is decisive to obtain molecular orbitals that agree with observations from ARPES experiments. To surpass the pure molecular-orbital interpretation of ARPES, I illustrate a more stringent scheme to calculate approximate Dyson orbitals by invoking Kohn-Sham Slater determinants, which are used as approximations to exact many-electron wavefunctions. Although individual molecular orbitals often explain ARPES spectra, experiments reveal features which are clearly beyond the molecular-orbital level but can be understood with the Dyson orbital scheme. Further, an interpretation of ARPES experiments in combination with this approach permits to unveil information on the electron-vibration coupling of specific modes in molecular materials.

Aspect (ii) focuses on the state of the emitted electron which can influence the simulation of ARPES spectra substantially. I introduce a real-time propagation approach to time-dependent DFT that allows to obtain final-state effects from first principles. As the emitted electron is subject to the Kohn-Sham potential, the interaction of the photoelectron with the remaining electrons is fully captured on the DFT level. The accuracy of this approach manifests in the prediction of four hallmark effects that are beyond the widely used plane-wave final-state approximation: relative photoemission cross-sections, emission perpendicular to the light polarization, circular dichroism in the photoelectron angular distribution, and a pronounced photon energy dependence of the photoemission intensity.

The holy grail of theoretical photoemission spectroscopy is the prediction of important material properties such as ionization potentials with utmost precision. In this respect, part (iii) deals with the GW approach to many-body perturbation theory, which is currently considered as the method of choice for ionization-potential predictions. Here, a major source for the discrepancy between experimental ionization potentials and theoretical quasiparticle energies is the deviation from the straight line error (DSLE), i.e., the spurious nonlinearity of the total energy as a function of fractional particle numbers. An unbiased assessment of the DSLE within the fully self-consistent GW scheme reveals a comparatively small DSLE with respect to common DFT approaches. For perturbative G_0W_0 calculations the DSLE depends on the starting point. Yet, the starting-point dependence can be exploited to reduce (or completely eliminate) the DSLE. I demonstrate that the agreement with experimental ionization potentials increases as the DSLE diminishes.

Kurzdarstellung

Quantenmechanische Systeme, wie zum Beispiel organische Halbleiter, bestehen häufig aus hunderten oder sogar tausenden von Elektronen. Um solche Systeme exakt zu beschreiben, müsste sich die korrelierte Vielteilchenwellenfunktion einerseits berechnen und andererseits auch speichern lassen können. Selbst mit den effizientesten Verfahren wird dies in absehbarer Zeit nicht möglich sein. Deshalb ist es eine häufig verfolgte Strategie, die Vielteilcheneffekte so gut wie möglich in handhabbaren Einteilchentheorien unterzubringen. Allerdings wird die physikalische Aussagekraft von Einteilchengrößen, allem voran von Molekülorbitalen, kontrovers diskutiert. Mithilfe von winkelaufgelöster Photoemissionspektroskopie (ARPES) an Molekülen ist es zum Beispiel kürzlich gelungen, tomographische Abbilder zu erstellen, die sich als Molekülorbitale interpretieren lassen. Diese Interpretation beruht aber auf einem einfachen Modell des Photoemissionsprozesses, das unter anderem eine ebene Welle für den Zustand des emittierten Elektrons annimmt. Zur Diskussion dieser Annahmen setzt sich meine Arbeit mit ausgewählten Aspekten zur theoretischen Beschreibung von ARPES und von Photoemission im Allgemeinen auseinander. Grob lassen sich diese Aspekte wie folgt gliedern: (i) die Beschreibung der elektronischen Struktur von Molekülen im Bezug auf die Simulation von Photoemission mithilfe Fermis goldener Regel, (ii) die Simulation von Photoemission in Echtzeit, vor allem im Hinblick auf die Beschreibung des emittierten Photoelektrons, und (iii) die Vorhersage von möglichst genauen Ionisationspotentialen mithilfe der Vielteilchenstörungstheorie unter der Einhaltung einer exakt formulierbaren Rahmenbedingung.

In Teil (i) steht die elektronische Struktur der untersuchten Moleküle im Vordergrund. Aus der Theorie zur Photoemission lässt sich zeigen, dass ARPES-Experimente eigentlich keine Molekülsondern Dysonorbitale abbilden. Beide Orbitaltypen beruhen auf unterschiedlichen physikalischen Konzepten, wobei Dysonorbitale formal exakte Quasiteilchenzustände sind, die sich aus Vielteilchenwellenfunktionen herleiten lassen. Liegt den Molekülorbitalen eine qualitativ hochwertige Einteilchentheorie zugrunde, lassen sich dennoch Argumente dafür finden, dass Molekülorbitale gute Näherungen an Dysonorbitale sein können. Innerhalb der Dichtefunktionaltheorie (DFT) liegt der Schlüssel zu physikalisch aussagekräftigen Molekülorbitalen, die sich mit Beobachtungen aus ARPES-Experimenten decken, in der Korrektur des Selbstwechselwirkungsfehlers. Um über die reine Molekülorbitalinterpretation hinauszugehen, stelle ich ein Modell vor, mit dem sich Dysonorbitale aus Kohn-Sham-Slaterdeterminanten näherungsweise konstruieren lassen. Die Slaterdeterminanten fungieren als Näherungen an die exakten Vielteilchenwellenfunktionen. Obwohl einzelne Molekülorbitale häufig experimentelle Beobachtungen erklären können, finden sich in ARPES-Spektren Signaturen, die sich mit dem stichhaltigeren Dysonorbitalansatz verstehen lassen. Darüber hinaus machen es ARPES-Experimente in Kombination mit dem Dysonorbitalansatz möglich, Informationen über die Elektron-Phonon-Kopplung spezifischer Moden in molekularen Systemen zu enthüllen.

In Punkt (ii) wird demonstriert, dass der Zustand des emittierten Photoelektrons ebenfalls großen Einfluss auf die korrekte Vorhersage von Photoemissionsspektren hat. Ich stelle eine Methode vor, die den Photoemissionsprozess in Echtzeit simuliert. Dadurch ergibt sich der Zustand des emittierten Elektrons auf natürliche Weise aus der Zeitentwicklung des Systems, ohne den Zustand explizit spezifizieren zu müssen. Außerdem wird die Wechselwirkung des Photoelektrons mit dem zurückbleibenden ionisierten System komplett auf DFT-Niveau beschrieben. Der Vorteil von Echtzeitsimulationen, vor allem im Vergleich zur häufig verwendeten Beschreibung des Pho-

toelektrons als ebene Welle, besteht darin, dass sich folgende Effekte vorhersagen lassen: Relative Photoemissionsintensitäten, Photoemission senkrecht zur Polarisierung des elektrischen Feldes, zirkularer Dichroismus in der Winkelabhängigkeit der Photoemissionsintensität und die Photonenenergieabhängigkeit.

Abschnitt (iii) behandelt die Vorhersage von Ionisationspotentialen mit höchstmöglicher Präzision. In diesem Zusammenhang gilt der *GW*-Ansatz innerhalb der Vielteilchenstörungstheorie als am vielversprechendsten. Unterschiede zwischen experimentell bestimmten Ionisationspotentialen und *GW*-Quasiteilchenenergien lassen sich hauptsächlich auf die Verletzung der *straight-line*-Bedingung zurückführen, die vorgibt, dass sich die Gesamtenergie eines Systems linear mit der fraktionellen Teilchenzahl ändert. Inwiefern diese exakte Bedingung für *GW* erfüllt ist, lässt sich mit selbstkonsistenten *GW*-Rechnungen zeigen. Im Vergleich zu typischen DFT-Rechnungen sind die Abweichungen von der *straight-line*-Bedingung klein. Für G_0W_0 -Rechnungen lässt sich die *straight-line*-Bedingung nutzen, um einen optimalen Startpunkt zu finden. Ich zeige in meiner Arbeit, dass sich die Qualität des vorhergesagten Ionisationspotentials verbessert, wenn die Abweichung von der *straight-line*-Bedingung kleiner wird.

Contents

Abstract	v
Kurzdarstellung	vii
I Electronic-structure approaches to photoemission	1
1 Probing the electronic structure with photoemission	3
1.1 Basic principles of photoemission	4
1.2 Angle-resolved photoemission	4
1.3 Electronic-structure theory and photoemission	6
2 Ground-state density-functional theory	9
2.1 Foundations of ground-state density-functional theory	9
2.2 Fundamental relations with respect to photoemission	11
2.3 Common exchange-correlation functional approximations	15
2.4 Self-interaction correction within the Kohn-Sham scheme	18
2.5 The molecular orbital interpretation and orbital tomography	20
2.6 Beyond the molecular-orbital interpretation: the wavefunction perspective	23
2.7 Visualizing electron-phonon coupling with ARPES	25
3 Photoemission as a dynamical process: time-dependent density-functional theory	27
3.1 Fundamentals of time-dependent density-functional theory	27
3.2 The linear-response approach: excited states from particle-hole expansions	29
3.3 Photoemission spectra from real-time propagations	31
4 Many-body perturbation theory in the <i>GW</i> approximation	39
4.1 The Green's function formalism	39
4.2 Hedin equations and the <i>GW</i> approximation	41
4.3 Perturbative G_0W_0	42
4.4 Fully self-consistent <i>GW</i>	44
4.5 Piecewise linearity and the accuracy of quasiparticle energies	44
A Complementing work	47
A.1 Coulomb-wave final state and the partial-wave expansion	47
A.2 Horizontal polarization and NTCDA	51
A.3 The energy dependence of the circular dichroism of CO	52
A.4 Adsorption effects of PTCDA on Ag(110)	54
A.5 Miscellaneous details on the real-time propagation scheme	56
A.6 Self-interaction correction: details	60

List of abbreviations	69
Bibliography	71
Acknowledgments	91
Eidesstattliche Versicherung	93
II Publications	95
Publication 0 from the end of my diploma Orbital density reconstruction for molecules	97
Publication 1 Angle resolved photoemission from organic semiconductors: orbital imaging beyond the molecular orbital interpretation	107
Publication 2 Electron-vibration coupling in molecular materials: assignment of vibronic modes from photoelectron momentum mapping	127
Publication 3 Angle-resolved photoemission from outer valence states: approximate Dyson orbitals from time-dependent density functional theory	137
Publication 4 Predicting photoemission intensities and angular distributions with real-time density-functional theory	149
Publication 5 Perpendicular emission, dichroism, and energy dependence in angle-resolved photoemis- sion: the importance of the final state	161
Publication 6 Outer-valence electron spectra of prototypical aromatic heterocycles from an optimally tuned range-separated hybrid functional	173
Publication 7 Piecewise linearity in the <i>GW</i> approximation for accurate quasiparticle energy predictions	195
Publication 8 Benchmark of <i>GW</i> approaches for the <i>GW100</i> testset	207

Part I

Electronic-structure approaches to photoemission

CHAPTER 1

Probing the electronic structure with photoemission

The attempts to understand the photoelectric effect were among the triggers for the development of quantum mechanics. Since then, photoemission has always been playing an invaluable role in the characterization of condensed matter systems. During the recent years a wealth of fascinating insights has been unveiled because steady efforts promoted the accuracy of photoemission experiments to a completely new level. A detailed examination of interface effects between metal surfaces and organic semiconductors with angle-resolved photoemission spectroscopy (ARPES) is one of the remarkable successes of this development. While studies of the latter kind are technologically relevant for the design of organic electronic devices and their interfaces with classical (semi)conductors, sophisticated photoemission experiments also provide access to the very fundamentals of quantum mechanics. On that score, an intriguing result of ARPES is the mapping of outer valence molecular orbitals since it visualizes an inherently quantum-mechanical phenomenon, i.e., the probability density of finding a single electron in a certain region of space. However, the common interpretation of ARPES data as showing a tomographic image of a one-electron state in a many-electron system is not straightforward to reconcile with the fundamentals of exact many-body quantum mechanics. Strictly speaking, nature does not know about the concept of molecular orbitals. So, to what extent is ARPES able to image what should actually be hidden behind the curtain of highly complex many-electron wavefunctions [Sch06]?

Apart from the fundamental perspective, the credibility of the molecular orbital concept is vital to the vast majority of electronic-structure theory methods. Density-functional theory (DFT), for example, does rely on orbitals, if only implicitly. It is, thus, kind of obvious that orbitals have significant influence on observables and that finding criteria for a physically sound interpretation of molecular orbitals is highly relevant for practical applications. Also the development of theoretical methods would benefit if it was possible to grasp the decisive physics behind experimentally verified orbitals. Completely aside from orbitals, photoemission has proved to be indispensable in the pursuit of increasingly reliable electronic-structure theories on a rather general level. Photoemission observables, where ionization energies are leading the way, are frequently employed as premier theory benchmarks. Due to photoemission's versatility it also offers valuable insights into various kinds of physical effects and material properties such as vibrational excitations.

A meticulous description of photoemission processes that captures all features observed in experiment can get arbitrarily complicated. To name but a few difficulties, the N -electron initial and the $N - 1$ -electron final state are described by correlated wavefunctions. While the former is usually assumed to be in the ground state, the latter can even be excited. In principle both states have to be known for the simulation of photoemission if a steady-state picture within Fermi's golden rule is assumed. I further want to emphasize that the description of the state of the ejected electron can

contribute to the simulated photoemission spectra significantly. Interaction effects with its ionized mother system, scattering events, or interferences of outgoing waves can deflect the trajectories of photoelectrons and alter the photoelectron yield. Last but not least, photoemission is a dynamical process. To unveil dynamical effects, the time evolution of the entire photoemission process has to be simulated. This ansatz is especially appealing as it goes beyond the prevalent notion of describing photoemission by a transition between steady states.

My thesis aims to shed some light on the topics raised. In Part I, I present the background to and brief summaries of my publications. Further, I discuss how the publications are related. Part II contains all publications, which are ordered according to their topics. As a first step, let me start with a concise introduction to photoemission and its relation to electronic-structure theory in this chapter.

1.1 Basic principles of photoemission

The first steps towards photoemission spectroscopy (PES) as it is applied nowadays date back to the late 19th century [BK95]. Triggered by the experiments of Heinrich Hertz [Her87], the photoelectric effect was discovered by the observation that electrons are dislodged from a metal only if light above a certain threshold frequency impinges on the sample. Albert Einstein's Nobel prize winning explanation of the photoelectric effect primarily rests on associating the light's frequency with the quantized energy $\hbar\omega$ of photons [Ein05]. According to his explanation, an electron can be emitted and retains the excess energy as kinetic energy E_{kin} if the workfunction ϕ and the electron binding energy E_{B} ¹ is overcome by the energy of the incident photon [Hüf03],

$$E_{\text{kin}} = \hbar\omega - \phi - |E_{\text{B}}|. \quad (1.1)$$

Over the years, the underlying principle of conducting PES experiments has remained similar. Yet, increasingly sophisticated setups have turned PES into a powerful technique for probing various kinds of systems. A detailed overview of experimental and practical aspects of PES can be found, for example, in Refs. [Hüf03, RH05]. Depending on the desired photon energy, a light source such as gas-phase discharge lamps, X-ray tubes, or synchrotron radiation is used. Placing a state-of-the-art electron analyzer into the trajectory of photoelectrons, it is possible to measure their kinetic energy with high precision. The great success of PES can be rationalized as one can deduce information about the binding characteristics of electrons in the probed sample from the energy conservation in Eq. (1.1). Besides, the availability of diverse photon sources that cover energies from the ultraviolet up to the X-ray regime makes it possible to probe outer-valence as well as core-level electrons. Probing the latter is used, for example, as a noninvasive method to identify elements and their concentration in compounds. Further, core-level binding energies are sensitive to their chemical environment which permits chemical analyses² [Hüf03].

1.2 Angle-resolved photoemission

Extending PES in such a way that the angular distribution of photoelectrons is additionally recorded paves the way for a large variety of further applications. Most prominently, ARPES is renowned as

¹For solids E_{B} is usually referred to the Fermi level. For free molecules and atoms E_{B} refers to the vacuum level. In my work E_{B} of composite systems such as molecular monolayers on metal surfaces is related to the Fermi level.

²X-ray PES is often called electron spectroscopy for chemical analysis (ESCA). Kai Siegbahn was awarded a Nobel prize in 1981 for his contribution to the development of ESCA.

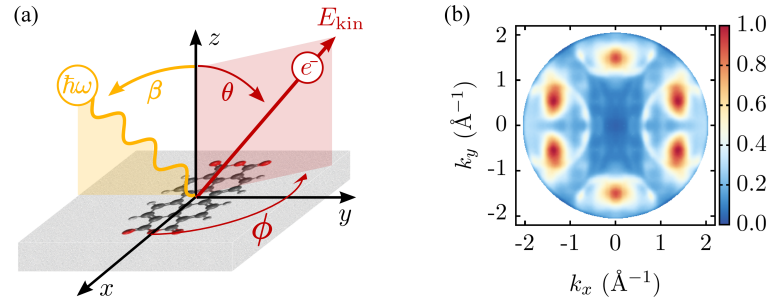


Figure 1.1: (a) Sketch of typical ARPES setups. A molecular monolayer is prepared on a metal surface. Photons are incoming under an angle β towards the surface normal with an energy of $\hbar\omega$. The photoelectron's kinetic energy and the azimuthal and polar emission angles (ϕ and θ , respectively) are recorded. (b) Measured momentum map corresponding to the photoemission intensity from the highest occupied molecular orbital of PTCDA. The setup details are: $\hbar\omega = 27$ eV, $\beta = 65^\circ$, and a light polarization that is parallel to the long molecular axis (x -axis). Courtesy of A. Schöll and M. Graus from the University of Würzburg.

a technique for probing the band structure of solids [AFN⁺98, Dam04, RH05]. However, studied systems are not only traditional metals and semi-conductors, but range up to superconductors, graphene monolayers, and adsorbed atoms and molecules [PEFK83, MW84, WBG89, HTY⁺93, DHS03, Dam04, RH05, KTY⁺06, BKP⁺08, UK08, SWLZ09, PBF⁺09, MGW⁺13, PL15]. In my work I will mainly focus on ARPES on monolayers of planar organic molecules adsorbed on metallic surfaces. Typical examples are 3,4,9,10-perylene-tetracarboxylic dianhydride (PTCDA) or 1,4,5,8-naphthalene-tetracarboxylic dianhydride (NTCDA) on Ag(110). Apart from studying interface effects themselves [ZFS⁺10, WHS⁺12, WZF⁺13, WKF⁺13, ULR⁺14], the major advantage of placing the molecules onto a substrate is that the molecules can be prepared to form well-ordered structures. Thus, the angular distribution of photoelectrons retains the geometrical and structural information about the molecules without averaging over all possible orientations as in gas-phase experiments. In the case of PTCDA the molecular monolayer can be arranged, e.g., in a brickwall-like structure [SAL⁺97, GSS⁺98, WHS⁺12]. The silver substrate and noble metal surfaces in general offer the benefit of being chemically inert and, hence, having a rather small influence on the electronic structure of the molecules. Yet, interfacial bonding can cause a hybridization of molecular and substrate states. This leads, e.g., for PTCDA and NTCDA, to a charge transfer into the lowest unoccupied molecular orbital (LUMO)³ [ZKS⁺06, ZFS⁺10, WHS⁺12, WKF⁺13] and a substrate mediated lateral band dispersion of the hybridized states [WZF⁺13, ULR⁺14].

A generic setup for ARPES experiments is sketched in Fig. 1.1. The sample is irradiated by photons with an energy of $\hbar\omega$ that come in from a predefined direction in the surface plane and under an angle β which is measured towards the surface normal. In addition to the photoelectron's kinetic energy also the emission intensities are recorded with respect to the polar angle θ and azimuthal angle ϕ . Measured ARPES spectra are usually visualized as photoelectron momentum maps. As the momentum of a photoelectron parallel to the substrate surface is conserved [Dam04], ARPES intensities are plotted as a function of the parallel components of the momentum (to be more precise as the parallel components of the wave vector \mathbf{k} , which are k_x and k_y according to the

³For clarity I will stick to the gas-phase notation of orbitals, i.e., to the term LUMO, although the LUMO is partially occupied in this kind of experiment.

sketch in Fig. 1.1) at a constant kinetic energy of the photoelectron. The parallel momenta follow directly from the emission angles and the photoelectron's kinetic energy $E_{\text{kin}} = \frac{\hbar^2 \mathbf{k}^2}{2m_e}$,

$$\hbar k_x = \sqrt{2m_e E_{\text{kin}}} \cos \phi \sin \theta, \quad (1.2)$$

$$\hbar k_y = \sqrt{2m_e E_{\text{kin}}} \sin \phi \sin \theta. \quad (1.3)$$

To exemplify, a measured momentum map of a PTCDA monolayer on Ag(110) is displayed in the right panel of Fig. 1.1. The photoemission intensity is normalized to one and encoded in colors, where deep blue represents no intensity and red maximal intensity. The spectrum is analyzed at a kinetic energy that corresponds to the binding energy of the highest occupied molecular orbital (HOMO). Hence, the observed ARPES signal can be interpreted as stemming from electrons that are ejected from the PTCDA HOMO. Most of the experiments presented in the publications in Part II were conducted by the group of Achim Schöll and Friedrich Reinert from the University of Würzburg at the Elettra synchrotron radiation facility using a nanoESCA photoemission microscope. For more details I refer the reader to Refs. [WPK⁺11, Wie13] and the Supplemental Material of Pubs. [P0], [P1], [P2], and [P5].

1.3 Electronic-structure theory and photoemission

Interpreting ARPES data on systems with high complexity solely from experimental observations is a challenging task if not impossible. Involved correlation effects in many-electron systems, interactions with a substrate, and last but not least interaction of the remaining system with the ejected electron might make important contributions to photoemission spectra. Yet, it is these effects that make studying PES attractive. An interpretation of PES in conjunction with electronic-structure theory, which ideally provides a sound theoretical framework of the PES process, can establish a promising avenue towards a comprehensive understanding of the central interaction mechanisms governing photoemission and the entire electronic structure of the probed systems.

The traditional approach to describe PES rests upon time-dependent perturbation theory. With Fermi's golden rule the transition probability between two states and, thus, the intensity J can in principle be calculated via [Hüf03]

$$J_I \propto |\langle \Psi_{I,\mathbf{k}}(N) | H_{\text{int}} | \Psi_0(N) \rangle|^2 \delta(\hbar\omega + E_0(N) - E_{I,\mathbf{k}}(N)). \quad (1.4)$$

The δ -function on the right side of Fermi's golden rule ensures energy conservation. Prior to the photoemission process the system is assumed to be in its ground state with a ground-state energy of $E_0(N)$ associated. $E_{I,\mathbf{k}}(N)$ describes the total energy of the final system which includes the kinetic energy of the photoelectron and the energy of the ionized molecule. The latter is not restricted to be in the ground state but generally can be found in its I th eigenstate. The transition matrix element consists of the initial N -electron state $\Psi_0(N)$, which is a solution of the N -electron Hamiltonian. Likewise, the N -electron final state $\Psi_{I,\mathbf{k}}(N)$ enters the matrix element. It is composed of the emitted electron and the ionized molecule with $N - 1$ electrons. An in practice common approximation neglects correlations between them. This allows for expressing $\Psi_{I,\mathbf{k}}$ as an antisymmetrized product of two separate states,

$$\Psi_{I,\mathbf{k}}(\mathbf{r}_1, \dots, \mathbf{r}_N) = \sum_{i=1}^N \frac{-1^{i+N}}{\sqrt{N}} \Psi_I(\mathbf{r}_1, \dots, \mathbf{r}_{i-1}, \mathbf{r}_{i+1}, \dots, \mathbf{r}_N) \chi_{\mathbf{k}}(\mathbf{r}_i). \quad (1.5)$$

Here, $\chi_{\mathbf{k}}$ stands for the emitted electron and $\Psi_I(N-1)$ for the I th eigenfunction of the $N-1$ -electron Hamiltonian that describes the singly ionized molecule.

The ionization process is prompted by H_{int} . It describes the interaction with a light field. In dipole approximation, which is justified if the wavelength of light is large compared to molecular distances⁴, H_{int} reads

$$H_{\text{int}} = \frac{e}{m_e c} \mathbf{A} \mathbf{P}. \quad (1.6)$$

Here, \mathbf{A} denotes the vector potential of the light field and $\mathbf{P} = \sum_{i=1}^N \mathbf{p}_i$ the many-body momentum operator.

Photoemission spectra are directly linked to the transition probability of Fermi's golden rule. Each transition from the initial ground state to a certain molecular final state $\Psi_I(N-1)$ will cause a photoemission peak. Its energetic location is uniquely determined by the energy conservation, i.e., by the δ -function in Eq. (1.4). Thus, photoemission peaks will only occur at photoelectron kinetic energies of

$$E_{\text{kin}} = \hbar\omega + E_0(N) - E_I(N-1) = \hbar\omega - IP_I. \quad (1.7)$$

The I th ionization energy IP_I is the minimal amount of energy that is required to eject an electron while leaving the ionized molecule in its I th excited state. The magnitude of the corresponding matrix element in Eq. (1.4) determines the emission peak heights.

The most involved ingredients to Fermi's golden rule that are needed to calculate PES spectra according to Eq. (1.4) are the correlated many-electron wavefunctions. They are solutions of the stationary Schrödinger equation $\hat{H}\psi = E\psi$ [Sch26]. In its nonrelativistic form the electronic Hamiltonian⁵ of an N -electron system under the influence of N_K nuclei is

$$H = \underbrace{-\sum_{i=1}^N \frac{\hbar^2}{2m_e} \nabla_i^2}_T + \underbrace{\frac{1}{2} \sum_{i,j=1, i \neq j}^N \frac{e^2}{|\mathbf{r}_i - \mathbf{r}_j|}}_{V_C} - \underbrace{\sum_{i=1}^N \sum_{j=1}^{N_K} \frac{e^2 Z_j}{|\mathbf{r}_i - \mathbf{R}_j|}}_{V_{\text{ext}}}. \quad (1.8)$$

The first term of Eq. (1.8) is the interacting kinetic energy operator T , the second is the electron-electron Coulomb interaction V_C , and the last term describes the interaction with an external potential V_{ext} , which is here given as the interaction with N_K individual nuclei placed at \mathbf{R}_j .

Solving the Schrödinger equation for many-electron systems exactly is far beyond the capability of state-of-the-art computational methods and will probably ever be. This is mainly caused by the intrinsic mathematical structure of the correlated many-body wavefunction. For N electrons, $\Psi(\mathbf{r}_1, \mathbf{r}_2, \dots, \mathbf{r}_N)$ depends on $3N$ spatial coordinates ($\mathbf{r} = (x, y, z)$) leaving the spin completely aside. The memory required for storing such an object scales with the power of $3N$. Even on sparse numerical grids one would quickly run into an enormous exponential barrier in terms of memory. Driven by the mentioned restriction, it is appealing to recast the many-body matrix element in Fermi's golden rule into an effective single-particle matrix element that formally depends on a single electronic coordinate,

$$J_I \propto |\langle \chi_{\mathbf{k}}(\mathbf{r}) | H_{\text{int}} | d_I(\mathbf{r}) \rangle|^2 \delta(\hbar\omega + E_0(N) - E_I(N-1) - E_{\text{kin}}). \quad (1.9)$$

All steps that are involved in the derivation are explicitly presented in Pubs. [P1], [P3], and Ref. [WH08]. The decisive idea behind Eq. (1.9) is to wrap up all information about the many-

⁴Photon energies used here are in the order of 10 eV, which corresponds to a wavelength of $\lambda \approx 10^3$ Å. The typical length scale of the studied molecules is at least one order of magnitude smaller.

⁵The adiabatic approximation [BO27] allows to decouple the description of electrons and nuclei.

body systems in the so-called Dyson orbital $d_I(\mathbf{r})$. Formally, it is defined as the projection of the molecular $N - 1$ -electron final state onto the N -electron initial state,

$$d_I(\mathbf{r}) = \sqrt{N} \langle \Psi_I(N-1) | \Psi_0(N) \rangle. \quad (1.10)$$

Yet, the Dyson orbital can be interpreted more intuitively: it pictures the photohole that arises during the photoemission process. In this line of thought, Eq. (1.9) can be understood as a transition from a quasiparticle state $d_I(\mathbf{r})$ to the state of an ejected photoelectron $\chi_{\mathbf{k}}(\mathbf{r})$. The notion of quasiparticles, which have their origin in many-body perturbation theory (MBPT) [FW71], provides a tremendous conceptual simplification for treating emergent phenomena in interacting many-body systems [Mat92]. One defines a quasiparticle as a bare particle that is dressed by the interaction with its environment, i.e., quasiparticles allow for conveniently accommodating complex many-body interactions in a single-particle quantity. Typical correlation effects are, for instance, the screening of the Coulomb interaction by the surrounding cloud of charges and electronic relaxation. Similar to single particles, quasiparticles can be attributed a quasiparticle energy. In the case of photoemission the quasiparticle energy ε_I has an exact physical meaning as it equates with IP_I .

To sum up, the prediction of PES and ARPES via Eq. (1.9) requires knowledge about the Dyson orbital, the state of the emitted electron, and the system's ionization energies. In practice there are several schemes to simulate photoemission intensities that follow distinct concepts. Dyson orbitals have been evaluated, for instance, with *ab initio* wavefunctions in the spirit of Eq. (1.10) [OK07]. However, this approach is only feasible for small systems as it easily exceeds the restrictions imposed by the wavefunctions presented above. In my work I will present different computationally traceable routes to calculate IPs and Dyson orbitals for a wider range of molecules, in particular molecular semiconductors. Publications [P0], [P1], [P3], and [P6] demonstrate in which cases single-particle orbitals and eigenvalues from DFT can be accurate approximations to Dyson orbitals and quasiparticle energies, respectively. I lay the foundations to these publications in chapter 2. Herein, I will present the basics of ground-state DFT, fundamental relations regarding photoemission, and offer an introduction to the publications. The second way to approximate Dyson orbitals from DFT, i.e., explicitly constructing Dyson orbitals from approximate wavefunctions according to Eq. (1.10), is to be presented in Pubs. [P1], [P2], and [P3].

I draft yet another perspective on photoemission in chapter 3. It completely breaks with the notion of describing the photoemission process by the evaluation of steady-state matrix elements as in Fermi's golden rule. Instead, the photoemission process is entirely described in the time domain. The exceptional feature of this approach is that it infers photoemission observables from simulating the time evolution of the probed system explicitly. The resulting advantages of such a method are delineated in Publ. [P4] for gas-phase PES and in Publ. [P5] for ARPES.

Finally, I give a brief synopsis of MBPT in the *GW* approximation in chapter 4. The merits of MBPT are that it provides a formally exact framework for quasiparticle calculations. In practice one still has to rely on computationally feasible approximations, as for example, the *GW* approximation. Nevertheless, *GW* is often heralded as the method of choice for quasiparticle calculations. Publications [P7] and [P8] demonstrate that the high accuracy of IPs from *GW* is strongly coupled to the satisfaction of the exact constraint of piecewise linearity.

CHAPTER 2

Ground-state density-functional theory

DFT has become one of the prevalent methods to predict PES. To explain the success and, of course, the limitations of DFT, this chapter gives a concise introduction to its principles. I focus on aspects that are wedded to photoemission in general and to my publications in particular. Therefore, Sec. 2.1 recaps the conceptual footings of DFT. Section 2.2 provides an overview of fundamental relations and exact constraints that are tied to photoemission. As DFT calculations rely on approximations for the exchange-correlation (xc) functional, I present frequently used representatives and briefly comment on their failures and achievements in Sec. 2.3. The subsequent section is devoted to the primary xc functional, i.e., a certain type of a self-interaction correction functional, which I employ throughout my work. One of the central aspects of my thesis is to examine the interpretability of Kohn-Sham orbitals in terms of quasiparticles in the context of ARPES, which I review in Secs. 2.5 and 2.6. In Sec. 2.6 I discuss a way to reveal the coupling of specific vibrational modes to electronic excitations. For details beyond the scope of my thesis and for a comprehensive textbook-like introduction to DFT, I recommend Refs. [PW89, DG90, FNM03, Cap06].

2.1 Foundations of ground-state density-functional theory

Recalling the obstructions imposed by the wavefunctions mentioned in the previous chapter, it seems appealing to consider the electron density as the fundamental property to describe many-electron systems as the spatial degrees of freedom can be reduced tremendously. This idea has been fueled particularly by the groundbreaking work of Hohenberg and Kohn, which proves that the ground-state electron density contains the same information as the exact ground-state wavefunction [HK64]. On a formal level the so-called Hohenberg-Kohn (HK) theorem, which sets the foundation of DFT, can be cast in two separate statements:

First, for a given electron-electron interaction there exists a one-to-one mapping between the ground-state electron density $n(\mathbf{r})$ and a local external potential $v_{\text{ext}}(\mathbf{r})$ (up to a physically irrelevant constant). Since the kinetic energy and the Coulomb operator are known, the entire electronic Hamiltonian of the system and, in turn, the ground-state wavefunction Ψ_0 are uniquely determined by the ground-state density. Therefore, all observables are in principle functionals of the ground-state density.

Second, minimizing the total-energy functional

$$E[n] = F[n] + \int v_{\text{ext}}(\mathbf{r})n(\mathbf{r}) \, d^3r \quad (2.1)$$

according to the Rayleigh-Ritz variational principle yields the exact ground-state density and energy [Lev82]. While the HK theorem proposes a formal way to solve the many-electron problem

that is in principle exact, there is one inherent flaw: the universal functional $F[n] = \langle \Psi[n] | \hat{T} + \hat{V}_C | \Psi[n] \rangle$, which is independent of the external potential, is typically not known exactly.

Finding a viable way to construct approximations for $F[n]$ led Kohn and Sham (KS) to invoke an auxiliary system of N noninteracting particles that is designed to reproduce the true electron density [KS65]¹. To do so, the many-body electron interaction is mapped onto a spatially local, multiplicative potential, the KS potential $v_\sigma^{\text{KS}}[n](\mathbf{r})$. Together with the noninteracting kinetic energy it determines the effective single-particle KS Hamiltonian and the KS equation,

$$\left(-\frac{\hbar^2}{2m_e} \nabla^2 + v_\sigma^{\text{KS}}[n](\mathbf{r}) \right) \varphi_{i\sigma}(\mathbf{r}) = \varepsilon_{i\sigma} \varphi_{i\sigma}(\mathbf{r}). \quad (2.2)$$

The eigenfunctions of Eq. (2.2), i.e., the KS orbitals $\varphi_{i\sigma}$, sum up to the true electron density,

$$n(\mathbf{r}) = \sum_{\sigma=\uparrow,\downarrow} \sum_{i=1}^{N_\sigma} f_{i\sigma} |\varphi_{i\sigma}(\mathbf{r})|^2 = \sum_{\sigma=\uparrow,\downarrow} \sum_{i=1}^{N_\sigma} f_{i\sigma} n_{i\sigma}(\mathbf{r}) = \sum_{\sigma=\uparrow,\downarrow} n_\sigma(\mathbf{r}). \quad (2.3)$$

Here, σ denotes the spin degree of freedom, $f_{i\sigma}$ are the Fermi occupation factors, and $\varepsilon_{i\sigma}$ are the KS eigenvalues. Behind the KS scheme lies a specific partitioning of the total energy and the universal functional, respectively,

$$E[n] = F[n] + \int v_{\text{ext}}(\mathbf{r}) n(\mathbf{r}) d^3r = T_s[\{\varphi_{i\sigma}[n_\sigma]\}] + E_H[n] + E_{\text{xc}}[n_\uparrow, n_\downarrow] + \int v_{\text{ext}}(\mathbf{r}) n(\mathbf{r}) d^3r. \quad (2.4)$$

To capture a major part of the Coulomb interaction, one draws on the well known classical Hartree interaction,

$$E_H[n] = \frac{e^2}{2} \int \int \frac{n(\mathbf{r}) n(\mathbf{r}')}{|\mathbf{r} - \mathbf{r}'|} d^3r d^3r'. \quad (2.5)$$

The second conceptually important step is to use the noninteracting kinetic energy functional,

$$T_s[\{\varphi_{i\sigma}[n_\sigma]\}] = -\frac{\hbar^2}{2m_e} \sum_{\sigma=\uparrow,\downarrow} \sum_{i=1}^{N_\sigma} f_{i\sigma} \int \varphi_{i\sigma}^*(\mathbf{r}) \nabla^2 \varphi_{i\sigma}(\mathbf{r}) d^3r, \quad (2.6)$$

which is an implicit functional of the electron density. Yet, $T_s[n]$ and $E_H[n]$ do not comprehensively describe the energies of interacting many-electron systems as they lack important contributions of the interacting kinetic energy T and the full Coulomb energy V_C . The neglected terms can formally be subsumed under the prominent xc functional,

$$E_{\text{xc}}[n_\uparrow, n_\downarrow] := (T[n] - T_s[\{\varphi_{i\sigma}[n_\sigma]\}]) + (V_C[n] - E_H[n]) = F[n] - E_H[n] - T_s[\{\varphi_{i\sigma}[n_\sigma]\}]. \quad (2.7)$$

While the magnitude of E_{xc} is typically small compared to T_s and E_H , it often makes the crucial contribution that is decisive for a correct description of various properties such as binding and ionization energies. Hence, E_{xc} is vital for every practical application of DFT.

Minimizing Eq. (2.4) with respect to the spin density leads to the noninteracting N -electron system proposed in Eq. (2.2), where the noninteracting electrons are subject to the KS potential

$$v_\sigma^{\text{KS}}[n](\mathbf{r}) = v_\sigma^{\text{xc}}[n](\mathbf{r}) + v_H[n](\mathbf{r}) + v_{\text{ext}}(\mathbf{r}). \quad (2.8)$$

It is composed of the xc, the Hartree, and the external potential. In practical applications, Eqs. (2.2),

¹An extension to spin-polarized systems is introduced in Ref. [vBH72].

(2.3), (2.4), and (2.8) are solved iteratively. They form the backbone of the KS scheme, which is in principle an exact reformulation of the many-body problem in quantum mechanics. The major advantage of the KS scheme is that it provides a significant conceptual and practical simplification of the many-body problem that is traceable for up to hundreds or even thousands of electrons when applying appropriate xc-functional approximations.

2.2 Fundamental relations with respect to photoemission

The persistent drawback of KS DFT is that the ultimate xc functional remains unknown for systems of practical relevance. Despite relying on approximations for the xc functional, one can formulate fundamental relations which the ultimate xc functional and potential, respectively, must obey. Satisfying as many of these exact constraints as possible has become one of the promising philosophies in the development of xc approximations [PRT⁺05]. I will mainly present relations that have impact on the prediction of photoemission observables, for more details on exact constraints I recommend Ref. [PK03].

The first relation that I want to discuss has immediate implications on photoemission. It guarantees that the HOMO eigenvalue obtained with the ultimate xc functional equals the negative, relaxed, vertical ionization potential [PPLB82, LPS84, AvB85, PL97],

$$\epsilon_{\text{HOMO}}(N) = E_0(N) - E_0(N-1) = -IP(N). \quad (2.9)$$

The relation follows from the asymptotic decay of the true electron density $n(\mathbf{r}) \sim \exp(-2\sqrt{2IP}r)$ of a finite system [AvB85]. As the KS density is governed by the least bound occupied KS orbital for large r which, in turn, decays with its eigenvalue $|\phi_{\text{HOMO}}(\mathbf{r})|^2 \sim \exp(-2\sqrt{-2\epsilon_{\text{HOMO}}}r)$ [KKG98], the IP and the exact HOMO eigenvalue have to be identical. Relation (2.9) is often referred to as the IP theorem. In contrast to Koopmans' theorem [Koo34], which is its counterpart in Hartree-Fock (HF), the IP theorem in DFT has the advantage of implementing the process of electronic relaxation. This is apparent from the total-energy difference of Eq. (2.9), where $E_0(N)$ and $E_0(N-1)$ are self-consistent ground-state energies. Accordingly, $E_0(N-1)$ and the underlying $N-1$ -electron density are fully adapted to the loss of one electron.

Since the IP theorem is rigorously valid only for the ultimate functional, HOMO eigenvalues from approximate functionals usually deviate from the exact IP. Whether approximate HOMO eigenvalues can still serve as reliable IP predictions will be part of the discussion within this chapter. To obtain an entire photoemission spectrum from DFT, also ionization energies of more strongly bound electrons have to be accessible. Unfortunately, DFT doesn't offer any equivalently exact relation between IPs and eigenvalues that lie energetically beneath the HOMO. It has been demonstrated, though, that KS eigenvalues from accurate *ab initio* densities can be decent approximations to IPs of outer valence electrons. Reported deviations to experiment are on the order of 0.1 eV [CGB02]. Furthermore, KS eigenvalues are connected to quasiparticle energies by an expansion in which they form the leading contribution [CGB02, GBB03, KK10]. These relations are of paramount importance as they put the customary approach of predicting photoemission spectra with DFT, i.e., approximating IPs by DFT eigenvalues from self-consistent ground-state calculations [BC95, AMH⁺00, MKHM06, SB09, KK10, KSRAB12], on solid ground.

An accurate IP prediction is further related to the asymptotic decay of the exact xc potential with $-e^2/r$ [LPS84, AvB85]. This fall-off is plausible considering a single electron far away from the system as it leaves behind a positively charged ion. The electron will experience the $-e^2/r$

potential, which matches the leading contribution from a multipole expansion of the electrostatic Coulomb potential of a single charge. A wrong asymptotic behavior is known to cause HOMO eigenvalues to deviate from the IP [CS13, SKKK14].

Yet another constraint can be deduced from one of the most paradigmatic systems: a single electron bound to a single nucleus. In this system there should obviously be no electron-electron interaction. However, if one inserts the density of a one-electron system $n_1(\mathbf{r})$ into the total-energy functional as it is partitioned in the KS scheme, the classical Hartree interaction will give a nonzero contribution,

$$E_{\text{H}}[n_1] = \frac{e^2}{2} \int \int \frac{n_1(\mathbf{r}) n_1(\mathbf{r}')}{|\mathbf{r} - \mathbf{r}'|} d^3r d^3r'. \quad (2.10)$$

To correct the artificial Hartree self-interaction energy, the xc functional has to compensate $E_{\text{H}}[n_1]$ exactly,

$$E_{\text{H}}[n_1] + E_{\text{xc}}[n_1, 0] = 0. \quad (2.11)$$

The bad news is that the most common xc approximations do not meet this requirement, giving rise to one of the prominent deficiencies of DFT, namely the spurious self-interaction error (SIE) [PZ81]. Since the SIE definition of Eq. (2.11) is rigorously defined only in the one-electron limit, it is difficult to find a universal criterion for many-electron systems. Yet, in 1981 Perdew and Zunger extended the concept of one-electron SIE (OE-SIE) to the many-electron case in a straightforward way. Keeping up the interpretation of individual orbital densities $n_i(\mathbf{r})$ as electrons, a system is declared to be free from OE-SIE if [PZ81]

$$\sum_{\sigma=\uparrow,\downarrow} \sum_{i=1}^{N_{\sigma}} (E_{\text{H}}[n_{i\sigma}] + E_{\text{xc}}[n_{i\sigma}, 0]) = 0. \quad (2.12)$$

Concerning photoemission, the presence of the OE-SIE manifests in severe distortions of the energetic location of eigenvalues. As demonstrated in Ref. [KKMK09, KKMK10], the distinctly varying energy contributions to eigenvalues which arise from the OE-SIE are depending on the degree of localization of the corresponding orbitals. Whereas localized orbitals often suffer from a large OE-SIE, delocalized states are less affected. The eigenvalue spectra of PTCDA or NTCDA are prime examples since their outer valence electronic structures are composed both of localized σ orbitals and of rather delocalized π orbitals. Particularly in scenarios like these, functionals affected by the OE-SIE predict orbitals in a notably distorted energetic order [DMK⁺06, KKMK09, KKMK10, SK16b], [P0], [P1], [P3], and [P6].

In their seminal work on fractional particle numbers within DFT, Perdew *et al.* [PPLB82] provided the basis for further relations. One of them states that the total energy of a quantum-mechanical ensemble, which is designed to describe a statistical mixture of the pure N and $N - 1$ -electron ground states of a system, has to change linearly with respect to fractional removal (or addition) of an electron,

$$E(f) = (1 - f)E_0(N - 1) + fE_0(N). \quad (2.13)$$

Here, f specifies the fractional charge, which is confined between $[0, 1]$ for each linear total-energy segment [PPLB82]. Figure 2.1 illustrates the straight-line condition for total energies between $N - 1$ and N as well as N and $N + 1$ electrons. Whether piecewise linearity is satisfied has been studied intensively on the DFT and HF level from various perspectives [ZY98, RPC⁺06, MSCY06, CMSY08, MSCY08, TDT08, KK13, CAR⁺14, KSKK15, VESN⁺15, AZH⁺16, SK16b]. A con-

cave (or convex) deviation from the straight-line condition is often dubbed (de-)localization error [CMSY08]. The latter term originates from the fact that, e.g., convex deviations from linearity cause spurious delocalization of charges, which can be seen best in stretched H_2^+ . Semilocal xc functional approximations yield a lower total energy compared to the piecewise linear total energy if both fragments are fractionally charged. Thus, the one electron erroneously favors a delocalization over both nuclei [CMSY08].

Further, the deviation from the straight line is often used as an alternative definition of the SIE in many-particle systems, termed many-electron SIE (ME-SIE). ME-SIE and the Perdew-Zunger definition of OE-SIE are not unrelated. Assuming that orbitals do not change when removing fractional charge from the HOMO (frozen-orbital approximation), only the occupation factor f_{HOMO} scales the total energy. While the kinetic energy and external energy are still changing linearly upon f_{HOMO} , the Hartree energy does not. More precisely, the Hartree contribution to the one-electron self-interaction energy corresponding to the density of the HOMO, $E_{\text{H}}[n_{\text{HOMO}}]$ as defined in Eq. (2.10), shows a quadratic dependence. Standard xc approximations are not able to compensate for the deviation from linearity. In fact, the OE-SIE often makes a major contribution to the total-energy behavior, giving rise to a close connection of both SIE definitions.

However, the definitions of the OE-SIE and the ME-SIE are not mutually interchangeable. This can be exemplified by some distinct properties of both definitions. Freedom of the OE-SIE, for example, does not automatically imply a vanishing ME-SIE and vice versa [RPC⁺07, HKKK12, SK16b]. On the one hand, the ME-SIE provides a stringent condition that is naturally fulfilled for the exact functional. On the other hand, single-particle densities obtained with the ultimate functional do not necessarily force the OE-SIE condition in Eq. (2.12) to be zero [HK12b]. In order to satisfy the OE-SIE condition, single-particle ground-state densities have to be used to evaluate Eq. (2.12) since xc functionals are only defined rigorously for ground-state densities. Single-particle densities that are part of many-electron systems typically don't meet this criterion. Yet, the compelling strength of the OE-SIE definition in the Perdew-Zunger sense is that it offers a intuitive and practical scheme to correct the OE-SIE [PZ81] while there is no obvious analogue for ME-SIE. Various studies point out that presently no xc expression is available that can globally restore (or intrinsically obey) the straight-line behavior without invoking system dependent parameters [MSCY06, VSP07, SK16b].

A consequence related to piecewise linearity is that the chemical potential

$$\mu = \begin{cases} \lim_{f \rightarrow 0} \partial E / \partial f |_{N-f} = -IP(N) \\ \lim_{f \rightarrow 0} \partial E / \partial f |_{N+f} = -EA(N) \end{cases} \quad (2.14)$$

jumps discontinuously at integer particle numbers resulting in a kink of the total energy curve between two linear segments [PPLB82, PL83]. This behavior is illustrated in Fig 2.1. The jump arises because the electron ejection energy $IP(N)$ and the electron affinity $EA(N)$ of an N -electron system differ by the fundamental gap

$$\Delta_{\text{f}} = IP(N) - EA(N). \quad (2.15)$$

In DFT the jump of the chemical potential can be attributed to two contributions. The first one stems from the discontinuity of the noninteracting kinetic energy that is equal to the KS HOMO-LUMO gap, $\Delta_{\text{KS}} = \epsilon_{\text{LUMO}}(N) - \epsilon_{\text{HOMO}}(N)$. The second part is due to a constant jump of the xc

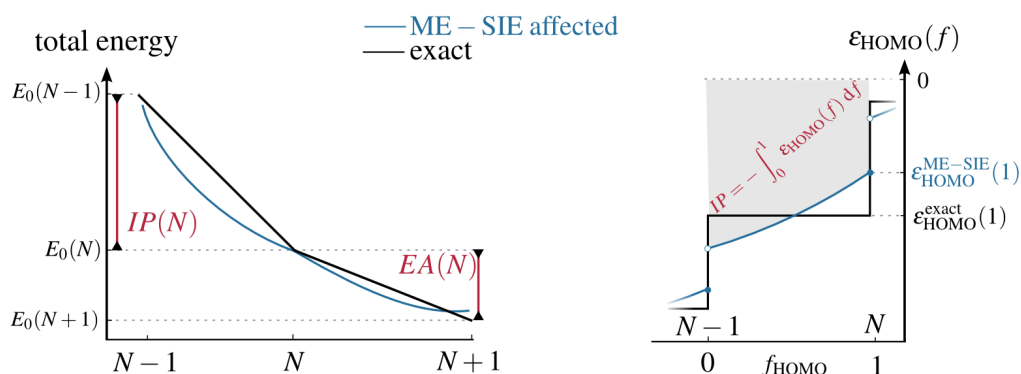


Figure 2.1: Left: Illustration of the straight-line condition. The black line corresponds to the linear total energy of the ultimate xc functional that is free from ME-SIE. The typical behavior of ME-SIE affected functionals (represented by the typical behavior of semilocal functionals) is sketched in blue. Right: Illustration of Janak's theorem and its relation to the IP.

potential when passing an integer electron number, which is the famous xc derivative discontinuity [PPLB82, PL83, SS83]. Critical for IP predictions from the KS HOMO eigenvalue in the spirit of the IP theorem in Eq. (2.9) is that common xc-functional approximations have an xc potential that is erroneously continuous at integer electron numbers. Instead of jumping, they yield an xc potential that averages over the xc derivative discontinuity which, in turn, results in a severe up-shift of ϵ_{HOMO} with respect to the true HOMO eigenvalue [PL83, TDT08].

The discussion of the constraints and relations has illustrated that most of them are closely connected. Even more insights into their relationship, especially regarding the IP prediction from approximate eigenvalues, is provided by Janak's theorem [Jan78]. It states that the derivative of the total energy with respect to the occupation number has to be equal to the occupation-number-dependent eigenvalue,

$$\frac{\partial E[n]}{\partial f_{i\sigma}} = \epsilon_{i\sigma}(f_{i\sigma}). \quad (2.16)$$

Remarkably, Janak's theorem holds for any approximate density-dependent xc functional. A closer look at this relation is particularly interesting for the HOMO eigenvalue. For a total energy that is piecewise linear between N and $N-1$ electrons the HOMO eigenvalue needs to be constant and independent of the occupation number. If Eq. (2.16) is reformulated by integration over f between both adjacent integer charges,

$$IP = E_0(N-1) - E_0(N) = -\int_0^1 df \epsilon_{\text{HOMO}}(f), \quad (2.17)$$

the HOMO eigenvalue can be tied to the IP directly. In the exact case in which the HOMO eigenvalue is constant upon f one arrives at the IP theorem as defined in Eq. (2.9). However, once the total energy exhibits a curvature, the eigenvalues necessarily have to be a nontrivial function of f . As a consequence it is unlikely that an f -dependent HOMO eigenvalue will suffice the IP theorem. This immediately affects the accuracy of IP predictions from HOMO eigenvalues of

individual N -electron ground-state calculations (illustrated on the right of Fig. 2.1) as it is done in the vast majority of applications. Functionals that are severely impaired by ME-SIE will lead to eigenvalues that strongly depend on f which, in turn, leads to lousy IPs. Thus, the bottom line of Janak's theorem viewed with respect to photoemission is that functionals which do not suffer from a large SIE can provide accurate eigenvalues for IP predictions.

In summary, this section suggests a few conditions which a functional should obey in order to be suited for a reliable description of photoemission spectra. To first rank comes the freedom of self-interaction (broadly speaking in the sense of both definitions) as it comprehensively affects a wide range of photoionization properties. I will therefore discuss an efficient scheme that corrects the OE-SIE in Sec. 2.4. Further, paying heed to the correct asymptotic decay and the presence of an xc derivative discontinuity is supposed to be vital for accurate eigenvalues. In the next section I will present practically relevant and instructive xc functional approximations. I will briefly comment on their capabilities regarding photoemission.

2.3 Common exchange-correlation functional approximations

From a historical point of view, the remarkable success of practical DFT was pioneered by the development of the local-density approximation (LDA) [HK64] (see Ref. [vBH72] for the spin-polarized case). It assumes that the electron density varies only slowly in space and, thus, is close to the spatially constant density of the uniform electron gas. This led to the idea of evaluating the xc energy density of the homogeneous electron gas with the local density $n(\mathbf{r})$ instead of a uniform density. For the exchange part of e_{xc}^{hom} an analytical expression is known [Dir30]. The correlation energy density e_c^{hom} is obtained from highly accurate Monte-Carlo calculations [CA80] with different parametrization as, for example, the one by Perdew and Wang [PW92]. The total LDA xc energy is the sum of both contributions,

$$E_{xc}^{\text{LDA}}[n] = \int d^3r \left(e_x^{\text{hom}}[n(\mathbf{r})] + e_c^{\text{hom}}[n(\mathbf{r})] \right). \quad (2.18)$$

Consistent improvements over the LDA are achieved by the class of semilocal generalized-gradient approximations (GGA) [PK03]. This class of functionals includes the gradients of the density to account for deviations from homogeneity in a controlled way, i.e., it preserves the correct features of the LDA while adding others [PK03]. All GGAs follow the general structure of

$$E_{xc}^{\text{GGA}}[n] = \int d^3r e_{xc}^{\text{GGA}}(n(\mathbf{r}), \nabla n(\mathbf{r})), \quad (2.19)$$

where e_{xc}^{GGA} is constructed to either fulfill exact constraints or by a suitable empirical fitting. The classic example of the former is the Perdew-Burke-Ernzerhof (PBE) functional [PBE96] and of the latter the Becke exchange, Lee-Yang-Parr correlation (BLYP) functional [Bec88, LYP88].

Although GGAs do not reach chemical accuracy for thermochemistry, they improve, for example, over the LDA in predicting atomization energies and bond strengths [PK03]. Yet, the LDA and typical GGAs suffer from similar notorious deficiencies [KK08]. Neither exhibits an xc derivative discontinuity and, instead, averages it. As discussed before, this leads to a serious underestimation of the IP and overestimation of the EA [PL83, TDT08]. Contrasting eigenvalues to PES data, this deficiency is usually compensated by rigidly shifting all eigenvalues such that the HOMO is in accord with the first experimental IP [KK14]. Further, both are grossly affected by SIE, which can

lead to severe distortions in the eigenvalue spectra [KKMK09, KMK10, KK14].

Besides semilocal functionals, the second major class of functionals involves not only the electron density (and gradients thereof) but explicitly depends on the orbitals and can have a spatially nonlocal xc potential [KK08], which promises more flexibility in the construction of functionals. A typical representative is the exact-exchange (EXX) functional as known from the Fock exchange of HF. Formulated in terms of KS orbitals it reads

$$E_x^{\text{EXX}}[\{\varphi_{i\sigma}[n_\sigma]\}] = -\frac{e^2}{2} \sum_{\sigma=\uparrow,\downarrow} \sum_{i,j=1}^{N_\sigma} f_{i\sigma} f_{j\sigma} \int \int d^3r d^3r' \frac{\varphi_{i\sigma}^*(\mathbf{r}) \varphi_{j\sigma}^*(\mathbf{r}') \varphi_{i\sigma}(\mathbf{r}') \varphi_{j\sigma}(\mathbf{r})}{|\mathbf{r} - \mathbf{r}'|}. \quad (2.20)$$

EXX cancels the Hartree self-interaction error entirely, induces the correct asymptotic decay of the corresponding EXX potential, but completely lacks correlation.

Recalling the deficiency of semilocal functionals, it seems to be a promising strategy to combine the merits of semilocal functionals and EXX. Conventional hybrids² do so by mixing a fixed amount α of EXX with approximate (app), typically semilocal, exchange and correlation,

$$E_{xc}^{\text{hyb}} = \alpha E_x^{\text{EXX}} + (1 - \alpha) E_x^{\text{app}} + E_c^{\text{app}}. \quad (2.21)$$

This general type of functional together with a certain nonempirical mixing α can be substantiated by the adiabatic connection theorem [HJ74, Bec93b, EPB97]. A typical representative is the PBE hybrid (PBEh) functional. It combines PBE exchange and EXX by a ratio of α with full PBE correlation. A specific and nonempirically parametrized case is the PBE0 functional with $\alpha = 0.25$ [PEB96, AB99]. The Becke, 3-parameter, Lee-Yang-Parr (B3LYP) global hybrid functional, which is heavily used for thermochemistry, employs even three parameters in its construction [Bec93a, SDCF94]. They are determined by extensive empirical fitting [Bec93a]. Due to the inclusion of a fraction of EXX, hybrids at least partly remedy the OE-SIE, have an improved asymptotic $\sim -\alpha e^2/r$ decay³, and they exhibit an xc derivative discontinuity because of the explicit orbital dependence [KK08]. The prediction of IPs and generally outer valence PES spectra benefit from hybrid functionals, yet there are still unsatisfying deviations to experimental PES spectra [KK14].

More sophisticated hybrid schemes, for instance local hybrid functionals [JSE03, SKM⁺14] or range-separated hybrids [SF95, LSWS97], depart from a globally fixed mixing. For range-separated hybrids the electron-electron interaction is split into a short-range (typically described by semilocal exchange) and a long-range part (typically described by EXX) [LSWS97]. The range separation is mediated via a smooth, r dependent function which is controlled by a range-separation parameter. The approach is ideally suited for finding a well tempered balance between EXX, which enforces the correct long-range asymptotic of the potential, and short-range semilocal exchange, which, in turn, maintains the delicate balance with semilocal correlation. In optimally-tuned range-separated hybrids (OT-RSH) [SKB09, SEKB10, BLS10, KSRAB12, RASG⁺12], [P6] the range-separation parameter can be tuned such that the IP theorem (2.9) is obeyed. As discussed in Publ. [P6] for the case of prototypical organic molecules, OT-RSHs serve as an excellent tool for predicting highly

²The term hybrid was coined by the fact that they were understood as a hybrid of DFT and HF theory [Bec93b]. Yet, hybrid functionals were later shown to be well founded in the realm of DFT by virtue of the generalized KS scheme [SGV⁺96] or optimized effective potential method [KK08].

³For the discussion of the potential asymptotics of orbital-dependent functionals I always refer to an evaluation within the optimized effective potential formalism [KK08] as it leads to a local potential that is the same for all orbitals.

accurate ionization energies and photoemission spectra, respectively. Particularly, a comparison to OE-SIE free approaches illustrates that OT-RSHs are able to mitigate OE-SIE efficiently although they are not completely free from the OE-SIE.

Evaluating orbital functionals

To make practical use of orbital functionals one has to face a difficulty arising from the orbital dependence: in order to construct a local, multiplicative xc potential, as it is required in the KS equation (2.2), the derivative of the xc functional has to be taken with respect to the density,

$$v_{\sigma}^{\text{xc}}(\mathbf{r}) = \frac{\delta E_{\text{xc}}[\{\varphi_{i\alpha}\}]}{\delta n_{\sigma}(\mathbf{r})}. \quad (2.22)$$

There are two distinct strategies to tackle this problem [KK08]. Either the KS scheme is generalized in the sense that the derivative is taken with respect to the orbitals instead of the density, or one exploits the fact that the orbitals themselves are functionals of the density, which allows to take the derivative with respect to the density. While the former approach, the so-called generalized Kohn-Sham (GKS) scheme [SGV⁺96], resides in the realm of DFT, it leaves the scope of KS theory. The GKS approach roots in a mapping of an interacting N -electron system onto an auxiliary, partially interacting system that is represented by a single Slater determinant. Minimizing the energy with respect to the orbitals leads to a set of single-particle equations. Each equation has an orbital specific and in general nonlocal potential. In light of this, the GKS equations require more effort to be solved. Yet, it is the most popular way to apply hybrids in practice (which I also have used in Pubs. [P7] and [P8]).

The optimized effective potential (OEP) formalism marks the second approach [SH53, TS76, Cas95a, KK08]. It sticks to the conceptual realm of KS DFT by applying the functional derivative chain rule to Eq. (2.22),

$$v_{\sigma}^{\text{xc,OEP}}(\mathbf{r}) = \sum_{\tau=\uparrow,\downarrow} \sum_{j=1}^{N_{\tau}} \int \frac{\delta E_{\text{xc}}[\{\varphi_{i\alpha}\}]}{\delta \varphi_{j\tau}(\mathbf{r}')} \frac{\delta \varphi_{j\tau}(\mathbf{r}')}{\delta n_{\sigma}(\mathbf{r})} d^3r' + c.c.. \quad (2.23)$$

This equation can be transformed into its typical form, i.e., the OEP integral equation [KK08]. Solving it for the local, multiplicative xc potential $v_{\sigma}^{\text{xc,OEP}}$ is a feasible, yet tedious task that can be realized by applying the S-iteration scheme proposed in Refs. [KP03a, KP03b]. Due to the high computational demands, approximations to the full OEP are often preferred in practice. Most frequently used is the Krieger-Li-Iafrate (KLI) approximation [KLI92]. It can be interpreted as a mean-field approximation to the OEP [KK08].

Concerning the interpretation of eigenvalues as quasiparticle energies, the GKS and KS (also via OEP) schemes lead to differences which are discussed, for example, in Publ. [P6] and Ref. [KK10]. The nonlocal exchange contribution in GKS can bring the outer valence eigenvalues closer to quasiparticle energies. This can be explained from two perspectives. First, the additional nonlocality resembles the in general nonlocal self-energy operator of the quasiparticle equation (Dyson's equation) of MBPT more closely [KK08, KSRAB12, KK14]. Second, the fraction of nonlocal Fock exchange can be understood as mimicking a part of the first-order correction of KS eigenvalues towards ionization energies as derived by Chong *et al.* [CGB02, KK10]. When the effect of a nonlocal xc contribution is evaluated non-self-consistently on top of semilocal KS eigenvalues and orbitals, it results in an effective stretching of the KS eigenvalue spectrum [KK10]. On the other hand, the OEP formalism establishes a closer connection between pairs of KS orbitals

and eigenvalues due to one local potential. This particularly eases a combined interpretation of orbitals and eigenvalues [P0]. Further, the OEP guarantees all benefits of KS DFT [KK08] such as the interpretation of the KS HOMO eigenvalue via Janak’s theorem, which is only valid in the KS framework.

2.4 Self-interaction correction within the Kohn-Sham scheme

As discussed in the previous sections, correcting the SIE is one of the keys towards reliable eigenvalue spectra. Starting from the OE-SIE definition of Eq. (2.12), one can formulate the famous self-interaction correction (SIC) scheme suggested by Perdew and Zunger [Per79, PZ81]. If one identifies the OE-SIE contribution per particle arising from the spurious Hartree energy and an approximate xc functional with

$$\delta_{i\sigma} = E_{\text{H}}[n_{i\sigma}] + E_{\text{xc}}^{\text{app}}[n_{i\sigma}, 0], \quad (2.24)$$

it seems natural to correct for this energy contribution. On top of an approximate functional such as LDA⁴ a new SIC functional can be defined by subtracting the OE-SIE energies from the approximate $E_{\text{xc}}^{\text{app}}$,

$$\begin{aligned} E_{\text{xc}}^{\text{SIC}}[\{\phi_{i\sigma}\}] &= E_{\text{xc}}^{\text{app}}[n_{\uparrow}, n_{\downarrow}] - \sum_{\sigma=\uparrow, \downarrow} \sum_{i=1}^{N_{\sigma}} \delta_{i\sigma}[n_{i\sigma}] \\ &= E_{\text{xc}}^{\text{app}}[n_{\uparrow}, n_{\downarrow}] - \sum_{\sigma=\uparrow, \downarrow} \sum_{i=1}^{N_{\sigma}} (E_{\text{H}}[n_{i\sigma}] + E_{\text{xc}}^{\text{app}}[n_{i\sigma}, 0]). \end{aligned} \quad (2.25)$$

By construction, the SIC expression is an explicitly orbital-dependent functional and, thus, an implicit functional of the density. This makes a first choice necessary: either it is evaluated via a direct minimization of $E_{\text{xc}}^{\text{SIC}}$ with respect to the orbitals as done in the first application [PZ81], or one reverts to the KS world via the OEP formalism. As discussed in Refs. [VSP07, KK08], the former would lead to generally nonorthogonal and spatially localized orbitals from orbital-specific potentials and to eigenvalues that are not straightforward to interpret. These issues can be avoided by the OEP method. Supportive of IP predictions, the well-defined KS SIC xc potential shows the desired $-e^2/r$ decay in the asymptotic limit. This is owed to the fast exponential fall-off of the LDA xc potential leaving the field to the correct decay of the Hartree part of the SIC xc potential. It is also worth noting that SIC exhibits integer discontinuities [Per90, HK12a]. Besides these general remarks, there is another important subtlety buried in the SIC expression. If two different sets of orbitals that reproduce the same total density are used, two different total energies will be obtained. Thus, the SIC expression is variant under unitary orbital transformations. At first glance this seems like a curious feature of SIC. Yet, it is deeply rooted in its definition as there is no rigorous way to define one-electron densities in a many-electron system. Neither KS orbitals nor any other type of single-particle orbitals are distinguished if their sum reproduces the true total density. Viewed from a different angle, the ambiguity – or more positively phrased the additional degree of freedom – can be exploited in a physically meaningful way. Vital to all electronic-structure approaches and DFT in particular is the energy-minimization principle. In the very same spirit, it seems encouraging to use a set of orbitals that minimizes the SIC energy. Starting from, e.g., the KS orbitals, one can

⁴I apply the LDA throughout this work. For a discussion of other choices I refer the reader to Refs. [HKKK12, HK12b].

construct a unitary orbital transformation

$$\tilde{\varphi}_{i\sigma} = \sum_{j=1}^{N_\sigma} U_{ij}^\sigma \varphi_{j\sigma}, \quad (2.26)$$

which can enforce the derived orbital set to, e.g., minimize the SIC energy while retaining the same total density $n_\sigma(\mathbf{r}) = \sum_{i=1}^{N_\sigma} |\varphi_{i\sigma}(\mathbf{r})|^2 = \sum_{i=1}^{N_\sigma} |\tilde{\varphi}_{i\sigma}(\mathbf{r})|^2$. Inserting the energy-minimizing orbitals $\tilde{\varphi}_{i\sigma}$ into the Perdew-Zunger SIC expression imposed on the LDA leads to the definition of the E_{\min} -SIC energy functional

$$E_{\text{xc}}^{E_{\min}\text{-SIC}}[\{\tilde{\varphi}_{i\sigma}\}] = E_{\text{xc}}^{\text{LDA}}[n_\uparrow, n_\downarrow] - \sum_{\sigma=\uparrow, \downarrow} \sum_{i=1}^{N_\sigma} (E_{\text{H}}[|\tilde{\varphi}_{i\sigma}|^2] + E_{\text{xc}}^{\text{LDA}}[|\tilde{\varphi}_{i\sigma}|^2, 0]). \quad (2.27)$$

The optimization of the unitary transformation builds on the works of Pederson *et al.* [PHL84, PHL85, PL88]. It was later refined such that the transformation allows for complex-valued orbitals [HKKK12]. On the one hand, complex transformations are required for a time-dependent generalization of the E_{\min} -SIC approach. On the other hand, complex-valued orbitals are promising from a fundamental point of view. In order to maintain orthogonality between the orbitals, complex orbitals need fewer nodal planes and are smoother in contrast to their real counterparts [HKKK12]. One may thus argue that complex orbitals are closer to ground-state orbitals. As any ground-state xc functional is rigorously defined only on the domain of ground-state densities, an evaluation of Eq. (2.27) with orbital densities that are closer to one-electron ground-state densities is more appropriate, especially in the OE-SIE context which explicitly identifies orbital densities with electrons [HK12b, HKKK12]. Whether complex-valued orbitals meet this criterion is discussed in appendix A.6. While I find that complex orbital densities have indeed fewer nodal planes compared to their real counterparts, they are generally not v -representable [Koh83], i.e., are not one-electron ground-state densities that arise from a local potential.

A second type of unitary transformation that I have used in my work employs spatially localized Foster-Boys (FOBO) orbitals [Boy60, FB60, KKM08]. As the Hartree energy is very sensitive to the degree of localization, E_{H} can be increased by inserting localized densities. Thus, similar to energy-minimizing orbitals, FOBO orbitals reduce the SIC energy. It was also shown that they are good approximations to real-valued energy-minimizing orbitals [HKKK12]. Finding a localizing transformation is numerically less expensive than an energy minimizing one, which offers a great trade-off for heavier calculations.

To generalize the OEP formalism in such a way that unitary transformations can be included in the construction of a KS SIC potential, the functional-derivative chain rule in Eq. (2.23) needs to be extended to the transformed orbitals [KKM08]. Also for the so-called generalized OEP (GOEP) a generalized KLI (GKLI) approximation exists [KKM08]. Especially for SIC it matters on which level the xc potential is computed. Employing energy-minimizing orbitals, GKLI is a reliable approximation to the full GOEP, while this is not necessarily the case without unitary optimization [KMK08, KKM08]. In the following I will use the abbreviation GSIC for approaches that utilize the Perdew-Zunger SIC expression in conjunction with a localizing or energy-minimizing orbital transformation which is evaluated within the GKLI approximation.

With respect to PES, an argument which suggests that SIC eigenvalues are good approximations to relaxed IPs can be established via Janak's theorem. As discussed earlier, SIC approaches are supposed to lead to total energies that should not severely deviate from piecewise linearity. Hence, Eqs. (2.16) and (2.17) substantiate the connection between presumably scarcely f -dependent GSIC

HOMO eigenvalues and relaxed IPs. Unfortunately, the unitary orbital transformation as used here does not permit to validate this argument explicitly as the total energy cannot be calculated at fractional particle numbers.

It was further argued by Perdew and Zunger that SIC eigenvalues should benefit from an effective cancellation of errors [PZ81]. The IP theorem can be reformulated as [PZ81]

$$IP = -\epsilon_{\text{HOMO}} + \Sigma + \Pi. \quad (2.28)$$

The non-Koopmans correction Π denotes all differences between the eigenvalue and the unrelaxed IP⁵. The orbital relaxation energy Σ measures the energy difference between the unrelaxed and relaxed IP. As demonstrated for the Perdew-Zunger SIC approach, both terms reasonably cancel each other in the case of atomistic densities [PZ81]. I will discuss whether this relation is fulfilled for a few systems beyond the atomic level in appendix A.6, where I employ the GSIC approach and SIC evaluated with the OEP using KS orbitals only. Here, it becomes apparent that the cancellation is not systematic, which is why I cannot make a general statement about an effective cancellation of errors.

Further, it turns out that SIC HOMO eigenvalues obtained by solving the traditional OEP tend to slightly overestimate experimental IPs, which is in clear contrast to the underestimation predicted by semilocal xc approximations [KKM08]. This tendency is further enhanced with GSIC due to the additional energy-minimization step of the unitary transformation. The additional energy-minimization procedure might deepen the KS potential and, therefore, moves down the eigenvalue spectrum in energy. In practice, this error is typically compensated by applying a rigid shift to all GSIC eigenvalues if the eigenvalue spectrum is contrasted to photoemission experiments, see, for example, Pubs. [P4] and [P6].

Despite overestimating absolute IPs, the power of the GSIC approach manifests in highly accurate relative eigenvalue differences and a vastly correct energetic ordering of the KS states [KKMK09, KKMK10], [P0], [P1], [P3], and [P6]. Particularly the latter feature is of paramount importance for a sound interpretation of KS orbitals in terms of photoemission, which I will discuss in the following section.

2.5 The molecular orbital interpretation and orbital tomography

With all the considerations about eigenvalues and photoemission spectra in mind it is natural to ask whether KS orbitals can be granted a physical meaning, too. For a long time it was commonly acknowledged that one should not have too high expectations of the interpretation of KS orbitals as they are merely auxiliary quantities of which the sum of the squares add up to the true total electron density. This is nicely reflected by a, as they have admitted, exaggerating statement of Ralf Stowasser and Roald Hoffmann [SH99]: “[...] the physicists and chemists who use density functional theory so fruitfully have by and large shied away from attributing to Kohn-Sham orbitals the reality that (we think) they deserve.” Yet, there are several arguments that are supportive of meaningful KS orbitals [BG97, SH99]. I will inspect the interpretation of KS orbitals in the context of photoemission, i.e., whether they may serve as approximations to Dyson orbitals.

To that end, I briefly introduce the quasiparticle framework behind Dyson orbitals and discuss their

⁵The term is adopted from HF since Koopmans’ theorem establishes a one-to-one correspondence between eigenvalues and unrelaxed IPs [Koo34].

relation to KS orbitals. Dyson orbitals are solutions to the so-called Dyson's quasiparticle equation [Mat92, FW71],

$$\left[-\frac{\hbar^2}{2m_e} \nabla^2 + v_H(\mathbf{r}) + v_{\text{ext}}(\mathbf{r}) \right] d_I(\mathbf{r}) + \int \Sigma_{\text{xc}}(\mathbf{r}, \mathbf{r}', \varepsilon_I^{\text{QP}}) d_I(\mathbf{r}') d^3 r' = \varepsilon_I^{\text{QP}} d_I(\mathbf{r}). \quad (2.29)$$

In the limit of full correlation, this definition and the one given in Eq. (1.10), i.e., the projection of the I th molecular $N \pm 1$ -electron onto the N -electron wavefunction, are equivalent. Equation (2.29) is a generalized eigenvalue equation whose quasiparticle solutions fall into two branches: ionization and electron attachment. I will only consider the photoionization solution here, where $\varepsilon_I^{\text{QP}}$ is the I th ionization energy and $d_I(\mathbf{r})$ are the corresponding Dyson orbitals⁶. Superficially speaking, the structure of Dyson's equation seems quite familiar to the KS equation (2.2) since both contain the noninteracting kinetic energy, the Hartree potential, and an external potential. However, there are essential differences. The KS equation and the Dyson's equation are motivated by distinct physical concepts (see chapter 4 or Refs. [FW71, Mat92] for the Dyson's equation). While the KS equation resembles a time-independent single-particle Schrödinger equation, Dyson's equation is in fact an exact many-body equation for charged excitations instead of steady-state energies. The difference arises from the xc self-energy operator Σ_{xc} . It is a nonlocal, nonmultiplicative, and energy-dependent operator, which includes many-body correlation effects such as relaxation, self-interaction correction to the Hartree potential, screening, and dynamic polarization. As the self-energy is also non-Hermitian, Dyson orbitals are neither normalized nor orthogonal. Despite these discrepancies, there are several formal arguments in favor of a close connection between Dyson and KS orbitals. For instance, the squares of the absolute values of both types of orbitals sum up to the exact electron density. If one finds regions in space that are dominated by one single orbital, Dyson and KS orbitals can differ by no more than a phase factor. Following the discussion of the IP theorem in Sec. 2.2, this is particularly interesting for the HOMO in the asymptotic limit. As all other orbitals fall off more quickly, the KS HOMO and the Dyson orbital HOMO must have the same exponential decay as the density. Thus, for the large r limit one finds [DCCS94]

$$\lim_{r \rightarrow \infty} \frac{|\varphi_{\text{HOMO}}(\mathbf{r})|^2}{|d_{\text{HOMO}}(\mathbf{r})|^2} = 1. \quad (2.30)$$

Duffy *et al.* [DCCS94] also pointed out that KS orbitals can be viewed as a zeroth-order approximation in a perturbation expansion where the difference between the xc potential and the xc self-energy is considered as the perturbation. First-order corrections are then due to the immediate difference of the xc self-energy to the xc KS potential,

$$d_I(\mathbf{r}) \approx \varphi_i(\mathbf{r}) + \sum_{j, j \neq i} \varphi_j(\mathbf{r}) \frac{\langle \varphi_j | \Sigma_{\text{xc}}(\varepsilon_I^{\text{QP}}) - v_{\text{xc}} | \varphi_i \rangle}{\varepsilon_i - \varepsilon_j}, \quad (2.31)$$

where $\varepsilon_I^{\text{QP}} = \varepsilon_i + \langle \varphi_i | \Sigma_{\text{xc}}(\varepsilon_I^{\text{QP}}) - v_{\text{xc}} | \varphi_i \rangle$ is the first-order quasiparticle energy [DCCS94]. Whether KS orbitals are suitable approximations to Dyson orbitals is therefore primarily a question of the extend to which the KS xc potential resembles the self-energy. As a matter of fact, it was demonstrated that the exact KS xc potential is the variationally best local approximation to the xc

⁶Extending the analogy to electron attachment within DFT, unoccupied states are responsible to describe quasidelectrons and electron affinities. This is problematic even in the exact case since the HOMO-LUMO gap differs from the fundamental gap by the xc derivative discontinuity [PL83, SS83]. For a detailed overview of the interpretation of virtual KS eigenvalues I recommend Ref. [BGvM13].

self-energy in the Dyson's equation [Cas95a]. Further, the local, multiplicative potential in KS DFT facilitates a mutual interpretation of KS eigenvalues and orbitals. Thus, high quality eigenvalues should indicate good KS orbitals.

Despite the fact that all these formal considerations suggest a close resemblance of both types of orbitals, they do not make strong statements about the quality of KS orbitals as approximations to Dyson orbitals. This is where ARPES comes into play.

In the seminal work of Puschnig *et al.* [PBF⁺09] on orbital tomography [P0], [SWR⁺12, WHS⁺14, WLU⁺15], the authors paved the way for a surprisingly simple, yet illuminating interpretation of ARPES experiments. They proposed a one-step model for the photoemission process where an electron that is localized in a certain molecular orbital is ejected into an unbound state. If the state of the emitted electron is assumed to be completely unperturbed, meaning it can be described reasonably well by a plane wave (PW) [Gad74], the photoemission intensity within Fermi's golden rule reads

$$J_i \propto |\langle e^{i\mathbf{k}\mathbf{r}} | \mathbf{A}\mathbf{p} | \varphi_i(\mathbf{r}) \rangle|^2 \delta(\hbar\omega + \varepsilon_i - E_{\text{kin}}). \quad (2.32)$$

The matrix element can be simplified by conducting a Fourier transform of the depleted orbital from real to momentum space, which leads to

$$J_i(k_x, k_y) \propto |\mathbf{A}\mathbf{k}|^2 |\varphi_i(\mathbf{k})|_{|\mathbf{k}|=\sqrt{2m_e E_{\text{kin}}/\hbar^2}}^2. \quad (2.33)$$

Due to the energy conservation, the kinetic energy of the photoelectron $E_{\text{kin}} = \frac{\hbar^2 \mathbf{k}^2}{2m_e}$ and, hence, $|\mathbf{k}|$, is constant if $\hbar\omega$ is fixed. Thus, for a predefined kinetic energy the ARPES intensity is obtained by a hemispherical cut through the k -space representation of the absolute value of the orbital. Plotted as a two dimensional momentum map, the ARPES intensity $J_i(k_x, k_y)$ can be interpreted as a tomographic image of a molecular orbital.

However, the notion of viewing the photoemission process in terms of molecular orbitals might be a serious simplification. As it is shown in Sec. 1.3 and in greater detail in Publs. [P1] and [P3], a solid theoretical model for photoemission and particularly ARPES can be derived from a stringent many-body perspective. Keeping up the PW approximation, the photoemission intensity can be formulated in terms of Dyson orbitals as follows (see also Eq. (1.9)):

$$J_I \propto |\langle e^{i\mathbf{k}\mathbf{r}} | \mathbf{A}\mathbf{p} | d_I(\mathbf{r}) \rangle|^2 \delta(\hbar\omega + \varepsilon_I - E_{\text{kin}}). \quad (2.34)$$

On the conceptual level, the change between the many-body and the molecular-orbital picture narrows down to the difference between the Dyson and the molecular orbital. Thus, instead of describing a transition of a photoelectron as to originate from a molecular orbital, Eq. (1.9) describes the transition from a quasiparticle state into an unbound sate. Also in this many-body picture the ARPES intensity of Eq. (1.9) boils down to a Fourier transform of the Dyson orbital from real to momentum space,

$$J_I(k_x, k_y) \propto |\mathbf{A}\mathbf{k}|^2 |d_I(\mathbf{k})|_{|\mathbf{k}|=\sqrt{2m_e E_{\text{kin}}/\hbar^2}}^2. \quad (2.35)$$

Except of the Dyson orbital, only the polarization⁷ dependent scaling factor $|\mathbf{A}\mathbf{k}|^2$ influences the ARPES intensity. The PW approximation has been demonstrated to work accurately for the case of planar molecular semiconductors if the ARPES spectrum is not crucially depending on the energy and if the light polarization direction is chosen such that it is aligned parallel to the favored photoemission directions [PBF⁺09]. More detailed comments on the validity of the PW approximation are presented in Chap. 3, Publ. [P5], and Refs. [PBF⁺09, BW15]. In particular, Publ. [P5] analyses the limits of the PW approximation explicitly and proposes a method to go beyond.

The compelling strength of Eq. (2.35) is the direct interpretation of ARPES momentum maps as tomographic images of Dyson orbitals. Thus, it establishes an ideally suited means to check whether KS orbitals do reflect Dyson orbitals by contrasting them to experimental data. This is precisely what is in the focus of Pubs. [P0], [P1], and [P3].

In summary, the publications reveal profound differences in the upper valence DFT orbitals as predicted by various xc functionals for prototypical organic semiconductors. Consequently, the theoretical momentum maps of the DFT orbitals can differ notably. Whether xc functionals yield orbitals that agree with experimental observations from ARPES experiments is a question of the complexity of the probed molecule's electronic structure. For molecules which have a rather simple electronic structure like pentacene even semilocal approaches achieve a reasonable description of the upper orbitals. This is due to the strong delocalization of all outer-valence orbitals on similar length scales. Consequently, the orbitals are all equally affected by a rather small OE-SIE. However, if the system's electronic structure gets more involved, more sophisticated approaches are required. In fact, the freedom of self-interaction is the primary key towards an agreement with measured momentum maps. This can be expected from the preliminary considerations within this chapter. The GSIC approach fulfills many of the demanded relations of Sec. 2.2, including its very feature of correcting the OE-SIE completely. The differences in the predictive power of various functionals become particularly apparent in the case of ARPES momentum maps of PTCDA and NTCDA. In contrast to the GSIC approach, OE-SIE affected functionals such as PBE or B3LYP (the latter to a lesser extend, though) often predict severely distorted eigenvalue spectra and, thus, different orderings of states. While GSIC correctly predicts delocalized π orbitals as the uppermost orbitals, OE-SIE affected functionals in many cases favor the σ orbitals to surface near the Fermi level. The more localized σ orbitals differ vastly in spatial shape from π states. The signatures of σ orbitals are not observed in ARPES experiments. Conversely, the momentum maps of π orbitals agree with measured ARPES spectra. It is also worth noting that not only the most physically sound HOMO but also outer valence GSIC orbitals were shown to yield matching momentum maps. All these results indicate that KS orbitals from self-interaction corrected xc functionals can indeed be able to capture essential aspects of Dyson orbitals.

2.6 Beyond the molecular-orbital interpretation: the wavefunction perspective

In chapter 1 I initially introduced the l th Dyson orbital as the projection of the molecular $N - 1$ -electron onto the N -electron wavefunction, see Eq. (1.10). In this section I propose an approach to approximate Dyson orbitals from DFT with the aid of Eq. (1.10), which aims to go beyond the purely molecular-orbital picture. As explained in Pubs. [P1] and [P3], the decisive idea is to

⁷The direction of the vector potential \mathbf{A} corresponds to the polarization direction of the electrical field as it can be seen using the Coulomb gauge (in absence of a scalar potential), $\mathbf{E} = -\partial_t\mathbf{A}$.

approximate the correlated many-body wavefunctions Ψ by KS Slater determinants Φ . This can be justified for the case of planar organic semiconductors as they are dominated by dynamic rather than by static correlation. As a consequence, their true electronic wavefunctions are of single reference character and do not exhibit a (near) degenerate ground state, which would require a superposition of at least two Slater determinants with similar weights [Cre01]. Besides, building an approximate determinant from occupied ground-state KS orbitals is generally a reasonable choice as DFT orbitals are designed to produce the correct spatial electron distribution [BG97].

As shown in Pubs. [P1] and [P3], inserting the KS determinants into Eq. (1.10) allows to write the Dyson orbital as a coherent superposition of all occupied orbitals of the initial state,

$$d_I(\mathbf{r}) \approx \sqrt{N} \langle \Phi_I(N-1) | \Phi(N) \rangle = \sum_{i=1}^N \varphi_i(\mathbf{r}) w_i^I. \quad (2.36)$$

The contributing orbitals are weighted by factors w_i^I . In principle, the w_i^I can be obtained by conducting the integration between the contributing determinants over $N-1$ coordinates, see Pubs. [P1] and [P3] for details. To write down Eq. (2.36) in a more universal fashion, I included the possibility of excited final states. How to obtain an expression for the I th excited final-state wavefunction from DFT is explained in Publ. [P3] and in Sec. 3.2. In this section I will concentrate on the transition to the ground state of the ionized molecule, which is described by one ground-state KS determinant (see also Publ. [P1]).

The wavefunction ansatz is interesting for a couple of reasons. First, it explicitly breaks away from the single-orbital interpretation of photoemission, i.e., from identifying one KS orbital with one Dyson orbital. In the previous section I argued that KS orbitals can serve as reasonable zeroth-order approximations to Dyson orbitals. However, the first-order correction in the spirit of the perturbation expansion of Eq. (2.31) points out that a superposition of orbitals is a more correct description. In this light, Eq. (2.36) might be interpreted as taking one systematic step beyond the mere single-orbital approximation.

Second, I want to mention that this ansatz generally leads to approximate Dyson orbitals that are neither orthogonal nor normalized, which is also a feature of exact Dyson orbitals. Since the orbitals of both Slater determinants, one for the initial state and one for the ionized final state, are computed self-consistently, the two sets of orbitals correspond to different KS Hamiltonians. Integrating over determinants which include sets of orbitals that are not orthogonal to each other results in Dyson orbitals with a norm between $[0; 1]$. Since the Dyson orbital directly enters the transition matrix element of Fermi's golden rule, its norm plays an important role for the magnitude of the transition matrix element and, hence, influences the ionization probability [P3].

Third, Dyson orbitals incorporate electronic relaxation effects. If only the ground-state transition is discussed, the ground-state Slater determinants of the N and $N-1$ -electron systems are inserted into Eq. (2.36). Thus, the orbitals of the ionized system entail all electronic reorganization effects caused by one missing electron. A detailed discussion of relaxation effects is offered in Publ. [P1]. In a nutshell, electronic relaxation leads to the structure of Eq. (2.36) with more than one orbital making a significant contribution, i.e., more than one w_i^I differing from zero. This becomes plausible by considering the limiting case of no relaxation, where the only change of the molecule's system upon ionization is the depletion of one orbital. If both determinants in Eq. (2.36) are built by the same set of orbitals, the structure of the Dyson orbital falls back to the single-orbital case because of orthogonality considerations. Thus, it is the spatial difference of the ionized system's orbitals with respect to the neutral system's orbitals that accounts for multiple orbital contributions. Although Publ. [P1] shows that in many cases Dyson orbitals are dominated by

one single orbital, which advocates the single-orbital approximation, it also provides experimental evidence for beyond single-orbital contributions to ARPES intensities. ARPES spectra recorded with high photon energies reveal additional intensities in the NTCDA HOMO momentum map, which can be explained by the presented ansatz in terms of a superposition of two orbitals.

Fourth, the ansatz has proven to be beneficial for less accurate xc functionals. While the single-orbital approximation is highly sensitive to the xc functional and to the right energetic ordering of states, respectively, the Slater determinant ansatz is considerably less. This is primarily due to the fact that the internal energetic ordering of the occupied KS states has no influence on the magnitude of the w_i^j . In fact, it is solely the overlap integral that determines the orbitals which have a nonvanishing contribution in Eq. (2.36). Thus, it is merely a question of the spatial structure of the orbitals involved. Despite predicting an internal orbital ordering that differs notably, most functionals predict spatially similar orbitals to be occupied for the studied systems since the HOMO-LUMO separation is rather large. Consequently, the Dyson orbital ansatz will yield similar weighting factors for similar orbitals and, thus, will widely mitigate the influence of the xc approximations.

Besides ARPES, also high harmonic generation techniques were able to image Dyson orbitals of diatomic molecules [ILZ⁺04, Lei07, PZBV07, MFBG08, HCB⁺10]. In Publ. [P1] I demonstrate the close resemblance of calculated Dyson orbitals of N₂ to measured reference orbitals presented in Ref. [ILZ⁺04].

2.7 Visualizing electron-phonon coupling with ARPES

Finally, the Dyson orbital approach allows for another fascinating application. It can be used for studying electron-phonon coupling in organic semiconductors. Publication [P2] illustrates that ARPES can reveal and visualize the coupling between specific vibronic modes and electronic excitations. Due to the highly accurate ARPES experiments conducted for Publ. [P2], it was possible to resolve the vibronic progression within the photoemission band that corresponds to the emission from the HOMO (in the sense of the molecular-orbital interpretation) of a coronene monolayer on Ag(111). The remarkable experimental observation is that the ARPES momentum maps change significantly when going to higher vibronic excitations, i.e., to slightly lower kinetic energies of the photoelectron. Whereas the (0-0)

transition yields goggle-shaped intensity patterns, the (0-2) transition reveals triangle shaped regions of high intensity in the corresponding momentum map. Here, (q-p) labels transitions in a Franck-Condon-like picture from the q th vibronic state of the initial electronic ground state to the p th vibronic level of the final electronic state, which is the state of the ionized system. So far, traditional PES studies on the coupling of electronic to vibronic excitations in organic semiconductors have only provided information on the vibrational energy [YNF⁺05, UK08, KYU09, SWLZ09]. An assignment to specific vibrational modes was difficult since restrictions could only be made by selection rules or symmetry considerations. Combining ARPES experiments and the Dyson orbital ansatz, Publ. [P2] demonstrates that only two in plane modes couple to the electronic excitation such that the triangular shaped intensities are reflected by the calculations. Thus, the method provides an unique tool to pinpoint electron-phonon coupling in organic systems. The advantage of the Dyson-orbital ansatz lies in the fact that the vibronic excitation of the molecular final state can be taken into account explicitly. A vibronic displacement of the nuclei can be used for the calculation of the electronic, molecular final state $\Phi(N-1)$ in Eq. (2.36).

CHAPTER 3

Photoemission as a dynamical process: time-dependent density-functional theory

In the previous chapter I discussed the prediction of photoemission observables from a steady-state perspective. However, photoemission is a highly dynamical process. As illustrated in Publs. [P3], [P4], and [P5], important characteristics of PES and ARPES spectra cannot be captured by ground-state DFT for fundamental reasons. In the course of this chapter I explain how to include the dynamical nature of the photoemission process in simulations with the aid of time-dependent DFT (TDDFT). Therefore, I introduce the conceptual framework of TDDFT in Sec. 3.1. In light of Publ. [P3], I outline the basic ideas behind TDDFT in the linear-response limit in Sec. 3.2. Finally, Sec. 3.3 highlights a method to predict PES and ARPES by a real-time propagation of the KS system, see Publs. [P4] and [P5]. A historical survey and more details about TDDFT can be found, for example, in Refs. [GDP96, MG03, MG04, BWG05, MUN⁺06, Cas09].

3.1 Fundamentals of time-dependent density-functional theory

To set the stage for a dynamical simulation of photoemission, an extension of DFT to the time domain promises to be a viable strategy. In analogy to the Hohenberg-Kohn theorem in ground-state DFT, TDDFT rests upon the Runge-Gross (RG) theorem¹ [RG84]. It establishes a one-to-one mapping, modulo a purely time-dependent function, between the time-dependent external potential $v_{\text{ext}}(t)$ [vL99] and the time-dependent electron density evolving from a given initial state and a given particle-particle interaction. Since the entire time-dependent Hamiltonian is determined by a known $v_{\text{ext}}(t)$, also the time-dependent wavefunction has to be a functional of the density and an initial state, again up to a purely time-dependent phase factor.

With the RG theorem it is possible to construct a time-dependent KS (TDKS) scheme if an auxiliary system of noninteracting particles subject to an external local potential $v_{\sigma}^{\text{KS}}(t)$ is introduced. Applied to the noninteracting system, the TDKS potential is unique by virtue of the RG theorem and is chosen in such a way that the KS density,

$$n(\mathbf{r}, t) = \sum_{\sigma=\downarrow, \uparrow} \sum_{i=1}^{N_{\sigma}} f_{i\sigma} |\varphi_{i\sigma}(\mathbf{r}, t)|^2, \quad (3.1)$$

is identical to the interacting system for all times. The noninteracting KS particles obey the time-

¹Due to formal intricacies in the original RG proof such as contradictions in symmetry and causality arising from the xc kernel used in the linear-response limit, the proof was later refined as discussed in Refs. [vL98, vL99, vL01, Vig08].

dependent single-particle Schrödinger equation,

$$i\hbar \frac{\partial}{\partial t} \varphi_{j\sigma}(\mathbf{r}, t) = \left[-\frac{\hbar^2}{2m_e} \nabla^2 + v_{\sigma}^{\text{KS}}(\mathbf{r}, t) \right] \varphi_{j\sigma}(\mathbf{r}, t). \quad (3.2)$$

As in TDDFT's precursor, the TDKS potential is partitioned into the external potential, the Hartree potential, and the xc potential,

$$v_{\sigma}^{\text{KS}}(\mathbf{r}, t) = v_{\text{H}}(\mathbf{r}, t) + v_{\text{ext}}(\mathbf{r}, t) + v_{\sigma}^{\text{xc}}(\mathbf{r}, t). \quad (3.3)$$

In addition to the interaction with the nuclei the external potential can include time-dependent fields. Ionization processes can be driven, for example, by introducing a time-dependent classical electric field of the form $v_{\text{ext}}^{\text{E}}(\mathbf{r}, t) = e \mathbf{E}_0 \mathbf{r} \sin(\omega t)$. While the Hartree potential adopts its time dependence directly from the time-dependent density, the time dependence of the xc potential is more subtle. It does not simply depend on the density at the present time t but also on its entire history, which also includes initial-state effects [GDP96, MB01a, MB01b, MBW02, TGK08, Thi09]. The role of the total-energy functional in the ground-state case is taken by an action functional $A[n]$ [vL98, vL01]. Based on the latter, the xc potential is formally defined as a functional derivative of the xc part of $A[n]$ using the Keldysh pseudotime formalism [vL98]. Further, the xc potential is responsible for many-body effects just as its ground-state complement. Considering all additional subtleties arising from the time dependence, how could it be any different that A_{xc} and v_{xc} , respectively, are typically not known exactly. Therefore, the most common approach is to refer to the so-called adiabatic approximation. In the adiabatic limit the xc potential is approximated via the ground-state xc functional evaluated with the instantaneous density at time t ,

$$v_{\sigma}^{\text{xc}}(\mathbf{r}, t) \approx \left. \frac{\delta E_{\text{xc}}[n]}{\delta n_{\sigma}(\mathbf{r})} \right|_{n_{\sigma}=n_{\sigma}(t)}. \quad (3.4)$$

Essentially, the adiabatic approximation is local in time, neglects all retardation effects², and assumes an instantaneous reaction of v_{xc} on temporal changes of the density. Due to its computational efficiency, the workhorse of TDDFT is the adiabatic LDA or time-dependent LDA (TDLDA) for which the ground-state expression of $E_{\text{xc}}^{\text{LDA}}[n]$ is used to evaluate Eq. (3.4). Although TDLDA is local in time and space, it performs reasonably well for a wide range of applications even beyond its scope of slowly varying densities in time and space [MMN⁺12].

Generally, most of the adiabatic time-dependent xc-functional approximations carry the notorious failures of their ground-state inspirations. To name but a few, the previously discussed self-interaction error, the xc derivative discontinuity, and the potential fall-off constitute issues, which should be addressed in time-dependent calculations [MK05, Mun07, HKK12]. From that perspective, it seems promising to transfer the successful SIC concept to the time domain. Besides other time-dependent SIC approaches [URS98, TC98, MCR01, MDRS08, VDR⁺13], also an extension of GSIC was realized [HKK12, HK12b]. Here, too, the explicit orbital dependence poses some challenges. Solving the OEP equation in the time-dependent realm [UGG95, MK06] is prohibitively demanding even in one spatial dimension and suffers from stability problems. Its approximate fellow, i.e., the time-dependent KLI, is also problematic regarding stability during the time evolution [MKvLR07]. However, the unitary variance of the SIC expression of Perdew and Zunger once again proves useful as employing energy-minimizing (or FOBO) orbital trans-

²Orbital dependent functionals inherit a memory dependence from the orbitals to some extent [MBW02, MMN⁺12]. In this sense, they are so-called orbital-adiabatic functionals [MMN⁺12].

formations mitigates the stability issue [HKK12, HK12b]. To utilize Eq. (2.26) in the time domain, the unitary transformation $U_{ij}^\sigma(t)$ and the orbitals are instantly updated at each time t . The generalization of the KLI to unitarily variant functionals for the time-dependent case is delineated in Refs. [HKK12, HK12b]. The very same works also outline the encouraging performance of the time-dependent GSIC (TDGSIC) approach even for delicate situations such as charge-transfer excitations [HKK12]. Publication [P4] complements these findings and sheds light on the benefits of describing photoemission with TDGSIC.

Having settled the fundamentals of TDDFT and having highlighted some aspects about the time-dependent xc functionals, there are two more subjects that require some thought. First, to make practical use of TDDFT, Eq. (3.2) has to be solved. I will explain two distinct ways in the following sections. Second, the question of how to obtain photoemission observables plays not a less significant role. By virtue of the RG theorem the existence of a density functional for photoemission intensities is guaranteed [RG84]. The exact form of such a functional has not yet been discovered, though. To acquire PES observables, I present two schemes, each tailored to the corresponding method of solving Eq. (3.2).

3.2 The linear-response approach: excited states from particle-hole expansions

The first approach is guided by the preliminary considerations made in Sec. 1.3. Photoemission peaks, which are specified through the energy conservation in Fermi's golden rule (see Eqs. (1.4), (1.7), and (1.9)), occur only at energies that are directly related to the eigenstates of the ionized $N - 1$ -electron system, i.e., $E_I(N - 1)$ and $\Psi_I(N - 1)$. Thus, the goal for this section is to get hold of the excited-state properties of the ionized molecular systems.

In general, excited-state properties can be gained by transforming the TDKS equation from time to the frequency domain³. The first-order density response of an interacting system to a perturbation $\delta v_{\text{ext}}(t)$ can be formulated in the frequency domain as [MG03]

$$\delta n(\mathbf{r}, \omega) = \int d^3 r' \chi(\mathbf{r}, \mathbf{r}', \omega) \delta v_{\text{ext}}(\mathbf{r}', \omega), \quad (3.5)$$

using the density-response function

$$\chi(\mathbf{r}, \mathbf{r}', \omega) = \lim_{\eta \rightarrow 0^+} \sum_{I=1}^{\infty} \left[\frac{\langle \Psi_0 | \hat{n}(\mathbf{r}) | \Psi_I \rangle \langle \Psi_I | \hat{n}(\mathbf{r}') | \Psi_0 \rangle}{\hbar\omega - \Omega_I + i\eta} - \frac{\langle \Psi_0 | \hat{n}(\mathbf{r}') | \Psi_I \rangle \langle \Psi_I | \hat{n}(\mathbf{r}) | \Psi_0 \rangle}{\hbar\omega + \Omega_I + i\eta} \right]. \quad (3.6)$$

The poles of χ at $\Omega_I = E_0 - E_I$ are the system's true excitation energies. \hat{n} denotes the density operator, Ψ_I the eigenstates of the system, and η a positive infinitesimal. The noninteracting KS system has an analogue, χ_{KS} , which tells how the KS density reacts on changes of the KS potential,

$$\delta n(\mathbf{r}, \omega) = \int d^3 r' \chi_{\text{KS}}(\mathbf{r}, \mathbf{r}', \omega) \delta v_{\text{KS}}(\mathbf{r}', \omega). \quad (3.7)$$

In contrast to the interacting χ , χ_{KS} exhibits poles only at the excitation energies of independent

³In the following I will consider a system with a fixed number of electrons, where all properties belong to the same number of electrons, be it a neutral or ionized system.

particles, i.e., at the KS ground-state eigenvalue differences. Since the RG theorem ensures that the density change of the interacting and exact noninteracting KS system is identical, one can derive an equation for χ from Eqs. (3.6) and (3.7) by invoking properties of the ground-state KS system only [PGG96],

$$\begin{aligned} \chi(\mathbf{r}, \mathbf{r}', \omega) &= \chi_{\text{KS}}(\mathbf{r}, \mathbf{r}', \omega) + \\ &+ \int d^3 r'' \int d^3 r''' \chi_{\text{KS}}(\mathbf{r}, \mathbf{r}'', \omega) f_{\text{H,xc}}(\mathbf{r}'', \mathbf{r}''', \omega) \chi(\mathbf{r}''', \mathbf{r}', \omega). \end{aligned} \quad (3.8)$$

The presence of the so-called Hartree-exchange-correlation kernel $f_{\text{H,xc}}$, inter alia, shifts the position of the single-particle poles to the real excitation energies [MZCB04, TK14]. In its time-dependent form, $f_{\text{H,xc}}$ arises from the functional derivative of the Hartree and xc potential with respect to the time-dependent density,

$$f_{\text{H,xc}}(\mathbf{r}, \mathbf{r}', t - t') = \frac{e^2}{|\mathbf{r} - \mathbf{r}'|} + f_{\text{xc}}(\mathbf{r}, \mathbf{r}', t - t') = \frac{\delta [v_{\text{H}}(\mathbf{r}, t) + v_{\text{xc}}(\mathbf{r}, t)]}{\delta n(\mathbf{r}', t')}. \quad (3.9)$$

Popular strategies to solve Eq. (3.8) for the excitation energies were suggested by Casida [Cas95b, Cas96, JCS96] and Petersilka *et al.* [PGG96]. The Casida equations [Cas95b, Cas96] can be written as a generalized eigenvalue problem for the excitation energies [BA96],

$$\begin{bmatrix} \mathbf{A} & \mathbf{B} \\ \mathbf{B}^* & \mathbf{A}^* \end{bmatrix} \begin{pmatrix} \mathbf{X} \\ \mathbf{Y} \end{pmatrix} = \Omega \begin{bmatrix} -\mathbf{1} & \mathbf{0} \\ \mathbf{0} & \mathbf{1} \end{bmatrix} \begin{pmatrix} \mathbf{X} \\ \mathbf{Y} \end{pmatrix}. \quad (3.10)$$

The matrix elements of \mathbf{A} and \mathbf{B} have the following structure (here for the sake of generality in spin polarized notation),

$$A_{ia\sigma, jb\tau} = \delta_{ij} \delta_{ab} \delta_{\sigma\tau} (\epsilon_{a\sigma} - \epsilon_{i\tau}) + K_{ia\sigma, jb\tau}, \quad (3.11)$$

$$B_{ia\sigma, jb\tau} = K_{ia\sigma, bj\tau}, \quad (3.12)$$

where $K_{ia\sigma, jb\tau}$ is defined as

$$K_{ia\sigma, jb\tau} = \int d^3 r \int d^3 r' \varphi_{i\sigma}^*(\mathbf{r}) \varphi_{a\sigma}(\mathbf{r}) f_{\text{H,xc},\sigma,\tau}(\mathbf{r}, \mathbf{r}', \omega) \varphi_{b\tau}^*(\mathbf{r}') \varphi_{j\tau}(\mathbf{r}'). \quad (3.13)$$

The indices σ and τ stand for the spin. i, j and a, b denote occupied and virtual orbitals, respectively.

Besides excitation energies, the linear-response formalism provides access to oscillator strengths and approximate excited-state wavefunctions [Cas95b, Cas96]. Having introduced a viable recipe to calculate excitation energies and their optical transition strengths, I will now come back to photoemission.

In the context of PES, i.e., to determine the ionization energies by virtue of Eq. (1.7), the generalized eigenvalue equation (3.10) has to be solved for the ionized molecular final state [WH08, HWSM13],[P3]. To predict ARPES spectra according to Eqs. (1.9) and (2.36), an expression for the final-state wavefunction is further needed. The excited-state wavefunction can approximately be associated with a particle-hole expansion of the ground-state Slater determinant. In particular, the Tamm-Dancoff approximation [HHG99, HHGB99] to Eq. (3.10), which essentially sets $\mathbf{B} = 0$,

allows to approximate the excited-state wavefunction in terms of configuration-interaction singles,

$$|\Psi_I\rangle = \sum_{\sigma} \sum_{a,i} X_{ia\sigma}^I c_{a\sigma}^{\dagger} c_{i\sigma} |\Psi_0\rangle. \quad (3.14)$$

The expansion coefficient $X_{ia\sigma}^I$ corresponds to the eigenvector of Eq. (3.10) in the Tamm-Dancoff approximation. Here, $c_{a\sigma}^{\dagger}$ and $c_{i\sigma}$ are the fermionic creation and annihilation operators, respectively.

This approach lies at the very heart of Publ. [P3]. Particularly, the wavefunction assignment of Eq. (3.14) provides an excellent means to calculate approximate Dyson orbitals. To be more specific, inserting Eq. (3.14) into Eq. (2.36) constitutes a straightforward extension of the discussion in Sec. 2.6. Dyson orbitals corresponding to excited molecular final states can be written as

$$d_I(\mathbf{r}) \approx \sqrt{N} \langle \Phi_I(N-1) | \Phi_0(N) \rangle = \sum_{i=1}^N \varphi_i(\mathbf{r}) w_i^I. \quad (3.15)$$

Just like in the ground-state situation, the Dyson orbitals can be processed to ARPES momentum maps by adopting the PW approximation.

From a practical perspective this ansatz is attractive because for PTCDA not only the momentum map belonging to the HOMO was revealed but also the maps of the four states located directly beneath it [P0],[PRU⁺11]. As already discussed in Sec. 2.5, less accurate xc functionals were shown to predict wrong orbitals at the respective energies. However, if excitations are properly taken into account with the linear-response TDDFT formalism (explained in more detail in Publ. [P3]), the resulting Dyson orbitals yield momentum maps that are in good agreement with experimental data.

3.3 Photoemission spectra from real-time propagations

All approaches to calculate ARPES spectra that I have presented up to now rely on the evaluation of Fermi's golden rule. Although TDDFT equips the Dyson orbitals with properly calculated excitations from TDDFT, there is still room for improvement. A mild restriction, at least for my purpose, is that the linear-response limit is not suited for strong-field applications. More to the point is the lack of an xc kernel corresponding to xc potentials constructed via the OEP scheme, which foils the use of GSIC within linear-response TDDFT. Aside from the issues related to the linear-response limit, the most severe restriction steps in at an earlier stage of the photoemission discussion. All Fermi's golden rule based ARPES simulations rely on approximations for the ejected electron's state. So far, I have deliberately used the PW approximation because of its simplicity and instructive interpretation of ARPES. However, it carries several major deficiencies. First of all, real photoelectrons do interact with the remaining ionized system. Hence, they are not correctly described by free-particle continuum states. This implies further restrictions.

Properly calculating photoemission peak heights necessitates an evaluation of the magnitude of the transition matrix element in Eq. (1.4). The reliability of such an evaluation is highly doubtful with the PW state. In ground-state DFT the customary approach is to ascribe a normalized intensity to each eigenvalue. This establishes a rather crude way to estimate transition probabilities, which is only sensitive to the degree of degeneracy of the states [BC95, AMH⁺00, KK10, RASG⁺12]. Within the wavefunction approaches and specifically with the TDDFT ansatz presented in the previous section, one can evaluate the norm of the Dyson orbitals in combination with oscillator strengths, see Publ. [P3]. Neither of these approaches allows for a rigorous assessment of emission intensities. Thus, a reliable strategy to account for the so-called matrix-element effects is highly

desired for predicting PES comprehensively.

Further, the scope of the PW approximation is rather narrow considering the orientation of the polarization of the ionizing light field. As discussed in Refs. [PBF⁺09, BW15], the PW yields accurate results if setups are chosen such that the favored emission directions and the light polarization are aligned parallel. A paradigm in which the PW approximation is deemed failing is circular light polarization. Here, the polarization vector is rotating in time and, thus, is never spatially constant hindering a parallel alignment. Finally, also the simplistic energy dependence of the PW approximation can be a massive obstacle for the correct prediction of photoemission intensities [Lie74]. Depending on the energy, ARPES intensities are merely modified by evaluating the k -space representation of an orbital on a hemisphere with a different radius corresponding to a different kinetic energy of the photoelectron. Since the k -space structure of typical orbitals is rather smooth, the PW is not able to explain significant variations in ARPES patterns.

A possible solution is either to forge more reliable approximations for the final state that go beyond the PW such as, for example, the independent atomic-center approximation [Gro78, PBF⁺09], multiple scattering X_α [DD74, SS08], and solutions to the Lippmann-Schwinger equation for frozen-core HF potentials [LRM82], or to circumvent the requisite for stationary final states completely. Within this section I outline such an approach. It departs from the notion of using matrix elements and Fermi's golden rule, respectively, to calculate PES observables.

Imagine a typical PES experiment that is rendered into a large numerical simulation box. At $t = t_0$ the probed molecule, which initially is in its ground state, is located at the center. The KS system is now allowed to evolve in time. If a light field intense enough to trigger an ionization process is switched on, parts of the electron density will be forced to travel towards the periphery of the simulation box. Eventually, the outgoing density will be measured by a photoelectron detector. I want to emphasize that also the photoelectron's state, which is specified by the outgoing density, is part of the KS density. As a consequence, the interaction of the outgoing density with the remaining ionized system is captured completely on the DFT level as the outgoing density experiences the full KS potential. In this scenario the time evolution intrinsically provides all information about the photoelectron from first principles, i.e., without making any a priori assumption about the emitted electron's state. How to realize this concept in practice and to what extent the prediction of photoemission benefits from it, is the topic of the following and of Pubs. [P4] and [P5].

The first step is to solve the TDKS equation in time. Starting from the ground-state as the initial condition, the time evolution can be computed by propagating the KS orbitals in real-time [YB96, CRS97, CAO⁺06, MK07],

$$\varphi_{j\sigma}(\mathbf{r}, t) = U(t, t_0)\varphi_{j\sigma}(\mathbf{r}, t_0) = \Gamma \exp\left[-\frac{i}{\hbar} \int_{t_0}^t dt' h_{\text{KS}}(\mathbf{r}, t')\right] \varphi_{j\sigma}(\mathbf{r}, t_0). \quad (3.16)$$

The time-propagation operator $U(t, t_0)$ originates from the formal solution of Eq. (3.2), where Γ is the time-ordering operator. To alleviate the time dependence of the integral in Eq. (3.16), i.e., to decompose the full propagator into smaller time intervals, $U(t, t_0)$ is split into N smaller time steps $\Delta t = (t - t_0)/N$,

$$U(t, t_0) = \prod_{n=0}^{N-1} U(t_0 + (n+1)\Delta t, t_0 + n\Delta t). \quad (3.17)$$

Among other schemes [CMR04], a widely used method to evaluate U (with the Hamiltonian in the exponential function) leans on a fourth-order Taylor expansion of U around Δt . Since the time-steps are chosen such that $h_{\text{KS}}(t)$ has only a weak time dependence within Δt , the time integral in

Eq. (3.16) can be approximated by the exponential mid-point rule yielding [Mun09]

$$U(t + \Delta t, t) \approx \sum_{m=0}^4 \frac{1}{m!} \left(\frac{-i\Delta t}{\hbar} h_{\text{KS}}(\mathbf{r}, t + \Delta t/2) \right)^m. \quad (3.18)$$

Knowing the orbitals and the density by virtue of Eq. (3.1) at all time steps, the question of how to extract the photoemission signal is remaining. Besides other solutions to this problem [URS97, VTM03, MK07, DVM⁺12, DRRS13], Pohl and co-workers suggested a method that can be realized numerically on real-space grids [PRS00, WFD⁺10, WDSR12]: At a specific detection point \mathbf{R}_D in the periphery, all occupied orbitals $\varphi_{j\sigma}(\mathbf{R}_D, t)$ are recorded as a function of time. If one thinks of each orbital as a superposition of plane waves, they can be understood as outgoing wavepackets arriving at \mathbf{R}_D , i.e., $\varphi_{j\sigma}(\mathbf{R}_D, t) = \int d\omega c_{j\sigma}(\omega) \exp[i(\mathbf{k}\mathbf{R}_D - \omega t)]$. Taking the Fourier transform of $\varphi_{j\sigma}(\mathbf{R}_D, t)$ from the time into the frequency domain reveals $|c_{j\sigma}(\omega)|^2$, which is the probability of finding a certain kinetic-energy component in the outgoing wavepacket. Summing up all orbitals yields the total probability density for detecting the kinetic energy E_{kin} at space-point \mathbf{R}_D ,

$$\begin{aligned} n(\mathbf{R}_D, E_{\text{kin}}/\hbar) &= \sum_{\sigma=\uparrow, \downarrow} \sum_{j=1}^N |\varphi_{j\sigma}(\mathbf{R}_D, E_{\text{kin}}/\hbar)|^2 \\ &= \sum_{\sigma=\uparrow, \downarrow} \sum_{j=1}^N |c_{j\sigma}(E_{\text{kin}}/\hbar)|^2. \end{aligned} \quad (3.19)$$

If the outgoing wavepackets are identified with outgoing electrons, the probability density is proportional to finding a photoelectron with kinetic energy E_{kin} at space-point \mathbf{R}_D , i.e.,

$$J(\mathbf{R}_D, E_{\text{kin}}) \propto n(\mathbf{R}_D, E_{\text{kin}}/\hbar). \quad (3.20)$$

In total these equations define an implicit density functional to extract the photoemission intensity that is attractive because of its palpable interpretation. It is approximate, too, which is apparent from the derivation of Eqs. (3.20) and (3.19): interpreting the TDKS orbitals at large R_D as outgoing wavepackets, one implicitly identifies KS particles with electrons. Another approximation is the obligatory reliance upon approximate xc functionals. The two issues are somewhat related: Because the photoemission scheme identifies KS particles with electrons, it is clear that it can be expected to work best with xc approximations that conform with this identification. The GSIC approaches meet this criterion, as discussed in Refs. [KKM08, HK12b].

An advantage of this scheme, which is satisfying from a formal DFT perspective, is that it avoids interpreting eigenvalues in order to obtain the photoemission peak positions. Besides, it is ideally suited for recording the spatial distribution of emitted electrons by placing detection points on a spherical surface around the probed molecule.

There is another, though technical, aspect that is essential for acquiring PES signals free of numerical noise. A wavepacket that ventures towards the numerical boundary has to be absorbed efficiently. Otherwise the density would be reflected and, in turn, strongly contaminate the recorded PES signal. To do so, I implemented smooth imaginary potentials [GS78, Man02, GLRM04, DLR15, SK16a], which have the property of being not norm conserving. When added to the usual KS Hamiltonian as

$$h_{\text{KS}}(\mathbf{r}, t) = h_{\text{KS}}^0(\mathbf{r}, t) - i v_{\text{abs}}(\mathbf{r}), \quad (3.21)$$

the potential acts as an absorber for $v_{\text{abs}}(\mathbf{r}) > 0$. Absorbing potentials can be designed to suppress

reflections efficiently within a certain kinetic-energy window [DLR15]. It is important that $v_{\text{abs}}(\mathbf{r})$ has an active length long enough to absorb all Fourier components of the wavepacket, even those with large wavelengths. However, it turned out that finding a suitable balance between a sufficient absorbing length and a numerically traceable grid size is a rather delicate task. Coupled to that issue is the proper choice of the detection points. It has to be adequately far away from the system such that the molecular potential has (sufficiently) faded but not within the absorbing region. Publication [P4] examines the raised restrictions and offers a possible implementation.

Apart from the technical issues, the main objective of Publ. [P4] is to assess traditional gas-phase photoemission spectra. As it turns out, the real-time propagation scheme is able to reasonably estimate the emission peak heights of the outer-valance PES spectra on benzene and pyridine. This improvement over the ground-state approach is a consequence of including dynamical effects and of not relying on the evaluation of Fermi's golden rule with its requisite of an approximation for the ejected electron's state. Recalling the discussion of Sec. 2.2, it comes by no means as a surprise that the chosen xc functional crucially influences the predicted PES spectra in terms of energy. TDLDA yields neither satisfying ionization energies nor intensity heights. TDGSIC, on the contrary, performs appreciatively better in both respects. It has to be noted, though, that there is hardly a difference between ionization energies predicted from the GSIC eigenvalues and from its time-dependent complement via Eq. (3.20). Apparently, the peak positions are primarily governed by the ground-state electronic structure and are barely affected by the system's dynamics. As expected, the TDGSIC yields spectra with an excellent assessment of the relative PES peak positions, the absolute IPs are overshoot by a few eV.

Another facet of Publ. [P4] deals with angular-resolved photoemission on benzene in the gas-phase, i.e., on benzene molecules that are randomly oriented. Experiments conducted with a spatially fixed light polarization reveal that individual photoemission peaks exhibit different emission characteristics with respect to the polarization direction [SK78, MKJS77, CGK⁺87, LAM⁺11]. Thus, two peaks that are located at different energies might each prefer a distinct emission direction. This allows to infer further information on the electronic structure and on orbitals in particular. For each emission peak, which is determined by its energetic location E , the intensity can be described via [Bet33, CZ68a, CZ68b, WFD⁺10]

$$J(E, \theta) \propto 1 + \beta(E)P_2(\cos \theta). \quad (3.22)$$

Here, P_2 is the Legendre polynomial of second order and θ denotes the emission angle with respect to the light polarization direction ($\theta = 0^\circ$ and $\theta = 180^\circ$ parallel; $\theta = 90^\circ$ perpendicular). The variation of the angularly resolved intensity is rated by $\beta(E)$, the anisotropy parameter. It ranges from $\beta = 2$ for a maximally parallel emission via $\beta = 0$ for completely uniform emission to $\beta = -1$ for maximally perpendicular emission. Importantly, each individual photoemission peak of benzene reveals its own characteristic β . This permits to check whether the angular variation can be traced back to be caused by individual molecular orbitals, i.e., whether each peak can be identified uniquely with one orbital. Particularly, the real-time propagation allows for an unbiased assignment of orbitals as no further assumptions, e.g., about the final state, have to be made. To do so, I tracked the emission signal of each orbital individually, i.e., calculated $J_i \propto |\varphi_i|^2$. Based on J_i , the anisotropy parameter β_i for orbital φ_i can be obtained, see Publ. [P4] for technical details. The anisotropy parameters appear to be in good agreement with experimental observations for the majority of emission peaks. Hence, this analysis provides further evidence that molecular orbitals from GSIC are a physically relevant and useful concept.

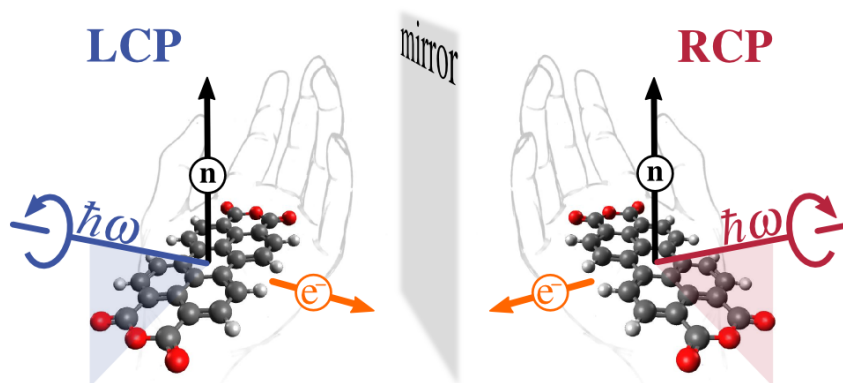


Figure 3.1: Setup for a circular dichroism experiment illustrated for one oriented PTCDA molecule. The handedness, i.e., the breaking of inversion symmetry, is implemented by the three distinctly oriented axes in combination with the two different directions of rotation of the electric field. The first axis is provided by the normal of the molecular plane of PTCDA (\mathbf{n}). The second axis is the emission direction of the electrons (e^-). The third one is the direction of the incoming photons with either left-handed circularly polarized light (LCP on the left panel) or right-handed circularly polarized light (RCP on the right panel).

Publication [P5] goes one step further. Beyond monitoring the gas-phase PES for small molecules, the complete photoemission angular distribution is recorded from time propagations. The combined experimental and theoretical study aims to emphasize the importance of an accurate final-state description. This is evidently shown for three hallmark examples: the dependence of ARPES spectra on the polarization directions of the electric field, the circular dichroism in the angular photoemission distribution, and the energy dependence of ARPES spectra. The first example considers photoemission caused by an electric field that is polarized horizontally. Intuitively, one would expect that the favored emission direction is somewhere close to the polarization direction, i.e., close to the direction of the electric field vector that drives the photoemission process. Yielding the main intensities in directions close to the light polarization direction, the PW approximation behaves just as expected. In fact, the PW approximation even forbids emission perpendicular to the light polarization as the $|\mathbf{A}\mathbf{k}|^2$ factor in Eq. (2.35) vanishes in that situation. In clear contrast, experiment and real-time propagation both unveil a different picture. There are strong intensities in perpendicular directions. A possible explanation of emission perpendicular to the electric field vector might be that interaction of the emitted electron with the ionized systems leads to a strong deflection of the photoelectron's trajectory. In studies on orbital tomography, measured ARPES momentum maps are often assigned to orbitals by comparing intensity patterns [KTY⁺06, PBF⁺09, PRU⁺11], [P0]. It is, thus, important to be aware of this issue, as additional intensities may lead to a false assignment.

The second example is photoemission induced by circularly polarized light. In this case, studies on adsorbed diatomic molecules suggest that the photoelectron angular distribution is largely governed by interference effects of partial-wave components of the final state [DDM85, WBG89, Sch90, DL14]. The first-principles description of the final state within the real-time approach promises a clear advantage since such interference effects are included in the time evolution of the outgoing density. Remarkably, ARPES experiments on PTCDA, NTCDA, and CO conducted

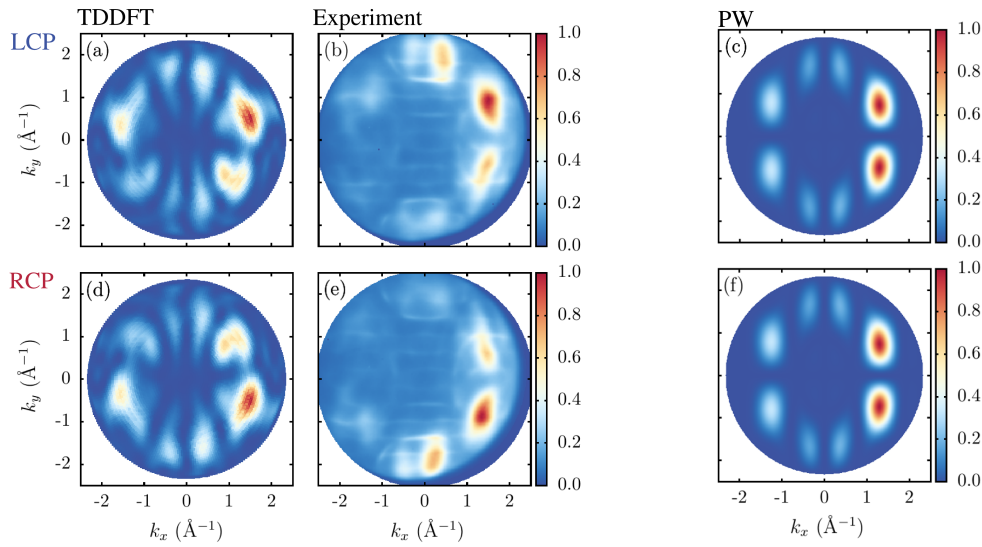


Figure 3.2: PTCDA probed with photons at $\hbar\omega = 27$ eV that incide in the xy -plane under an angle of 65° towards the surface normal. The x -axis denotes the long molecular axis, y the short one. (a) shows the LCP and (d) RCP from TDLDA. (b) and (e) are experimentally obtained spectra for LCP and RCP, respectively. (c) and (f) show the results of the single molecular-orbital interpretation of the LDA HOMO with the PW approximation for LCP and RCP. The experimental spectra are displayed by courtesy of M. Graus and A. Schöll from the University of Würzburg.

with circularly polarized light show a crucial dependence of the photoemission response on the photon's helicity [WBG89, WHS⁺14]. Thus, depending on whether the incident photons are left-handed or right-handed circularly polarized (LCP) and (RCP), respectively, ARPES spectra can differ significantly. This gives rise to a circular dichroism in the photoemission angular distribution (CDAD). A necessary criterion for observing a CDAD in photoemission is the presence of a definite handedness considering the entire system. Whereas chiral molecules, with amino acids and further biomolecules as prominent examples, inherently provide a handedness [Rit76, Pow00, BLS⁺01], the required breaking of inversion symmetry can be implemented by the overall experimental geometry for nonchiral species, too [Sch90]. As shown in Fig. 3.1, the ordered monolayer structure of the molecular semiconductors naturally provides a first distinct axis (represented by one spatially fixed PTCDA molecule in Fig. 3.1), the other directions are determined by the photon incidence and the photoemission direction. The dissymmetry is then introduced by the oppositely rotating electric fields, which are associated with LCP and RCP light.

I will discuss the results of Publ. [P5] concerning the CDAD based on one further example. Probing PTCDA with LCP and RCP light, respectively, leads to a distinct difference in the momentum maps, as shown in the left part of Fig. 3.2. Here, the molecule is oriented as illustrated in Fig. 3.1, where the long molecular axis is parallel to the x -direction. The short axis corresponds to the y -axis. Photons incide in the xz -plane with an angle of 65° towards the surface normal and an energy of $\hbar\omega = 27$ eV. Except of the photon incidence direction, the computational⁴ and experimental setup

⁴I performed the ground-state DFT calculations with the Bayreuth version of the PARSEC real-space code [Mun09, KMT⁺06] using LDA norm-conserving Troullier-Martins pseudopotentials [TM91]. The time-propagation was executed with an in large parts refined version of PARSEC that allows to propagate systems on large grids efficiently [SK].

is identical to what is shown in Publ. [P5]. Therefore, I refer to the Supplemental Material of Publ. [P5] and to appendix A.5 for more details on the time propagation and further technical aspects. The LCP and RCP spectra in Fig. 3.2(a) and (d), respectively, which I calculated with TDLDA⁵, clearly exhibit a left-right asymmetry with respect to the $k_y = 0$ axis for the photoemission signal of the HOMO. Remarkably, the most distinctly pronounced intensity peak at $k_x \approx 1.5 \text{ \AA}^{-1}$, $k_y \approx 0.6 \text{ \AA}^{-1}$ for LCP (Fig. 3.2(a)) switches sides to $k_x \approx 1.5 \text{ \AA}^{-1}$, $k_y \approx -0.6 \text{ \AA}^{-1}$ for RCP (Fig. 3.2(d)). The experimental analogues in Figs. 3.2(b) and (e) clearly confirm this feature. In contrast, less accurate final-state approximations, as demonstrated in Fig. 3.2(c) and (f) for the PW, do not exhibit a CDAD but instead average the left-right asymmetry. In appendix A.1 I discuss a stationary final-state approximation that goes beyond the PW final state.

The third point addressed in Publ. [P5] is the dependence of ARPES intensities on the photon energies. Particularly, the CDAD signal is shown to be sensitive to the energy, mounting in an inversion of the CDAD pattern. Again, the TDDFT simulation is able to capture this tendency as shown for the PTCDA HOMO and for emission from the 4σ orbital of oriented CO molecules. To underpin these findings, I present more details and further calculations on the energy dependence of the CDAD of the CO molecule in appendix A.3.

Admittedly, the numerical burden is considerably higher for the real-time propagation, particularly compared to the simple Fourier transform that is needed for the PW approximation. In return, the real-time propagation stands out with a first-principles description of the final state. In this way a reasonable assessment of photoemission peak heights is possible. Further, the approach is suited for any type of light polarization, in particular circularly polarized light, and is able to reproduce the energy dependence of CDAD patterns.

⁵The accuracy of the TDLDA is sufficient for this purpose as the correct orbital is predicted as the HOMO. Further, the calculations fortuitously benefit from the underestimation of the gas-phase IP within the LDA. Due to adsorption effects in experiment, the experimental HOMO IP is also decreased compared to the gas-phase and agrees well with the gas-phase HOMO energy predicted by the LDA.

CHAPTER 4

Many-body perturbation theory in the GW approximation

In the course of the previous chapters, the concept of quasiparticles has played a substantial role in the interpretation of DFT eigenstates. Within the following chapter I focus upon quasiparticles in more detail. Inextricably linked to quasiparticles is the single-particle Green's function formalism, which I introduce in the subsequent section. A mathematical framework for calculating the Green's function is provided by the Hedin equations that I present in Sec. 4.2. To make practical use of these equations one typically draws on the GW approximation, see also Sec. 4.2. The most widespread ways to solve the GW Hedin equations are outlined in Secs. 4.3 and 4.4. An introduction to Pubs. [P7] and [P8] is offered in Sec. 4.5, which deals with the accuracy of quasiparticle IPs in conjunction with the constraint of piecewise linearity. For an in-depth guide to MBPT, Green's functions, and GW , I recommend Refs. [FW71, Mat92, AG98, AJW00, ORR02].

4.1 The Green's function formalism

Central for quasiparticle calculations is the single-particle Green's function G . In its most basic form, G is defined as an expectation value with respect to the N -electron ground state $\Psi_0(N)$,

$$G(\mathbf{r}t, \mathbf{r}'t') = -\frac{i}{\hbar} \langle \Psi_0(N) | \hat{T} [\hat{\Psi}(\mathbf{r}t) \hat{\Psi}^\dagger(\mathbf{r}'t')] | \Psi_0(N) \rangle. \quad (4.1)$$

Here, $\hat{\Psi}(\mathbf{r}t)$ denotes the field operator of the second quantization in the Heisenberg picture where \hat{T} ensures a time-ordered product of the field operators,

$$\hat{T} [\hat{\Psi}(\mathbf{r}t) \hat{\Psi}^\dagger(\mathbf{r}'t')] = \begin{cases} \hat{\Psi}(\mathbf{r}t) \hat{\Psi}^\dagger(\mathbf{r}'t') & \text{for } t > t', \\ -\hat{\Psi}^\dagger(\mathbf{r}'t') \hat{\Psi}(\mathbf{r}t) & \text{for } t < t'. \end{cases} \quad (4.2)$$

Equations (4.1) and (4.2) allow for a quite intuitive interpretation of the Green's function. For the case of $t < t'$, the far right side of Eq. (4.1), which consists of $\hat{\Psi}(\mathbf{r}t) | \Psi_0(N) \rangle$, represents an $N-1$ -electron state with one electron being annihilated at point \mathbf{r} and time t . In combination with the left-hand side of the matrix element, $\langle \Psi_0(N) | \hat{\Psi}^\dagger(\mathbf{r}'t')$, the Green's function gives the probability amplitude to detect a missing electron at \mathbf{r}' and t' . Thus, G describes the propagation of a hole. If the time order is reversed, the Green's function can be interpreted in terms of electron injection, which is the propagation of an additional electron.

For practical purposes the Lehmann representation of G [Leh54],

$$G(\mathbf{r}, \mathbf{r}', \omega) = \sum_I \frac{d_I(\mathbf{r})d_I^*(\mathbf{r}')}{\hbar\omega - [\varepsilon_I + i\eta \operatorname{sgn}(\mu - \varepsilon_I)]}, \quad (4.3)$$

is often more convenient and widely used. Equation (4.3) can be derived from Eq. (4.1) by inserting a complete set of $N - 1$ -particle states $\sum_I |\Psi_I(N - 1)\rangle\langle\Psi_I(N - 1)|$ and of $N + 1$ -particle states $\sum_I |\Psi_I(N + 1)\rangle\langle\Psi_I(N + 1)|$, respectively, depending on the time ordering. Subsequently, the expression has to be Fourier transformed from the time to the frequency domain [FW71]. The positive infinitesimal η guarantees convergence of the Fourier transform and μ denotes the chemical potential. The denominator reveals one of the prominent features of the Green's function. It has poles exactly at the true quasiparticle energies ε_I . If the chemical potential in Eq. (4.3) is higher than ε_I , the poles lie at the exact ionization energies of the N -electron system. Otherwise ε_I describes the exact electron affinities. Also the numerator is comprised of familiar quantities, namely the Dyson orbitals d_I , which are often dubbed Lehmann amplitudes in this context. They can be expressed in terms of the spatial part of the field operators as follows [ORR02]

$$d_I(\mathbf{r}) = \begin{cases} \langle\Psi(N) | \hat{\Psi}(\mathbf{r}) | \Psi_I(N + 1)\rangle & \text{for } \varepsilon_I > \mu, \\ \langle\Psi_I(N - 1) | \hat{\Psi}(\mathbf{r}) | \Psi_I(N)\rangle & \text{for } \varepsilon_I < \mu. \end{cases} \quad (4.4)$$

A direct connection of the Green's function to PES spectra can be established via the spectral function,

$$A(\omega) = \frac{1}{\pi} \left| \int d^3r \lim_{r' \rightarrow r} \Im(G(\mathbf{r}, \mathbf{r}', \omega)) \right|. \quad (4.5)$$

It is proportional to the photoemission intensity when a PW final state is assumed for the ejected electron [Hed99, ORR02]. Commonly, two types of photoemission peaks arising from $A(\omega)$ are distinguished: Sharp peaks are related to single-particle-like excitations with long quasiparticle lifetimes. Broader satellite peaks, which are associated with short lifetimes and arise from collective excitations such as plasmons, can contribute significantly to the spectral function especially in the case of metallic systems.

Apart from the quasiparticle energies and amplitudes, the Green's function contains observable properties of any single-particle expectation value [FW71]. Further, the total energy of a system [FW71] can be obtained from G . A common choice is the Galitskii-Migdal total-energy functional [GA58, FW71],

$$E_{\text{GM}}[G] = -i\hbar \int d^3r \lim_{t' \rightarrow t^+} \lim_{r' \rightarrow r} \left[i\hbar \frac{\partial}{\partial t} - \frac{\hbar^2}{2m_e} \nabla^2 \right] G(\mathbf{r}t, \mathbf{r}'t'), \quad (4.6)$$

which I employed for the calculations presented in Publ. [P7]. The Galitskii-Migdal total-energy functional is, however, not unique [GA58, LW60, Kle61]. This is important for the evaluation of approximate and especially problematic for not self-consistently obtained Green's functions (in the sense of being a self-consistent solution of the Dyson equation, see Sec. 4.3) as the total energy might depend on the functional expression employed [DvLvB06]. Moreover, the electron density can be written as a functional of G ,

$$n(\mathbf{r}) = -2i\hbar G(\mathbf{r}t, \mathbf{r}t^+), \quad (4.7)$$

where the superscript $+$ denotes an infinitesimal shift of the respective time coordinate.

4.2 Hedin equations and the GW approximation

I now want to discuss how to make practical use of the Green's function formalism. The catch is, once again, that an evaluation of the exact Green's function as defined in Eqs. (4.1) and (4.3) would either require the ground-state many-body wavefunctions and the entire eigenspectrum of the $N \pm 1$ -electron systems or equivalently all Dyson orbitals and quasiparticle energies. To attack the issue in a different way, MBPT is used [Mat92]. The essential idea here is to start from an assembly of noninteracting electrons where the propagation of a noninteracting particle is described by the noninteracting Green's function G_0 ¹ [Mat92]. The interacting nature of the propagated particle is then introduced by scattering events caused by the Coulomb interaction. When all possible scattering probability amplitudes with the cloud of the surrounding particles are summed up, one obtains the Dyson's equation for the fully interacting Green's function. It is equivalent to the Dyson's equation presented in Eq. (2.29) yet representing an integro-differential equation for G ,

$$G(1,2) = G_0(1,2) + \int d3 \int d4 G_0(1,3) \Sigma_{xc}(3,4) G(4,2). \quad (4.8)$$

For the sake of clarity I use a contracted notation for time and spatial coordinates in which $1 = \{\mathbf{r}, t\}$, $2 = \{\mathbf{r}', t'\}$, etc. (The spin is neglected here but can be included in a straightforward manner.). Σ_{xc} is the self-energy. In this picture, the self-energy represents the contribution to a particle's energy arising from the interaction with the surrounding cloud of particles. Now, the next step is to find an expression for the self-energy.

The gist of MBPT is to construct the self-energy from a perturbation expansion of the Coulomb interaction, where the unperturbed system is represented by the noninteracting particle case. Thus, Σ_{xc} is supposed to be increasingly accurate the higher the expansion order gets. As an example, the Fock exchange operator is nothing else but the first-order contribution² to the self-energy, $\Sigma_{xc} \approx i\hbar G v_x^{\text{HF}}$. Yet, achieving improvement over Hartree-Fock is laborious as already the second order of the Coulomb interaction is not necessarily finite and the convergence rate of the expansion is poor especially with increasing polarizability of systems [FW71]. To circumvent this issue, Hedin proposed to expand the self-energy in a Taylor series in powers of the screened instead of the bare Coulomb interaction $v(\mathbf{r}', \mathbf{r}'')$ [Hed65]. In this expansion, the dynamically screened Coulomb interaction, which additionally depends on the frequency ω , is defined as

$$W(\mathbf{r}, \mathbf{r}', \omega) = \int d\mathbf{r}'' \varepsilon^{-1}(\mathbf{r}, \mathbf{r}'', \omega) v(\mathbf{r}', \mathbf{r}''). \quad (4.9)$$

In this picture, the presence of other charges acts as a dielectric medium that generally reduces, i.e., screens, the interaction strength. Incorporating the dielectric matrix ε^{-1} thus gives hope for a more rapidly convergent perturbation treatment. Moreover, Hedin showed that W , ε^{-1} , and G can be calculated by solving a set of integro-differential equations [Hed65].

As it has been demonstrated extensively for solids and more recently also for molecules, the first order in W ,

$$\Sigma_{xc}(1,2) = i\hbar G(1,2)W(1^+,2), \quad (4.10)$$

already yields quite accurate results for ionization energies and fundamental gaps [AG98, AJW00, ORR02, RJT10, BAO11, vCS⁺15]. It is exactly Eq. (4.10) that coined the term *GW* approximation.

¹Here, G_0 corresponds to $h = h_{\text{Hartree}}$, i.e., the Hartree interaction is already included in G_0 . In most practical applications that are based upon DFT, G_0 corresponds to $h = h_{\text{Hartree}} + v_{xc}$. In this situation the self-energy in Eq. (4.8) has the form $\tilde{\Sigma}_{xc} = \Sigma_{xc} - v_{xc}$.

²The zeroth-order contribution is the Hartree interaction, which is included in G_0 .

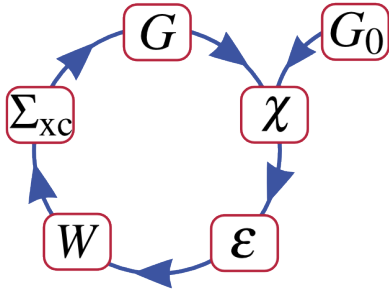


Figure 4.1: Self-consistency cycle for an iterative solution of the GW Hedin equations. A noninteracting G_0 is used as the starting point. For perturbative G_0W_0 the cycle is left after the self-energy is calculated for the first time, i.e., before the Green's function is updated.

All in all the Hedin equations in the GW approximation read,

$$G(1,2) = G_0(1,2) + \int d3 \int d4 G_0(1,3) \Sigma_{xc}(3,4) G(4,2) \quad (4.11)$$

$$\chi(1,2) = -i\hbar G(1,2) G(2,1) \quad (4.12)$$

$$\epsilon(1,2) = \delta(1,2) - \frac{i}{\hbar} \int d3 v(1,3) \chi(3,2) \quad (4.13)$$

$$W(1,2) = \int d3 \epsilon^{-1}(1,3) v(3,2) \quad (4.14)$$

$$\Sigma_{xc}(1,2) = i\hbar G(1,2) W(1^+,2). \quad (4.15)$$

Here, χ denotes the irreducible polarizability, which in GW accords to the polarizability of the Random-Phase Approximation (RPA) [ORR02]. To include second or higher orders of W , i.e., everything that is missing in GW, the GW Hedin equations have to be augmented. These contribution are commonly referred to as vertex corrections [Hed65, BSO⁺05]. The GW Hedin equations still need to be solved self-consistently as illustrated in Fig. 4.1 since W and Σ depend on G and vice versa. As such a self-consistent treatment is quite expensive for large systems, various schemes have been suggested to evaluate the self-energy in a non-self-consistent fashion [BG14].

4.3 Perturbative G_0W_0

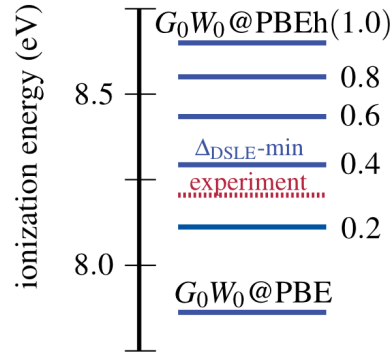
On the lowest rung of the GW self-consistency hierarchy ladder one constructs a noninteracting Green's function G_0 that is as accurate as possible. Instead of traversing the full cycle of Eqs. (4.11)-(4.15) more than once, only G_0 is used to calculate all subsequent properties. The Green's function itself is never updated. From G_0 follows a zeroth-order expression for the screened Coulomb interaction W_0 . The self-energy is then evaluated as

$$\Sigma_{xc} = i\hbar G_0 W_0. \quad (4.16)$$

In this so-called G_0W_0 scheme [HL85, HL86] the quasiparticle energies are now evaluated with first-order perturbation theory in the following way.

Since single-particle energies and orbitals from DFT can be reasonable approximations to quasiparticle energies and Dyson orbitals, as I have discussed in Sec. 2.5, they can be used to construct a zeroth-order Green's function. Identifying a complete set of KS or GKS single-particle orbitals

Figure 4.2: Quasiparticle IPs of PTCDA from $G_0W_0@PBEh(\alpha)$ for various amount of EXX α . Predicted IPs lie in a range of about 1 eV. The experimental reference value adopted from Refs. [DMK⁺06, SWLZ09] lies at 8.2 eV. The DSLE-minimized ($\Delta_{DSLE-min}$) starting point with $\alpha = 0.4$ shows a quasiparticle IP of 8.29 eV.



with the Dyson orbitals and the corresponding eigenvalues with the quasiparticle energies in Eq. (4.3), G_0 reads³

$$G_0(\mathbf{r}, \mathbf{r}', \omega) = \sum_i \frac{\varphi_i(\mathbf{r}) \varphi_i^*(\mathbf{r}')}{\hbar\omega - [\varepsilon_i + i\eta \text{sgn}(\mu - \varepsilon_i)]}. \quad (4.17)$$

Assuming that the G_0W_0 self-energy makes only a small correction to the single-particle eigenvalues, its difference to the xc functional employed in the preliminary DFT calculation can be treated as a perturbation $v_{\text{pert}} = \Sigma_{xc}^{G_0W_0} - v_{xc}^{\text{DFT}}$. First-order perturbation theory, thus, yields the first-order quasiparticle-energy equation

$$\varepsilon_i^{\text{QP}} = \varepsilon_i + \int d^3r \int d^3r' \varphi_i(\mathbf{r}) \left[\Sigma_{xc}^{G_0W_0}(\mathbf{r}, \mathbf{r}', \varepsilon_i^{\text{QP}}) - v_{xc}^{\text{DFT}}(\mathbf{r}) \delta(\mathbf{r} - \mathbf{r}') \right] \varphi_i(\mathbf{r}'). \quad (4.18)$$

As the self-energy is depending on the quasiparticle energy itself, Eq. (4.18) has to be solved for $\varepsilon_i^{\text{QP}}$.

Since its first application to metals, the G_0W_0 approach has proved to be quite successful for computing band structures of metals, semiconductors, and insulators [AG98, AJW00, ORR02]. In recent years G_0W_0 is increasingly used for molecules, too, with a mostly satisfying accuracy for IPs and PES [BAO11, FAO⁺11, QUM11, MCR⁺12, Bru12, SBKN12].

Decisive for a successful first-order perturbation treatment is an appropriate zeroth-order approximation or starting point. Particularly the considerations on the accuracy of DFT eigenvalues and orbitals in chapter 2 suggest that large variations of the results might occur depending on the choice of the xc functional employed in the preliminary DFT calculation. Indeed, significant deviations on the order of 1 eV for IP predictions of molecules have been reported [RQN⁺05, FFB⁺07, MCR⁺12, BM13]. As an example, I illustrate the starting-point dependence in Fig. 4.2 for the quasiparticle IPs of PTCDA⁴. To properly define a G_0W_0 calculation, the notation “ $G_0W_0@$ starting point” has been established. While $G_0W_0@PBE$ underestimates the experimental IP by about 0.34 eV, a starting point with 100% EXX, as included in $G_0W_0@PBEh(\alpha = 1.0)$, overshoots the IP by about 0.44 eV. Varying the amount of EXX via the parameter α in $G_0W_0@PBEh(\alpha)$, pretty much every quasiparticle energy in between can be obtained. The rather broad range of predictions certainly introduces some degree of arbitrariness in the results. A pragmatic solution to this issue would be empirical benchmarking or an a posteriori choice of the starting point. However, these approaches are rather unsatisfying from a formal perspective. Systematic schemes to find optimized starting

³HF orbitals and eigenvalues are also often used.

⁴I performed all G_0W_0 calculations with the FHI-aims code [BGH⁺09, RRB⁺12] employing numeric atom-centered Tier 4 augmented by Gaussian aug-cc-pV5Z basis functions [Dun89, RRB⁺12].

points were proposed, for example, by K rd rfer *et al.* [KM12] and Atalla *et al.* [AYC⁺13]. A central aspect of Publ. [P7] is to determine an optimized starting point from hybrid functionals by satisfying the constraint of piecewise linearity as well as possible.

The starting-point dependence is not the only drawback of G_0W_0 calculations. For example, particle and momentum conservation laws are violated [BK61, SGGG01]. Also ground-state properties such as the total energy are not unambiguously defined as mentioned before [DvLvB06]. Since neither the Green’s function nor the orbitals are updated in the calculations, the electron density from G_0 is qualitatively wrong [CRR⁺12].

One rung beyond G_0W_0 are various flavors of partially self-consistent schemes. Self-consistency in the quasiparticle energies mitigates the starting-point dependence [HL86, MCR⁺12]. Here, the quasiparticle energies are inserted into the Green’s function in Eq. (4.17) after each iteration loop while keeping the single-particle orbitals. Another approach is GW_0 in which only G is updated until self-consistency [vBH96]. The screened Coulomb interaction remains on the W_0 level, which alleviates computational cost since calculating W is the most expensive step in the iteration scheme. Yet another approach, namely the quasiparticle self-consistent GW , aims to find the single-particle Hamiltonian that minimizes the G_0W_0 correction in a self-consistent manner [vSKF06, KvF07, BG14]. Publication [P8] offers a comparison of various GW flavors for a benchmark set of 100 molecules [vCS⁺15].

4.4 Fully self-consistent GW

At the highest rung, i.e., a fully self-consistent implementation of GW , most pathologies of G_0W_0 can be cured. In fully self-consistent GW (scGW) [HvB98, FVK04, RJT10, CRR⁺12, Car13] the Hedin equations are iterated until deviations between the Green’s functions of two succeeding iterations fall beneath a certain threshold [CRR⁺13]. This procedure eliminates the starting-point dependence completely. Unlike perturbative approaches, scGW provides unique and accurate total energies and electron densities, which makes a unified description of the ground state and of charged excitations possible [CRR⁺12]. Moreover, scGW permits an unbiased assessment of the intrinsic accuracy of the GW approximation to the exact self-energy. For molecules it has been shown that quasiparticle IPs typically improve over G_0W_0 with purely semilocal or HF starting points [RJT10, CRR⁺12], [P7]. In Publ. [P7] ionization energies from self-consistently obtained total-energy differences are shown to deviate from vertical experimental IPs by a mean absolute error of 0.2 eV (for a set of 48 benchmark molecules). In contrast to perturbative G_0W_0 , the quasiparticle energies are evaluated from the spectral function (4.5) in scGW.

4.5 Piecewise linearity and the accuracy of quasiparticle energies

Since GW is an approximate theory, a critical survey of its level of exactitude is fundamental to reveal sources of error. Exact constraints supply an ideal means to do so. Therefore, I will revisit the condition of piecewise linearity, which not only has to be obeyed by DFT but is a valid relation for quantum-mechanical ensembles in general. Unfortunately, a direct evaluation of Eq. (2.13) is presently not possible for GW because a rigorous ensemble generalization has not yet been achieved and might even necessitate an augmentation of the GW self-energy [vLS12]. For the special case of G_0W_0 it was shown that an approximate generalization is possible under the assumption of the frozen orbital approximation [YMSC13].

Due to this obstruction, the central idea of Publ. [P7] is to assess piecewise linearity in an indirect manner. The linearity condition in Eq. (2.13) implies that the first derivative of the total energy with respect to the fractional occupation number f (i.e., $\partial E/\partial f$) should be constant and that it exhibits discontinuities at integer occupations ($f = 0$ and $f = 1$). Additionally, $\partial E/\partial f$ equals the electron removal energy $E_0(N) - E_0(N - 1)$ or, equivalently, the energy for adding an electron to the positively charged system. Therefore, the vertical IP of the neutral system with N electrons can be expressed as:

$$\left. \frac{\partial E(f)}{\partial f} \right|_1 = E_0(N) - E_0(N - 1) = -\text{IP}(N). \quad (4.19)$$

A similar relation holds for the electron affinity of the cation (EA_c):

$$\left. \frac{\partial E(f)}{\partial f} \right|_0 = E_0(N) - E_0(N - 1) = -\text{EA}_c(N - 1). \quad (4.20)$$

Equations (4.19) and (4.20) illustrate that $\text{IP} = \text{EA}_c$ in an exact theory. Thus, the difference between IP and EA_c ,

$$\Delta_{\text{DSLE}} = \text{EA}_c(N - 1) - \text{IP}(N), \quad (4.21)$$

can be seen as a criterion for a deviation from the straight line error (DSLE). The major asset of Eq. (4.21) is that it lends itself to an evaluation of the DSLE within GW , which only provides access to properties at integer particle numbers. These include the quasiparticle IP and EA. Since $\Delta_{\text{DSLE}} = 0$ is a necessary condition for piecewise linearity, this indicator tells precisely if piecewise linearity can be fulfilled. However, in an approximate treatment of electronic exchange and correlation such as, for example, in GW , the IP and the EA_c may differ. To make a statement also about the severity of the DSLE via Eq. (4.21), another assumption has to be made. If an ensemble generalization to GW was known, additional contributions to the self-energy have to be small near integer electron numbers. Note that for G_0W_0 the quasiparticle energies correspond to the slopes of the total energy of the RPA if the frozen orbital approximation is assumed [Wan10].

Another reason why the indicator Δ_{DSLE} is proposed in Publ. [P7] relates to the self-screening in GW , which provides an alternative view on the DSLE perspective. Self-screening can be seen as an analogue to the self-interaction present in some DFT functionals. Yet, the origin of self-screening is differing as the Hartree self-interaction as defined in Eq. (2.10) is canceled in GW . This can be shown if the GW self-energy is split into an exchange and correlation part, $\Sigma_{\text{xc}} = \Sigma_{\text{x}} + \Sigma_{\text{c}}$. The former corresponds to the Fock operator and, hence, cancels the Hartree self-interaction exactly [NBRG07]. The correlation part of Σ has no counterpart, though. Invoking the hydrogen atom example, the residual correlation part leads to one electron erroneously screening itself. As the screening in GW apparently is not sophisticated enough, also $\text{IP}(N)$ and $\text{EA}(N - 1)$ will most likely not be the same. In the calculation for the $N - 1$ -particle system, the screening will be that of $N - 1$ electrons and, thus, typically less than that in the N -particle system. Again, this is most evidently seen for 1-electron systems such as the hydrogen atom where the calculation for $N-1$ -electron system, i.e., the proton, correctly gives zero screening. The calculation for the neutral H atom already includes screening. Following this line of thought, the $\text{EA}(N - 1)$ and $\text{IP}(N)$ difference measures the severity of the self-screening.

Publication [P7] shows that the GW approach is inherently in error concerning piecewise linearity because Δ_{DSLE} does not vanish for scGW calculations for the studied molecules. Compared to semilocal DFT or HF, scGW reduces the severity of the DSLE significantly. The second major subject of Publ. [P7] is to examine the DSLE with respect to the starting-point dependence of G_0W_0 . As discussed above, varying the starting point leads to varying accuracies in the IP predic-

tions. Evaluating Δ_{DSLE} for G_0W_0 with PBEh(α) starting points, a clear correlation of the quality of IPs and the DSLE indicator is demonstrated. Particularly the starting points that minimize Δ_{DSLE} show the best agreement to experimental reference IPs with mean average deviations of only 0.21 eV for a set of 48 molecules and atoms. I present further analysis for another set of 100 molecules and atoms in Publ. [P8] that underpins the findings of Publ. [P7], i.e., the DSLE minimized starting points yield an accurate IP description. That the minimization is not only a concept applicable to GW is demonstrated in Publ. [P7] by an analysis that utilizes a perturbative method beyond GW [RMC⁺15].

The problem of charge transfer in donor-acceptor systems provides an ideal test case for illustrating the reliability of the DSLE-minimized GW approach. For a weakly coupled donor-acceptor system, such as the tetrathiafulvalene donor (TTF) and the tetracyanoquinodimethane acceptor (TCNQ) [CAR⁺14], the energy required to promote an electron from the donor's HOMO to the acceptor's LUMO level can be approximated by the energy difference [CAR⁺14]

$$E_{\text{CT}} = \text{IP}(\text{donor}) - \text{EA}(\text{acceptor}). \quad (4.22)$$

In scGW⁵, the charge-transfer energy $E_{\text{CT}} = 5.96 \text{ eV} - 4.24 \text{ eV} = 1.71 \text{ eV}$ significantly underestimates the reference value of 3.5 eV. The reference is composed of the vertical experimental IP(N) of TTF, which lies at 6.7 eV [KYA⁺84], and the EA(N) of TCNQ from coupled-cluster singles, doubles, and perturbative triples [RTPHG89] calculations, which lies at 3.2 eV [MPAVO04].

First, I want to discuss the accuracy of the IP description of TTF. The deviation of the IP predicted by scGW from the reference IP can be explained by a rather large Δ_{DSLE} of 1.1 eV. The accuracy of the IP can be increased by drawing on Δ_{DSLE} -minimized G_0W_0 calculations. For the optimal starting point that minimizes Δ_{DSLE} , G_0W_0 yields an IP of 6.7 eV, which perfectly coincides with the experimental value.

Second, the accuracy of the electron affinity EA(N) of the acceptor has to be assessed. Here, the proposed DSLE concept can analogously be transferred to the N and $N + 1$ -electron interval of the total-energy curve. By adapting Eqs. (4.19) and (4.20), Δ_{DSLE} compiles to $\Delta_{\text{DSLE}} = \text{EA}(N) - \text{IP}(N + 1)$, which again has to vanish for an exact theory. Here, scGW yields a $\Delta_{\text{DSLE}} = \text{EA}(N) - \text{IP}(N + 1) = 1.0 \text{ eV}$ for the acceptor TCNQ. The nonvanishing Δ_{DSLE} suggests that EA(N) from scGW differs from the true value. With EA(N) = 4.24 eV scGW indeed overestimates the reference EA(N) significantly. Turning to G_0W_0 with the Δ_{DSLE} -minimized starting point, I find EA(N) = 3.9 eV. This prediction is still too high compared to the reference. Consequently, the charge-transfer energy $E_{\text{CT}} = 2.8 \text{ eV}$ is too low but indicates the right direction when compared to the non- Δ_{DSLE} -minimized scGW prediction. That EAs of molecules are usually overestimated is a well known problem of G_0W_0 (even for starting points that employ a high fraction of Fock exchange), which is often discussed in the context of predicting fundamental gaps (see Eq. (2.15)) [BAO11, SBKN12].

⁵I use Tier 3 basis sets [RRB⁺12] for all scGW calculations.

APPENDIX A

Complementing work

A.1 Coulomb-wave final state and the partial-wave expansion

As I have discussed in the main part of my thesis, a reliable approximation for the photoelectron's final state is desirable. To improve upon the simple PW state, the interaction with the positively charged molecule has to be taken into account. The most straightforward approach is to expose the photoelectron to a single positive charge that is located at the molecule's center. This situation can be described by the Schrödinger equation of the hydrogen atom. Yet, the spatial extend of the molecule, any screening effects of the remnant electrons, and a delocalization of the photohole over the molecule are still neglected. Based on these assumptions, the photoelectron's state, $\chi_{\mathbf{k}}$, can be approximated by a continuum eigenstate of

$$\left[-\frac{\hbar^2}{2m_e} \nabla^2 - \frac{Ze^2}{r} \right] \chi_{\mathbf{k}}(\mathbf{r}) = \varepsilon_k \chi_{\mathbf{k}}(\mathbf{r}), \quad (\text{A.1})$$

with a kinetic energy of $\varepsilon_k = \frac{\hbar^2 k^2}{2m_e} > 0$. Z is the number of positive charges. Expressed as an expansion of partial waves, i.e., an expansion in an angular basis in terms of the spherical harmonics Y_l^m , the regular continuum solutions of Eq. (A.1) have the following form [Mes14]

$$\chi_{\mathbf{k}}(\mathbf{r}) = 4\pi \sum_{l=0}^{\infty} \sum_{m=-l}^l i^l e^{i\sigma_l} Y_l^{m*}(\theta_k, \phi_k) Y_l^m(\theta_r, \phi_r) \frac{F_l(kr, \eta)}{kr}. \quad (\text{A.2})$$

The angles θ_k, ϕ_k and θ_r, ϕ_r refer to the representation of the vectors \mathbf{k} and \mathbf{r} in spherical coordinates. $\sigma_l = \text{Arg}[\Gamma(l+1+i\eta)]$ describes the phase shift of different outgoing partial waves, which arise due to the Coulomb potential. Thereby, Γ denotes the gamma function [AS72] and $\eta = -Z \frac{me^2}{k\hbar^2}$. The radial part of the final state, $F_l(kr, \eta)$, is the so-called Coulomb wave (CW) [AS72]. It is the solution of the radial part of Eq. (A.1),

$$\frac{\partial^2}{\partial \rho^2} F_l(\rho, \eta) + \left[1 - \frac{2\eta}{\rho} - \frac{l(l+1)}{\rho^2} \right] F_l(\rho, \eta) = 0, \quad (\text{A.3})$$

which can be derived by separating the spherical part of the Laplacian from the radial part and projecting the equation onto a specific Y_l^m . The coordinate ρ stands for the product kr . The second parameter of the CW is $\eta = -Z \frac{me^2}{k\hbar^2}$. It is worth pointing out that the CW final state merges into the partial-wave expansion of the PW final state for $\eta \rightarrow 0$, which means that the number of positive

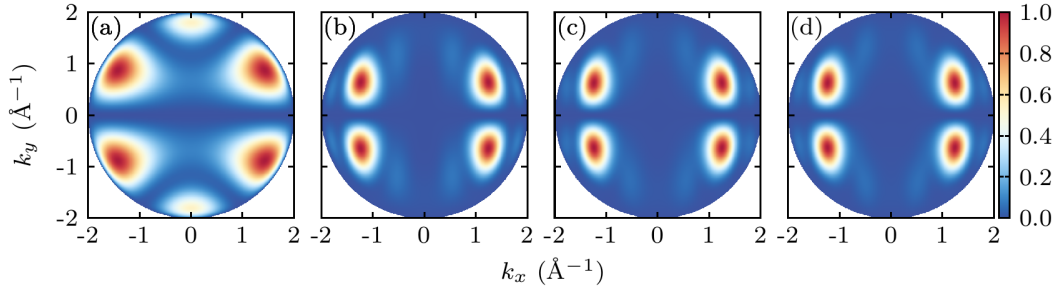


Figure A.1: ARPES intensity momentum maps computed with the CW final state for the GSIC HOMO of PTCDA with horizontal polarization parallel to the long molecular axis. The momentum of the photoelectron corresponds to $|\mathbf{k}| = 2.0 \text{ \AA}^{-1}$. The partial-wave expansion in Eq. (A.6) is truncated at (a) $l = 5$, (b) 10, (c) 15, and (d) 20.

charges goes to zero for a finite k [Mes14]. The partial-wave expansion of the PW reads

$$\chi_{\mathbf{k}}(\mathbf{r}) = e^{i\mathbf{k}\mathbf{r}} = 4\pi \sum_{l=0}^{\infty} \sum_{m=-l}^l i^l Y_l^{m*}(\theta_k, \phi_k) Y_l^m(\theta_r, \phi_r) j_l(kr), \quad (\text{A.4})$$

where $j_l(kr)$ stands for the spherical Bessel function [AS72].

I implemented the CW and PW final state, respectively, with the adjustable parameter η according to the recursive algorithms presented in Ref. [AS72]. Based on Eq. (A.2), CW and PW ARPES intensities can be computed via Fermi's golden rule. Inserting the CW final state into Eq. (1.9), the transition matrix element becomes

$$\begin{aligned} \langle \chi_{\mathbf{k}}(\mathbf{r}) | \mathbf{A}\mathbf{p} | d_I(\mathbf{r}) \rangle &= 4\pi \sum_{l=0}^{\infty} \sum_{m=-l}^l (-i)^l e^{-i\sigma_l} \left\langle Y_l^m(\theta_r, \phi_r) \frac{F_l(kr, \eta)}{kr} | \mathbf{A}\mathbf{p} | d_I(\mathbf{r}) \right\rangle Y_l^m(\theta_k, \phi_k) \\ &= \sum_{l=0}^{\infty} \sum_{m=-l}^l c_l^m Y_l^m(\theta_k, \phi_k). \end{aligned} \quad (\text{A.5})$$

For a fixed kinetic energy of $E_{\text{kin}} = \frac{\hbar^2 \mathbf{k}^2}{2m_e}$ the photoemission intensity can then be written in terms of the expansion coefficients c_l^m and the spherical harmonics,

$$J(\theta_k, \phi_k) \propto \left| \sum_{l=0}^{\infty} \sum_{m=-l}^l c_l^m Y_l^m(\theta_k, \phi_k) \right|^2. \quad (\text{A.6})$$

The expansion along the angular momentum l is usually well converged for systems such as CO or PTCDA for $l_{\text{max}} = 20$ (for both the PW and CW case). This is demonstrated in Fig. A.1 for the momentum maps corresponding to the GSIC HOMO of PTCDA obtained with the CW final state with increasing l_{max} . To ensure convergence in all further CW and PW calculations in this thesis and in the publications, I never truncate the sum in Eq. (A.6) before $l = 20$. A reason for the rapid convergence is due to the behavior of $F_l(\rho, \eta)/kr$, which goes to zero at the molecular region with increasing l as displayed in Fig. A.2. Therefore, the expansion coefficients c_l^m , which are governed by the overlap of the final and initial state, approach zero for large l .

For most ARPES momentum maps on PTCDA and NTCDA there is no significant difference

Figure A.2: Behavior of the radial part $\frac{F_l(kx, \eta)}{kx}$ of the CW final state for different angular momenta l displayed on the x -axis of a Cartesian grid. The probability distribution at the center of the numerical box vanishes with increasing l . Each radial function is computed with $k = 3.8 \text{ \AA}^{-1}$ that corresponds to a kinetic energy of 55 eV.

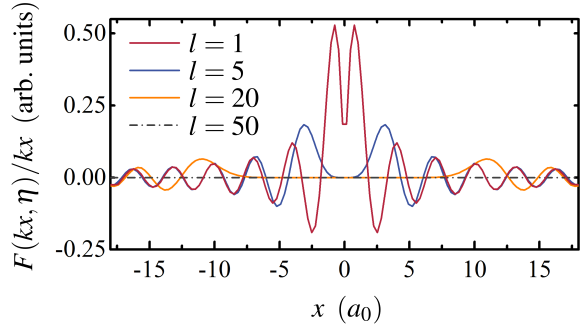
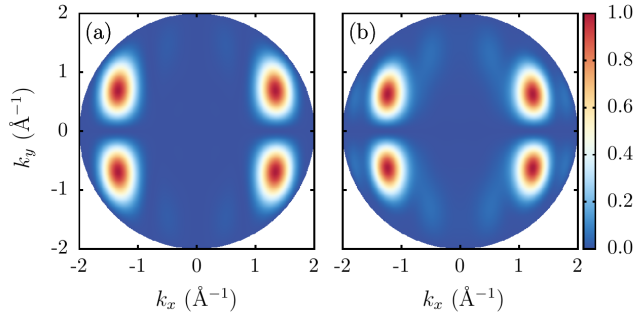


Figure A.3: ARPES intensity momentum maps obtained from the GSIC HOMO of PTCDA with horizontal polarization parallel to the long molecular axis. The momentum of the photoelectron corresponds to $|\mathbf{k}| = 2.0 \text{ \AA}^{-1}$. (a) depicts the PW result whereas (b) shows the CW intensity pattern.



between the PW and the CW final state. Representative for linearly polarized fields, I display the momentum map of the PTCDA HOMO and horizontal polarization that is parallel to the long molecular axis in Fig. A.3. The momentum of the photoelectron corresponds to $|\mathbf{k}| = 2.0 \text{ \AA}^{-1}$. The corresponding measured momentum map is shown and discussed in Fig. 1 of Publ. [P5]. Comparing the PW and CW results in Fig. A.3 (a) and (b), both momentum maps hardly differ. Only the positions of the four spots of high intensity are slightly shifted. The CW final state also fails to predict the prominent intensity features at $k_x = 0.0 \text{ \AA}^{-1}$ present in experiment, see Publ. [P5].

The implementation of the CW approximation was mainly prompted by the hope that the CW is able to predict the circular dichroism observed for the organic semiconductors molecules. As nicely illustrated for the toy model of emission from atomic orbitals in Ref. [Sch90], the circular dichroism can be explained as arising from interference effects between different partial-wave components of the CW final state. Thereby, the photon helicity can reverse the relative phasing of partial-wave components leading to distinct interference patterns for both circular polarization directions.

While the CW final state is able to produce a significant CDAD for atomistic systems and small molecules (see Sec. A.3), it is clearly limited for systems with a larger spatial extent. This is demonstrated in Fig A.4 for the PTCDA HOMO. Although there is a slight difference in the intensity pattern between positive and negative k_y , a CDAD effect is barely visible. Thus, the CW final state seems to be too crude to capture important aspects such as the emission from a large molecule with a photohole that can be delocalized over large parts of the systems.

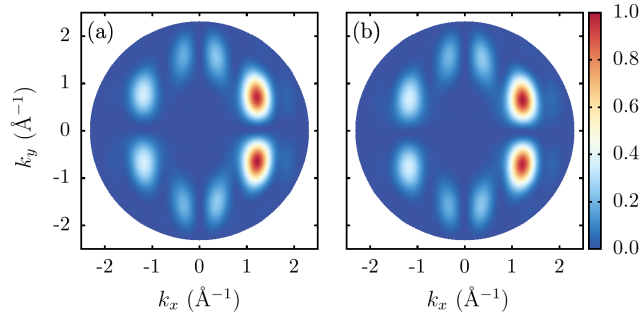


Figure A.4: ARPES intensity momentum maps obtained from the GSIC HOMO of PTCDA with circularly polarized light using the CW approximation. Photon incident direction is the long molecular axis with an angle of 65° towards the normal (z -axis) of the molecular plane. The photoelectron's momentum corresponds to $|\mathbf{k}| = 2.3 \text{ \AA}^{-1}$. (a) depicts the LCP result, whereas (b) shows the RCP intensity pattern.

A.2 Horizontal polarization and NTCDA

Besides PTCDA, ARPES experiments on NTCDA adsorbed on Ag(110) were conducted. To underpin the results of Publ. [P5], I want to demonstrate that effects beyond the PW final state can be observed for NTCDA, too. As an example, Fig. A.5 (b) shows the experimentally recorded momentum map of the NTCDA HOMO. The system was probed with photons of $\hbar\omega = 26$ eV that are polarized horizontally. However, the alignment of the polarization vector parallel to the long molecular axis is imperfect in this measurement. To improve the quality of the spectrum, it was symmetrized with respect to the molecular principal axes and a constant background intensity was subtracted.

Nevertheless, the measured momentum map in Fig. A.5 (b) demonstrates that intensities arise at $k_x \approx 0 \text{ \AA}^{-1}$, which corresponds to an emission direction that is approximately perpendicular to the polarization direction. Whereas the PW results displayed in Fig. A.5 (a) shows no intensities at this particular spots, the real-time approach does, see Fig. A.5 (c). In addition to the experimental uncertainties due to the imperfect alignment, another reason for deviations might be deficiencies of TDLDA. For NTCDA the OE-SIE distorts the ordering of the upper orbitals. In particular, the measured HOMO momentum map matches the (TD)LDA HOMO-2 orbital. Thus, the spectrum in Fig. A.5 (c) actually corresponds to the TDLDA HOMO-2 and not to the HOMO.

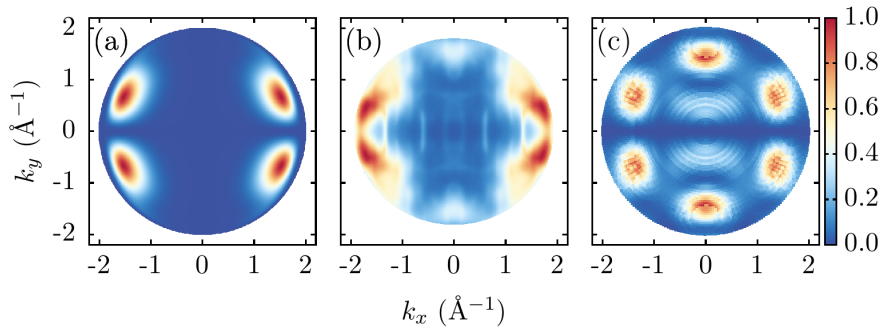


Figure A.5: ARPES intensity momentum maps obtained with horizontal polarized light that is aligned parallel to the long molecular axis (x -axis). (a) Momentum map of the GSIC HOMO of NTCDA obtained with the PW approximation. The momentum of the photoelectron corresponds to $|\mathbf{k}| = 2.0 \text{ \AA}^{-1}$. (b) shows the experimental intensity, courtesy of A. Schöll and M. Graus. The experiment is performed on an NTCDA monolayer on top of Ag(110) at $\hbar\omega = 26$ eV. Note that the polarization direction deviates from the long molecular axis by a few degrees, which influences the ARPES pattern. The spectrum was symmetrized and a constant background was subtracted before normalization. (c) TDLDA real-time propagation results.

A.3 The energy dependence of the circular dichroism of CO

A significant energy dependence of the circular dichroism was further reported for uniformly oriented CO molecules adsorbed on a Pd(111) surface [DDM85, WBG89, Sch90, WBG⁺91]. For my calculations I oriented an isolated CO molecule according to Fig. A.6, which is consistent with the experimental geometry in [WBG89, Sch90, WBG⁺91].

The right part of Fig. A.6 shows the energy dependence of the fully angle-resolved CDAD for the emission from the 4σ orbitals of CO. Here, the normalized CDAD intensities are defined as

$$J_{\text{CDAD}} = (J_{\text{LCP}} - J_{\text{RCP}})/(J_{\text{LCP}} + J_{\text{RCP}}). \quad (\text{A.7})$$

The angle of photon incidence is set to $\beta = 50^\circ$. The left column of Fig. A.6 displays the results of the real-time propagation scheme, whereas the right column shows the CW results. Each row corresponds to a different photon energy. I now want to discuss some of the features observed in Fig. A.6.

As it can be anticipated from the change of the helicity of the photons, the CDAD patterns reveal a mirror symmetry of the emission intensities with respect to the plane of photon incidence (xz -

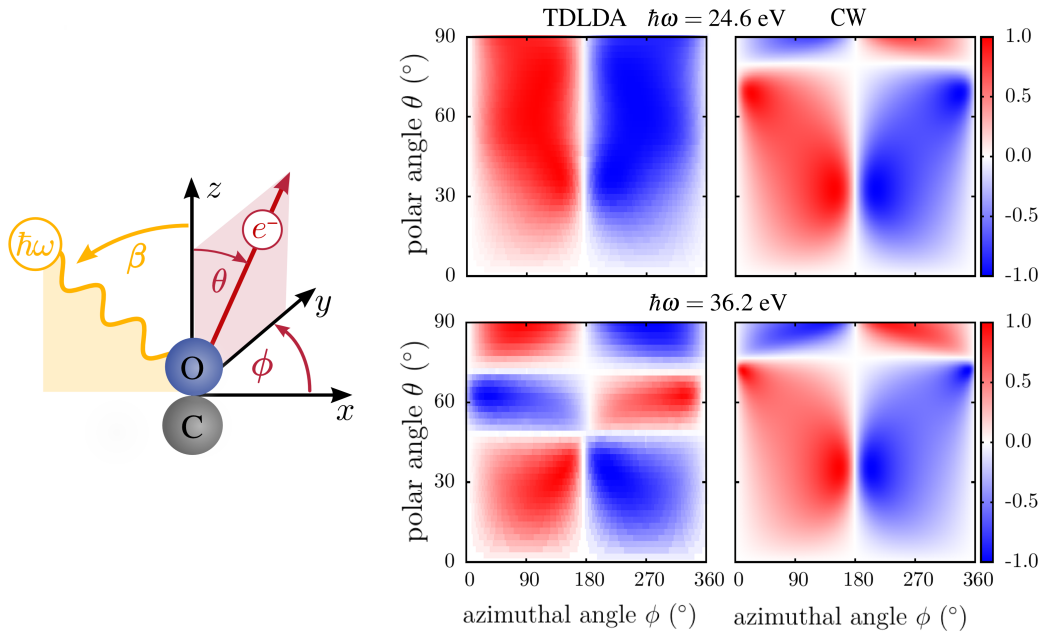


Figure A.6: Left: Setup for ARPES on a spatially aligned CO molecule, which accords with the experimental setup used to probe a monolayer of CO molecules adsorbed on a Pb(111) surface [Sch90]. Photons are incoming under an angle of $\beta = 50^\circ$. The angular dependence as depicted in Fig. A.7 is recorded in the yz -plane, i.e., under an angle of $\phi = 90^\circ$.

Right: Fully angle-resolved, normalized CDAD intensity $J_{\text{CDAD}} = (J_{\text{LCP}} - J_{\text{RCP}})/(J_{\text{LCP}} + J_{\text{RCP}})$ obtained from an individual CO molecule, which is oriented as depicted on the left. Red areas indicate regions with emission predominately caused by LCP light, blue by RCP. The left column shows the real-time propagation results from TDLDA for the emission from the 4σ orbital of CO. The right column shows the CW results. Each row corresponds to a different photon energy.

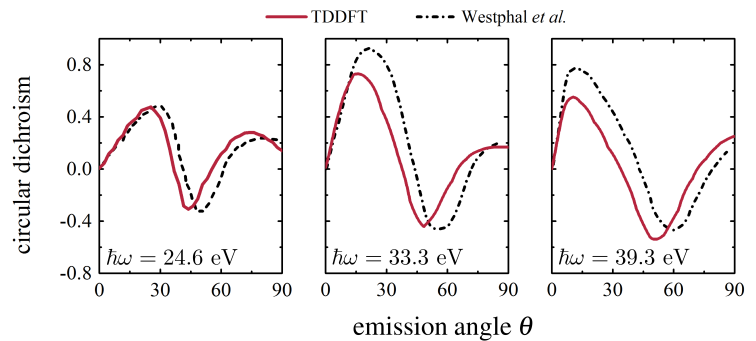
plane). Emission in the xz -plane corresponds to $\phi = 0, 180^\circ$. As an example, the upper left CDAD spectrum of Fig. A.6 indicates that emission caused by LCP is dominating for $0^\circ < \phi < 180^\circ$ (red colored area). On the other side of the plane of incidence, i.e., for $180^\circ < \phi < 360^\circ$, the prevalent emission is triggered by RCP (blue colored area). The intensities ratios of RCP to LCP are exactly the same on both sides, yet with different sign.

Further, the CDAD must vanish for emission angles that lie in the plane of photon incidence. Since two of the three distinct axes merge, the system doesn't provide a definite handedness for this particular emission direction. A similar argument holds for $\theta = 0^\circ$ as the surface normal coincides with the emission direction. The limiting cases given by the geometry, which are completely independent of the photon energy, are predicted correctly by both approaches. Note that small deviations of the real-time results from this behavior are due to the coarse angular resolution.

Regions at which the CDAD vanishes or switches sign for nongeometrical reasons are characteristic of the energy dependence. Whereas the real-time approach for a photon energy of $\hbar\omega = 24.6$ eV predicts no such nodes for $0^\circ < \theta < 90^\circ$, there are two for $\hbar\omega = 36.6$ eV. The energy dependence of the emission from the 4σ orbital is discussed in more detail in Publ. [P5]. Figure. 3 of Publ. [P5] shows the CDAD signal for a fixed emission angle of $\phi = 90^\circ$. While the real-time approach captures the energy dependence in accordance with frozen-core HF reference calculations presented in Refs. [LRM82, WBG⁺91], the CW is too simplistic for predicting the energy dependence correctly.

In addition to the emission from the 4σ orbital, also the emission from the 5σ and the twofold degenerate 1π orbitals were measured in Refs. [WBG89, Sch90, WBG⁺91]. For CO adsorbed on Pd(111) the three orbitals are too close in energy to be recorded separately. Therefore, Fig. A.7 shows the superposition of the emission signals of all three orbitals. The panels correspond to different photon energies. In general, the frozen-core HF and real-time calculations are in good agreement and follow the same trend, i.e., from a positive CDAD at small θ to negative CDAD values around $\theta = 45^\circ$ and back to a positive CDAD for $\theta = 90^\circ$. This feature is characteristic of all three energies displayed. Yet, the magnitude changes as the energy increases. Compared to the reference calculations, the real-time results show a slightly less pronounced CDAD signal around $\theta \approx 20^\circ$ for $\hbar\omega = 33.3$ eV and 39.3 eV. Contrasted to the experimental data shown in [WBG⁺91], the real-time approach seems favorable for small angles θ due to the smaller CDAD values.

Figure A.7: Normalized CDAD intensity as given in Eq. (A.7) from a superposition of the emission signals from the 5σ and the twofold degenerate 1π orbitals of CO. Red solid line: TDLDA real-time results. Black dotted line: frozen-core HF calculations adopted from Ref. [WBG⁺91].



A.4 Adsorption effects of PTCDA on Ag(110)

Adsorption effects of molecules on noble metal substrates can play an important role. Among others, it was shown that the functional side groups of PTCDA are bent towards the Ag(110) surface. The deflection of the nuclei positions are illustrated in Fig. A.8. In a first attempt to grasp adsorption effects and particularly their effect on ARPES, I used the measured nuclei displacements from Ref. [MBW⁺13] for my calculations. To be more precise, I manipulated the gas-phase equilibrium geometry of PTCDA in such a way that the functional side groups are deflected as displayed in Fig. A.8. With the bent geometry as a refined input for the DFT ground-state calculations, I inspected the ARPES intensity maps of the frontier KS orbitals. While the influence of the geometrical change seems to be small for energetically well separated KS states, it affects the degenerate HOMO-3 and HOMO-4 predicted by FOBO GSIC used in Publ. [P0]. A superposition of the degenerate HOMO-3 and HOMO-4 leads to the intensity depicted in Fig. A.9(a). Including the geometrical change in the FOBO GSIC calculation splits the degeneracy of the orbitals. The resulting ARPES intensities of the energetically separated HOMO-3(d) and HOMO-4(b) are presented in the middle of Fig. A.9. Comparing the spectra with experiment, which is shown on the right panel of Fig. A.9, reveals a decent agreement of the intensities. However, the geometrical deformation does not improve upon the relative energetic position of the FOBO GSIC states.

To sum up, the geometrical distortion of the molecule makes a rather small contribution in terms of modeling the substrate-molecule interaction effects. However, it can be decisive for degenerate states. For a more accurate description of adsorption effects it seems necessary to include a Ag(110) surface slab in the calculations explicitly [AS09, ULR⁺14].

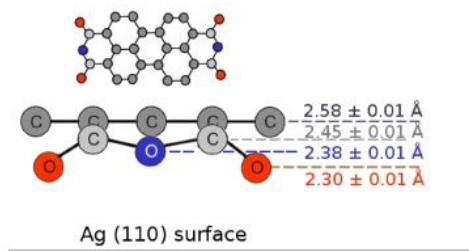


Figure A.8: Geometrical deformation of PTCDA adsorbed on Ag(110). The functional side groups are bent towards the metal surface and are deflected from the gas-phase position according to the values presented in the panel, which are adopted from Ref. [MBW⁺13].

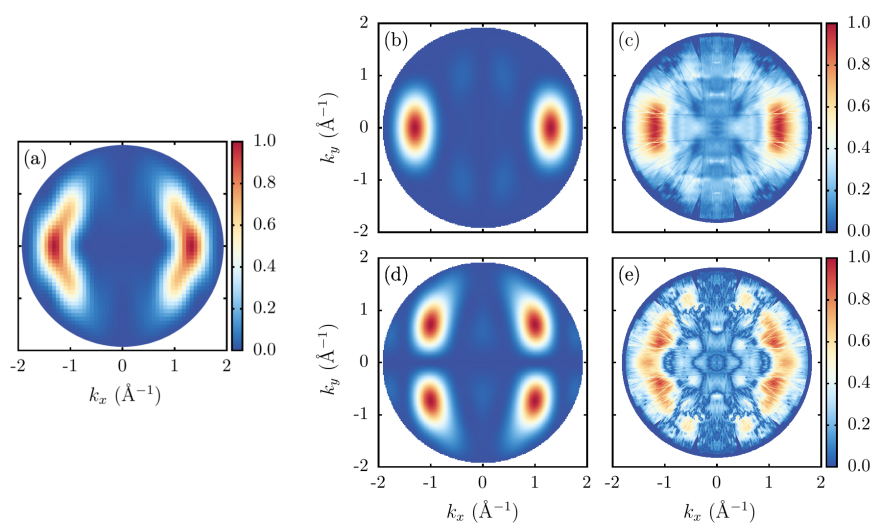


Figure A.9: Influence of the geometrical deformation of PTCDA adsorbed on Ag(110) on the degenerate FOBO GSIC HOMO-3 and HOMO-4 orbitals. The degeneracy is split resulting in two well separated states that show a decent agreement with measured spectra. (a) shows the incoherent superposition of the ARPES spectra of the FOBO GSIC orbitals calculated with the gas-phase equilibrium geometry. In the middle, the ARPES intensities of the separated HOMO-3 (d) and HOMO-4 (b) orbitals calculated with the bent geometry are shown. The right column corresponds to the experimental intensities adopted from Publ. [P0]. The calculated spectra are evaluated within the PW approximation at $k = 1.92 \text{ \AA}^{-1}$. The polarization factor $|\mathbf{A}\mathbf{k}|^2$ is set to one.

A.5 Miscellaneous details on the real-time propagation scheme

In this section I discuss some additional results and technical aspects of the real-time propagation scheme that are not covered by the main part of my thesis or by the publications and the corresponding Supporting Material.

Implementation of circular polarized fields

Monochromatic circularly polarized light can be described by an electric field that is rotating in time. The frequency of the rotation is given by the light's frequency ω . For the example of light incoming from the z -direction with a wave vector $\mathbf{k} = (0, 0, k_z)$ and a field vector rotating in the xy -plane, the electric field reads

$$\mathbf{E}^\delta(z, t) = \mathbf{E}_0 \begin{pmatrix} 1 \\ e^{i\delta} \end{pmatrix} e^{i(\omega t - kz)}. \quad (\text{A.8})$$

The phase shift between the two opposing rotation directions is denoted by δ . It is either $+\pi/2$ or $-\pi/2$ and, thus, the electric field becomes

$$\mathbf{E}^\pm(z, t) = \mathbf{E}_0 \begin{pmatrix} 1 \\ \pm i \end{pmatrix} e^{i(\omega t - kz)}. \quad (\text{A.9})$$

Considering only the real part of Eq. (A.9), the electric field reads

$$\mathbf{E}^\pm(z, t) = \mathbf{E}_0 \begin{pmatrix} \cos(\omega t - kz) \\ \mp \sin(\omega t - kz) \end{pmatrix}. \quad (\text{A.10})$$

Circular polarization may be referred to as right-handed or left-handed, and clockwise or anti-clockwise, respectively, depending on the direction in which the electric field vector rotates. Unfortunately, two opposing conventions exist and are used in the literature. To avoid confusion, I consider the rotation of the electric field from the viewpoint of the molecule's center ($z = 0$ in Eqs. (A.8)-(A.10)) for all of my calculations. If the incoming light rotates clockwise in time, I refer to the polarization as right-handed polarized. This is the case for the upper sign in Eqs. (A.9)-(A.12). In the case of anti-clockwise rotating fields, I denote the field as left-handed circularly polarized, which is given by the lower sign in Eqs. (A.9)-(A.12).

In order to be able to specify the orientation of the electric field freely, I implemented the field vector's direction depending on two angles,

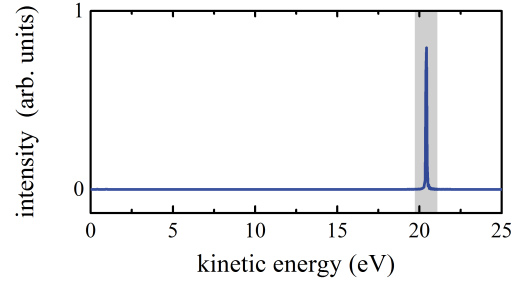
$$\mathbf{E}^\pm(t) = \mathbf{E}_0 \begin{pmatrix} \cos \alpha \cos \beta \cos \omega t \mp \sin \beta \sin \omega t \\ -\cos \alpha \sin \beta \cos \omega t \mp \cos \beta \sin \omega t \\ \sin \alpha \cos \omega t \end{pmatrix}. \quad (\text{A.11})$$

Here, α denotes the photon incident angle, which is counted towards the normal of the xy -plane. β stands for the angle within the xy -plane, which is counted from the negative x -axis ($\beta = 0^\circ$) towards the positive y -axis ($\beta = 90^\circ$)¹.

The polarization of a field can also be described by its complex valued Jones vector. For the example of circularly polarized light incoming from the z -direction, the Jones vector is given by the $(1, \pm i)$ vector in Eq. (A.9). In the Coulomb gauge the directions of \mathbf{E} and \mathbf{A} are parallel. Thus,

¹In the TDDFT code, the key for setting α is "inc_angle_a" and "inc_angle_b" for β .

Figure A.10: Angle-integrated emission signal from the TDLDA PTCDA HOMO as a function of the kinetic energy. The system was probed with LCP light incoming from the $-x$ -axis under an angle of 65° to the normal of the molecular plane (xy -plane). The photon energy was set to $\hbar\omega = 27$ eV. The gray marked area indicates the energy range that is integrated to obtain an ARPES signal.



the Jones vector of the vector potential \mathbf{A} for an arbitrary photon incident direction reads

$$\mathbf{A}^\pm = \begin{pmatrix} \cos \alpha \cos \beta \pm i \sin \beta \\ -\cos \alpha \sin \beta \pm i \cos \beta \\ \sin \alpha \end{pmatrix}. \quad (\text{A.12})$$

I use \mathbf{A} of Eq. (A.12) to evaluate the transition matrix elements of Fermi's golden rule.

Evaluation of intensities

To track the angular dependence of the photoemission signal, I distribute the detection points on a hemispherical surface in such a way that they lie on an equidistant angular grid, i.e., at $\Delta\phi = \Delta\theta = \text{const}$ with $0 \leq \phi \leq 2\pi$ and $0 \leq \theta \leq \pi/2$. As the orbitals are recorded for every time step and each detector position, the density of the angular grid should be chosen carefully in order to keep the memory demands within feasible limits. A reasonable choice for angle-integrated spectra is a resolution of 120×30 detection points in ϕ and θ direction, respectively. For typical momentum maps I recommend a resolution of 240×60 .

The calculation of the PES signal from the recorded orbitals is done with an external program. The first step is to Fourier transform the recorded orbitals from the time to the frequency domain. Second, the angle-integrated emission intensity within the upper hemisphere is calculated by integrating

$$J_i(E_{\text{kin}}) = \int_0^{2\pi} d\phi \int_0^{\pi/2} d\theta R_D^2 \sin \theta |\varphi_i(R_D, \phi, \theta, E_{\text{kin}})|^2. \quad (\text{A.13})$$

Figure A.10 shows the angle-integrated intensity from the HOMO of PTCDA as a function of the kinetic energy using TDLDA and LCP light with $\hbar\omega = 27$ eV. The spectrum reveals the emission peak positions. Since the fully angle-resolved emission signal depends on the kinetic energy at which it is evaluated, the kinetic energy can be chosen on the basis of the angle-integrated PES spectrum. To obtain the entire ARPES signal within a photoemission peak, I integrate over the width of the emission peak of interest. Usually, I choose a suitably narrow kinetic energy range of 0.2 eV on each side of the emission peak maximum, which is represented by the gray area in Fig. A.10. Explicitly angle-dependent spectra can be converted to momentum maps via Eqs. (1.2) and (1.3). The resulting momentum map corresponding to Fig. A.10 is displayed in Fig. A.11 (a).

Technical aspects and computational parameters

I now want to present additional details and technical aspects on the real-time propagation scheme. All technical aspects for the propagation of benzene and pyridine are delineated in Publ. [P2].

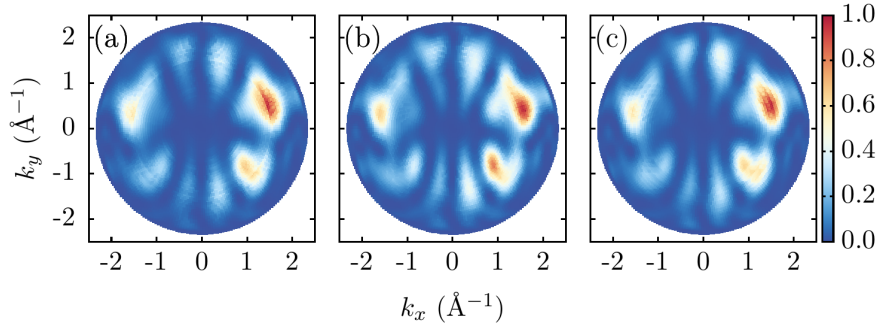


Figure A.11: ARPES intensity momentum maps from the TDLDA HOMO of PTCDA. Photons of $\hbar\omega = 27$ eV are incoming from $-x$ -axis under an angle of 65° to the normal of the molecular plane (xy -plane). The polarization is LCP. Spectra are obtained at different detection radii: (a) $R_D = 27a_0$, (b) $28a_0$, and (c) $29a_0$.

Some of the aspects presented here are meant to complement the in-depth discussion of the technical aspects given in Publ. [P2].

The calculations of PTCDA, NTCDA, and CO were performed on an equally spaced real-space grid [SK]. The radius of the numerical box for the time-propagation was $R = 40a_0$ for PTCDA, $R = 32a_0$ for NTCDA, and $R = 26a_0$ for CO. The grid spacing was set to $\Delta r = 0.38a_0$ for each calculation. I used the Crank-Nicholson propagator [CMR04] to evaluate the time evolution. Compared to other possible propagation schemes the latter allows a relatively large time-step of $\Delta t = 0.002$ fs. I employed LDA norm-conserving Troullier-Martins pseudopotentials [TM91] with cutoff radii of $r_c = 1.39a_0$ for H, $1.09a_0$ for C, and $1.10a_0$ for O. In most applications the intensity of the incoming light was ramped up to a constant intensity between 10^8 W/cm² and 10^9 W/cm² within 0.5 fs and remained constant throughout the total propagation time of $T = 50$ fs ($T = 40$ fs in the case of CO). Differences in ARPES observables arising due to different intensities are small. For a sufficient photoelectron yield I recommend intensities around 10^9 W/cm².

To prevent reflections at the numerical boundaries, I augmented the KS Hamiltonian, $h'_{\text{KS}} = h_{\text{KS}} - iv$, by a complex absorbing potential of the form

$$v(r) = \frac{4\hbar^2}{2mc^2} \left(\frac{2\pi}{\Delta R} \right)^2 \left[\left(\frac{\Delta R}{R_E - 2R_S + r} \right)^2 + \left(\frac{\Delta R}{R_E - r} \right)^2 - 2 \right], \quad (\text{A.14})$$

which is based on the absorbing potentials presented in Refs. [Man02, GLRM04, SK16a]. Here, R_S denotes the radius where the potential starts acting ($R_S = 28a_0$ for PTCDA, $R_S = 24a_0$ for NTCDA, and $R_S = 14a_0$ for CO). For $r < R_S$ the potential is set to zero. $R_E = R + \Delta$ is the radius of the numerical box R plus a shift $\Delta = 3a_0$ that is needed to prevent the potential from diverging at the numerical boundary. $\Delta R = R - R_S$ is the “active length“ of the potential.

The photoemission signals were evaluated at a detection radius of $R_D = 27a_0$ for PTCDA, $R_D = 24a_0$ for NTCDA, and $R_D = 14.5a_0$ for CO.

Representative for the majority of applications, Fig. A.11 illustrates the dependence of ARPES momentum maps on the detection radius for the case of the TDLDA HOMO of PTCDA with LCP and photons of $\hbar\omega = 27$ eV incoming from $-x$ -axis under an angle of 65° to the normal of the molecular plane. The spectra were obtained at different detection radii (a) $R_D = 27a_0$, (b) $28a_0$, and (c) $29a_0$. There are minor differences in the intensity patterns, for example, at $k_x \approx 1.0 \text{ \AA}^{-1}$,

$k_y \approx 1.0 \text{ \AA}^{-1}$. It has to be noted that for some setups the deviation between various R_D can be more pronounced. This may be caused by the overall numerical setup as simultaneous optimization of the relevant parameter space is laborious and often limited by computational feasibility. Further, the parameters are depending on the system. I also cannot rule out that the detection point dependence is one of the inherent limitations of this method.

A.6 Self-interaction correction: details

In this section I discuss two issues regarding the GSIC calculations.

Relaxation effects

As discussed in Chap. 2, the exact HOMO eigenvalue coincides with the first vertical and relaxed IP. In practice, the level of approximation used for the xc functional has a huge influence on how well this relation is fulfilled.

An aspect that I briefly touched in Sec. 2.4 is to what extent electronic relaxation effects are incorporated in eigenvalues. Perdew and Zunger argued in their seminal work that SIC eigenvalues benefit from an effective cancellation of errors [PZ81]. While this was based on the evaluation of atomistic densities and orbital-specific SIC calculation, it is tempting to check whether these arguments transfer to larger systems and the SIC scheme presented in Sec. 2.4.

The IP theorem can be reformulated as [PZ81]

$$IP = -\varepsilon_{\text{HOMO}} + \Sigma + \Pi. \quad (\text{A.15})$$

In the exact case, the two additional contributions have to cancel. The first quantity,

$$\Sigma = IP^{\text{R}} - IP^{\text{U}}, \quad (\text{A.16})$$

measures the severity of relaxation effects and is called orbital-relaxation energy. It consists of the difference of the completely unrelaxed ionization potential IP^{U} and the vertical ionization potential IP^{R} that includes electronic relaxation. The second contribution,

$$\Pi = IP^{\text{U}} + \varepsilon_{\text{HOMO}}, \quad (\text{A.17})$$

is the so-called non-Koopmans correction. The term was coined by Koopmans' theorem, which states that HF eigenvalues are equal to unrelaxed IPs [Koo34]. In the context of DFT, Π can be interpreted as to measure to what extent approximate DFT HOMOs go beyond IPs from Koopmans' theorem. Here, IP^{R} always refers to the total-energy difference between the self-consistent calculation of the ground-state energy of the neutral system and the ground-state energy of the corresponding singly ionized system.

To determine the unrelaxed IP, one assumes that the only change of the molecule's electronic system upon ionization is the depopulation of the HOMO. Employing the same set of orbitals as for the neutral molecule, the unrelaxed ionized density reads

$$n_{\uparrow}^{+}(\mathbf{r}) = n_{\uparrow} - |\phi_{\text{HOMO},\uparrow}(\mathbf{r})|^2, \quad (\text{A.18})$$

$$n^{+}(\mathbf{r}) = n_{\uparrow}^{+}(\mathbf{r}) + n_{\downarrow}(\mathbf{r}). \quad (\text{A.19})$$

For density dependent functionals the unrelaxed total energy of the ionized system can be calculated according to

$$IP^{\text{U}} = E_0^{\text{U}}[n^{+}] - E_0[n], \quad (\text{A.20})$$

where

$$E_0^{\text{U}}[n^{+}] = T[\{n_{i\sigma}^{+}\}] + E_{\text{H}}[n^{+}] + E_{\text{xc}}[n_{\uparrow}^{+}, n_{\downarrow}] + E_{\text{ext}}[n^{+}]. \quad (\text{A.21})$$

The situation gets more involved considering GSIC. Here, the orbital-dependent SIC energy is

evaluated with orbitals from the unitary orbital transformation

$$\tilde{\varphi}_{i\sigma} = \sum_{j=1}^{N_\sigma} U_{ij}^\sigma \varphi_{j\sigma}. \quad (\text{A.22})$$

The depopulation of the HOMO orbital can be introduced by means of the occupation numbers $f_{i\sigma}$, which are set to zero if the index $i\sigma$ corresponds to the HOMO. Otherwise the occupation numbers are set to one. The transformed orbitals read

$$\tilde{\varphi}_{i\sigma} = \sum_{j=1}^{N_\sigma} \sqrt{f_{j\sigma}} U_{ij}^\sigma \varphi_{j\sigma}, \quad (\text{A.23})$$

where U_{ij}^σ is exactly the same as for the neutral N -orbital case. Both sets of orbitals reproduce the same density $n_\sigma^+(\mathbf{r}) = \sum_{i=1}^{N_\sigma} f_{i\sigma} |\varphi_{i\sigma}(\mathbf{r})|^2 = \sum_{i=1}^{N_\sigma} |\tilde{\varphi}_{i\sigma}(\mathbf{r})|^2$ as demonstrated below:

$$\begin{aligned} n_\sigma^+(\mathbf{r}) &= \sum_{i=1}^{N_\sigma} |\tilde{\varphi}_{i\sigma}(\mathbf{r})|^2 \\ &= \sum_{i=1}^{N_\sigma} \sum_{k=1}^{N_\sigma} \sqrt{f_{k\sigma}} U_{ik}^{\sigma*} \varphi_{k\sigma}^* \sum_{l=1}^{N_\sigma} \sqrt{f_{l\sigma}} U_{il}^\sigma \varphi_{l\sigma} \\ &= \sum_{k,l=1}^{N_\sigma} \sqrt{f_{k\sigma}} \sqrt{f_{l\sigma}} \varphi_{k\sigma}^* \varphi_{l\sigma} \sum_{i=1}^{N_\sigma} U_{ik}^{\sigma*} U_{il}^\sigma \\ &= \sum_{k,l=1}^{N_\sigma} \sqrt{f_{k\sigma}} \sqrt{f_{l\sigma}} \varphi_{k\sigma}^* \varphi_{l\sigma} \delta_{lk} \\ &= \sum_{k=1}^{N_\sigma} f_{k\sigma} |\varphi_{k\sigma}|^2 \end{aligned} \quad (\text{A.24})$$

Yet, the transformed orbitals are no longer orthonormal:

$$\begin{aligned} \langle \tilde{\varphi}_{i\sigma}(\mathbf{r}) | \tilde{\varphi}_{j\sigma}(\mathbf{r}) \rangle &= \sum_{k,l=1}^{N_\sigma} \sqrt{f_{k\sigma}} \sqrt{f_{l\sigma}} U_{ik}^{\sigma*} U_{jl}^\sigma \langle \varphi_{k\sigma} | \varphi_{l\sigma} \rangle \\ &= \sum_{k=1}^{N_\sigma} \sqrt{f_{k\sigma}} \sqrt{f_{k\sigma}} U_{ik}^{\sigma*} U_{jk}^\sigma \\ &= \sum_{k=1}^{N_\sigma} U_{ik}^{\sigma*} U_{jk}^\sigma - U_{iN}^{\sigma*} U_{jN}^\sigma \\ &= \delta_{ij} - U_{iN}^{\sigma*} U_{jN}^\sigma \neq \delta_{ij} \end{aligned} \quad (\text{A.25})$$

The matrix elements U_{jN}^σ of the transformation denote the contribution of the depleted HOMO. I label an evaluation of the total energy with this kind of orbital transformation as the unrelaxed transformation.

An alternative way is to construct a completely new unitary transformation \tilde{U}_{ij}^σ that minimizes the

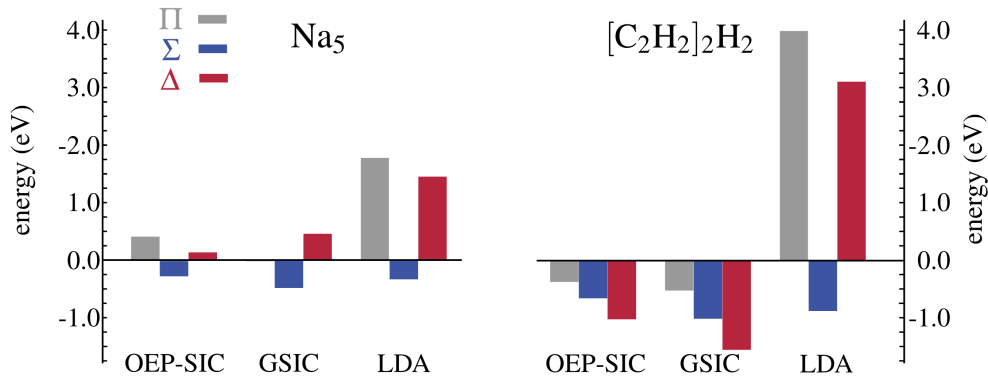


Figure A.12: Non-Koopmans correction Π , orbital-relaxation energy Σ , and $\Delta = \Pi + \Sigma$ for Na₅ (left) and [C₂H₂]₂H₂ (right). For each system calculations were performed with LDA, GSIC with a complex, energy-minimizing, relaxed unitary transformation, and SIC evaluated with OEP without unitary optimization.

SIC energy using only $N-1$ orbitals,

$$\bar{\varphi}_{i\sigma} = \sum_{j=1}^{N_{\sigma}-1} \bar{U}_{ij}^{\sigma} \varphi_{j\sigma}. \quad (\text{A.26})$$

To be more specific, it is only based on the $N - 1$ orbitals $\varphi_{i\uparrow}$ that constitute $n_{\uparrow}^+(\mathbf{r})$. This procedure implies that \bar{U}_{ij}^{σ} is adopted to the loss of one electron, i.e., an additional energy-minimizing step is performed before the unrelaxed total energy is computed. I will denote this procedure as the relaxed transformation method. It is not a priori clear which scheme is to be favored to quantify Σ and Π as there is no unique and rigorous way to determine the unrelaxed ionization potential for GSIC.

To avoid the restrictions due to the unitary transformation, I computed the unrelaxed IP for SIC energies from solving the full OEP without unitary optimization. Figure A.12 illustrates Π , Σ , and $\Delta = \Pi + \Sigma$ for Na₅ and two repeat units of polyacetylene ([C₂H₂]₂H₂). For Na₅ I find a reasonable cancellation of Σ and Π leading to a good description of the relaxed IP. In the case of GSIC with a relaxed, complex, energy-minimizing transformation, Π is close to zero and therefore does not cancel Σ . Consequently, the IP is slightly worse than for the OEP calculation. As a reference I also display the LDA results that suggest a poor description of electronic relaxation. The right part of Fig. A.12 displays the results for polyacetylene. GSIC and the OEP calculation yield negative Σ and Π values. Instead of canceling each other, both add up to a high Δ . Predictions by LDA are inferior to the SIC calculation results. Turning towards the organic semiconductor NTCDA and PTCDA reveals a rather inconsistent picture. Here, $\Pi + \Sigma$ from GSIC is on the same level as LDA and in case of NTCDA even larger, see Tab. A.1. Unfortunately, a comparison to OEP KS SIC calculations is not possible because convergence of the ground-state calculations for ionized PTCDA and NTCDA has not yet been achieved.

Table A.1 also compares the results for Π and Σ for GSIC evaluated with the relaxed and the unrelaxed unitary transformation. While the sum of $\Pi + \Sigma$ is in both cases the same, the assessment of relaxation effects reveals massive differences. As it can be anticipated, the relaxed unitary transformation yields distinctly lower values for Π and Σ . Generally, this analysis shows that relaxation effects are difficult to quantify with GSIC, as the values strongly depend on the method

used to take the unitary transformation for the calculation of the unrelaxed total energy into account. Further, the results suggest that no general statement can be made about the extent to which non-Koopmans and orbital-relaxation energy cancel each other.

Table A.1: Non-Koopmans correction Π , orbital-relaxation energy Σ , and $\Pi + \Sigma$ for PTCDA and NTCDA. Complex, energy-minimizing GSIC and LDA calculations were performed. The GSIC calculations were conducted with the relaxed (R GSIC) and unrelaxed (UR GSIC) transformations. All values are presented in eV.

	PTCDA			NTCDA		
	LDA	R GSIC	UR GSIC	LDA	R GSIC	UR GSIC
Π	2.13	-1.05	3.93	2.88	-1.20	4.29
Σ	-0.38	-1.13	-6.11	-1.81	-2.00	-7.49
$\Pi + \Sigma$	1.74	-2.18	-2.18	1.07	-3.20	-3.20

v -representability of complex-valued orbitals

Within the introduction of the GSIC approach in the main part of my thesis in Sec. 2.4, a large share of the discussion focused on the definition of SIC as a single-particle based correction. As I pointed out, the SIC expression should be evaluated with one-electron ground-state densities to fulfill the premise that xc functionals are only defined rigorously for ground-state densities [HK12b]. Usually, KS orbitals of many-electron systems are far away from ground-state orbitals since they have to fulfill the orthogonality condition. One way to maintain orthogonality between orbitals is to equip them with an increasing number of nodal planes. In GSIC calculations the SIC expression is evaluated with orbitals from a unitary transformation. In general, the latter can be complex-valued, which introduces an additional degree of freedom to enforce orthogonality. As it was shown in Ref. [HKKK12], complex orbitals can indeed have a smoother spatial structure and fewer nodal planes. One may therefore ask whether complex orbital densities are closer to one-electron ground-state densities than their real-valued counterpart.

In general, a one-electron ground-state density is generated by a local external potential. For a single-particle orbital without nodal planes the single-particle Schrödinger equation

$$-\frac{\hbar^2 \nabla^2}{2m_e} \varphi_i(\mathbf{r}) + v(\mathbf{r}) \varphi_i(\mathbf{r}) = \varepsilon_i \varphi_i(\mathbf{r}) \quad (\text{A.27})$$

can be inverted such that a potential can be obtained from the single-particle density

$$v(\mathbf{r}) - \varepsilon_i = \frac{\hbar^2 \nabla^2 \sqrt{n_i(\mathbf{r})}}{2m_e \sqrt{n_i(\mathbf{r})}}. \quad (\text{A.28})$$

Such a density is called v -representable [Koh83].

Starting from this consideration, I evaluate Eq. (A.28) for the example of the CO molecule. After subtracting the electrons that are treated by the pseudopotential, CO has five occupied orbitals (spin-unpolarized). I performed two self-consistent ground-state GSIC calculations, one with a real-valued energy-minimizing transformation, the other with a complex-valued. Note that a specific ordering of transformed orbitals has no physical significance. Therefore, I contrast a pair

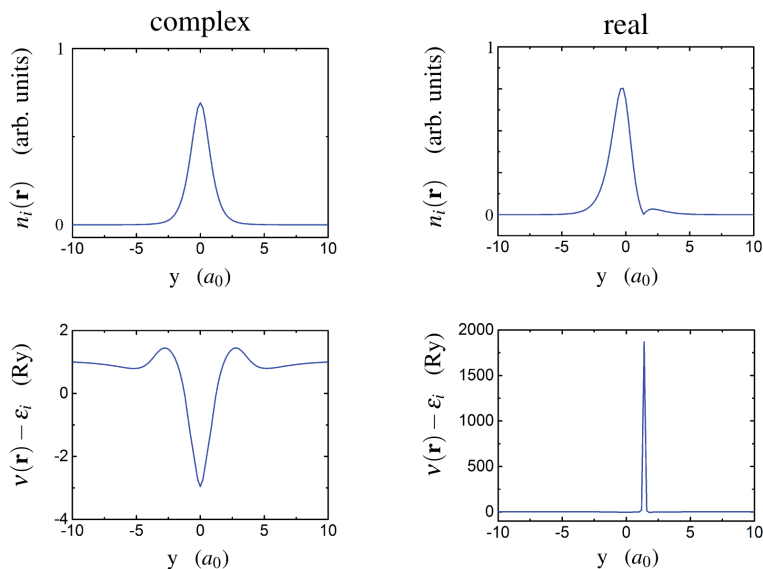


Figure A.13: v -representability of real- and complex-valued orbital densities of CO. Upper row: orbital densities $n_i(\mathbf{r})$ of a real (right) and a corresponding complex-valued (left) energy-minimizing unitary orbital transformation. The displayed axis is perpendicular to the molecular axis. Lower row: Potential that is reconstructed from the displayed orbitals.

of transformed orbitals which I assigned due to their close resemblance, see Ref. [HKKK12] for iso-surface plots of all the transformed orbitals of CO. The upper row of Fig. A.13 shows the orbital densities $n_i(\mathbf{r})$ of one pair of transformed orbitals along the y -axis, which is perpendicular to the molecular axis (x -axis). The left corresponds to the complex-valued orbital transformation and the right to the corresponding real-valued orbital. While the orbital density of the complex orbital is smooth on this axis, the real-valued shows a kink at $1.5a_0$ resulting from a nodal plane. This affects the second derivative needed to evaluate Eq. (A.28) substantially. The potential is dominated by a sharp peak at the position of the kink. Opposed to that, the potential from the complex orbital is smooth and shows a reasonable behavior.

If plotted along the molecular axis, the structure of both orbital types exhibits kinks as illustrated in Fig. A.14. For the same reason as mentioned above, the potentials show an unphysical structure that does not resemble ground-state potentials. The remaining CO orbitals show a similar behavior. Each orbital (be it complex or real) shows at least one direction that exhibits a kink and, thus, produces a nonphysical potential. Therefore, this analysis suggests that while complex orbital densities are smoother and presumably closer to ground-state densities, they are generally not v -representable.

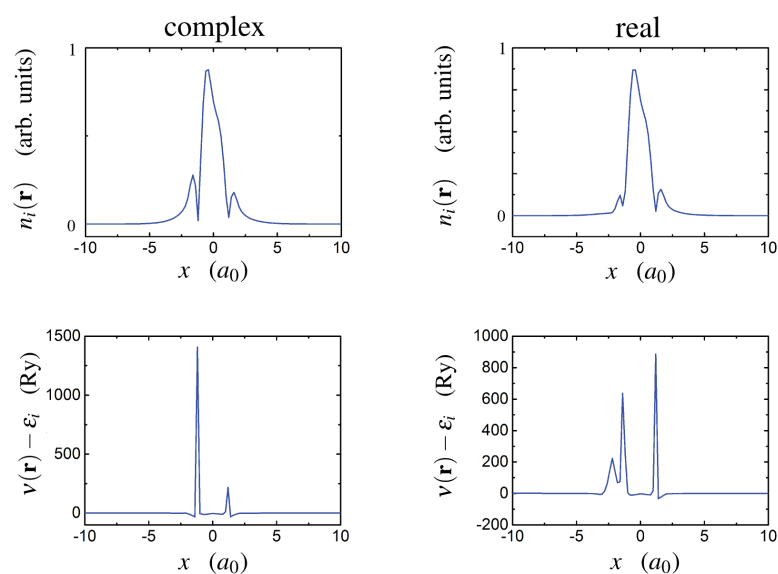


Figure A.14: v -representability of real- and complex-valued orbital densities of CO. Upper row: orbital densities $n_i(\mathbf{r})$ of a real (right) and a corresponding complex-valued (left) energy-minimizing unitary orbital transformation. The displayed axis is perpendicular to the molecular axis. Lower row: Potential that is reconstructed from the displayed orbitals.

List of abbreviations

ARPES	angle-resolved photoemission spectroscopy	3
B3LYP	Becke, 3-parameter, Lee-Yang-Parr exchange-correlation functional	16
BLYP	Becke exchange, Lee-Yang-Parr correlation functional	15
CDAD	circular dichroism in the photoemission angular distribution	36
CW	Coulomb wave, usually referring to approximating the ejected electron's state by a Coulomb wave	47
DFT	density-functional theory	3
DSLE	deviation from the straight line error	43
E_{\min}-SIC	energy-minimizing self-interaction correction	19
EA	electron affinity	15
EXX	exact-exchange functional	16
FOBO	spatially localized Foster-Boys orbitals	19
GGA	a class of semilocal exchange-correlation functionals that is based on a generalized-gradient approximation	15
GKLI	generalized Krieger-Li-Iafrate approximation to the generalized optimized effective potential equation for unitarily variant orbital functionals	19
GKS	generalized Kohn-Sham scheme	17
GOEP	generalized optimized effective potential	19
GSIC	self-interaction corrected exchange-correlation functional evaluated with the generalized Krieger-Li-Iafrate approximation that uses energy-minimizing or localizing unitary orbital transformations	19
HF	Hartree-Fock	11
HK	Hohenberg Kohn, usually referring to the Hohenberg-Kohn theorem	9
HOMO	highest occupied molecular orbital	6

IP	vertical ionization potential	11
KLI	approximation to the optimized effective potential equation proposed by Krieger, Li, and Iafrate	17
KS	Kohn-Sham, usually referring to the KS scheme, orbitals, eigenvalues, potential, or equation	10
LCP	left-handed circularly polarized light	36
LDA	local-density approximation exchange-correlation functional	15
LUMO	lowest unoccupied molecular orbital	5
MBPT	many-body perturbation theory	8
ME-SIE	many-electron self-interaction error	13
NTCDA	1,4,5,8-naphthalene-tetracarboxylic dianhydride	5
OE-SIE	one-electron self-interaction error	12
OEP	optimized effective potential	17
OT-RSH	optimally-tuned range-separated hybrid exchange-correlation functional . . .	16
PBE	Perdew-Burke-Ernzerhof exchange-correlation functional	15
PBEh	global hybrid xc functional that mixes exact exchange with PBE exchange according to the parameter α	16
PES	photoemission spectroscopy	4
PTCDA	3,4,9,10-perylene-tetracarboxylic dianhydride	5
PW	plane wave, usually referring to approximating the ejected electron's state by a plane wave	22
RCP	right-handed circularly polarized light	36
RG	Runge Gross, usually referring to the Runge-Gross theorem	27
RPA	random-phase approximation	42
scGW	self-consistent <i>GW</i>	44
SIC	self-interaction correction	18
SIE	self-interaction error	12
TCNQ	tetracyanoquinodimethane	46
TDDFT	time-dependent density-functional theory	27

TDGSIC	time-dependent self-interaction corrected exchange-correlation functional evaluated with the generalized Krieger-Li-Iafrate approximation that uses energy minimizing or localizing unitary orbital transformations	29
TDKS	time-dependent Kohn-Sham, usually referring to the time-dependent KS scheme, potential, or equation	27
TDLDA	time-dependent local-density approximation exchange-correlation functional	28
TTF	tetrathiafulvalene	46
xc	exchange-correlation	9

Please note that the listed abbreviations might differ from the ones used in the publications presented in Part II.

Bibliography

- [AB99] C. Adamo and V. Barone, *Toward reliable density functional methods without adjustable parameters: The PBE0 model*, J. Chem. Phys. **110**, 6158 (1999).
- [AFN⁺98] P. Aebi, R. Fasel, D. Naumović, J. Hayoz, T. Pillo, M. Bovet, R. G. Agostino, L. Patthey, L. Schlapbach, F. P. Gil, H. Berger, T. J. Kreutz and J. Osterwalder, *Angle-scanned photoemission: Fermi surface mapping and structural determination*, Surf. Sci. **402-404**, 614 (1998).
- [AG98] F. Aryasetiawan and O. Gunnarsson, *The GW method*, Rep. Prog. Phys. **61**, 237 (1998).
- [AJW00] W. G. Aulbur, L. Jönsson and J. W. Wilkins, *Quasiparticle Calculations in Solids*, Solid State Phys. **54**, 1 (2000).
- [AMH⁺00] J. Akola, M. Manninen, H. Häkkinen, U. Landman, X. Li and L.-S. Wang, *Aluminum cluster anions: Photoelectron spectroscopy and ab initio simulations*, Phys. Rev. B **62**, 13216 (2000).
- [AS72] M. Abramowitz and I. A. Stegun, *Handbook of mathematical functions*, Dover publications, New York, 1972.
- [AS09] A. Abbasi and R. Scholz, *Ab initio calculation of the dispersion interaction between a polyaromatic molecule and a noble metal substrate: PTCDA on Ag(110)*, J. Phys. Chem. C **113**, 19897 (2009).
- [AvB85] C.-O. Almbladh and U. von Barth, *Exact results for the charge and spin densities, exchange-correlation potentials, and density-functional eigenvalues*, Phys. Rev. B **31**, 3231 (1985).
- [AYC⁺13] V. Atalla, M. Yoon, F. Caruso, P. Rinke and M. Scheffler, *Hybrid density functional theory meets quasiparticle calculations: A consistent electronic structure approach*, Phys. Rev. B **88**, 165122 (2013).
- [AZH⁺16] V. Atalla, I. Zhang, O. T. Hofmann, P. Rinke and M. Scheffler, *Enforcing the linear behavior of the total energy with hybrid functionals*, Phys. Rev. B **94**, 035140 (2016).
- [BA96] R. Bauernschmitt and R. Ahlrichs, *Treatment of electronic excitations within the adiabatic approximation of time dependent density functional theory*, Chem. Phys. Lett. **256**, 454 (1996).
- [BAO11] X. Blase, C. Attaccalite and V. Olevano, *First-principles GW calculations for fullerenes, porphyrins, phtalocyanine, and other molecules of interest for organic photovoltaic applications*, Phys. Rev. B **83**, 115103 (2011).

- [BC95] N. Binggeli and J. R. Chelikowsky, *Photoemission Spectra and Structures of Si Clusters at Finite Temperature*, Phys. Rev. Lett. **75**, 493 (1995).
- [Bec88] A. D. Becke, *Density-functional exchange-energy approximation with correct asymptotic behavior*, Phys. Rev. A **38**, 3098 (1988).
- [Bec93a] A. D. Becke, *Density-functional thermochemistry. III. The role of exact exchange*, J. Chem. Phys. **98**, 5648 (1993).
- [Bec93b] A. D. Becke, *A new mixing of Hartree-Fock and local density-functional theories*, J. Chem. Phys. **98**, 1372 (1993).
- [Bet33] H. A. Bethe, *Handbuch der Physik*, Vol. 24, page 483, Springer, Berlin, 1933.
- [BG97] E. J. Baerends and O. V. Gritsenko, *A Quantum Chemical View of Density Functional Theory*, J. Phys. Chem. A **101**, 5383 (1997).
- [BG14] F. Bruneval and M. Gatti, *Quasiparticle Self-Consistent GW Method for the Spectral Properties of Complex Materials*, Top. Curr. Chem. **347**, 99 (2014).
- [BGH⁺09] V. Blum, R. Gehrke, F. Hanke, P. Havu, V. Havu, X. Ren, K. Reuter and M. Scheffler, *Ab initio molecular simulations with numeric atom-centered orbitals*, Comput. Phys. Commun. **180**, 2175 (2009).
- [BGvM13] E. J. Baerends, O. V. Gritsenko and R. van Meer, *The Kohn-Sham gap, the fundamental gap and the optical gap: the physical meaning of occupied and virtual Kohn-Sham orbital energies*, Phys. Chem. Chem. Phys. **15**, 16408 (2013).
- [BK61] G. Baym and L. P. Kadanoff, *Conservation Laws and Correlation Functions*, Phys. Rev. **124**, 287 (1961).
- [BK95] H. P. Bonzel and C. Kleint, *On the history of photoemission*, Prog. in Surf. Sci. **49**, 107 (1995).
- [BKP⁺08] S. Berkebile, G. Koller, P. Puschnig, C. Ambrosch-Draxl, F. P. Netzer and M. G. Ramsey, *Angle-resolved photoemission of chain-like molecules: the electronic band structure of sexithiophene and sexiphenyl*, Appl. Phys. A **95**, 101 (2008).
- [BLS⁺01] N. Böwering, T. Lischke, B. Schmidtke, N. Müller, T. Khalil and U. Heinzmann, *Asymmetry in photoelectron emission from chiral molecules induced by circularly polarized light*, Phys. Rev. Lett. **86**, 1187 (2001).
- [BLS10] R. Baer, E. Livshits and U. Salzner, *Tuned range-separated hybrids in density functional theory*, Annu. Rev. Phys. Chem. **61**, 85 (2010).
- [BM13] F. Bruneval and M. A. L. Marques, *Benchmarking the starting points of the GW approximation for molecules*, J. Chem. Theory Comput. **9**, 324 (2013).
- [BO27] M. Born and R. Oppenheimer, *Zur Quantentheorie der Molekeln*, Ann. Phys. **389**, 457 (1927).
- [Boy60] S. F. Boys, *Construction of Some Molecular Orbitals to Be Approximately Invariant for Changes from One Molecule to Another*, Rev. Mod. Phys. **32**, 296 (1960).

- [Bru12] F. Bruneval, *Ionization energy of atoms obtained from GW self-energy or from random phase approximation total energies*, J. Chem. Phys. **136**, 194107 (2012).
- [BSO⁺05] F. Bruneval, F. Sottile, V. Olevano, R. Del Sole and L. Reining, *Many-body perturbation theory using the density-functional concept: Beyond the GW approximation*, Phys. Rev. Lett. **94**, 186402 (2005).
- [BW15] A. M. Bradshaw and D. P. Woodruff, *Molecular orbital tomography for adsorbed molecules: is a correct description of the final state really unimportant?*, New J. Phys. **17**, 013033 (2015).
- [BWG05] K. Burke, J. Werschnik and E. K. U. Gross, *Time-dependent density functional theory: past, present, and future*, J. Chem. Phys. **123**, 062206 (2005).
- [CA80] D. M. Ceperley and B. J. Alder, *Ground State of the electron Gas by a Stochastic Method*, Phys. Rev. Lett. **45**, 566 (1980).
- [CAO⁺06] A. Castro, H. Appel, M. Oliveira, C. Rozzi, X. Andrade, F. Lorenzen, M. Marques, E. Gross and A. Rubio, *Octopus: a tool for the application of time-dependent density functional theory*, Phys. Stat. Sol. B **243**, 2465 (2006).
- [Cap06] K. Capelle, *A Bird's-Eye View of Density-Functional Theory*, Braz. J. Phys. **36**, 1318 (2006).
- [Car13] F. Caruso, *Self-consistent GW approach for the unified description of ground and excited states of finite systems*, PhD thesis, Freie Universität Berlin, 2013.
- [CAR⁺14] F. Caruso, V. Atalla, X. Ren, A. Rubio, M. Scheffler and P. Rinke, *First-principles description of charge transfer in donor-acceptor compounds from self-consistent many-body perturbation theory*, Phys. Rev. B **90**, 085141 (2014).
- [Cas95a] M. E. Casida, *Generalization of the optimized-effective-potential model to include electron correlation: A variational derivation of the Sham-Schlüter equation for the exact exchange-correlation potential*, Phys. Rev. A **51**, 2005 (1995).
- [Cas95b] M. E. Casida, *Time-dependent density functional response theory for molecules*, in *Recent advances in density functional methods, part I*, edited by D. P. Chong, Berlin, 1995, World Scientific.
- [Cas96] M. E. Casida, in *Recent Developments and Applications in Density-Functional Theory*, edited by J. M. Seminario, pages 391-439, Amsterdam, 1996, Elsevier Science.
- [Cas09] M. E. Casida, *Time-dependent density-functional theory for molecules and molecular solids*, J. Mol. Struct. THEOCHEM **914**, 3 (2009).
- [CGB02] D. P. Chong, O. V. Gritsenko and E. J. Baerends, *Interpretation of the Kohn-Sham orbital energies as approximate vertical ionization potentials*, J. Chem. Phys. **116**, 1760 (2002).
- [CGK⁺87] T. Carlson, P. Gerard, M. O. Krause, F. A. Grimm and B. P. Pullen, *Photoelectron dynamics of the valence shells of benzene as a function of photon energy*, J. Chem. Phys. **86**, 6918 (1987).

- [CMR04] A. Castro, M. A. L. Marques and A. Rubio, *Propagators for the time-dependent Kohn-Sham equations*, J. Chem. Phys. **121**, 3425 (2004).
- [CMSY08] A. J. Cohen, P. Mori-Sánchez and W. Yang, *Insights into current limitations of density functional theory*, Science **321**, 792 (2008).
- [Cre01] D. Cremer, *Density functional theory: coverage of dynamic and non-dynamic electron correlation effects*, Mol. Phys. **99**, 1899 (2001).
- [CRR⁺12] F. Caruso, P. Rinke, X. Ren, M. Scheffler and A. Rubio, *Unified description of ground and excited states of finite systems: The self-consistent GW approach*, Phys. Rev. B **86**, 081102(R) (2012).
- [CRR⁺13] F. Caruso, P. Rinke, X. Ren, A. Rubio and M. Scheffler, *Self-consistent GW: All-electron implementation with localized basis functions*, Phys. Rev. B **88**, 075105 (2013).
- [CRS97] F. Calvayrac, P.-G. Reinhard and E. Suraud, *Spectral Signals from Electronic Dynamics in Sodium Clusters*, Ann. Phys. **255**, 125 (1997).
- [CS13] W. Cencek and K. Szalewicz, *On asymptotic behavior of density functional theory*, J. Chem. Phys. **139**, 024104 (2013).
- [CZ68a] J. Cooper and R. N. Zare, *Angular Distribution of Photoelectrons*, J. Chem. Phys. **48**, 942 (1968).
- [CZ68b] J. Cooper and R. N. Zare, *Erratum: Angular Distribution of Photoelectrons*, J. Chem. Phys. **49**, 4252 (1968).
- [Dam04] A. Damascelli, *Probing the Low-Energy Electronic Structure of Complex Systems by ARPES*, Phys. Scr. **T109**, 61 (2004).
- [DCCS94] P. Duffy, D. P. Chong, M. E. Casida and D. R. Salahub, *Assessment of Kohn-Sham density-functional orbitals as approximate Dyson orbitals for the calculation of electron-momentum-spectroscopy scattering cross sections*, Phys. Rev. A **50**, 4707 (1994).
- [DD74] D. Dill and J. L. Dehmer, *Electron-molecule scattering and molecular photoionization using the multiple-scattering method*, J. Chem. Phys. **61**, 692 (1974).
- [DDM85] R. L. Dubs, S. N. Dixit and V. McKoy, *Circular dichroism in Photoelectron Angular Distributions from Oriented Linear Molecules*, Phys. Rev. Lett. **54**, 1249 (1985).
- [DG90] R. M. Dreizler and E. K. U. Gross, *Density Functional Theory: An Approach to the Quantum Many-Body Problem*, Springer, Berlin, 1990.
- [DHS03] A. Damascelli, Z. Hussain and Z.-X. Shen, *Angle-resolved photoemission studies of the cuprate superconductors*, Rev. Mod. Phys. **75**, 473 (2003).
- [Dir30] P. A. M. Dirac, *Note on Exchange Phenomena in the Thomas Atom*, Proc. Camb. Phil. Soc. **26**, 376 (1930).

- [DL14] I. Dreissigacker and M. Lein, *Photoelectron circular dichroism of chiral molecules studied with a continuum-state-corrected strong-field approximation*, Phys. Rev. A **89**, 053406 (2014).
- [DLR15] U. De Giovannini, A. H. Larsen and A. Rubio, *Modeling electron dynamics coupled to continuum states in finite volumes with absorbing boundaries*, Eur. Phys. J. B **88**, 56 (2015).
- [DMK⁺06] N. Dori, M. Menon, L. Kilian, M. Sokolowski, L. Kronik and E. Umbach, *Valence electronic structure of gas-phase 3,4,9,10-perylene tetracarboxylic acid dianhydride: Experiment and theory*, Phys. Rev. B **73**, 195208 (2006).
- [DRRS13] P. M. Dinh, P. Romaniello, P.-G. Reinhard and E. Suraud, *Calculation of photoelectron spectra: A mean-field-based scheme*, Phys. Rev. A **87**, 032514 (2013).
- [Dun89] T. H. Dunning, *Gaussian basis sets for use in correlated molecular calculations. I. The atoms boron through neon and hydrogen*, J. Chem. Phys. **90**, 1007 (1989).
- [DvLvB06] N. E. Dahlen, R. van Leeuwen and U. von Barth, *Variational energy functionals of the green function tested on molecules*, Phys. Rev. A **73**, 012511 (2006).
- [DVM⁺12] U. De Giovannini, D. Varsano, M. A. L. Marques, H. Appel, E. K. U. Gross and A. Rubio, *Ab initio angle- and energy-resolved photoelectron spectroscopy with time-dependent density-functional theory*, Phys. Rev. A **85**, 062515 (2012).
- [Ein05] A. Einstein, *Über einen die Erzeugung und Verwandlung des Lichtes betreffenden heuristischen Gesichtspunkt*, Ann. Phys. **322**, 123 (1905).
- [EPB97] M. Ernzerhof, J. P. Perdew and K. Burke, *Coupling-constant dependence of atomization energies*, Int. J. Quantum Chem. **64**, 285 (1997).
- [FAO⁺11] C. Faber, C. Attaccalite, V. Olevano, E. Runge and X. Blase, *First-principles GW calculations for DNA and RNA nucleobases*, Phys. Rev. B **83**, 115123 (2011).
- [FB60] J. M. Foster and S. F. Boys, *Canonical configurational interaction procedure*, Rev. Mod. Phys. **32**, 300 (1960).
- [FFB⁺07] F. Fuchs, J. Furthmüller, F. Bechstedt, M. Shishkin and G. Kresse, *Quasiparticle band structure based on a generalized Kohn-Sham scheme*, Phys. Rev. B **76**, 115109 (2007).
- [FNM03] C. Fiolhais, F. Nogueira and M. A. L. Marques, *A primer in density functional theory*, Springer, Berlin-Heidelberg, 2003.
- [FVK04] S. V. Faleev, M. Van Schilfgaarde and T. Kotani, *All-electron self-consistent GW approximation: Application to Si, MnO, and NiO*, Phys. Rev. Lett. **93** (2004).
- [FW71] A. L. Fetter and J. D. Walecka, *Quantum theory of many-particle systems*, McGraw-Hill, New York, 1971.
- [GA58] M. V. Galitskii and A. B. Migdal, *Application of Quantum Field Theory Methods to the Many Body Problem*, Sov. Phys. JETP **7**, 96 (1958).

- [Gad74] J. W. Gadzuk, *Surface molecules and chemisorption. II. Photoemission angular distributions*, Phys. Rev. B **10**, 5030 (1974).
- [GGB03] O. V. Gritsenko, B. Braïda and E. J. Baerends, *Physical interpretation and evaluation of the Kohn-Sham and Dyson components of the ϵ -I relations between the Kohn-Sham orbital energies and the ionization potentials*, J. Chem. Phys. **119**, 1937 (2003).
- [GDP96] E. K. U. Gross, J. F. Dobson and M. Petersilka, *Density functional theory of time-dependent phenomena*, in *Density Functional Theory II*, edited by R. Nalewajski, volume 181 of *Topics in Current Chemistry*, page 81, Springer, Berlin-Heidelberg, 1996.
- [GLRM04] T. Gonzalez-Lezana, E. J. Rackham and D. E. Manolopoulos, *Quantum reactive scattering with a transmission-free absorbing potential*, J. Chem. Phys. **120**, 2247 (2004).
- [Gro78] W. D. Grobman, *Angle-resolved photoemission from molecules in the independent-atomic-center approximation*, Phys. Rev. B **17**, 4573 (1978).
- [GS78] A. Goldberg and B. W. Shore, *Modelling laser ionisation*, J. Phys. B: Atom. Molec. Phys. **11**, 3339 (1978).
- [GSS⁺98] K. Glöckler, C. Seidel, A. Soukopp, M. Sokolowski, E. Umbach, M. Böhringer, R. Berndt and W. D. Schneider, *Highly ordered structures and submolecular scanning tunnelling microscopy contrast of PTCDA and DM-PBDCI monolayers on Ag(111) and Ag(110)*, Surf. Sci. **405**, 1 (1998).
- [HCB⁺10] S. Haessler, J. Caillat, W. Boutu, C. Giovanetti-Teixeira, T. Ruchon, T. Auguste, Z. Diveki, P. Breger, A. Maquet, B. Carré, R. Taïeb and P. Salières, *Attosecond imaging of molecular electronic wavepackets*, Nature Physics **6**, 2000 (2010).
- [Hed65] L. Hedin, *New Method for Calculating the One-Particle Green's Function with Application to the Electron-Gas Problem*, Phys. Rev. **139**, A796 (1965).
- [Hed99] L. Hedin, *On correlation effects in electron spectroscopies and the GW approximation*, J. Phys.: Condens. Matter **11**, 489 (1999).
- [Her87] H. Hertz, *Ueber einen Einfluss des ultravioletten Lichtes auf die elektrische Entladung*, Ann. Phys. **267**, 983 (1887).
- [HHG99] S. Hirata and M. Head-Gordon, *Time-dependent density functional theory within the Tamm-Dancoff approximation*, Chem. Phys. Lett. **314**, 291 (1999).
- [HHGB99] S. Hirata, M. Head-Gordon and R. J. Bartlett, *Configuration interaction singles, time-dependent Hartree-Fock, and time-dependent density functional theory for the electronic excited states of extended systems*, J. Chem. Phys. **111**, 10774 (1999).
- [HJ74] J. Harris and R. O. Jones, *The surface energy of a bounded electron gas*, J. Phys. F **4**, 1170 (1974).
- [HK64] P. Hohenberg and W. Kohn, *Inhomogeneous electron gas*, Phys. Rev. **136**, B864 (1964).

- [HK12a] D. Hofmann and S. Kümmel, *Integer particle preference during charge transfer in Kohn-Sham theory*, Phys. Rev. B **86**, 201109(R) (2012).
- [HK12b] D. Hofmann and S. Kümmel, *Self-interaction correction in a real-time KS scheme: Access to difficult excitations in time-dependent density functional theory*, J. Chem. Phys. **137**, 064117 (2012).
- [HKK12] D. Hofmann, T. Körzdörfer and S. Kümmel, *Kohn-Sham Self-Interaction Correction in Real Time*, Phys. Rev. Lett. **108**, 146401 (2012).
- [HKKK12] D. Hofmann, S. Klüpfel, P. Klüpfel and S. Kümmel, *Using complex degrees of freedom in the Kohn-Sham self-interaction correction*, Phys. Rev. A **85**, 062514 (2012).
- [HL85] M. S. Hybertsen and S. G. Louie, *First-Principles Theory of Quasiparticles: Calculation of Band Gaps in Semiconductors and Insulators*, Phys. Rev. Lett. **55**, 1418 (1985).
- [HL86] M. S. Hybertsen and S. G. Louie, *Electron correlation in semiconductors and insulators: Band gaps and quasiparticle energies*, Phys. Rev. B **34**, 5390 (1986).
- [HTY⁺93] S. Hasegawa, S. Tanaka, Y. Yamashita, H. Inokuchi, H. Fujimoto, K. Kamiya, K. Seki and N. Ueno, *Molecular orientation in thin films of bis(1,2,5-thiadiazolo)-p-quinobis(1,3-dithiole) on graphite studied by angle-resolved photoelectron spectroscopy*, Phys. Rev. B **48**, 2596 (1993).
- [Hüf03] S. Hüfner, *Photoelectron spectroscopy: Principles and applications*, Springer, Berlin, 2003.
- [HvB98] B. Holm and U. von Barth, *Fully self-consistent GW self-energy of the electron gas*, Phys. Rev. B **57**, 2108 (1998).
- [HWSM13] A. Humeniuk, M. Wohlgemuth, T. Suzuki and R. Mitrić, *Time-resolved photoelectron imaging spectra from non-adiabatic molecular dynamics simulations*, J. Chem. Phys. **139**, 134104 (2013).
- [ILZ⁺04] J. Itatani, J. Levesque, D. Zeidler, H. Niikura, H. Pépin, J. C. Kieffer, P. B. Corkum and D. M. Villeneuve, *Tomographic imaging of molecular orbitals*, Nature **432**, 867 (2004).
- [Jan78] J. F. Janak, *Proof that $dE/dn_i = \epsilon_i$ in density-functional theory*, Phys. Rev. B **18**, 7165 (1978).
- [JCS96] C. Jamorski, M. E. Casida and D. R. Salahub, *Dynamic polarizabilities and excitation spectra from a molecular implementation of time-dependent density-functional response theory: N₂ as a case study*, J. Chem. Phys. **104**, 5134 (1996).
- [JSE03] J. Jaramillo, G. E. Scuseria and M. Ernzerhof, *Local hybrid functionals*, J. Chem. Phys. **118**, 1068 (2003).
- [KK08] S. Kümmel and L. Kronik, *Orbital-dependent density functionals: Theory and applications*, Rev. Mod. Phys. **80**, 3 (2008).

- [KK10] T. Körzdörfer and S. Kümmel, *Single-particle and quasiparticle interpretation of Kohn-Sham and generalized Kohn-Sham eigenvalues for hybrid functionals*, Phys. Rev. B **82**, 155206 (2010).
- [KK13] E. Kraisler and L. Kronik, *Piecewise Linearity of Approximate Density Functionals Revisited: Implications for Frontier Orbital Energies*, Phys. Rev. Lett. **110**, 126403 (2013).
- [KK14] L. Kronik and S. Kümmel, *Gas-Phase Valence-Electron Photoemission Spectroscopy Using Density Functional Theory*, in *First Principle Approaches to Spectroscopic Properties of Complex Materials*, edited by C. D. Valentin, S. Botti and M. Cococcioni, volume 347 of *Topics in Current Chemistry*, page 137, Springer, Berlin-Heidelberg, 2014.
- [KKG98] T. Kreibich, S. Kurth, T. Grabo and E. K. U. Gross, *Asymptotic Properties of the optimized effective potential*, Adv. Quantum Chem. **33**, 31 (1998).
- [KKM08] T. Körzdörfer, S. Kümmel and M. Mundt, *Self-Interaction correction and the optimized effective potential*, J. Chem. Phys. **129**, 014110 (2008).
- [KKMK09] T. Körzdörfer, S. Kümmel, N. Marom and L. Kronik, *When to trust photoelectron spectra from Kohn-Sham eigenvalues: The case of organic semiconductors*, Phys. Rev. B **79**, 201205(R) (2009).
- [KKMK10] T. Körzdörfer, S. Kümmel, N. Marom and L. Kronik, *Erratum: When to trust photoelectron spectra from Kohn-Sham eigenvalues: The case of organic semiconductors*, Phys. Rev. B **82**, 129903(E) (2010).
- [Kle61] A. Klein, *Perturbation theory for an infinite medium of fermions. II*, Phys. Rev. **112**, 950 (1961).
- [KLI92] J. B. Krieger, Y. Li and G. J. Iafrate, *Systematic approximations to the optimized effective potential: Application to orbital-density-functional theory*, Phys. Rev. A **46**, 5453 (1992).
- [KM12] T. Körzdörfer and N. Marom, *Strategy for finding a reliable starting point for G_0W_0 demonstrated for molecules*, Phys. Rev. B **86**, 041110(R) (2012).
- [KMK08] T. Körzdörfer, M. Mundt and S. Kümmel, *Electrical Response of Molecular Systems: The Power of Self-Interaction Corrected Kohn-Sham Theory*, Phys. Rev. Lett. **100**, 133004 (2008).
- [KMT⁺06] L. Kronik, A. Makmal, M. L. Tiago, M. M. G. Alemany, M. Jain, X. Huang, Y. Saad and J. R. Chelikowsky, *PARSEC – the pseudopotential algorithm for real-space electronic structure calculations: recent advances and novel applications to nanostructures*, Phys. Stat. Sol. B **243**, 1063 (2006).
- [Koh83] W. Kohn, *V-Representability and density functional theory*, Phys. Rev. Lett. **51**, 1596 (1983).
- [Koo34] T. Koopmans, *Über die Zuordnung von Wellenfunktionen und Eigenwerten zu den Einzelnen Elektronen Eines Atoms*, Physica **1**, 104 (1934).

- [KP03a] S. Kümmel and J. P. Perdew, *Optimized effective potential made simple: Orbital functionals, orbital shifts, and the exact Kohn-Sham exchange potential*, Phys. Rev. B **68**, 035103 (2003).
- [KP03b] S. Kümmel and J. P. Perdew, *Simple Iterative Construction of the Optimized Effective Potential for Orbital Functionals, Including Exact Exchange*, Phys. Rev. Lett. **90**, 43004 (2003).
- [KS65] W. Kohn and L. J. Sham, *Self-Consistent Equations Including Exchange and Correlation Effects*, Phys. Rev. **140**, A1133 (1965).
- [KSKK15] E. Kraisler, T. Schmidt, S. Kümmel and L. Kronik, *Effect of ensemble generalization on the highest-occupied Kohn-Sham eigenvalue*, J. Chem. Phys. **143**, 104105 (2015).
- [KSRAB12] L. Kronik, T. Stein, S. Refaely-Abramson and R. Baer, *Excitation Gaps of Finite-Sized Systems from Optimally Tuned Range-Separated Hybrid Functionals*, J. Chem. Theory Comput. **8**, 1515 (2012).
- [KTY⁺06] S. Kera, S. Tanaka, H. Yamane, D. Yoshimura, K. K. Okudaira, K. Seki and N. Ueno, *Quantitative analysis of photoelectron angular distribution of single-domain organic monolayer film: NTCDA on GeS(001)*, Chem. Phys. **325**, 113 (2006).
- [KvF07] T. Kotani, M. van Schilfgaarde and S. V. Faleev, *Quasiparticle self-consistent GW method: A basis for the independent-particle approximation*, Phys. Rev. B **76**, 165106 (2007).
- [KYA⁺84] T. Kobayashi, Z.-i. Yoshida, H. Awaji, T. Kawase and S. Yoneda, *Intramolecular Orbital Interactions in 6,6'-Bi(1,4-dithiafulvenyl) Studied by Photoelectron Spectroscopy*, Bull. Chem. Soc. Jpn. **57**, 2591 (1984).
- [KYU09] S. Kera, H. Yamane and N. Ueno, *First-principles measurements of charge mobility in organic semiconductors: Valence hole-vibration coupling in organic ultrathin films*, Prog. in Surf. Sci. **84**, 135 (2009).
- [LAM⁺11] S.-Y. Liu, K. Alnama, J. Matsumoto, K. Nishizawa, H. Kohguchi, Y.-P. Lee and T. Suzuki, *He I ultraviolet photoelectron spectroscopy of benzene and pyridine in supersonic molecular beams using photoelectron imaging*, J. Phys. Chem. A **115**, 2953 (2011).
- [Leh54] H. Lehmann, *Über Eigenschaften von Ausbreitungsfunktionen und Renormierungskonstanten quantisierter Felder*, Il Nuovo Cimento **XI**, 342 (1954).
- [Lei07] M. Lein, *Molecular imaging using recolliding electrons*, J. Phys. B: At. Mol. Opt. Phys. **40**, R135 (2007).
- [Lev82] M. Levy, *Electron densities in search of Hamiltonians*, Phys. Rev. A **26**, 1200 (1982).
- [Lie74] A. Liebsch, *Theory of angular resolved photoemission from adsorbates*, Phys. Rev. Lett. **32**, 1203 (1974).

- [LPS84] M. Levy, J. P. Perdew and V. Sahni, *Exact differential equation for the density and ionization energy of a many-particle system*, Phys. Rev. A **30**, 2745 (1984).
- [LRM82] R. R. Lucchese, G. Raseev and V. McKoy, *Studies of differential and total photoionization cross sections of molecular nitrogen*, Phys. Rev. A **25**, 2572 (1982).
- [LSWS97] T. Leininger, H. Stoll, H.-J. Werner and A. Savin, *Combining long-range configuration interaction with short-range density functionals*, Chem. Phys. Lett. **275**, 151 (1997).
- [LW60] J. M. Luttinger and J. C. Ward, *Ground-State Energy of a Many-Fermion System. II*, Phys. Rev. **118**, 1417 (1960).
- [LYP88] C. Lee, W. Yang and R. G. Parr, *Development of the Colle-Salvetti correlation-energy formula into a functional of the electron density*, Phys. Rev. B **37**, 785 (1988).
- [Man02] D. E. Manolopoulos, *Derivation and reflection properties of a transmission-free absorbing potential*, J. Chem. Phys. **117**, 9552 (2002).
- [Mat92] R. D. Mattuck, *A Guide to Feynman Diagrams in the Many-Body Problem*, Dover publications, New York, 1992.
- [MB01a] N. T. Maitra and K. Burke, *Demonstration of initial-state dependence in time-dependent density-functional theory*, Phys. Rev. A **63**, 042501 (2001).
- [MB01b] N. T. Maitra and K. Burke, *Erratum: Demonstration of initial-state dependence in time-dependent density-functional theory*, Phys. Rev. A **64**, 039901 (2001).
- [MBW02] N. T. Maitra, K. Burke and C. Woodward, *Memory in Time-Dependent Density Functional Theory*, Phys. Rev. Lett. **89**, 023002 (2002).
- [MBW⁺13] G. Mercurio, O. Bauer, M. Willenbockel, N. Fairley, W. Reckien, C. H. Schmitz, B. Fiedler, S. Soubatch, T. Bredow, M. Sokolowski and F. S. Tautz, *Adsorption height determination of nonequivalent C and O species of PTCDA on Ag(110) using x-ray standing waves*, Phys. Rev. B **87**, 045421 (2013).
- [MCR01] M. A. L. Marques, A. Castro and A. Rubio, *Assessment of exchange-correlation functionals for the calculation of dynamical properties of small clusters in time-dependent density functional theory*, J. Chem. Phys. **115**, 3006 (2001).
- [MCR⁺12] N. Marom, F. Caruso, X. Ren, O. T. Hofmann, T. Körzdörfer, J. R. Chelikowsky, A. Rubio, M. Scheffler and P. Rinke, *Benchmark of GW methods for azabenzenes*, Phys. Rev. B **86**, 245127 (2012).
- [MDRS08] J. Messud, P. M. Dinh, P.-G. Reinhard and E. Suraud, *Time-dependent density-functional theory with a self-interaction correction*, Phys. Rev. Lett. **101**, 096404 (2008).
- [Mes14] A. Messiah, *Quantum mechanics*, Dover publications, Mineola, New York, 2014.
- [MFBG08] B. K. McFarland, J. P. Farrell, P. H. Bucksbaum and M. Gühr, *High harmonic generation from multiple orbitals in N₂*, Science **322**, 1232 (2008).

- [MG03] M. A. L. Marques and E. K. U. Gross, Time-dependent density functional theory, in *A primer in density functional theory*, edited by C. Fiolhais, F. Nogueira and M. A. L. Marques, Lecture Notes in Physics, pages 144–184, Springer, Berlin-Heidelberg, 2003.
- [MG04] M. A. L. Marques and E. K. U. Gross, *Time-dependent density functional theory*, *Annu. Rev. Phys. Chem.* **55**, 427 (2004).
- [MGW⁺13] E. Moreau, S. Godey, X. Wallart, I. Razado-Colambo, J. Avila, M. C. Asensio and D. Vignaud, *High-resolution angle-resolved photoemission spectroscopy study of monolayer and bilayer graphene on the C-face of SiC*, *Phys. Rev. B* **88**, 075406 (2013).
- [MK05] M. Mundt and S. Kümmel, *Derivative Discontinuities in Time-Dependent Density-functional Theory*, *Phys. Rev. Lett.* **95**, 203004 (2005).
- [MK06] M. Mundt and S. Kümmel, *Optimized effective potential in real time: Problems and prospects in time-dependent density-functional theory*, *Phys. Rev. A* **74**, 022511 (2006).
- [MK07] M. Mundt and S. Kümmel, *Photoelectron spectra of anionic sodium clusters from time-dependent density-functional theory in real time*, *Phys. Rev. B* **76**, 035413 (2007).
- [MKHM06] M. Mundt, S. Kümmel, B. Huber and M. Moseler, *Photoelectron spectra of sodium clusters: The problem of interpreting Kohn-Sham eigenvalues*, *Phys. Rev. B* **73**, 205407 (2006).
- [MKJS77] L. Mattsson, L. Karlsson, R. Jadrny and K. Siegbahn, *Valence Electron Spectrum of C₆H₆ Excited by Linearly Polarized HeI Radiation*, *Phys. Scr.* **16**, 221 (1977).
- [MKvLR07] M. Mundt, S. Kümmel, R. van Leeuwen and P.-G. Reinhard, *Violation of the zero-force theorem in the time-dependent Krieger-Li-Iafrate approximation*, *Phys. Rev. A* **75**, 050501(R) (2007).
- [MMN⁺12] M. A. L. Marques, N. T. Maitra, F. M. S. Nogueira, E. K. U. Gross and A. Rubio, *Fundamentals of Time-Dependent Density Functional Theory*, volume 837 of *Lecture Notes in Physics*, Springer, Berlin-Heidelberg, 2012.
- [MPAVO04] B. Milián, R. Pou-Amérgo, R. Viruela and E. Ortí, *On the electron affinity of TCNQ*, *Chem. Phys. Lett.* **391**, 148 (2004).
- [MSCY06] P. Mori-Sánchez, A. J. Cohen and W. Yang, *Many-electron self-interaction error in approximate density functionals*, *J. Chem. Phys.* **125**, 201102 (2006).
- [MSCY08] P. Mori-Sánchez, A. J. Cohen and W. Yang, *Localization and Delocalization Errors in Density Functional Theory and Implications for Band-Gap Prediction*, *Phys. Rev. Lett.* **100**, 146401 (2008).
- [MUN⁺06] M. A. L. Marques, C. A. Ullrich, F. Nogueira, A. Rubio, K. Burke and E. K. U. Gross, *Time-dependent density functional theory*, Lecture Notes in Physics, Springer, 2006.

- [Mun07] M. Mundt, *Orbital functionals in Time-Dependent Density-Functional Theory*, PhD thesis, University of Bayreuth, 2007.
- [Mun09] M. Mundt, *Real-Time Approach To Time-Dependent Density-Functional Theory in the Linear and Nonlinear Regime*, J. Theor. Comput. Chem. **8**, 561 (2009).
- [MW84] R. Miranda and K. Wandelt, *Angle-resolved photoemission of CO chemisorption on Pd(111)*, Surf. Sci. **139**, 430 (1984).
- [MZCB04] N. T. Maitra, F. Zhang, R. J. Cave and K. Burke, *Double excitations within time-dependent density functional theory linear response*, J. Chem. Phys. **120**, 5932 (2004).
- [NBRG07] W. Nelson, P. Bokes, P. Rinke and R. W. Godby, *Self-interaction in Green's-function theory of the hydrogen atom*, Phys. Rev. A **75**, 032505 (2007).
- [OK07] C. M. Oana and A. I. Krylov, *Dyson orbitals for ionization from the ground and electronically excited states within equation-of-motion coupled-cluster formalism: theory, implementation, and examples*, J. Chem. Phys. **127**, 234106 (2007).
- [ORR02] G. Onida, L. Reining and A. Rubio, *Electronic excitations: density-functional versus many-body Green's-function approaches*, Rev. Mod. Phys. **74**, 601 (2002).
- [PBE96] J. P. Perdew, K. Burke and M. Ernzerhof, *Generalized Gradient Approximation Made Simple*, Phys. Rev. Lett. **77**, 3865 (1996).
- [PBF⁺09] P. Puschnig, S. Berkebile, A. J. Fleming, G. Koller, K. Emtsev, T. Seyller, J. D. Riley, C. Ambrosch-Draxl, F. P. Netzer and M. G. Ramsey, *Reconstruction of molecular orbital densities from photoemission data*, Science **326**, 702 (2009).
- [PEB96] J. P. Perdew, M. Ernzerhof and K. Burke, *Rationale for mixing exact exchange with density functional approximations*, J. Chem. Phys. **105**, 9982 (1996).
- [PEFK83] T. Permien, R. Engelhardt, C. A. Feldmann and E. E. Koch, *Angle-resolved photoemission from oriented films of lead phthalocyanine on a Cu(100) surface*, Chem. Phys. Lett. **98**, 527 (1983).
- [Per79] J. P. Perdew, *Orbital functional for exchange and correlation: self-interaction correction to the local density approximation*, Chem. Phys. Lett. **64**, 127 (1979).
- [Per90] J. P. Perdew, *Size-Consistency, Self-Interaction Correction, and Derivative Discontinuity in Density Functional Theory*, Adv. Quantum Chem. **21**, 113 (1990).
- [PGG96] M. Petersilka, U. J. Gossmann and E. K. U. Gross, *Excitation Energies from Time-Dependent Density-Functional Theory*, Phys. Rev. Lett. **76**, 1212 (1996).
- [PHL84] M. R. Pederson, R. A. Heaton and C. C. Lin, *Local-density Hartree-Fock theory of electronic states of molecules with self-interaction correction*, J. Chem. Phys. **80**, 1972 (1984).
- [PHL85] M. R. Pederson, R. A. Heaton and C. C. Lin, *Density-functional theory with self-interaction correction: Application to the lithium molecule*, J. Chem. Phys. **82**, 2688 (1985).

- [PK03] J. P. Perdew and S. Kurth, Density Functionals for Non-relativistic Coulomb Systems in the New Century, in *A primer in density functional theory*, edited by C. Fiolhais, F. Nogueira and M. A. Marques, Lecture Notes in Physics, pages 1–155, Springer, Berlin-Heidelberg, 2003.
- [PL83] J. P. Perdew and M. Levy, *Physical content of the exact kohn-sham orbital energies: Band gaps and derivative discontinuities*, Phys. Rev. Lett. **51**, 1884 (1983).
- [PL88] M. R. Pederson and C. C. Lin, *Localized and canonical atomic orbitals in self-interaction corrected local density functional approximation*, J. Chem. Phys. **88**, 1807 (1988).
- [PL97] J. P. Perdew and M. Levy, *Comment on “Significance of the highest occupied Kohn-Sham eigenvalue”*, Phys. Rev. B **56**, 16021 (1997).
- [PL15] P. Puschnig and D. Lüftner, *Simulation of angle-resolved photoemission spectra by approximating the final state by a plane wave: From graphene to polycyclic aromatic hydrocarbon molecules*, J. Elec. Spec. Rel. Phenom. **200**, 193 (2015).
- [Pow00] I. Powis, *Photoelectron circular dichroism of the randomly oriented chiral molecules glyceraldehyde and lactic acid*, J. Chem. Phys. **112**, 301 (2000).
- [PPLB82] J. P. Perdew, R. G. Parr, M. Levy and J. L. Balduz Jr, *Density-Functional Theory for Fractional Particle Number: Derivative Discontinuities of the Energy*, Phys. Rev. Lett. **49**, 1691 (1982).
- [PRS00] A. Pohl, P.-G. Reinhard and E. Suraud, *Towards single-particle spectroscopy of small metal clusters*, Phys. Rev. Lett. **84**, 5090 (2000).
- [PRT⁺05] J. P. Perdew, A. Ruzsinszky, J. Tao, V. N. Staroverov, G. E. Scuseria and G. I. Csonka, *Prescription for the design and selection of density functional approximations: more constraint satisfaction with fewer fits.*, J. Chem. Phys. **123**, 62201 (2005).
- [PRU⁺11] P. Puschnig, E.-M. Reinisch, T. Ules, G. Koller, S. Soubatch, M. Ostler, L. Romaner, F. S. Tautz, C. Ambrosch-Draxl and M. G. Ramsey, *Orbital tomography: Deconvoluting photoemission spectra of organic molecules*, Phys. Rev. B **84**, 235427 (2011).
- [PW89] R. G. Parr and W. Yang, *Density-Functional Theory of Atoms and Molecules*, International Series of Monographs on Chemistry, Vol. 16, Oxford University Press, New York, 1 edition, 1989.
- [PW92] J. P. Perdew and Y. Wang, *Accurate and simple analytic representation of the electron-gas correlation energy*, Phys. Rev. B **45**, 13244 (1992).
- [PZ81] J. P. Perdew and A. Zunger, *Self-interaction correction to density-functional approximations for many-electron systems*, Phys. Rev. B **23**, 5048 (1981).
- [PZBV07] S. Patchkovskii, Z. Zhao, T. Brabec and D. M. Villeneuve, *High harmonic generation and molecular orbital tomography in multielectron systems*, J. Chem. Phys. **126**, 114306 (2007).
- [QUM11] X. Qian, P. Umari and N. Marzari, *Photoelectron properties of DNA and RNA bases from many-body perturbation theory*, Phys. Rev. B **84**, 075103 (2011).

- [RASG⁺12] S. Refaely-Abramson, S. Sharifzadeh, N. Govind, J. Autschbach, J. B. Neaton, R. Baer and L. Kronik, *Quasiparticle Spectra from a Nonempirical Optimally Tuned Range-Separated Hybrid Density Functional*, Phys. Rev. Lett. **109**, 226405 (2012).
- [RG84] E. Runge and E. K. U. Gross, *Density-Functional Theory for Time-Dependent Systems*, Phys. Rev. Lett. **52**, 997 (1984).
- [RH05] F. Reinert and S. Hüfner, *Photoemission spectroscopy—from early days to recent applications*, New J. Phys. **7**, 97 (2005).
- [Rit76] B. Ritchie, *Theory of the angular distribution of photoelectrons ejected from optically active molecules and molecular negative ions*, Phys. Rev. A **13**, 1411 (1976).
- [RJT10] C. Rostgaard, K. W. Jacobsen and K. S. Thygesen, *Fully self-consistent GW calculations for molecules*, Phys. Rev. B **81**, 085103 (2010).
- [RMC⁺15] X. Ren, N. Marom, F. Caruso, M. Scheffler and P. Rinke, *Beyond the GW approximation: A second-order screened exchange correction*, Phys. Rev. B **92**, 081104(R) (2015).
- [RPC⁺06] A. Ruzsinszky, J. P. Perdew, G. I. Csonka, O. A. Vydrov and G. E. Scuseria, *Spurious fractional charge on dissociated atoms: Pervasive and resilient self-interaction error of common density functionals*, J. Chem. Phys. **125**, 194112 (2006).
- [RPC⁺07] A. Ruzsinszky, J. P. Perdew, G. I. Csonka, O. A. Vydrov and G. E. Scuseria, *Density functionals that are one- and two- are not always many-electron self-interaction-free, as shown for H_2^+ , He_2^+ , LiH^+ , and Ne_2^+* , J. Chem. Phys. **126**, 104102 (2007).
- [RQN⁺05] P. Rinke, A. Qteish, J. Neugebauer, C. Freysoldt and M. Scheffler, *Combining GW calculations with exact-exchange density-functional theory: an analysis of valence-band photoemission for compound semiconductors*, New J. Phys. **7**, 126 (2005).
- [RRB⁺12] X. Ren, P. Rinke, V. Blum, J. Wieferink, A. Tkatchenko, A. Sanfilippo, K. Reuter and M. Scheffler, *Resolution-of-identity approach to Hartree-Fock, hybrid density functionals, RPA, MP2 and GW with numeric atom-centered orbital basis functions*, New J. Phys. **14**, 053020 (2012).
- [RTPHG89] K. Raghavachari, G. W. Trucks, J. A. Pople and M. Head-Gordon, *A fifth-order perturbation comparison of electron correlation theories*, Chem. Phys. Lett. **157**, 479 (1989).
- [SAL⁺97] C. Seidel, C. Awater, X. Liu, R. Ellerbrake and H. Fuchs, *A combined STM, LEED and molecular modelling study of PTCDA grown on Ag(110)*, Surf. Sci. **371**, 123 (1997).
- [SB09] U. Salzner and R. Baer, *Koopmans' springs to life*, J. Chem. Phys. **131**, 231101 (2009).
- [SBKN12] S. Sharifzadeh, A. Biller, L. Kronik and J. B. Neaton, *Quasiparticle and optical spectroscopy of the organic semiconductors pentacene and PTCDA from first principles*, Phys. Rev. B **85**, 125307 (2012).

- [Sch26] E. Schrödinger, *An undulatory theory of the mechanics of atoms and molecules*, Phys. Rev. **28**, 1049 (1926).
- [Sch90] G. Schönhense, *Circular Dichroism and Spin Polarization in Photoemission from Adsorbates and Non-Magnetic Solids*, Phys. Scr. **T31**, 255 (1990).
- [Sch06] W. H. E. Schwarz, *Measuring orbitals: Provocation or reality?*, Angew. Chem. **45**, 1508 (2006).
- [SDCF94] P. J. Stephens, F. J. Devlin, C. F. Chabalowski and M. J. Frisch, *Ab Initio Calculation of Vibrational Absorption and Circular Dichroism Spectra Using Density Functional Force Fields*, J. Phys. Chem. **98**, 11623 (1994).
- [SEKB10] T. Stein, H. Eisenberg, L. Kronik and R. Baer, *Fundamental Gaps in Finite Systems from Eigenvalues of a Generalized Kohn-Sham Method*, Phys. Rev. Lett. **105**, 266802 (2010).
- [SF95] A. Savin and H.-J. Flad, *Density functionals for the Yukawa electron-electron interaction*, Int. J. Quantum Chem. **56**, 327–332 (1995).
- [SGGG01] A. Schindlmayr, P. García-González and R. W. Godby, *Diagrammatic self-energy approximations and the total particle number*, Phys. Rev. B **64**, 235106 (2001).
- [SGV⁺96] A. Seidl, A. Görling, P. Vogl, J. A. Majewski and M. Levy, *Generalized Kohn-Sham schemes and the band-gap problem*, Phys. Rev. B **53**, 3764 (1996).
- [SH53] R. T. Sharp and G. K. Horton, *A variational approach to the unipotential many-electron problem*, Phys. Rev. **90**, 317 (1953).
- [SH99] R. Stowasser and R. Hoffmann, *What do the Kohn-Sham orbitals and eigenvalues mean?*, J. Am. Chem. Soc. **121**, 3414 (1999).
- [SK] I. Schelter and S. Kümmel, in preparation .
- [SK78] J. A. Sell and A. Kuppermann, *Angular distributions in the photoelectron spectra of benzene and its monohalogenated derivatives*, Chem. Phys. **33**, 367 (1978).
- [SK16a] P. Schaffhauser and S. Kümmel, *Using time-dependent density functional theory in real time for calculating electronic transport*, Phys. Rev. B **93**, 035115 (2016).
- [SK16b] T. Schmidt and S. Kümmel, *One- and many-electron self-interaction error in local and global hybrid functionals*, Phys. Rev. B **93**, 165120 (2016).
- [SKB09] T. Stein, L. Kronik and R. Baer, *Prediction of charge-transfer excitations in coumarin-based dyes using a range-separated functional tuned from first principles*, J. Chem. Phys. **131**, 244119 (2009).
- [SKKK14] T. Schmidt, E. Kraisler, L. Kronik and S. Kümmel, *One-electron self-interaction and the asymptotics of the Kohn-Sham potential: an impaired relation*, Phys. Chem. Chem. Phys. **16**, 14357 (2014).
- [SKM⁺14] T. Schmidt, E. Kraisler, A. Makmal, L. Kronik and S. Kümmel, *A self-interaction-free local hybrid functional: Accurate binding energies vis-à-vis accurate ionization potentials from Kohn-Sham eigenvalues*, J. Chem. Phys. **140**, 18A510 (2014).

- [SS83] L. J. Sham and M. Schlüter, *Density-functional theory of the energy gap*, Phys. Rev. Lett. **51**, 1888 (1983).
- [SS08] Y.-i. Suzuki and T. Suzuki, *Photoelectron Angular Distribution in Valence Shell Ionization of Heteroaromatic Molecules Studied by the continuum Multiple Scattering X_α Method*, J. Phys. Chem. A **112**, 402 (2008).
- [SWLZ09] J. Sauther, J. Wüsten, S. Lach and C. Ziegler, *Gas phase and bulk ultraviolet photoemission spectroscopy of 3,4,9,10-perylene-tetracarboxylic dianhydride, 1,4,5,8-naphthalene-tetracarboxylic dianhydride, and 1,8-naphthalene-dicarboxylic anhydride*, J. Chem. Phys. **131**, 034711 (2009).
- [SWR⁺12] B. Stadtmüller, M. Willenbockel, E. M. Reinisch, T. Ules, F. C. Bocquet, S. Soubatch, P. Puschnig, G. Koller, M. G. Ramsey, F. S. Tautz and C. Kumpf, *Orbital tomography for highly symmetric adsorbate systems*, Europhys. Lett. **100**, 26008 (2012).
- [TC98] X.-M. Tong and S.-I. Chu, *Time-dependent density-functional theory for strong-field multiphoton processes: Application to the study of the role of dynamical electron correlation in multiple high-order harmonic generation*, Phys. Rev. A **57**, 452 (1998).
- [TDT08] A. M. Teale, F. De Proft and D. J. Tozer, *Orbital energies and negative electron affinities from density functional theory: Insight from the integer discontinuity*, J. Chem. Phys. **129**, 044110 (2008).
- [TGK08] M. Thiele, E. K. U. Gross and S. Kümmel, *Adiabatic approximation in nonperturbative time-dependent density-functional theory*, Phys. Rev. Lett. **100**, 153004 (2008).
- [Thi09] M. Thiele, *Correlated electron dynamics and memory in time-dependent density functional theory*, PhD thesis, University of Bayreuth, 2009.
- [TK14] M. Thiele and S. Kümmel, *Frequency dependence of the exact exchange-correlation kernel of time-dependent density-functional theory*, Phys. Rev. Lett. **112**, 083001 (2014).
- [TM91] N. Troullier and J. L. Martins, *Efficient pseudopotentials for plane-wave calculations*, Phys. Rev. B **43**, 1993 (1991).
- [TS76] J. D. Talman and W. F. Shadwick, *Optimized effective atomic central potential*, Phys. Rev. A **14**, 36 (1976).
- [UGG95] C. A. Ullrich, U. J. Gossmann and E. K. U. Gross, *Time-Dependent Optimized Effective Potential*, Phys. Rev. Lett. **74**, 872 (1995).
- [UK08] N. Ueno and S. Kera, *Electron spectroscopy of functional organic thin films: Deep insights into valence electronic structure in relation to charge transport property*, Prog. Surf. Sci. **83**, 490 (2008).
- [ULR⁺14] T. Ules, D. Lüftner, E. M. Reinisch, G. Koller, P. Puschnig and M. G. Ramsey, *Orbital tomography of hybridized and dispersing molecular overlayers*, Phys. Rev. B **90**, 155430 (2014).
- [URS97] C. A. Ullrich, P.-G. Reinhard and E. Suraud, *Metallic clusters in strong femtosecond laser pulses*, J. Phys. B: At. Mol. Opt. Phys. **30**, 5043 (1997).

- [URS98] C. A. Ullrich, P.-G. Reinhard and E. Suraud, *Electron dynamics in strongly excited sodium clusters: a density-functional study with self-interaction correction*, J. Phys. B: At. Mol. Opt. Phys. **31**, 1871 (1998).
- [vBH72] U. von Barth and L. Hedin, *A local exchange-correlation potential for the spin polarized case: I*, J. Phys. C **5**, 1629 (1972).
- [vBH96] U. von Barth and B. Holm, *Self-consistent GW_0 results for the electron gas: Fixed screened potential W_0 within the random-phase approximation*, Phys. Rev. B **54**, 8411 (1996).
- [vCS⁺15] M. J. van Setten, F. Caruso, S. Sharifzadeh, X. Ren, M. Scheffler, F. Liu, J. Lischner, L. Lin, J. R. Deslippe, S. G. Louie, C. Yang, F. Weigend, J. B. Neaton, F. Evers and P. Rinke, *GW 100: Benchmarking G_0W_0 for Molecular Systems*, J. Chem. Theor. Comput. **11**, 5665 (2015).
- [VDR⁺13] M. Vincendon, P. M. Dinh, P. Romaniello, P.-G. Reinhard and É. Suraud, *Photoelectron spectra from full time dependent self-interaction correction*, Eur. Phys. J. D **67**, 97 (2013).
- [VESN⁺15] V. Vlček, H. R. Eisenberg, G. Steinle-Neumann, L. Kronik and R. Baer, *Deviations from piecewise linearity in the solid-state limit with approximate density functionals.*, J. Chem. Phys. **142**, 034107 (2015).
- [Vig08] G. Vignale, *Real-time resolution of the causality paradox of time-dependent density-functional theory*, Phys. Rev. A **77**, 062511 (2008).
- [vL98] R. van Leeuwen, *Causality and Symmetry in Time-Dependent Density-Functional Theory*, Phys. Rev. Lett. **80**, 1280 (1998).
- [vL99] R. van Leeuwen, *Mapping from Densities to Potentials in Time-Dependent Density-Functional Theory*, Phys. Rev. Lett. **82**, 3863 (1999).
- [vL01] R. van Leeuwen, *Key Concepts in Time-Dependent Density-Functional Theory*, Int. J. Mod. Phys. B **15**, 1969 (2001).
- [vLS12] R. van Leeuwen and G. Stefanucci, *Wick theorem for general initial states*, Phys. Rev. B **85**, 115119 (2012).
- [vSKF06] M. van Schilfhaarde, T. Kotani and S. Faleev, *Quasiparticle Self-Consistent GW Theory*, Phys. Rev. Lett. **96**, 226402 (2006).
- [VSP07] O. A. Vydrov, G. E. Scuseria and J. P. Perdew, *Tests of functionals for systems with fractional electron number*, J. Chem. Phys. **126**, 154109 (2007).
- [VTM03] V. Véniard, R. Taïeb and A. Maquet, *Photoionization of Atoms Using Time-Dependent Density Functional Theory*, Laser Phys. **13**, 465 (2003).
- [Wan10] L.-W. Wang, *Relationship between the random-phase approximation ground-state total energy and GW quasiparticle energy*, Phys. Rev. B **82**, 115111 (2010).
- [WBG⁺91] C. Westphal, J. Bansmann, M. Getzlaff, G. Schönhense, N. A. Cherepkov, M. Braunstein, V. McKoy and R. L. Dubs, *Circular dichroism in photoemission from oriented molecules at surfaces*, Surf. Sci. **253**, 205 (1991).

- [WBG89] C. Westphal, J. Bansmann, M. Getzlaff and G. Schönhense, *Circular dichroism in the angular distribution of photoelectrons from oriented CO molecules*, Phys. Rev. Lett. **63**, 151 (1989).
- [WDSR12] P. Wopperer, P. M. Dinh, E. Suraud and P.-G. Reinhard, *Frequency dependence of photoelectron angular distributions in small Na clusters*, Phys. Rev. A **85**, 015402 (2012).
- [WFD⁺10] P. Wopperer, B. Faber, P. M. Dinh, P.-G. Reinhard and E. Suraud, *Angular distributions of photoelectrons from free Na clusters*, Phys. Rev. A **82**, 063416 (2010).
- [WH08] M. Walter and H. Häkkinen, *Photoelectron spectra from first principles: from the many-body to the single-particle picture*, New J. Phys. **10**, 043018 (2008).
- [WHS⁺12] M. Wießner, D. Hauschild, A. Schöll, F. Reinert, V. Feyer, K. Winkler and B. Krömker, *Electronic and geometric structure of the PTCDA/Ag(110) interface probed by angle-resolved photoemission*, Phys. Rev. B **86**, 045417 (2012).
- [WHS⁺14] M. Wießner, D. Hauschild, C. Sauer, V. Feyer, A. Schöll and F. Reinert, *Complete determination of molecular orbitals by measurement of phase symmetry and electron density*, Nat. Commun. **5**, 4156 (2014).
- [Wie13] M. Wießner, *Isolierte Moleküle und delokalisierte Zustände: Einblick in die elektronische Struktur organischer Adsorbate mittels winkelaufgelöster Photoemission*, PhD thesis, University of Würzburg, 2013.
- [WKF⁺13] M. Wießner, J. Kübert, V. Feyer, P. Puschnig, A. Schöll and F. Reinert, *Lateral band formation and hybridization in molecular monolayers: NTCDA on Ag(110) and Cu(100)*, Phys. Rev. B **88**, 075437 (2013).
- [WLU⁺15] S. Weiß, D. Lüftner, T. Ules, E. M. Reinisch, H. Kaser, A. Gottwald, M. Richter, S. Soubatch, G. Koller, M. G. Ramsey, F. S. Tautz and P. Puschnig, *Exploring three-dimensional orbital imaging with energy-dependent photoemission tomography*, Nat. Commun. **6**, 8287 (2015).
- [WPK⁺11] C. Wiemann, M. Patt, I. P. Krug, N. B. Weber, M. Escher, M. Merkel and C. M. Schneider, *A New Nanospectroscopy Tool with Synchrotron Radiation: NanoESCA@Elettra*, e-J. Surf. Sci. Nanotechnol. **9**, 395 (2011).
- [WZF⁺13] M. Wießner, J. Ziroff, F. Forster, M. Arita, K. Shimada, P. Puschnig, A. Schöll and F. Reinert, *Substrate-mediated band-dispersion of adsorbate molecular states*, Nat. Commun. **4**, 1514 (2013).
- [YB96] K. Yabana and G. F. Bertsch, *Time-dependent local-density approximation in real time*, Phys. Rev. B **54**, 4484 (1996).
- [YMSC13] W. Yang, P. Mori-Sánchez and A. J. Cohen, *Extension of many-body theory and approximate density functionals to fractional charges and fractional spins*, J. Chem. Phys. **139**, 104114 (2013).
- [YNF⁺05] H. Yamane, S. Nagamatsu, H. Fukagawa, S. Kera, R. Friedlein, K. K. Okudaira and N. Ueno, *Hole-vibration coupling of the highest occupied state in pentacene thin films*, Phys. Rev. B **72**, 153412 (2005).

- [ZFS⁺10] J. Ziroff, F. Forster, A. Schöll, P. Puschnig and F. Reinert, *Hybridization of Organic Molecular Orbitals with Substrate States at Interfaces: PTCDA on Silver*, Phys. Rev. Lett. **104**, 233004 (2010).
- [ZKS⁺06] Y. Zou, L. Kilian, A. Schöll, T. Schmidt, R. Fink and E. Umbach, *Chemical bonding of PTCDA on Ag surfaces and the formation of interface states*, Surf. Sci. **600**, 1240 (2006).
- [ZY98] Y. Zhang and W. Yang, *A challenge for density functionals: Self-interaction error increases for systems with a noninteger number of electrons*, J. Chem. Phys. **109**, 2604 (1998).

Acknowledgments

Creating this thesis would certainly not have been possible without the strong support of numerous people that accompanied me along the way. Therefore, I sincerely wish to thank

- **Stephan Kümmel** who guided my work with his enormous support, suggestions, and advice. Meeting him and having him as a mentor was a great privilege and fortune. His enthusiasm for science paired with his personality has always been an inspiring example to me.
- **Achim Schöll, Martin Graus, Michael Wießner, Christian Metzger, Manuel Grimm,** and **Friedrich Reinert** for an extremely fruitful cooperation. I thank them for sharing all ideas with me openly and for all the explanations on the art of conducting ARPES experiments.
- **Patrick Rinke** for his hospitality, support, explanations on *GW*, and the amazing and unforgettable time at Aalto.
- **Fabio Caruso** for his support and patience in preparing the *GW* manuscripts and discussing the data.
- **Monika Birkelbach, Claudia Geier, Markus Hilt, and Bernhard Winkler** for helping me with administrative matters and solving all computer issues.
- **Tobias Schmidt**, who is one of the most humorous, smartest, most helpful, and simply coolest guys I have met. It has been an awful lot of fun to share an office with him during the last five years. Besides all the compliments, I want to use the opportunity to unveil his secret weak spot: He is just bad at playing FIFA.
- **All alumni and current members of the TP IV group.** I really appreciate the friendly atmosphere and the great private and physics discussions. I also want to thank them for always giving a hand no matter what the problem was.
- **All my friends** and in particular **Christoph Meichner, Stephan Hain, and Daniel Reck** with whom I went through my whole diploma studies with countless nights of solving exercise sheets or evaluating data for lab courses and nevertheless making it a hilarious time.
- My parents **Adam** and **Anette** as well as my brothers **Markus** and **Lucas** for supporting me in countless ways during the past years.
- **Katha** for teaching me English grammar and carefully proofreading the thesis and all the manuscripts, but most importantly for her appreciation, love, and care.

For financial and intellectual support I am grateful to the GRK 1640 of the DFG, the German Israeli Foundation, and the SolTech program of the Bavarian ministry of culture and arts.

Eidesstattliche Versicherung

Hiermit versichere ich an Eides statt, dass ich die vorliegende Arbeit selbstständig verfasst und keine anderen als die von mir angegebenen Quellen und Hilfsmittel verwendet habe.

Zusätzlich erkläre ich hiermit, dass ich keinerlei frühere Promotionsversuche unternommen habe.

Weiterhin erkläre ich, dass ich die Hilfe von gewerblichen Promotionsberatern bzw. -vermittlern oder ähnlichen Dienstleistern weder bisher in Anspruch genommen habe, noch künftig in Anspruch nehmen werde.

Matthias Dauth
Bayreuth, 25.07.2016

Part II

Publications

Publication 0

from the end of my diploma

Orbital density reconstruction for molecules

Physical Review Letters **107**, 193002 (2011)

M. Dauth, T. Körzdörfer, and S. Kümmel

Theoretical Physics IV, University of Bayreuth, D-95440 Bayreuth, Germany

J. Ziroff, M. Wiessner, A. Schöll, and F. Reinert

Experimental Physics 7 and Röntgen Research Center for Complex Materials (RCCM), University of Würzburg, D-97074 Würzburg, Germany and

Karlsruhe Institute of Technology, Nanoanalytik, D-76021 Karlsruhe, Germany

M. Arita and K. Shimada

Synchrotron Radiation Center, Hiroshima University, Higashi-Hiroshima 739-0046, Japan

My contribution

I performed all calculations, prepared all graphs, and contributed to the interpretation of the results.

Publ.0

Orbital Density Reconstruction for Molecules

M. Dauth, T. Körzdörfer, and S. Kümmel

Theoretical Physics IV, University of Bayreuth, D-95440 Bayreuth, Germany

J. Ziroff, M. Wiessner, A. Schöll, and F. Reinert

Experimental Physics 7 and Röntgen Research Center for Complex Material Systems (RCCM), University of Würzburg, D-97074 Würzburg, Germany

Karlsruhe Institute of Technology (KIT), Gemeinschaftslabor für Nanoanalytik, D-76021 Karlsruhe, Germany

M. Arita and K. Shimada

Hiroshima Synchrotron Radiation Center and Graduate School of Science, Hiroshima University, Hiroshima 739-8526, Japan

(Received 13 July 2011; published 4 November 2011)

The experimental imaging of electronic orbitals has allowed one to gain a fascinating picture of quantum effects. We here show that the energetically high-lying orbitals that are accessible to experimental visualization in general differ, depending on which approach is used to calculate the orbitals. Therefore, orbital imaging faces the fundamental question of which orbitals are the ones that are visualized. Combining angular-resolved photoemission experiments with first-principles calculations, we show that the orbitals from self-interaction-free Kohn-Sham density functional theory are the ones best suited for the orbital-based interpretation of photoemission.

DOI: 10.1103/PhysRevLett.107.193002

PACS numbers: 33.60.+q, 31.15.E-, 79.60.-i

Experiments that are interpreted as the visualization of molecular orbitals have become possible in rather different fields of science [1–3]. Angular-resolved photoemission spectroscopy (ARPES) has emerged as a particularly powerful tool [4–6], allowing one to visualize interface effects and substrate influences, thus gaining practical relevance by giving one access to properties that are fundamental to molecular electronics. However, the reconstruction of orbital densities is also fascinating from a fundamental point of view, as it allows one to visualize quantum mechanical properties that are considered elusive, revealing what is interpreted as a picture of the probability density for finding “an electron” in a molecule. However, for the very same reason, the results of “orbital measurements” may be debated: Nature does not know about one-electron orbitals, because electrons in a many-electron system are described by a correlated wave function and not by one-electron orbitals. Orbitals are a theoretical concept, introduced for noninteracting particles and used in interacting theories merely to build up a correlated wave function or to construct the density.

Typically, the photoemission intensity is written as [7]

$$I_f \propto \sum_i |\langle \Psi_f | \mathbf{A} \cdot \mathbf{p} | \Psi_i \rangle|^2 \delta(E_f - E_i - \hbar\omega) \quad (1)$$

for a transition from state $|\Psi_i\rangle$ to $|\Psi_f\rangle$ triggered by one photon of frequency ω in the semiclassical electromagnetic field \mathbf{A} . The final-state energy E_f is determined by the material’s work function and the kinetic energy of the measured electron. Writing the final state as an (antisymmetrized) product of a plane wave for the emitted electron

and the $N - 1$ electron state of the ionized system leads to a representation of the ionization process in terms of Dyson orbitals [8]. Even when the conditions under which the plane-wave approximation can be used [5] are fulfilled, it is not clear why the density of states on the right-hand side of Eq. (1) should be the one that one straightforwardly obtains from Hartree-Fock (HF) or density functional theory (DFT) calculations, and why ARPES should reflect the corresponding HF or DFT orbitals. In principle, the density of states should be the one of quasiparticles, e.g., as approximately obtained in a *GW* calculation [9]. The amazing observation is, though, that previous experiments could directly be related to the orbitals obtained from HF theory or semilocal density functional calculations. Here, we take this puzzle one step further and turn it into a serious question. We show that, for molecules that are of greater complexity than previously studied cases, different theories predict upper orbitals of different spatial character. What will orbital reconstruction techniques visualize in such cases? Combining first-principles calculations with ARPES experiments, we show that there is a systematic relation between the orbitals from self-interaction-free Kohn-Sham (KS) DFT and the measured intensities.

The orbital that typically is of greatest interest in orbital density reconstruction is the highest occupied molecular orbital (HOMO), and one of the so far largest molecules for which accurate orbital density visualization of the HOMO has been reported is pentacene [3,5,10]. In Ref. [5], ARPES data was explained based on generalized gradient approximation (GGA) orbitals, and our Fig. 1 confirms this approach: It hardly matters which theory is used to

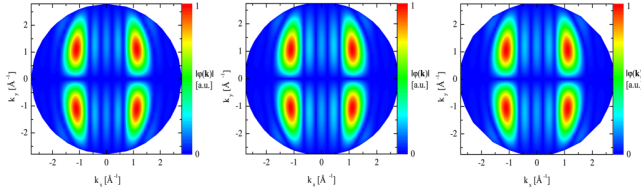


FIG. 1 (color online). Pentacene HOMO in momentum space. $|\varphi(\mathbf{k})|$ was evaluated on a hemisphere of radius $|\mathbf{k}| = 2.80 \text{ \AA}^{-1}$. Left: HF. Middle: PBE GGA [24]. Right: KS SIC [17].

calculate the HOMO. This is a consequence of pentacene's simple electronic structure. The upper valence orbitals are delocalized on similar length scales; thus, the relative ordering of the orbitals and the momentum distributions are not sensitive to possible shortcomings of theoretical methods [11,12].

The situation changes for molecules of greater complexity. A prominent example in this respect is the 1,4,5,8-naphthalene-tetracarboxylic dianhydride (NTCDA) molecule. Neither HF nor GGAs lead to eigenvalues [13] that match the gas phase photoelectron spectrum [14]. Contracting [4] or stretching [15] theoretical spectra can improve spectral agreement. However, with the full momentum distribution available from ARPES, theory and experiment can be compared in much greater detail. Kera *et al.* [4] have shown in an important study that the ARPES for the NTCDA HOMO can be understood based on HF. However, GGAs yield different results, as shown below. So while for specific systems, HF or GGA-based DFT can yield a reliable description [4,5], there is the pressing question of whether there exists a theoretical approach which generally yields the correct orbital ordering and momentum distributions for molecules—in other words, which single-particle orbitals are the best approximation to Dyson orbitals. This question is at the heart of “molecular orbital reconstruction.”

To answer these questions, we investigate several single-particle approaches: HF and different density functionals, namely, the Perdew-Burke-Ernzerhof (PBE) GGA, the Becke three-parameter Lee-Yang-Parr (B3LYP) hybrid [16], and the KS self-interaction correction (SIC) functional. The KS SIC approach used here has been described in detail in Ref. [17]. Its essential feature is that a spatially local, multiplicative potential that is the same for all orbitals is constructed according to the generalized optimized effective potential equation (see [18] for technical details). In this way, the powerful arguments of KS theory can be brought to bear despite the functional's orbital dependence.

There are pronounced differences between the NTCDA HOMOs obtained by different approaches. The top-left and top-middle panels of Fig. 2 show $|\varphi(\mathbf{k})| = |\int \varphi(\mathbf{r})e^{-i\mathbf{k}\cdot\mathbf{r}}d^3r|$ of the NTCDA HOMO from the PBE and the KS SIC calculation, respectively, both evaluated at $|\mathbf{k}| = 2.75 \text{ \AA}^{-1}$ (see [18] for technical details). The

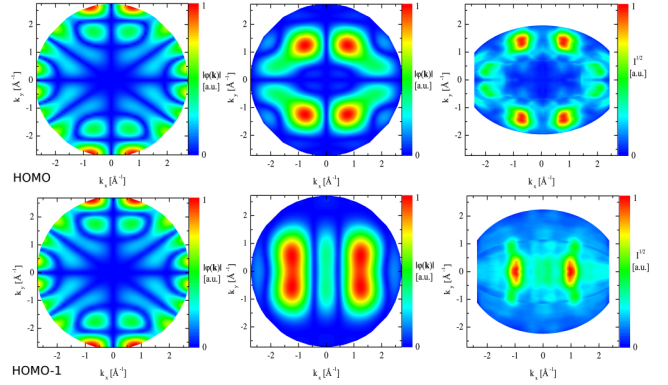


FIG. 2 (color online). Top: HOMO of NTCDA from PBE (left), KS SIC (middle), and square root of the ARPES intensity (right). Bottom: HOMO-1 from B3LYP (left), KS SIC (middle), and experiment (right).

observed marked differences have an important implication, because, as discussed in detail, e.g., in Ref. [5], $|\varphi(\mathbf{k})|$ can be related to the square root of the photoemission intensity. As the different calculations make rather different predictions for this quantity, NTCDA puts the orbital density interpretation to a serious test, allowing one to check which orbital, if any, will be seen in experiment.

The ARPES intensity distribution for the first emission peak is shown in the right plot of the top row of Fig. 2. The result is unambiguous: The experimental data reveal a close relation to the SIC orbital and none to the GGA orbital. The HOMO from HF and B3LYP (not shown) are similar to the SIC HOMO. The latter two approaches use integral-operator potentials, and the generalized Kohn-Sham equation resembles the Dyson equation [19,20]; thus, one may be tempted to believe that HF or hybrid functionals may approximate quasiparticle excitations better than any KS approach.

However, this is not the case, as seen by investigating the orbital below the HOMO, called HOMO-1 in the following. In the bottom row of Fig. 2, we compare $|\varphi(\mathbf{k})|$ for the HOMO-1 as found by B3LYP (left) and KS SIC (middle), each evaluated on a hemisphere of radius $|\mathbf{k}| = 2.73 \text{ \AA}^{-1}$, to the ARPES data (right). The SIC approach shows the experimentally observed features, whereas the B3LYP HOMO-1 does not resemble the experiment at all. The HF HOMO-1 (not shown) is similar to the HOMO-1 from KS SIC, but the characteristic “outward bending” seen experimentally for $k_x \approx \pm 1 \text{ \AA}^{-1}$, $k_y \geq 0.5 \text{ \AA}^{-1}$ is better reproduced by the SIC orbital. Furthermore, HF eigenvalues below HOMO-1 do not match the experiment at all, whereas the ones from self-interaction-free DFT are much more realistic, as shown in detail in Refs. [12,13]. Thus, we arrive at a decisive twofold insight. First, the orbital interpretation of photoemission can be used also for complex systems. Second, the self-interaction-free KS approach yields eigenvalues that reflect relative PES

peak positions and orbitals that correspond to ARPES intensities. It thus matches the “orbital density measurement” interpretation best.

This, of course, raises the question of whether one can understand why the orbitals from certain calculations cannot be related to the ARPES measurements. In KS DFT with its local multiplicative potential, the interpretabilities of orbitals and eigenvalues are closely tied to each other. Traditional DFT literature vigorously denied the KS eigenvalues any physical meaning. This, however, is not correct. Chong, Gritsenko, and Baerends [21] showed that KS eigenvalues can be very accurate approximations to the ionization potentials of upper valence electrons, and Duffy *et al.* [20] discussed in detail the relation between KS orbitals and Dyson orbitals. The decisive aspect for when an exchange-correlation functional will not yield physically interpretable eigenvalues and orbitals can be understood from Janak’s theorem [22], which states that relaxed ionization potentials can be obtained by integrating over the occupation number- (f -) dependent KS eigenvalues ε_i :

$$V_i = - \int_0^1 \varepsilon_i(f) df. \quad (2)$$

In a non-self-interaction-free KS calculation, the eigenvalues depend strongly and unphysically on the occupation numbers [11]. In KS approaches that eliminate self-interaction, the integrand in Eq. (2) does change much less over the integration range and can therefore be approximately taken out of the integral, and the eigenvalue at the upper integration limit approximately reflects the ionization potential. In other words, Kohn-Sham DFT can benefit from a cancellation of relaxation effects and “non-Koopmans” corrections. Earlier work gave semianalytical arguments for a near cancellation in atoms [11]. Our results show that in KS SIC the cancellation is excellent even for complex systems. Furthermore, any approach that is self-interaction-free and uses a multiplicative (KS) potential should yield physical orbitals and eigenvalues, and indeed we found that x -only optimized effective potential orbitals are qualitatively similar to the ones from KS SIC.

HF theory neglects correlation and does not employ a local multiplicative potential as KS theory does. Its eigenvalues correspond to an unrelaxed x -only approximation. They are thus less amenable to physical interpretation. The case of hybrid functionals is yet more involved. B3LYP combines $\approx 20\%$ of HF with a GGA, and thus the potential is neither self-interaction-free nor purely multiplicative—nevertheless, it yields eigenvalues that qualitatively often match photoemission peak positions [13,15], in particular, for NTCDA. However, the ARPES experiment presented here for the NTCDA HOMO-1 shows that the B3LYP orbital whose eigenvalue is at the right energy does not yield the experimentally observed momentum distribution; i.e., the energy agreement in this case is fortuitous.

As discussed in Refs. [4,5], scattering effects may influence the ARPES signal. Yet, for the present systems, their influence is much smaller [5] than the pronounced differences that are due to different molecular orbitals.

However, we can take the concept of measuring orbital densities to the edge by investigating a particularly challenging system. 3,4,9,10-perylene-tetracarboxylic acid dianhydride (PTCDA), another model organic semiconductor [6], is a complicated case, because different theoretical approaches agree on the structure of the HOMO, but the predictions for the lower lying orbitals differ largely, and there is not one distinct HOMO-1 but several energetically close-lying orbitals. We again focus on the PBE GGA and on KS SIC as the paradigm examples for a semilocal and self-interaction-free functional, respectively.

The PBE GGA finds two degenerate orbitals (HOMO-1 and HOMO-2) about 0.82 eV below the HOMO. The next orbital (HOMO-3) is energetically well separated from this degenerate pair, being lower by another 0.51 eV. The upper right plot in Fig. 3(a) shows the normalized sum of the absolute values of the Fourier transforms of the two degenerate GGA orbitals, evaluated at $|\mathbf{k}| = 1.92 \text{ \AA}^{-1}$. Based on the GGA calculation, one would thus expect one experimental peak about 0.82 eV below the HOMO peak that should be associated with a distinct ARPES intensity distribution.

The prediction from the KS SIC calculation is very different. SIC finds four orbitals in close energetic vicinity of each other. HOMO-1 lies 1.2 eV below the HOMO and is separated from HOMO-2 by just 0.19 eV. HOMO-2 itself is quasidegenerate (0.08 eV difference) with HOMO-3 and HOMO-4, the latter being strictly degenerate with each other. The lower left plot in Fig. 3(a) shows the absolute value of the Fourier transform of the SIC HOMO-1, the lower right the one of HOMO-2, and the upper left the normalized sum of the absolute values of the Fourier transforms of the two degenerate SIC orbitals HOMO-3 and HOMO-4. We used $|\mathbf{k}| = 1.92 \text{ \AA}^{-1}$ in each case. Thus, based on the SIC calculation, one expects that the ARPES intensity below the HOMO peak should have different contributions appearing in a rather small energy interval with distinctly different spatial patterns.

Turning to the ARPES experiment, one notes that, in contrast to the photoemission signals at the binding energies $E_B = 1.9 \text{ eV}$ and $E_B = 0.7 \text{ eV}$, which are directly assigned to the HOMO and the former lowest unoccupied molecular orbital, respectively, the signal between $E_B = 3.0 \text{ eV}$ and $E_B = 3.6 \text{ eV}$ (close to the onset of Ag 4d emission at $E_B \approx 4 \text{ eV}$) shows great complexity. A principal component analysis (see [18]) showed that at least four contributions need to be considered. We located these at binding energies of 3.1, 3.2, 3.3, and 3.5 eV. The corresponding data are shown in Fig. 3(b).

For the GGA calculation, neither the energetic position of the HOMO-1 nor the intensity pattern match the

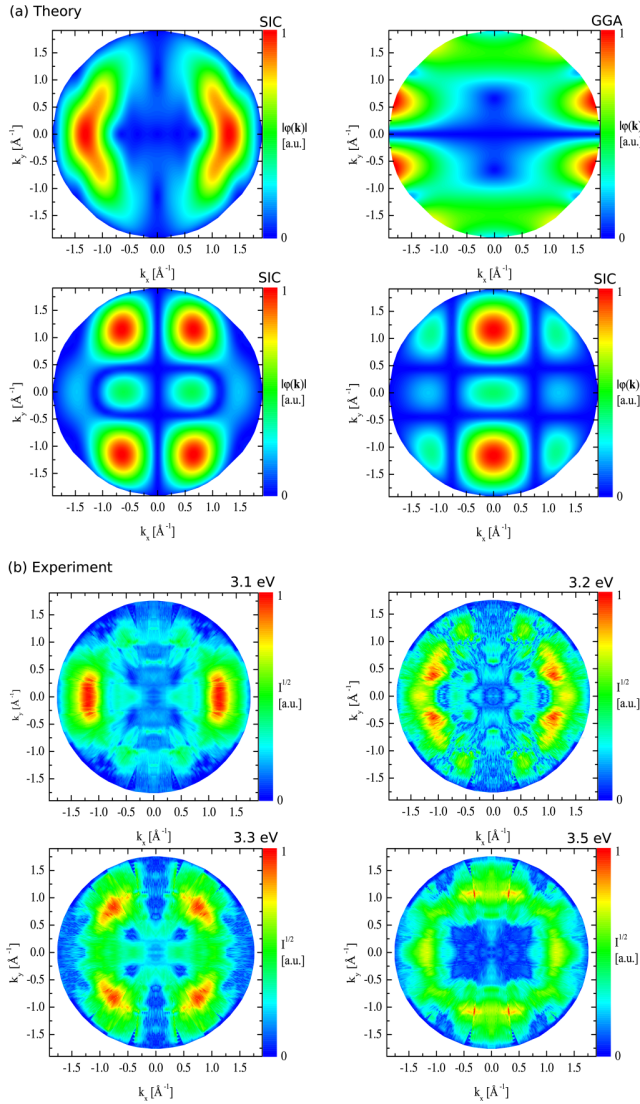


FIG. 3 (color online). (a) Absolute value of the Fourier transforms of PTCDA orbitals: SIC HOMO-1 (bottom left), SIC HOMO-2 (bottom right), normalized superposition of the degenerate SIC HOMO-3 and HOMO-4 (top left), and normalized superposition of the degenerate GGA HOMO-1 and HOMO-2 (top right). (b) Square root of the ARPES intensity at the four indicated binding energies.

experiment. The comparison of the experiment to the SIC calculation, on the other hand, is much clearer. The energetic separation between the HOMO and the next lower peak matches, and the experiment also very clearly confirms several different contributions. The intense signal at $E_B = 3.1$ eV is similar to the contribution one expects from the strictly degenerate SIC orbitals as seen in the upper left plot in Fig. 3(a). The measured intensity at $E_B = 3.3$ eV clearly reflects the lower left pattern in Fig. 3(a). Furthermore, the ARPES signal at $E_B = 3.5$ eV shows intensity at $k_x \approx 0$, $k_y = \pm 1 \text{ \AA}^{-1}$, which may stem from the orbital shown in the lower right plot in Fig. 3(a).

A finding that is puzzling at first sight is that the orbital ordering in the SIC calculation does not match the energetic ordering in which the corresponding ARPES intensities appear in the experiment, and we cannot determine unambiguously whether the experimental pattern at $E_B = 3.2$ eV should be reflected by a separate orbital. However, these discrepancies have a deeper reason, as can be seen from a comparison with a *GW* calculation for PTCDA [9]: *GW* predicts the same HOMO-1 pattern as KS SIC. This confirms that effects beyond the molecular orbital level must play a role.

At second sight, these discrepancies hardly come as a surprise given the complex situation that we investigate here. First, the Ag *d*-electron bands become increasingly important with increasing binding energy. Second, with the energetic differences between the SIC (or *GW*) orbitals being as small as found here, one cannot rule out that substrate influences or structural deformations such as bending [23] may change the ordering of the orbitals or may split degeneracies, and interactions between the various orbitals may be non-negligible. Yet, it is important to note that it can already be inferred from the calculation that the limits of the simple orbital interpretation are reached, as it results in a set of energetically close but spatially different orbitals.

In summary, we showed that for complex molecular systems different theories predict different upper orbitals, forcing us to face the question which of these orbitals, if any, can be related to experiments that are interpreted as measuring orbital densities. ARPES data unambiguously reveals a close correspondence to the orbitals from self-interaction-free KS theory, and we gave arguments for why this is the case. The combination of self-interaction-free density functional theory and angular-resolved photoemission reveals itself as a powerful tool for gaining insight into electronic properties.

S. K. acknowledges support by DFG GRK 1640 and GIF, T. K. by the AvH Foundation, F. R. and A. S. by DFG GRK 1221, FOR 1162, and the BMBF (Contracts No. 05K10WW2 and No. 03SF0356B), and F. R. and J. Z. from JSPS fellowships.

- [1] J. Itatani *et al.*, *Nature (London)* **432**, 867 (2004).
- [2] B. K. McFarland *et al.*, *Science* **322**, 1232 (2008).
- [3] J. Repp *et al.*, *Phys. Rev. Lett.* **94**, 026803 (2005).
- [4] S. Kera *et al.*, *Chem. Phys.* **325**, 113 (2006).
- [5] P. Puschnig *et al.*, *Science* **326**, 702 (2009).
- [6] J. Ziroff *et al.*, *Phys. Rev. Lett.* **104**, 233004 (2010).
- [7] S. Hüfner, *Photoelectron Spectroscopy* (Springer, Berlin, 2003), pp. 10–19.
- [8] M. Walter and H. Häkkinen, *New J. Phys.* **10**, 043018 (2008).
- [9] N. Dori *et al.*, *Phys. Rev. B* **73**, 195208 (2006).
- [10] J. Repp *et al.*, *Science* **312**, 1196 (2006).

- [11] J.P. Perdew and A. Zunger, *Phys. Rev. B* **23**, 5048 (1981).
- [12] T. Körzdörfer *et al.*, *Phys. Rev. B* **79**, 201205(R) (2009).
- [13] T. Körzdörfer, S. Kümmel, N. Marom, and L. Kronik, *Phys. Rev. B* **82**, 155206 (2010); **82**, 129903(E) (2010).
- [14] J. Sauther *et al.*, *J. Chem. Phys.* **131**, 034711 (2009).
- [15] N. Marom and L. Kronik, *Appl. Phys. A* **95**, 159 (2008).
- [16] P.J. Stephens *et al.*, *J. Phys. Chem.* **98**, 11 623 (1994).
- [17] T. Körzdörfer, M. Mundt, and S. Kümmel, *J. Chem. Phys.* **129**, 014110 (2008).
- [18] See Supplemental Material at <http://link.aps.org/supplemental/10.1103/PhysRevLett.107.193002> for details of our evaluation.
- [19] A. Seidl *et al.*, *Phys. Rev. B* **53**, 3764 (1996).
- [20] P. Duffy *et al.*, *Phys. Rev. A* **50**, 4707 (1994).
- [21] D. P. Chong, O. V. Gritsenko, and E. J. Baerends, *J. Chem. Phys.* **116**, 1760 (2002).
- [22] J.F. Janak, *Phys. Rev. B* **18**, 7165 (1978).
- [23] A. Hauschild *et al.*, *Phys. Rev. B* **81**, 125432 (2010).
- [24] J. P. Perdew, K. Burke, and M. Ernzerhof, *Phys. Rev. Lett.* **77**, 3865 (1996).

Supplemental material

We here present technical details of our study.

The ARPES data for NTCDA was recorded for a monolayer of NTCDA on an Ag(110) single crystal surface at beamline 9A of the Hiroshima Synchrotron Radiation Center (HiSOR) using photons with circular polarization and a photon energy $h\nu = 36$ eV. The beamline is equipped with a 6-axes manipulator (i-GONIO, R-Dec Co.) and a Scienta R4000 photoelectron analyzer enabling photoemission measurements with an energy resolution better than 10 meV. The Ag(110) surface was prepared by several sputtering and annealing cycles as described elsewhere [1]. The NTCDA films were grown at room temperature and the coverage was controlled by monitoring the characteristic LEED-pattern of the commensurate monolayer superstructure, which consists of molecules with uniform alignment [2]. Moreover, the well known valence band spectra of the chemisorbed monolayer [3, 4] were used as a reference. The ARPES measurements were performed at $T = 80$ K. Note that the room temperature order was maintained after rapid cool-down. To access a larger k -space region the polar angle was varied in 2° degree steps and the sample was then tilted, resulting in an overall momentum resolution of approximately $\Delta k = 0.1 \text{ \AA}^{-1}$ analogous to Ref. [5]. To plot the angular photoemission intensity distribution the NTCDA HOMO was integrated over an energy window of $\Delta E_B = 110$ meV at $E_B = 2.4$ eV covering the main part of the photoemission line. The individual angle scans were then joined and symmetrized according to the C_{2v} symmetry of the system [2]. The data for the NTCDA HOMO-1 was obtained following an equivalent procedure.

The ARPES data for PTCDA was recorded with a monochromatized vacuum ultraviolet lamp for He I_α radiation ($h\nu = 21.2$ eV) and a Scienta SES200 photoelectron analyzer (energy resolution better than 10 meV) at room temperature. The preparation of the PTCDA monolayer on Ag(110) is described in detail elsewhere [6] [7] [5], and results in a similar overlayer with parallel molecules as in the case of NTCDA. In this angle-resolved experiment the polar angle was varied in steps of 2° and the azimuthal angle was scanned at a fixed tilt angle. We combined the individual angle scans into one map for each contribution, for doing so we used the C_{2v} symmetry of the PTCDA molecules.

Fig. (S1) displays a deconvolution of the averaged spectra (black curve) of PTCDA into four components which were derived from the four distinct points in reciprocal space that are listed in the inset. These are points with high intensity. In the evaluation of the complete photoemission data set these components were (together with a Lorentzian shaped background for

the Ag4d-states) represented by one Gaussian each at the energy position of the intensity maximum of the respective energy distribution curve. The experimental data in panel (b) of Fig. (4) of the manuscript show the resulting intensities of the four Gaussians derived from the curve fit analysis of the ARPES data as a function of k_x and k_y . Note that artefacts due to dispersing sp-bands are inevitable, but do not affect the overall interpretation of the intensity variations.

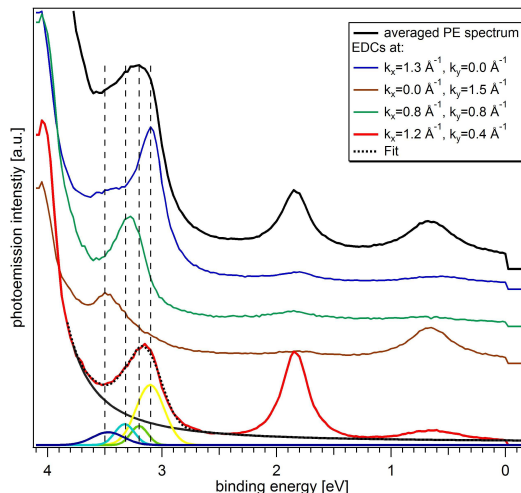


Fig. S1: Decomposition of the so-called “HOMO-1”-peak in the PTCDA spectrum into four contributions. The four Gaussian functions respected in the fit analysis are at 3.1 eV (yellow), 3.2 eV (green), 3.3 eV (lightblue) and 3.5 eV (purple).

The relation between $|\mathbf{k}|$ -values at which the Fourier transforms of the calculated orbitals are taken and the experimental binding energies follows from the arguments given in the main manuscript. In detail, the numbers are the following.

For the NTCDA HOMO, the experiment used photons with an energy of 36 eV. The Fermi edge of Ag(110) is at 4.7 eV. The binding energy (measured against the Fermi edge) of the HOMO is 2.46 eV. This results in a kinetic energy of the emitted photoelectron of 28.84 eV, corresponding to a wavevector of magnitude $|\mathbf{k}| = 2.75 \text{ \AA}^{-1}$. Following Ref. [8] this is the radius of the hemisphere in k -space at which the absolute value of the Fourier transform of the molecular orbital which is taken as the initial state is to be evaluated. For the HOMO-1 of NTCDA the same argument leads to a kinetic energy of 28.40 eV, corresponding to $|\mathbf{k}| = 2.73 \text{ \AA}^{-1}$. For PTCDA the situation is more complicated due to the different contributions to the here studied photoemission peak which

occur at slightly different binding energies. However, for the theoretical evaluation we used $|\mathbf{k}| = 1.92 \text{ \AA}^{-1}$ for all orbitals, corresponding to a kinetic energy of 14.0 eV. This is perfectly justified as the differences that one obtains from evaluating the theoretical data for a kinetic energy of, e.g., 13.7 eV instead of 14.0 eV, are negligible in the plots. For Pentacene we followed Ref. [8] and used $|\mathbf{k}| = 2.80 \text{ \AA}^{-1}$, corresponding to a kinetic energy of 29.80 eV.

In our KS-SIC approach we constructed a spatially local, multiplicative exchange-correlation potential that is the same for all orbitals via the Optimized-Effective Potential (OEP) equation. A direct construction of the OEP is possible but numerically tedious for the SIC energy functional [9]. Here, this problem did not arise as we employed the generalized OEP (GOEP) equation for unitarily variant functionals [10]. The Krieger-Li-Iafrate (KLI) approximation to the OEP can fail badly for the SIC [9], but the generalized KLI approximation has been shown to be an excellent approximation to the GOEP [10] and was used here. For the localizing transformation we employed the Foster-Boys procedure; an energy minimizing transformation leads to negligible differences for the observables discussed here. We solved the self-consistent SIC and GGA equations on equidistant real space grids with a grid spacing of 0.3 Bohr and a spherical boundary of 21 Bohr (Pentacene and PTCDA) or 16 Bohr (NTCDA) using the Bayreuth version [10, 11] of the PARSEC electronic structure package [12]. Molecular geometries were obtained by minimizing the total energy using the B3LYP functional as implemented in the Turbomole program suite [13, 14]. The observables discussed in this work do not change significantly when

PBE geometries are used instead of B3LYP geometries. Hartree-Fock orbitals were obtained using Turbomole.

We verified that it is not only the orbitals from the PBE GGA that do not match the ARPES data for NTCDA and PTCDA, but that also other local or semi-local functionals show similar discrepancies. For example, calculating the orbitals using the local density approximation in exactly the same parameterization from which we constructed the SIC leads to orbital shapes that are nearly identical to the PBE ones. This shows that it is indeed the self-interaction freeness that is decisive for the correct prediction of the orbitals and not the (semi-)local parameterization.

-
- [1] F. Reinert et al., Phys. Rev. B **63**, 115415 (2001).
 - [2] R. Fink et al., Phys. Rev. B **60**, 2818 (1999).
 - [3] A. Bendounan et al., Surface Science **601**, 4013 (2007).
 - [4] A. Schöll et al., Science **329**, 303 (2010).
 - [5] J. Ziroff et al., Phys. Rev. Lett. **104**, 233004 (2010).
 - [6] K. Glöckler et al., Surface Science **405**, 1 (1998).
 - [7] Y. Zou et al., Surface Science **600**, 1240 (2006).
 - [8] P. Puschnig et al., Science **326**, 702 (2009).
 - [9] T. Körzdörfer, M. Mundt, and S. Kümmel, Phys. Rev. Lett. **100**, 133004 (2008).
 - [10] T. Körzdörfer, M. Mundt, and S. Kümmel, J. Chem. Phys. **129**, 014110 (2008).
 - [11] M. Mundt et al., Phys. Rev. B **73**, 205407 (2006).
 - [12] L. Kronik et al., Phys. Status Solidi B **243**, 1063 (2006).
 - [13] R. Ahlrichs et al., Chem. Phys. Lett. **162**, 165 (1989).
 - [14] TURBOMOLE V5.10 2008, a development of University of Karlsruhe and Forschungszentrum Karlsruhe GmbH, 1989-2007, TURBOMOLE GmbH, since 2007; available from <http://www.turbomole.com>.

Publication 1

Publ.1

Angle resolved photoemission from organic semiconductors: orbital imaging beyond the molecular orbital interpretation

New Journal of Physics **16**, 103005 (2014)

M. Dauth¹, M Wiessner², V. Feyer³, A. Schöll², P. Puschnig⁴, F. Reinert² and
S. Kümmel¹

¹ Theoretical Physics IV, University of Bayreuth, D-95440 Bayreuth, Germany

² Experimental Physics 7 and Röntgen Research Center for Complex Material Systems (RCCM),
University of Würzburg, D-97074 Würzburg, Germany

³ Peter Grünberg Institute (PGI-6) and Jülich Aachen Research Alliance, Fundamentals of Future
Information Technology, Research Center Jülich, D-52425 Jülich, Germany

⁴ Institute of Physics, NAWI Graz, University of Graz, Universitätsplatz 5, A-8010 Graz, Austria

My contribution

I performed all calculations presented in the manuscript, implemented the algorithms to compute the Dyson orbitals, and wrote a first draft of the manuscript. S. Kümmel and myself lead the scientific discussion.

Publ.1

Angle resolved photoemission from organic semiconductors: orbital imaging beyond the molecular orbital interpretation

M Dauth¹, M Wiessner², V Feyer³, A Schöll², P Puschnig⁴, F Reinert² and S Kümmel¹

¹Theoretical Physics IV, University of Bayreuth, D-95440 Bayreuth, Germany

²Experimental Physics 7 and Röntgen Research Center for Complex Material Systems (RCCM), University of Würzburg, D-97074 Würzburg, Germany

³Peter Grünberg Institute (PGI-6) and Jülich Aachen Research Alliance, Fundamentals of Future Information Technology, Research Center Jülich, D-52425 Jülich, Germany

⁴Institute of Physics, NAWI Graz, University of Graz, Universitätsplatz 5, A-8010 Graz, Austria
E-mail: stephan.kuemmel@uni-bayreuth.de

Received 14 May 2014, revised 25 July 2014

Accepted for publication 11 September 2014

Published 7 October 2014

New Journal of Physics **16** (2014) 103005

doi:[10.1088/1367-2630/16/10/103005](https://doi.org/10.1088/1367-2630/16/10/103005)


Abstract

Fascinating pictures that can be interpreted as showing molecular orbitals have been obtained with various imaging techniques. Among these, angle resolved photoemission spectroscopy (ARPES) has emerged as a particularly powerful method. Orbital images have been used to underline the physical credibility of the molecular orbital concept. However, from the theory of the photoemission process it is evident that imaging experiments do not show molecular orbitals, but Dyson orbitals. The latter are not eigenstates of a single-particle Hamiltonian and thus do not fit into the usual simple interpretation of electronic structure in terms of molecular orbitals. In a combined theoretical and experimental study we thus check whether a Dyson-orbital and a molecular-orbital based interpretation of ARPES lead to differences that are relevant on the experimentally observable scale. We discuss a scheme that allows for approximately calculating Dyson orbitals with moderate computational effort. Electronic relaxation is taken into account explicitly. The comparison reveals that while molecular orbitals are frequently good approximations to Dyson orbitals, a detailed understanding of



Content from this work may be used under the terms of the [Creative Commons Attribution 3.0 licence](https://creativecommons.org/licenses/by/3.0/). Any further distribution of this work must maintain attribution to the author(s) and the title of the work, journal citation and DOI.

photoemission intensities may require one to go beyond the molecular orbital picture. In particular we clearly observe signatures of the Dyson-orbital character for an adsorbed semiconductor molecule in ARPES spectra when these are recorded over a larger momentum range than in earlier experiments.

 Online supplementary data available from stacks.iop.org/njp/16/103005/mmedia

Keywords: orbital imaging, photoemission spectroscopy, density functional theory, Dyson orbitals, NTCDA, PTCDA, ARPES

1. Angle resolved photoemission from molecules

The imaging of molecular orbitals has attracted great attention in recent years in rather different areas of physics [1–10]. This interest is fueled by at least two motivations. First, images that in some sense reflect quantum mechanical probability densities are fascinating from a quantum mechanical, many-body point of view, because they have been interpreted to visualize ‘a single electron’ in a many-electron system, i.e. an object whose observability may be questioned on fundamental grounds. Second, the molecular orbital picture, although approximate, has proved invaluable for understanding many-particle systems and is frequently and successfully used in particular in the field of organic semiconductors. Having tools to visualize, e.g. the highest-occupied and lowest-unoccupied molecular orbitals (HOMO and LUMO, respectively) that are frequently employed for understanding charge transfer and interface effects helps our understanding of this important class of materials [3, 7]. Angle resolved photoemission spectroscopy (ARPES) has emerged as one of the most powerful techniques in the field [3, 6–12] as it allows for studying large molecules in setups of technological relevance, e.g. adsorbed and interacting with a substrate. The question of what actually is visualized in molecular orbital (density) imaging experiments has been discussed from several perspectives [8, 13, 14] and the power of the molecular orbital interpretation of ARPES experiments has been impressively demonstrated. In this work, however, we take one step further and demonstrate in a combined theoretical and experimental study that in certain cases the interpretation of ARPES experiments for molecular semiconductors may require one to go beyond the single molecular orbital point of view. To demonstrate this, we review in section 2 the theory of the photoemission process which reveals the Dyson orbitals as the fundamental quantities for describing photoemission. In section 3 we present an approximate way of calculating Dyson orbitals that combines computational feasibility with predictive power for the qualitative features of ARPES intensity patterns. A decisive aspect of our approach is that it explicitly takes into account electronic relaxation effects, i.e. the changes in electronic structure that occur when one electron leaves the system. The latter effect is typically neglected in the molecular orbital interpretation of photoemission data. We discuss the approximations that are made in our approach and show how it can be implemented as a straightforward extension of existing electronic structure theory methods. Finally, we discuss how our calculated Dyson orbitals compare to orbital imaging data for the N₂ molecule and the molecular semiconductors pentacene, 3,4,9,10-perylene-tetracarboxylic-dianhydride (PTCDA), and 1,4,5,8-

naphthalene-tetracarboxylic-dianhydride (NTCDA). We show that imaging experiments resolve the differences between molecular orbitals and Dyson orbitals. This demonstrates that even for organic semiconductor molecules for which the molecular orbital picture is frequently employed, a detailed understanding of ARPES experiments can require one to go beyond the molecular orbital point of view.

2. Photoemission and the Dyson orbitals

To set the ground for explaining our approach, we first review the basic equations from which the Dyson orbital emerges as the fundamental concept for interpreting vertical (in the Franck–Condon sense) photoemission intensities [15–18]. In doing so we explicitly point out the steps in which approximations are made.

According to Fermi’s golden rule the probability for a transition from an initial N -particle state Ψ_{in}^N to a final state Ψ_{f}^N that is triggered by a photon of energy $\hbar\omega$ of an electromagnetic field that is described by a vector potential \mathbf{A} is given by

$$W_{\text{in}\rightarrow\text{f}} \propto \left| \left\langle \Psi_{\text{f}}^N \left| \mathbf{A} \cdot \mathbf{P} \right| \Psi_{\text{in}}^N \right\rangle \right|^2 \delta(\hbar\omega + E_{\text{in}} - E_{\text{f}}). \quad (1)$$

Here, \mathbf{P} is the momentum operator, and E_{in} and E_{f} are initial and final state energy, respectively. This matrix element describes photoemission, i.e. the photoemission intensity is proportional to $W_{\text{in}\rightarrow\text{f}}$, if the final state is one in which an electron has been detached. We presume that the N -electron molecule is initially in its ground state $\Psi_{\text{in},0}^N$ with energy $E_{\text{in},0}$. In writing the final state one commonly makes a first approximation by assuming that the correlation between the emitted electron and the remaining ones can be neglected. Then, the final state can be approximated as an antisymmetrized product of the wavefunction $\gamma_{\mathbf{k}}(\mathbf{x})$ of the liberated electron, with momentum $\hbar\mathbf{k}$ and with $\mathbf{x} = (\mathbf{r}, \sigma)$ denoting spatial and spin degree of freedom, and the wavefunction $\Psi_I^{N-1}(\mathbf{x}_1, \dots, \mathbf{x}_{N-1})$, which is the I th eigenfunction of the $(N-1)$ -electron Hamiltonian of the ionized system. Note that for vertical photoemission, which we consider here, the $(N-1)$ -electron Hamiltonian contains the same nuclear coordinates as the N -electron Hamiltonian because nuclear relaxation is occurring on a significantly longer timescale. Thus, the final state wavefunction is written as

$$\begin{aligned} \Psi_{\text{f},I,\mathbf{k}}^N = (\mathbf{x}_1, \dots, \mathbf{x}_N) &= \sum_{i=1}^N \frac{(-1)^{i+1}}{\sqrt{N}} \Psi_I^{N-1}(\mathbf{x}_1, \dots, \mathbf{x}_{i-1}, \mathbf{x}_{i+1}, \dots, \mathbf{x}_N) \gamma_{\mathbf{k}}(\mathbf{x}_i) \\ &= \sum_{i=1}^N \frac{(-1)^{i+1}}{\sqrt{N}} \Psi_I^{N-1}(\{\mathbf{x} \setminus i\}) \gamma_{\mathbf{k}}(\mathbf{x}_i). \end{aligned} \quad (2)$$

The abbreviation $\{\mathbf{x} \setminus i\}$ denotes the set of N coordinates from which \mathbf{x}_i has been excluded. The energy of this final state is $E_I + E_{\text{kin}}$, where the first term is given by the expectation value of the $N-1$ electron Hamiltonian of the ionized system taken with Ψ_I^{N-1} , and the second term is the kinetic energy of the emitted electron. Thus

$$W_{\text{in}\rightarrow\text{f}} \propto \left| \left\langle \Psi_{\text{f},I,\mathbf{k}}^N \left| \mathbf{A} \cdot \mathbf{P} \right| \Psi_{\text{in},0}^N \right\rangle \right|^2 \delta(\hbar\omega + E_{\text{in},0} - E_I - E_{\text{kin}}), \quad (3)$$

with $\mathbf{A} \cdot \mathbf{P} = \sum_{j=1}^N \mathbf{A} \cdot \mathbf{p}_j(\mathbf{x}_j)$. Making a second approximation by assuming that \mathbf{A} is constant in space, one can write the matrix element as

$$\begin{aligned}
& \langle \Psi_{f,I,\mathbf{k}}^N \mid \mathbf{A} \cdot \mathbf{P} \mid \Psi_{in,0}^N \rangle \\
&= \sum_{j=1}^N \sum_{i=1}^N \frac{(-1)^{i+1}}{\sqrt{N}} \langle \Psi_I^{N-1}(\{\mathbf{x} \setminus i\}) \gamma_{\mathbf{k}}(\mathbf{x}_i) \mid \mathbf{A} \cdot \mathbf{p}_j(\mathbf{x}_j) \mid \Psi_{in,0}^N(\{\mathbf{x}\}) \rangle \\
&= \sum_{\substack{i,j=1 \\ i \neq j}}^N \frac{(-1)^{i+1}}{\sqrt{N}} \int d^3\{\mathbf{x} \setminus i\} \Psi_I^{N-1*}(\{\mathbf{x} \setminus i\}) \mathbf{A} \cdot \mathbf{p}_j(\mathbf{x}_j) \left[\int d^3x_i \gamma_{\mathbf{k}}^*(\mathbf{x}_i) \Psi_{in,0}^N(\{\mathbf{x}\}) \right] \\
&\quad + \sum_{\substack{i,j=1 \\ i=j}}^N \frac{(-1)^{i+1}}{\sqrt{N}} \int d^3\{\mathbf{x}\} \Psi_I^{N-1*}(\{\mathbf{x} \setminus i\}) \gamma_{\mathbf{k}}^*(\mathbf{x}_i) \mathbf{A} \cdot \mathbf{p}_j(\mathbf{x}_j) \Psi_{in,0}^N(\{\mathbf{x}\}). \tag{4}
\end{aligned}$$

In the second step we split the sum into the direct term $i = j$ and the remainder $i \neq j$. Photoemission results from the direct term because in this expression the perturbation only acts on the liberated electron. The term with $i \neq j$ is responsible for other effects, e.g. Auger transitions [16], and will not be considered in the following—which is the third approximation. The transition matrix element can then approximately be written as

$$\begin{aligned}
& \langle \Psi_{f,I,\mathbf{k}}^N \mid \mathbf{A} \cdot \mathbf{P} \mid \Psi_{in,0}^N \rangle \\
&= \sum_{\substack{i,j=1 \\ i=j}}^N \frac{(-1)^{i+1}}{\sqrt{N}} \int d^3\{\mathbf{x}\} \Psi_I^{N-1*}(\{\mathbf{x} \setminus i\}) \gamma_{\mathbf{k}}^*(\mathbf{x}_i) \mathbf{A} \cdot \mathbf{p}_j(\mathbf{x}_j) \Psi_{in,0}^N(\{\mathbf{x}\}) \\
&= \sum_{i=1}^N \frac{(-1)^{i+1}}{N} \int d^3x_i \gamma_{\mathbf{k}}^*(\mathbf{x}_i) \mathbf{A} \cdot \mathbf{p}_i(\mathbf{x}_i) \underbrace{\left[\sqrt{N} \int d^3\{\mathbf{x} \setminus i\} \Psi_I^{N-1*}(\{\mathbf{x} \setminus i\}) \Psi_{in,0}^N(\{\mathbf{x}\}) \right]}_{:= d_I(\mathbf{x}_i)}. \tag{5}
\end{aligned}$$

This naturally leads to the definition

$$d_I(\mathbf{x}_i) = \sqrt{N} \int d^3\{\mathbf{x} \setminus i\} \Psi_I^{N-1*}(\{\mathbf{x} \setminus i\}) \Psi_{in,0}^N(\{\mathbf{x}\}) \tag{6}$$

of the I th Dyson orbital d_I . It is the decisive concept for the present work. With the Dyson orbital, the many particle matrix element can be written in the form of a single-particle matrix element

$$\langle \Psi_{f,I,\mathbf{k}}^N \mid \mathbf{A} \cdot \mathbf{P} \mid \Psi_{in,0}^N \rangle = \sum_{i=1}^N \frac{(-1)^{i+1}}{N} \int d^3x_i \gamma_{\mathbf{k}}^*(\mathbf{x}_i) \mathbf{A} \cdot \mathbf{p}_i(\mathbf{x}_i) d_I(\mathbf{x}_i). \tag{7}$$

By defining $\mathbf{x} = \mathbf{x}_N$ and using the relation

$$d_I(\mathbf{x}) := d_I(\mathbf{x}_N) = (-1)^{N-i} d_I(\mathbf{x}_i), \tag{8}$$

which follows directly from the antisymmetric properties of the wavefunctions, one can simplify the matrix element to find

$$\left| \langle \Psi_{f,I,\mathbf{k}}^N \mid \mathbf{A} \cdot \mathbf{P} \mid \Psi_{in,0}^N \rangle \right| = \left| \int d^3x \gamma_{\mathbf{k}}^*(\mathbf{x}) \mathbf{A} \cdot \mathbf{p}(\mathbf{x}) d_I(\mathbf{x}) \right|. \tag{9}$$

For further evaluation of the matrix element we need to specify the final state of the emitted electron, $\gamma_{\mathbf{k}}$. With the assumption that this is a plane-wave, i.e. assuming that the emitted electron is completely free and not affected by the remaining molecule's potential (which is the

fourth approximation), one obtains a transparent and charmingly simple result: inserting $\gamma_{\mathbf{k}} \propto \exp(i\mathbf{k}\mathbf{r})$ into the matrix element and Fermi's golden rule, respectively, and letting the momentum operator act on the plane wave, the probability of finding an emitted electron with momentum $\hbar\mathbf{k}$ becomes proportional to the Fourier transform of the Dyson orbital

$$W_{\text{in} \rightarrow \text{f}} \propto |\mathbf{A} \cdot \mathbf{k}|^2 |d_I(\mathbf{k})|_{|\mathbf{k}|=\text{const}}^2. \quad (10)$$

The plane wave's wave-vector, i.e. the emitted electron's momentum, follows from the energy conservation law

$$|\mathbf{k}| = \sqrt{\frac{2m}{\hbar} (\hbar\omega + E_{\text{in},0} - E_I)}. \quad (11)$$

Equation (10) shows that, apart from the light-polarization dependent scaling factor $|\mathbf{A} \cdot \mathbf{k}|^2$, the photoemission intensity is determined by the Fourier transform of the Dyson orbital. This opens a fascinating interpretation of angular resolved photoemission experiments: the ARPES intensity maps a (hemi)spherical cut [6] through the momentum representation of the Dyson orbital, or more precisely, through its absolute value, with the radius of the cut being determined by the kinetic energy of the emitted electron via equation (11). As the conditions for the validity of the four approximations that were mentioned in the course of the derivation are usually well fulfilled, ARPES experiments can be interpreted as visualizing Dyson orbitals. However, from the perspective of the above reviewed derivation the question 'When and why can molecular orbitals be observed?', which is underlying imaging experiments, can be phrased more precisely in the form 'It is plausible that Dyson orbitals can be observed, but when and why are Dyson orbitals close to molecular orbitals?' In the following we take a closer look at this question and give some answers.

3. Approximate Dyson orbitals from DFT

The most straightforward relation between Dyson orbitals and molecular orbitals is to identify one with the other. Within this approach, which we call the 'molecular orbital interpretation' or 'single orbital picture' of photoemission, the i th Dyson orbital (i.e. the Dyson orbital corresponding to the i th ionization potential) is identified with the molecular orbital $\varphi_i(\mathbf{x})$ corresponding to the i th eigenvalue

$$d_i(\mathbf{x}) \approx \varphi_i(\mathbf{x}). \quad (12)$$

In Hartree–Fock (HF) theory, Koopmans' theorem and its complete neglect of correlation and electronic relaxation build a formal bridge, but the accuracy of HF orbitals and eigenvalues in practice is very limited [19–21]. It has been argued that the identification of DFT orbitals with Dyson orbitals can be much more accurate because of the inclusion of correlation and the formal similarity between the Dyson equation and the Kohn–Sham (KS) or generalized KS equation [15, 22, 23]. Whether the KS or the generalized KS approach are to be preferred in the context of photoemission can be viewed from different perspectives. On the one hand, if one is interested in eigenvalues that well map ionization potentials and electron affinities, the generalized KS approach has benefits [21, 23]. On the other hand it has been stressed that the KS orbitals are more physical than the generalized KS orbitals [20], and exact KS eigenvalues have been shown to be excellent approximations to the ionization potentials of upper valence

electrons [19]. We will show below that in our present work it is not the difference between KS and generalized KS theory (which we both use here) that is decisive, but the quality of the approximation used for the exchange-correlation (xc) potential. Systems in which all orbitals are delocalized on similar length scales [24, 25] can be well described by semi-local functionals [6, 9]. For systems with a more complicated electronic structure, semi-local functionals and global hybrid functionals can lead to a distorted spectrum, whereas a self-interaction correction carried out in the KS approach [26] has been shown to yield KS orbitals that well reproduce ARPES experiments also in such situations [8]. However, despite these successes it must be kept in mind that even when the exact xc potential could be used, the identification between KS orbitals and Dyson orbitals remains approximate and cannot include exactly all the physical effects that play a role in ionization [23, 27, 28].

An inherent limitation of the single orbital picture of photoemission is the assumption that the only change in the electronic structure of a molecule upon photoionization is the depopulation of just one specific orbital. The state of the remaining, positively charged ion is assumed to be equal or at least very similar to the initial state except for the emptied orbital. This neglect of electronic relaxation, i.e. neglecting that the remaining electrons restructure once one electron has been removed, is to be questioned for typical molecular systems. In the following we explicitly go beyond the ‘one-orbital emission and no relaxation’ picture and study the first photoionization event, i.e. the transition from the ground state of the initial molecule to the ground state of the singly ionized system, from a many-particle perspective. We focus on the first transition because the first ionization potential is often the most relevant one in practical applications. In the single particle picture it corresponds to the view of ‘an electron is emitted from the HOMO’. A formal reason for why it is natural to focus on the first transition is that the HOMO plays a special role in DFT, because its eigenvalue can rigorously be related to the ionization energy [29].

The starting point for our considerations is the above reviewed definition of the Dyson orbital as the overlap of the initial and final molecular ground-state wavefunctions, equations (6), (8). Using this definition for calculating the Dyson orbital of molecular semiconductors in practice requires one to face two challenges.

The first is that one needs to calculate the N - and $(N-1)$ -electron wavefunctions, respectively. For molecules with many tens to hundreds of electrons, calculating an explicitly correlated wavefunction is not just a very demanding task—it is prohibitively expensive. Therefore, we here focus on the alternative approach of approximating the true wavefunction Ψ by a single Slater determinant Φ . This is possibly a very serious approximation. However, for the molecules that we are interested in it is typically justified because they are dominated not by static but by dynamical correlation and their wavefunction is predominantly of single-reference character. In other words, when written as a configuration interaction expansion, the fully correlated many-body wavefunction has one leading, dominating determinant with small corrections from many other determinants. The paradigm one-determinant approach of HF theory may still be inaccurate in such a situation. However, a KS Slater determinant, i.e. the Slater determinant built from the occupied orbitals that are obtained after converging a self-consistent KS calculation, is often an acceptable approximation to the true wavefunction. While there is no guarantee, even if the exact xc functional were known, that the KS determinant approximates the true wavefunction well, experience shows that for systems that are not strongly correlated this is very often the case [30]. This finding can be rationalized by the observation that the KS determinant is density-optimal instead of energy optimal [31, 32].

The second challenge is the calculation of the overlap integral between the N - and the $(N-1)$ -electron wavefunction according to equation (6). We address it by expanding the N electron Slater determinant in minors [16]

$$\Phi_{\text{in}}^N \{\mathbf{x}\} = \frac{1}{\sqrt{N}} \sum_{i=1}^N \varphi_{\text{in},i}(\mathbf{x}) (-1)^{i+N} \Phi_{\text{in},i}^{N-1} \{\mathbf{x} \setminus N\}, \quad (13)$$

i.e. decompose it into a sum of Slater determinants build up by $N-1$ orbitals. Each Slater determinant is multiplied by the single orbital $\varphi_{\text{in},i}$ that depends on the remaining coordinate. Thereby, the Dyson orbital can be rewritten as

$$\begin{aligned} d(\mathbf{x}) &= \sum_{i=1}^N \varphi_{\text{in},i}(\mathbf{x}) \frac{1}{\sqrt{N}} (-1)^{i+N} \left\langle \Phi_{\text{f}}^{N-1} \{\mathbf{x} \setminus N\} \middle| \Phi_{\text{in},i}^{N-1} \{\mathbf{x} \setminus N\} \right\rangle \\ &= \sum_{i=1}^N \varphi_{\text{in},i}(\mathbf{x}) w_i. \end{aligned} \quad (14)$$

This shows explicitly that the Dyson orbital does not correspond to a single-particle orbital, but is a coherent superposition of all N occupied orbitals that build the initial Slater determinant, weighted by w_i . The weighting factors are given by the overlaps of $(N-1)$ -particle determinants. The calculation of the w_i is mostly a technical issue. We delineate the procedure in appendix A.

Central for our work is the choice of orbitals that we use to build up the initial and final state Slater determinants. The crudest approximation would be to use a simple Koopmans like picture where relaxation effects are completely neglected. The only change of the molecule's electronic system upon ionization would then be that one initially occupied orbital is unoccupied after the ionization process. Hence, one would use the same set of orbitals to build the initial and final state Slater determinants. The expansion in minors of the initial state according to equation (13) would lead to one contribution where the single orbital is equal to the depopulated orbital and the $N-1$ determinant from the corresponding expansion term would be equal to the unrelaxed ionized state. The overlap between the two latter determinants would therefore be one, whereas all other overlaps respectively weighting factors would be zero due to orthogonality. As a consequence the Dyson orbital would be equal to the emptied orbital and one would return to the single orbital picture.

Our aim is, however, to treat electronic relaxation explicitly in order to check how large its impact on vertical photoemission and orbital interpretation is, respectively. Therefore, we perform two separate self-consistent calculations, one for the ionized and one for the initial system, while keeping the molecule's nuclear geometry fixed. In this way we find in addition to the initial orbitals a second set of orbitals—non-orthogonal to the first—representing the ground state electron density that minimizes the total energy of the positively charged molecule. Having two nonorthogonal orbital sets $\varphi_{\text{in},n}$ and $\varphi_{\text{f},m}$ in general leads to non-vanishing overlaps in equation (13), i.e. weighting factors w_i that are not restricted to zero or one. Hence, relaxation effects can lead to more than one molecular orbital contributing to the Dyson orbital. How much the structure of the Dyson orbital differs from the one of a single molecular orbital therefore depends on how strongly electronic relaxation influences the ionization process, and on how large the differences between the different molecular orbitals are. A detailed description of the calculation of the overlaps with two different sets of orbitals is given in appendix A.

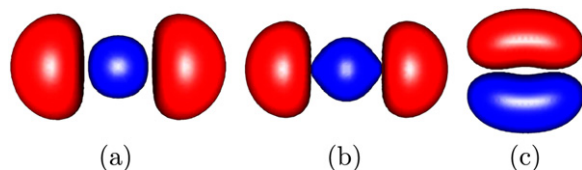


Figure 1. Isosurface plots of the relaxed Slater determinant Dyson orbital constructed based on (a) a KS-SIC calculation and (b) a HF calculation for the N_2 molecule. (c) One of the two degenerate HF π -HOMOs that would correspond to a Dyson orbital in the unrelaxed, molecular orbital interpretation.

4. Photoemission from the N_2 molecule

As a first test for the relaxed Slater determinant approach (RSA) that we introduced in the previous section, we chose the nitrogen molecule because here the spatial structure of the Dyson orbital is known from higher harmonic generation (HHG) experiments [1]. As a first step we examine the influence that the choice of the DFT xc-functional has on the structure of the RSA Dyson orbital. Therefore, we have performed calculations with the widely used semilocal Perdew–Burke–Ernzerhof generalized-gradient-approximation (PBE-GGA) [33] and the Becke three-parameter Lee–Yang–Parr (B3LYP) [34–36] hybrid as a representative for a non-local generalized KS approach. In addition we used a self-interaction-correction (SIC) KS approach based on the generalized optimized effective potential (KS-SIC) [26, 37]. In all cases the resulting RSA Dyson orbitals have an almost indistinguishable spatial structure, displayed in figure 1(a), and this is in very good agreement with the orbital that has been experimentally reconstructed by Itatani *et al* [1]. The Dyson orbital in each case is mainly dominated by the corresponding σ -HOMO, $d(x) \approx \varphi_{\text{HOMO}}^\sigma(x)$. All other orbital contributions are at least 30 times smaller.

It is quite instructive to investigate the situation with HF theory as the single-particle starting point. In contrast to the DFT results described above, HF theory leads to a degenerate highest eigenvalue which is associated with two π -shaped orbitals, see figure 1(c). This implies that the unrelaxed approximation, i.e. the molecular orbital interpretation in the HF approximation, leads to a Dyson orbital that is a superposition of these orbitals, in disagreement with the experiment. However, when one builds the final state from relaxed HF orbitals, i.e. uses a HF-based RSA, one finds a Dyson orbital that solely corresponds to the HF σ -HOMO-1, $d(x) \approx \varphi_{\text{HOMO-1}}^\sigma$ (for a detailed explanation see appendix A). It is shown in figure 1(b) and, again, reflects all features of the orbital reconstructed by HHG. Therefore, a HF-based calculation leads to dramatically different results depending on whether electronic relaxation effects are taken into account or not. This failure of the unrelaxed HF approximation of course is not a major surprise since correlation effects are known to be important in multiple bonds [38], and HF theory for N_2 leads to the wrong energetic ordering of the HF HOMO and HOMO-1.

In summary, this first, small-molecule example demonstrates two things. First, treating relaxation effects can be decisive for a correct description of photoionization in terms of orbitals. Second, it points out a strength of the RSA. Equation (14) shows that the RSA Dyson orbital only depends on the overlaps w_i . Therefore, as long as two different single particle calculations, e.g. a HF and a DFT one, lead to the same set of occupied orbitals, the corresponding DFT and HF RSA Dyson orbital will look the same, i.e. are independent of the

internal energetic orbital ordering. The question of having the correct orbital ordering that can complicate ARPES interpretation based on molecular orbitals [6, 8, 9] thus becomes immaterial or at least mitigated.

5. Photoemission from organic semiconductor molecules

Next, we turn to orbitals as reconstructed by ARPES experiments. In particular, three π -conjugated model molecular semiconductors have been intensively studied in recent years, namely pentacene, PTCDA and NTCDA [3, 6–10, 39–41]. Therefore, we here focus on these systems.

Beginning with the simplest case, pentacene, we know that the molecular orbital ordering hardly depends on the used xc-functional [21], i.e. all functionals yield very similar HOMOs. (The corresponding momentum maps are compared to each other in detail in [8].) It is a reassuring finding that it also does not matter which approach we use as a basis for the RSA calculation. For the above mentioned functionals and HF, the RSA Dyson orbital is equivalent to the HOMO

$$d^{\text{RSA}}(\mathbf{x}) \approx 0.99 \cdot \varphi_{\text{HOMO}}(\mathbf{x}). \quad (15)$$

This simplicity in the analysis is due to pentacene’s simple electronic structure: with all frontier orbitals being π -orbitals delocalized on the same length scale, the ordering is not sensitive to the used xc-functional, and ionization hardly changes the spatial structure of the orbitals. The impressive resemblance of the pentacene HOMO momentum space map to the corresponding measured ARPES intensity has been discussed in detail in [6].

For the more complex molecule PTCDA the situation is quite similar. Again all approaches yield the same orbital, i.e. the obtained Dyson orbital is very close to the HOMO, and relation (15) holds in this case too. In appendix B, in particular figure A.1, we show in detail that the RSA Dyson orbital as well as the HOMO momentum space maps are in good agreement with experimental ARPES data.

However, the situation gets more involved for NTCDA, which is the main focus of the present investigation. In contrast to pentacene, the outer valence orbitals of NTCDA are alternately of π - or σ -character. Their ordering is very much influenced by which xc-functional is used. An important aspect in explaining this finding is the self-interaction error whose magnitude strongly depends on the orbital character [24]. We see this effect in particular for the HOMO. Whereas B3LYP, HF and KS-SIC predict a π -HOMO, PBE shows a σ -HOMO. The two orbital types π and σ show distinct momentum space maps as displayed in figure 2. The π -orbital has its four main features at $k_x \approx \pm 1.2 \text{ \AA}^{-1}$ and $k_y \approx \pm 0.8 \text{ \AA}^{-1}$. The σ -orbital on the other hand primarily has high intensities at higher $|\mathbf{k}|$ -values. This is a consequence of the nodal structure of the probability density in real space: the σ -orbital’s nodes are more closely spaced than those of the π -orbital.

Again we want to contrast the molecular orbital interpretation with the RSA, where PBE is particularly interesting, as it is the odd one out. With the HF N_2 case in mind our hope is that the RSA approach can compensate for shortcomings of the underlying single-particle theory. Indeed, the RSA based on PBE yields a Dyson orbital that differs from the PBE HOMO. It is a superposition of the PBE HOMO and the HOMO-1, in detail

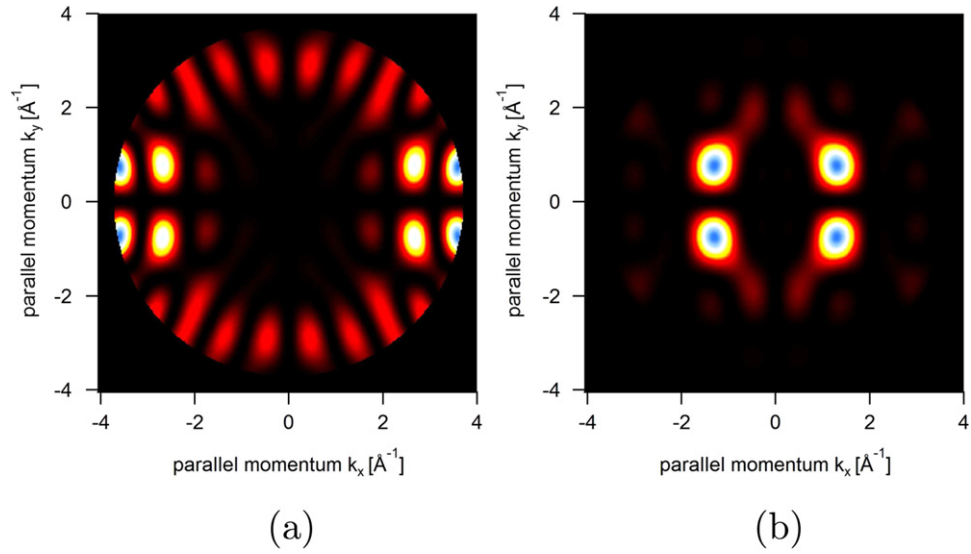


Figure 2. Momentum space maps for the NTCDA molecule within the molecular orbital interpretation. The molecular orbitals are calculated with the PBE xc-functional where (a) shows the σ -HOMO and (b) the π -HOMO-1. The momentum space maps are evaluated at a kinetic photoelectron energy of $E_k = 52.6$ eV and with k_x being parallel to the long and k_y to the short molecular axis.

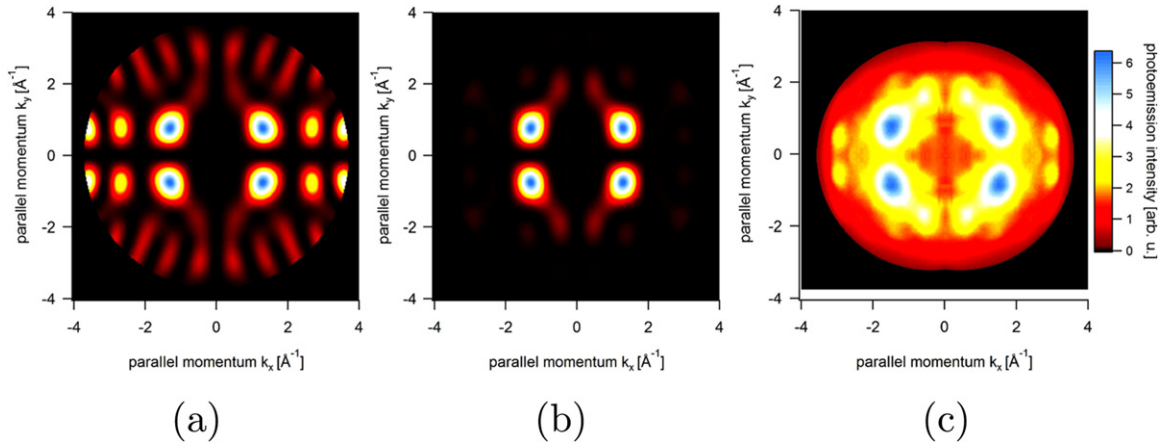


Figure 3. Momentum space maps for the NTCDA molecule: (a) RSA Dyson orbital based on PBE, (b) RSA Dyson orbital based on KS-SIC and (c) the corresponding measured ARPES signal at a binding energy of $E_B = 2.4$ eV, shown as the sum of left- and righthanded circular polarized light at 55 eV photon energy.

$$d^{\text{PBE}}(\mathbf{x}) \approx 0.76 \cdot \varphi_{\text{HOMO}}^{\sigma}(\mathbf{x}) - 0.63 \cdot \varphi_{\text{HOMO}-1}^{\pi}(\mathbf{x}). \quad (16)$$

The momentum space map of the PBE-based RSA Dyson orbital (figure 3(a)) shows the four characteristic peaks at $k_x \approx \pm 1.2 \text{ \AA}^{-1}$ and $k_y \approx \pm 0.8 \text{ \AA}^{-1}$ that also the KS-SIC, B3LYP, and HF HOMO show. In addition, it inherits features of the σ -orbital. Thus, the RSA as hoped for leads to a more unified prediction of which intensity pattern should be expected for the first

photoemission process. However, for NTCDA the ‘unification’ is not as complete as for, e.g. the above discussed case of N₂. This becomes visible when one builds the RSA Dyson orbital starting from a KS-SIC calculation. In this case the Dyson orbital is mostly determined by the KS-SIC π -HOMO

$$d^{\text{KS-SIC}}(\mathbf{x}) \approx \varphi_{\text{HOMO}}^{\pi}(\mathbf{x}). \quad (17)$$

Also in the KS-SIC Dyson orbital there is more than one contribution, but the weighting factor for the HOMO is $w_{\text{HOMO}} = 0.98$, whereas the next contribution (HOMO-16) comes with a much smaller weight of $w_{\text{HOMO-16}} = 0.06$, and the intensity scales with the square of the weighting factors. Summarizing the results obtained for NTCDA, we can therefore say that for the momentum range $k \lesssim 2.5 \text{ \AA}^{-1}$ that had been studied in previous ARPES experiments [8], the prediction from the two RSA Dyson orbitals (the PBE and the KS-SIC one) are very similar, agree with the KS-SIC HOMO, and match well the experimentally observed pattern in the spirit of the orbital density reconstruction [6] interpretation. However, for larger momenta the different theoretical approaches lead to different predictions.

Therefore, we have performed further ARPES experiments (see appendix C for details). Measurements were performed at a kinetic photoelectron energy of $E_{\text{kin}} = 52.6 \text{ eV}$, allowing us to display $|\mathbf{k}|$ -values up to $|\mathbf{k}| \leq 3.7 \text{ \AA}^{-1}$, i.e. compared to previous experiments we extended the observation range to larger momenta. For PTCDA and NTCDA the influence of the Ag substrate on the orbital which is the HOMO of the isolated molecules is small [7, 42]. The experimental pattern observed for the peak that traditionally has been associated with ‘the HOMO’ is depicted in figure 3(c). Comparing it to figure 2(a) shows without doubt that the measured intensity cannot be explained just by the PBE HOMO. The latter lacks the four peaks at $k_x \approx \pm 1.2 \text{ \AA}^{-1}$ and $k_y \approx \pm 0.8 \text{ \AA}^{-1}$ which in the experiment have the highest intensity. The most interesting observation, however, is that in addition to these four prominent features there are four additional peaks with lower intensity located at $k_x \approx \pm 3.1 \text{ \AA}^{-1}$ and $k_y \approx \pm 0.5 \text{ \AA}^{-1}$. From an experimental point of view there is no doubt that all of these features belong to the same ionization process, as their intensities occur uniformly in the same energy interval and well separated from other peaks.

Comparing to the RSA Dyson orbital in figure 3(a) shows that the PBE based RSA Dyson orbital clearly shows such features. In order to reveal them more clearly, we repeated the evaluation of the theoretical spectra and the experiment with horizontal light polarization (i.e. s-polarization). In this way high $|\mathbf{k}|$ -values are more accentuated. In our setup the NTCDA monolayer is aligned such that the polarization is parallel to the long molecular axis (in our notation defined as the x -axis). On the theoretical side this brings the polarization factor of equation (10) into play. With the vector potential being parallel to the x -axis, the relation of the Dyson orbitals to the measured spectra is thus augmented by the smooth, here k_x -dependent $|\mathbf{A}_x \cdot \mathbf{k}_x|^2$ factor, and becomes

$$W_{\text{in} \rightarrow \text{f}} \propto |\mathbf{A}_x \cdot \mathbf{k}_x|^2 |d(\mathbf{k})|_{|\mathbf{k}|=\text{const}}^2. \quad (18)$$

As a consequence features at large $|\mathbf{k}|$ -values that are not well visible in figures 3(a) and (b) can now be compared much better to the experimental data.

In figure 4 we display the ARPES intensity as measured with horizontal light polarization. The experimental data has been overlaid with the contours of the PBE Dyson orbital on the left hand side and with the ones from the KS-SIC Dyson orbital on the right hand side. Both Dyson

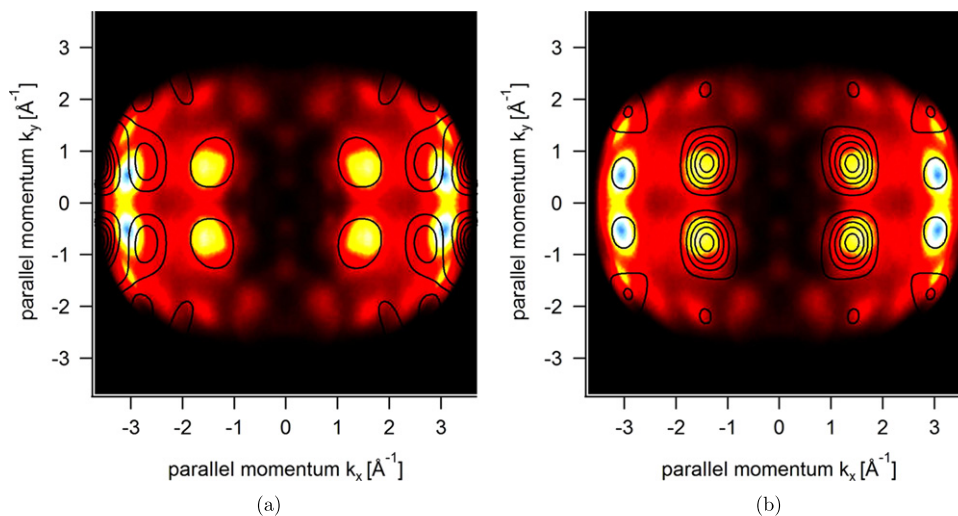


Figure 4. Both images show the measured ARPES intensity for NTCDA (interpreted as a momentum space map) at a binding energy of $E_B = 2.4$ eV with horizontal polarized light of $\hbar\omega = 55$ eV. The spectra are overlaid with the contours of the (a) RSA Dyson orbital based on PBE and (b) the KS-SIC RSA Dyson orbital. Both Dyson orbitals were therefore calculated with the horizontal polarization scaling factor.

orbitals show features at large $|\mathbf{k}|$. This in itself is a reassuring observation. There are, however, differences between the two calculations. First, in the PBE case the outer features emerge from the σ -orbital, whereas in KS-SIC they are purely attributed to the π -orbital. Second, there are differences in the relative intensities. For the PBE contour lines in figure 4(a) we see the trend that the intensity of the peaks increases with their position on the k_x -axis so that the features at high k_x are more apparent. This is in better agreement with the experiment than the relative intensities from the KS-SIC Dyson orbital. Third, however, there are also differences in the positions of the outer peaks, and in terms of these the RSA KS-SIC Dyson orbital is in better agreement with the experiment than the PBE one. For putting these findings into perspective one needs to be aware of additional issues. One of them is that higher $|\mathbf{k}|$ -values correspond to emission angles closer to the substrate. Thus, the interaction between the outgoing photo electron and the remaining system could be stronger and lead to larger inaccuracies within the plane wave approach. Another one is that for the high k_{\parallel} -values the slight misalignment of the crystals surface normal with respect to the optical axis of the photoemission electron microscope leads to different k_x - and k_y -ranges. Additionally, this leads to distortions of the k -image that can lead to a mismatch of the k_x -position of the emission peaks. We are therefore not able to make an unambiguous statement about which approach yields the better result. However, the overall picture that emerges from this study is consistent. It has been argued for a long time [43] that SIC eigenvalues can approximate *relaxed* ionization energies well. It thus appears natural that the SIC molecular orbitals can reflect effects which in another approach such as PBE must be included via explicit consideration of relaxation. The RSA Dyson orbital calculation for NTCDA amends the peaks at high $|\mathbf{k}|$ -values and as well captures the intensities at lower $|\mathbf{k}|$ that are completely missing in the molecular orbital interpretation of the PBE HOMO. Thus, the experimental data can be explained over the full range of measured electron momenta.

6. Conclusions

Motivated by ARPES experiments that can be interpreted as revealing orbital densities, we reviewed the theory of photoemission in which the Dyson orbitals, defined as the overlaps between N - and $(N - 1)$ -particle states, emerge as the relevant quantities. When Dyson orbitals are a priori approximated by single molecular orbitals the quality of the so predicted ARPES intensities can depend sensitively on which electronic structure method is used to calculate the molecular orbitals. We demonstrated that by approximating the initial and final molecular states by relaxed N - and $(N - 1)$ -electron Slater determinants, one achieves a description of the first photoemission process that is considerably less sensitive to the underlying single-particle picture and its orbital ordering. More importantly yet, this procedure allows for explicitly taking into account relaxation effects. ARPES experiments were done for the model organic semiconductors PTCDA and NTCDA covering a larger range of electron momenta than covered by previous experiments, and using variable light polarization. For PTCDA the RSA Dyson orbital approach leads to the same result as the molecular orbital approach and both are in agreement with the experimental data. For NTCDA the experiment reveals previously unobserved intensities at large electron momenta that cannot be explained based on molecular orbitals as obtained from, e.g. a usual GGA DFT calculation. The RSA Dyson orbitals show the additional intensities. Thus, ARPES experiments have reached an accuracy at which a simple molecular orbital interpretation may not be sufficient for explaining all of the observed features. The RSA Dyson orbitals discussed here provide a non-empirical and computationally relatively efficient approach for going beyond the molecular orbital interpretation of photoemission. Seen from a different angle, one can also argue that the present work gives further credibility to the concept of orbital imaging—as long as one keeps in mind that it is Dyson orbitals that are imaged.

Acknowledgments

We thank D Hauschild, J Alsmeier, and H Harutyunyan for support during beamtime at Elettra and acknowledge Elettra for providing good quality synchrotron light. SK and MD acknowledge support by Deutsche Forschungsgemeinschaft Graduiertenkolleg 1640 and the Bavarian State Ministry of Science, Research, and the Arts for the Collaborative Research Network Solar Technologies go Hybrid. AS and FR acknowledge support by the Bundesministerium für Bildung und Forschung (BMBF; Grant Nos. 05K10WW2 and 03SF0356B), and by the Deutsche Forschungsgemeinschaft (DFG; Grant Nos. GRK1221, SCHO-1260/4-1 and RE1469/9-1). PP acknowledges support from the Austrian Science Foundation (FWF) project P23190-N16. This publication was funded by the German Research Foundation (DFG) and the University of Bayreuth in the funding programme Open Access Publishing.

Appendix A. Calculating the weighting factors

We here explain the calculation of the weighting factors

$$w_i = \frac{1}{\sqrt{N}} (-1)^{i+N} \langle \Phi_f \{ \mathbf{x} \setminus N \} | \Phi_{\text{in},i} \{ \mathbf{x} \setminus N \} \rangle. \quad (\text{A.1})$$

The overlap of two Slater determinants with the same number of orbitals can be expressed as a determinant of overlap matrix elements between all single-particle orbitals

$$\langle \Phi_f \{ \mathbf{x} \setminus N \} | \Phi_{in} \{ \mathbf{x} \setminus N \} \rangle = \det \left[\langle \varphi_{f,n} | \varphi_{in,m} \rangle \right]. \quad (\text{A.2})$$

This leads to the following expression for the weighting factor

$$w_i = \frac{1}{\sqrt{N}} (-1)^{i+N} \det \left[\langle \varphi_{f,n} | \varphi_{in,m,m \neq i} \rangle \right]. \quad (\text{A.3})$$

Looking again at the expansion for the initial ground state

$$\Phi_{in} \{ \mathbf{x} \} = \frac{1}{\sqrt{N}} \sum_{i=1}^N \varphi_{in,i}(\mathbf{x}) (-1)^{i+N} \Phi_{in,i} \{ \mathbf{x} \setminus N \}, \quad (\text{A.4})$$

the index i implies that the reduced initial state Slater determinant $\Phi_i \{ \mathbf{x} \setminus N \}$ does not contain orbital $\varphi_{in,i}$. Therefore, this orbital is not involved in the calculation of the weighting factors w_i and in the $(N-1)^2$ overlap matrix elements of equation (A.3), respectively. If both orbital sets do not differ much, then the single particle overlaps will be close to either one or zero. Consequently, only the matrix element of the one reduced Slater determinant which contains the orbitals that are similar to the orbitals in the ionized determinant will be close to one. When there is only little relaxation the Dyson orbital is dominated by the depopulated orbital. Strong relaxation leads to two clearly different orbital sets and several non-vanishing weighting factors.

With this we can also elucidate why the HF N_2 Dyson orbital is determined by the σ -HOMO-1, in spite of the existence of the degenerate π -HOMOs: in the cation N_2^+ the ordering of orbitals is inverted such that the σ -orbital lies about 14 eV above the two π -orbitals. According to equation (A.1) the weighting factors are determined by the overlap of the reduced Slater determinant $\Phi_{in,i} \{ \mathbf{x} \setminus N \}$ with the Slater determinant of the ionized system, each containing $N-1$ orbitals. As the σ -orbital of N_2^+ is not populated and also is spatially similar to the N_2 HOMO-1, the only combination of two determinants that can be close to one involves neither of the two σ -orbitals. This can happen only for the overlap corresponding to the weighting factor of the σ -HOMO-1 of N_2 . In a similar manner, the Dyson orbitals' structure of NTCDA and PTCDA can be explained. All approaches for PTCDA^+ yield a depopulated orbital that has a spatial structure that is close to the PTCDA HOMO. Therefore, the overlap argument strikes again and forces all weighting factors to be small, except for the one that corresponds to the HOMO. In the case of PBE NTCDA⁺ the depopulated orbital is rather a superposition of the π -HOMO-1 and σ -HOMO of NTCDA, which is why the Dyson orbital also emerges as a superposition of these two orbitals.

Also note that the norm of the Dyson orbital is not one, but ranges between zero and one. It can be interpreted as a measure of the ionization probability.

Appendix B. Photoemission from the PTCDA/NTCDA molecule

For the sake of completeness, we here discuss the PTCDA results in greater detail. As mentioned in section 5, all approaches lead to a similar intensity pattern for the first ionization of PTCDA, independent of the inclusion of relaxation and the used functional. Therefore, the Dyson orbital is in each case given by the corresponding π -HOMO. Contrary to the NTCDA case there are no additional orbital contributions. In figure A.1(d) we show the momentum map

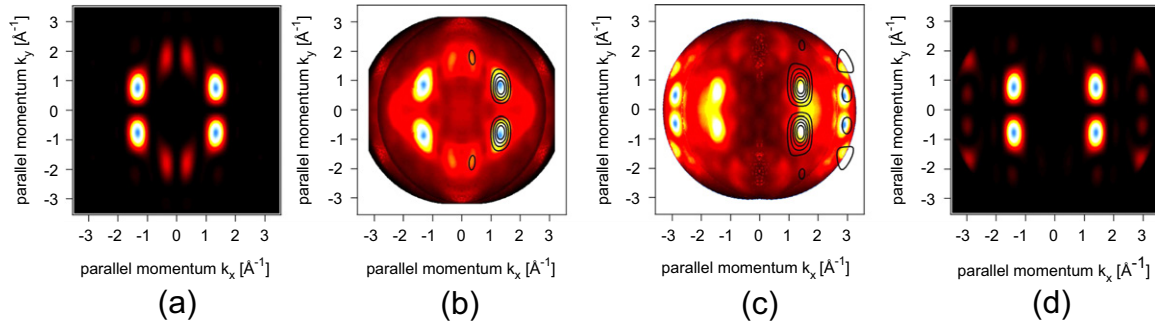


Figure A.1. Momentum space maps for the PTCDA molecule at a kinetic photoelectron energy of $E_k = 48.6$ eV. (a) The RSA Dyson orbital based on KS-SIC, (b) the corresponding measured ARPES with vertical polarized light overlaid with the RSA Dyson KS-SIC contour. (c) The measured ARPES with horizontal polarized light overlaid with the contours of the KS-SIC RSA Dyson orbital calculated with the horizontal polarization scaling factor shown in (d).

of the RSA Dyson orbital with horizontal light polarization and in figure A.1(a) with vertical light polarization (i.e. p-polarization). The figures A.1(b) and (c) show the measured ARPES intensities, overlaid with the Dyson orbital contours for ease of comparison. All spectra correspond to a kinetic photoelectron energy of $E_{\text{kin}} = 48.6$ eV, i.e. $|k| = 3.6 \text{ \AA}^{-1}$. The horizontally polarized case, which should reveal any additional σ -orbital contributions if there are any, is well reproduced by the calculation as far as the peak positions are concerned. The trend is similar to the KS-SIC NTCDA result, i.e. the outer features are higher in intensity in the experiment than in the calculation. The magnitude of the differences, however, is smaller for PTCDA than for NTCDA. For PTCDA we thus come to the conclusion that the single molecular orbital approach is well justified, and relaxation effects are smaller than for NTCDA. Expressed in numbers, the difference between the relaxed and unrelaxed first ionization potential calculated with PBE for NTCDA is about 0.93 eV, whereas for PTCDA we find only a difference of 0.16 eV. This appears plausible, as a larger system with more electrons should be less affected by removing one charge.

Appendix C. Experimental and computational details

All experiments were performed under ultrahigh vacuum conditions at a base pressure of 2×10^{-10} mbar. The NTCDA and PTCDA monolayer films were prepared in an attached preparation chamber by organic molecular beam deposition. Prior to deposition the Ag(110) substrate was cleaned by several sputter and annealing cycles. The cleanliness and surface quality was checked by low energy electron diffraction (LEED) and the absence of characteristic carbon 1s signals in core level photoelectron spectra. The coverage and quality of the organic monolayers was monitored by their characteristic LEED patterns [39, 44–46] and the absence of any second layer signal in valence photoelectron spectra [40, 47, 48]. The k_{\parallel} -dependent photoemission intensity distributions were recorded at the NanoESCA beamline at Elettra [49] using a FOCUS GmbH/Omicron NanoESCA photoelectron microscope [50, 51]. With this setup the complete photoemission hemisphere can be measured at once, if the Fourier plane of the microscope is imaged with an activated transfer lens. A detailed description of the

measurement and evaluation process is given in [40]. In contrast to previous investigations [6–10, 40] we used different light polarizations (linear horizontal and vertical, and circular) to enhance and suppress photoemission intensities. To maximize the available k_{\parallel} -range at manageable beam damage we used photon energies of around 50 eV and carefully checked degradation effects for each measurement.

The KS-SIC and PBE calculations for NTCDA, PTCDA, pentacene and N_2 were performed with the Bayreuth version [28] of the PARSEC real-space code, [52] where we employed a grid-spacing of 0.3 bohr (for N_2 0.2 bohr) and Troullier–Martins norm-conserving pseudopotentials [53].

The KS-SIC method has been explained in detail in [26, 37], so we here just summarize very briefly its main features. Based on the self-interaction-correction functional of Perdew and Zunger [43] we construct—in contrast to traditional SIC approaches—a spatially local, multiplicative xc potential via the optimized-effective potential (OEP) equation [54]. This ensures that we stay within the realm of KS DFT with all its benefits. The direct construction of the OEP, which is possible but tedious for the SIC energy functional [55], was avoided by resorting to the generalized OEP equation and the corresponding generalized KLI approximation [26] with a complex-valued energy minimizing unitary orbital transformation [37].

For all HF and B3LYP calculations we used the QChem program package [56] and cc-PVTZ basis functions [57]. We explicitly checked and verified that the use of the pseudopotentials does not lead to any differences with respect to the all electron calculations in the PBE RSA Dyson orbitals.

References

- [1] Itatani J, Levesque J, Zeidler D, Niikura H, Pepin H, Kieffer J C, Corkum P B and Villeneuve D M 2004 *Nature* **432** 867
- [2] Repp J, Meyer G, Stojković S M, Gourdon A and Joachim C 2005 *Phys. Rev. Lett.* **94** 026803
- [3] Kera S, Tanaka S, Yamane H, Yoshimura D, Okudaira K K, Seki K and Ueno N 2006 *Chem. Phys.* **325** 113
- [4] Lein M 2007 *J. Phys. B: At. Mol. Opt. Phys.* **40** R135
- [5] McFarland B K, Farrell J P, Bucksbaum P H and Gühr M 2008 *Science* **322** 1232
- [6] Puschnig P, Berkebile S, Fleming A J, Koller G, Emtsev K, Seyller T, Riley J D, Ambrosch-Draxl C, Netzer F P and Ramsey M G 2009 *Science* **326** 702
- [7] Ziroff J, Forster F, Schöll A, Puschnig P and Reinert F 2010 *Phys. Rev. Lett.* **104** 233004
- [8] Dauth M, Körzdörfer T, Kümmel S, Ziroff J, Wießner M, Schöll A, Reinert F, Arita M and Shimada K 2011 *Phys. Rev. Lett.* **107** 193002
- [9] Puschnig P *et al* 2011 *Phys. Rev. B* **84** 235427
- [10] Lüftner D, Ules T, Reinisch E-M, Koller G, Soubatch S, Tautz F S, Ramsey M G and Puschnig P 2014 *Proc. Natl Acad. Sci.* **111** 605
- [11] Gadzuk J W 1974 *Phys. Rev. B* **10** 5030
- [12] Wopperer P, Dinh P M, Suraud E and Reinhard P-G 2012 *Phys. Rev. A* **85** 015402
- [13] McCarthy I E and Weigold E 1988 *Rep. Prog. Phys.* **51** 299
- [14] Schwarz W H E 2006 *Angew. Chem.* **45** 1508
- [15] Duffy P, Chong D, Casida M E and Salahub D R 1994 *Phys. Rev. A* **50** 4707
- [16] Walter M and Häkkinen H 2008 *New J. Phys.* **10** 043018
- [17] Oana C M and Krylov A I 2007 *J. Chem. Phys.* **127** 234106
- [18] Humeniuk A, Wohlgemuth M, Suzuki T and Mitrić R 2013 *J. Chem. Phys.* **139** 134104

- [19] Chong D P, Gritsenko O V and Baerends E J 2002 *J. Chem. Phys.* **116** 1760
- [20] Baerends E J, Gritsenko O V and van Meer R 2013 *Phys. Chem. Chem. Phys.* **15** 16408
- [21] Körzdörfer T and Kümmel S 2010 *Phys. Rev. B* **82** 155206
- [22] Casida M E 1995 *Phys. Rev. A* **51** 2005
- [23] Kronik L, Stein T, Refaely-Abramson S and Baer R 2012 *J. Chem. Theory Comput.* **8** 1515
- [24] Körzdörfer T, Kümmel S, Marom N and Kronik L 2009 *Phys. Rev. B* **79** 201205 (R)
- [25] Körzdörfer T, Kümmel S, Marom N and Kronik L 2010 *Phys. Rev. B* **82** 129903 (E)
- [26] Körzdörfer T, Mundt M and Kümmel S 2008 *J. Chem. Phys.* **129** 014110
- [27] Mundt M, Kümmel S, Huber B and Moseler M 2006 *Phys. Rev. B* **73** 205407
- [28] Mundt M and Kümmel S 2007 *Phys. Rev. B* **76** 035413
- [29] Almbladh C-O and von Barth U 1985 *Phys. Rev. B* **31** 3231
- [30] Cremer D 2001 *Mol. Phys.* **99** 1899
- [31] Kohn W, Becke A D and Parr R G 1996 *J. Phys. Chem.* **100** 12974
- [32] Baerends E J and Gritsenko O V 1997 *J. Phys. Chem. A* **101** 5383
- [33] Perdew J P, Burke K and Ernzerhof M 1996 *Phys. Rev. Lett.* **77** 3865
- [34] Becke A D 1988 *Phys. Rev. A* **38** 3098
- [35] Lee C, Yang W and Parr R G 1988 *Phys. Rev. B* **37** 785
- [36] Stephens P J *et al* 1994 *J. Phys. Chem.* **98** 11623
- [37] Hofmann D, Klüpfel S, Klüpfel P and Kümmel S 2012 *Phys. Rev. A* **85** 062514
- [38] Ernzerhof M, Perdew J P and Burke K 1997 *Int. J. Quantum Chem.* **64** 285
- [39] Wießner M, Kübert J, Feyer V, Puschnig P, Schöll A and Reinert F 2013 *Phys. Rev. B* **88** 075437
- [40] Wießner M, Hauschild D, Schöll A, Reinert F, Feyer V, Winkler K and Krömker B 2012 *Phys. Rev. B* **86** 045417
- [41] Berkebile S, Puschnig P, Koller G, Oehzelt M, Netzer F P, Ambrosch-Draxl C and Ramsey M G 2008 *Phys. Rev. B* **77** 115312
- [42] Wiener M, Hauschild D, Sauer C, Feyer V, Schöll A and Reinert F 2014 *Nat. Commun.* **5** 4156
- [43] Perdew J P and Zunger A 1981 *Phys. Rev. B* **23** 5048
- [44] Seidel C, Awater C, Liu X, Ellerbrake R and Fuchs H 1997 *Surf. Sci.* **371** 123
- [45] Glöckler K, Seidel C, Soukopp A, Sokolowski M, Umbach E, Böhringer M, Berndt R and Schneider W-D 1998 *Surf. Sci.* **405** 1
- [46] Fink R, Gador D, Stahl U, Zou Y and Umbach E 1999 *Phys. Rev. B* **60** 2818
- [47] Jung M, Baston U, Schnitzler G, Kaiser M, Papst J, Porwol T, Freund H and Umbach E 1993 *J. Mol. Struct.* **293** 239
- [48] Zou Y, Kilian L, Schöll A, Schmidt T, Fink R and Umbach E 2006 *Surf. Sci.* **600** 1240
- [49] Wiemann C, Patt M, Krug I P, Weber N B, Escher M, Merkel M and Schneider C M 2011 *e-J. Surf. Sci. Nanotechnology* **9** 395
- [50] Escher M *et al* 2005 *J. Phys.: Condens. Matter* **17** S1329
- [51] Escher M *et al* 2005 *J. Electron. Spectrosc.* **144-147** 1179
- [52] Kronik L, Makmal A, Tiago M L, Alemany M M G, Jain M, Huang X, Saad Y and Chelikowsky J R 2006 *Phys. Status Solidi b* **243** 1063
- [53] Troullier N and Martins J L 1991 *Phys. Rev. B* **43** 1993
- [54] Kümmel S and Kronik L 2008 *Rev. Mod. Phys.* **80** 3
- [55] Körzdörfer T, Mundt M and Kümmel S 2008 *Phys. Rev. Lett.* **100** 133004
- [56] Shao Y *et al* 2006 *Phys. Chem. Chem. Phys.* **8** 3172
- [57] Dunning T H 1989 *J. Chem. Phys.* **90** 1007

Publication 2

Electron-vibration coupling in molecular materials: assignment of vibronic modes from photoelectron momentum mapping

Physical Review Letters **116**, 147601 (2016)

M. Graus¹, M. Grimm¹, C. Metzger¹, **M. Dauth**², C. Tusche^{3,4}, J. Kirschner³,
S. Kümmel², A. Schöll¹, and F. Reinert¹

¹ University of Würzburg, Experimental Physics VII, 97074 Würzburg, Germany

² University of Bayreuth, Theoretical Physics IV, 95440 Bayreuth, Germany

³ Max Planck Institute of Microstructure Physics, 06120 Halle, Germany

⁴ Peter Grünberg Institut (PGI-6), Forschungszentrum Jülich GmbH, 52425 Jülich, Germany

Publ.2

My contribution

I calculated the Dyson orbitals and momentum maps, was part of the scientific discussion, and wrote a first draft of the theory part of the paper.

Publ.2

Electron-Vibration Coupling in Molecular Materials: Assignment of Vibronic Modes from Photoelectron Momentum Mapping

M. Graus,¹ M. Grimm,¹ C. Metzger,¹ M. Dauth,² C. Tusche,^{3,4} J. Kirschner,³ S. Kümmel,²
A. Schöll,¹ and F. Reinert¹

¹University of Würzburg, Experimental Physics VII, 97074 Würzburg, Germany

²University of Bayreuth, Theoretical Physics IV, 95440 Bayreuth, Germany

³Max Planck Institute of Microstructure Physics, 06120 Halle, Germany

⁴Peter Grünberg Institut (PGI-6), Forschungszentrum Jülich GmbH, 52425 Jülich, Germany

(Received 5 February 2016; published 6 April 2016)

Electron-phonon coupling is one of the most fundamental effects in condensed matter physics. We here demonstrate that photoelectron momentum mapping can reveal and visualize the coupling between specific vibrational modes and electronic excitations. When imaging molecular orbitals with high energy resolution, the intensity patterns of photoelectrons of the vibronic sidebands of molecular states show characteristic changes due to the distortion of the molecular frame in the vibronically excited state. By comparison to simulations, an assignment of specific vibronic modes is possible, thus providing unique information on the coupling between electronic and vibronic excitation.

DOI: 10.1103/PhysRevLett.116.147601

The coupling of charge to vibronic excitation plays a crucial role for various physical phenomena from superconductivity [1–3] to the nonradiative decay pathways involved in photosynthesis [4]. In molecular materials, charge-vibration coupling influences the optical and electronic properties [5] and is a decisive quantity for the hopping transport [6–8]. In the case of hopping, the predominant transport mechanism for molecular solids relevant for device application [9], the charge mobility is immediately connected to the reorganization energy. The latter quantity is a measure of the energy cost for the deformation of the molecular frame upon adding or subtracting an electron. It has been demonstrated that photoelectron spectroscopy (PES) can be applied to quantify this reorganization energy from the analysis of the electron-vibration coupling from first principles [7,10].

The coupling of electronic to vibronic excitations has been studied for a long time by several methods such as PES [7,10,11], optical spectroscopy [12], x-ray absorption [13,14], and electron energy loss spectroscopy [15]. Nevertheless, an assignment of the specific vibrational modes that couple to the electronic excitation is complicated, since the experiment provides only information on the mode energy and restrictions on possible symmetries by selection rules.

Here we show that the angle-dependent intensity distribution in a PES experiment can provide a fingerprint of the coupled vibration. In the case of the paradigmatic molecule coronene [C₂₄H₁₂; see Fig. 3(c) for the molecular structure] investigated in this work, our analysis provides evidence that the mode which couples to an ionization of the highest occupied molecular orbital (HOMO) is an A_g in-plane mode with a vibronic excitation energy of 196 meV.

For our experiments the coronene molecules were prepared in a commensurate monolayer (ML) with 4 × 4 superstructure on an Au(111) substrate [16]. The interfacial bonding in this particular case is comparatively weak, thus leading only to a relatively small broadening of the molecular states due to hybridization with the metal. The momentum-resolved PES data were recorded at a sample temperature of 15 K and with He-I excitation (21.22 eV) utilizing a state-of-the-art photoelectron momentum microscope which collects all photoelectrons emitted into the complete half-sphere above the sample. This provides a three-dimensional data set of the photoemission spectral function $I(k_x, k_y, E_B)$, depending on the in-plane momentum coordinates (k_x, k_y) and the binding energy (E_B) with a momentum resolution of 0.005 Å⁻¹ and energy resolution of 20 meV [17] (see Supplemental Material [18] for experimental details).

Figure 1(a) presents the energy distribution curve (EDC) derived from a data set recorded between the Fermi energy and the low-energy onset of the Au 5*d* band. The data were integrated over a circular area with diameter 0.5 Å⁻¹ in momentum space centered at ($k_x = 1.45$ Å⁻¹; $k_y = 0$ Å⁻¹). The resulting spectrum shows a prominent peak at 1.5 eV, which can be assigned to the coronene HOMO. In addition, two shoulders appear on the high binding energy side, which resemble the equidistant vibronic overtones observed for several similar molecules in the gas and condensed phase [7,10].

For a detailed analysis of the fine structure of the coronene HOMO signal, shorter energy scans between 1.23 and 2.03 eV were performed to reduce the measurement time and radiation damage, which manifests itself in a

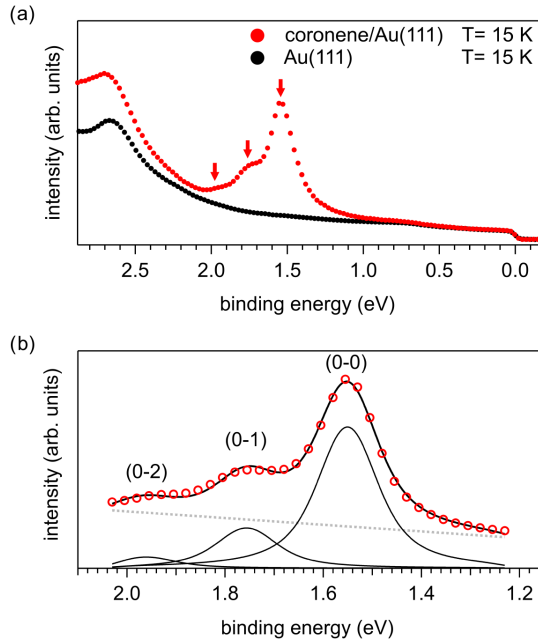


FIG. 1. (a) Momentum-integrated EDCs of 1 ML coronene on Au(111) recorded at a sample temperature of 15 K (red data points). The HOMO signal consists of three components (indicated by arrows). The corresponding data derived from a clean Au(111) sample considering the backfolding on the 4×4 superstructure of the adsorbate are plotted in black [see Fig. 2(d) and the corresponding text for details]. (b) Experimental spectrum derived from a short scan (red data points), fitted by a vibrational progression consisting of three equally spaced Voigt peaks of identical line width (black solid curves) and a linear background (black dotted line).

broadening and slight energy shift of the molecular signals and the occurrence of additional low-energy features. With the applied settings, damage was visible after about 15 min of irradiation, while all data presented in the following were recorded in less than 10 min.

Figure 1(b) shows a spectrum derived from such a short scan after the same integration in momentum space as described above. To demonstrate the vibronic origin of the peaks on the high binding energy side, a least-squares fit was performed with three equidistant Voigt functions of equal width plus an additional linear background. The fit reproduces the experimental data well with Gaussian and Lorentzian widths of (79 ± 25) and (106 ± 25) meV, respectively, and an energy spacing of (206 ± 10) meV, representing the energy of the coupled vibration.

Figures 2(a)–2(c) show the photoelectron momentum maps recorded at a binding energy of 1.55, 1.75, and 1.95 eV, respectively, corresponding to the three individual vibronic peaks, which we will in the following refer to as (0-0), (0-1), and (0-2), respectively. (n - m) indicates a transition from the vibronic state n in the electronic ground state to the vibronic state m in the electronic excited state. No background subtraction was applied, and the color scale

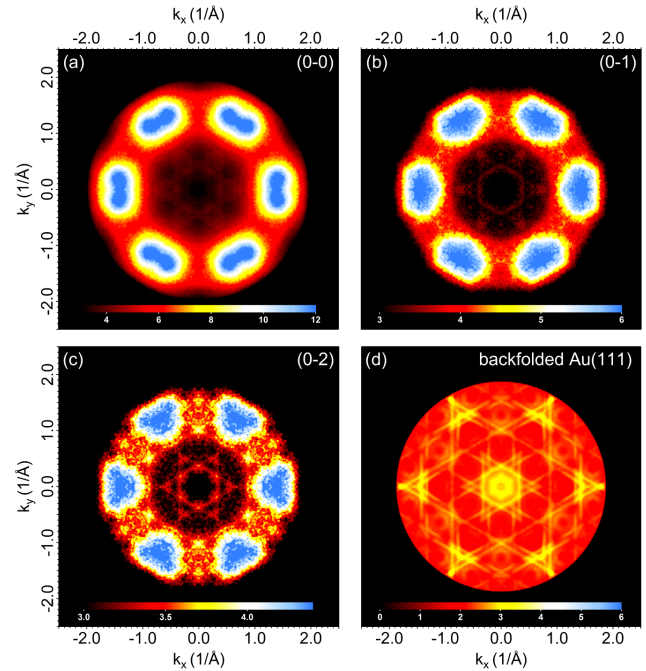


FIG. 2. (a)–(c) Photoelectron momentum maps of the HOMO of coronene/Au(111) recorded at the energy of the (0-0) peak and the vibronic sidebands (0-1) and (0-2). (d) Simulated background from the Au substrate derived by backfolding of a momentum map of a clean Au(111) sample (recorded at $E_B = 1.95$ eV; see Fig. S1 in Supplemental Material [18]) on the 4×4 superstructure of the adsorbate (see the text for details). The color scaling of the intensity was chosen individually to optimize the contrast.

was adapted to enhance the color contrast of the individual patterns.

It has been demonstrated that the angle-dependent intensity distribution of photoelectrons is immediately connected to the electron density in real space [19,20]. In the case of planar organic molecules, a plane-wave final-state approximation of the photoemission final state allows furthermore a direct comparison of experimental momentum maps with calculated real-space orbitals by a Fourier transform [19,21]. In this sense, the intensity pattern recorded for the (0-0) peak in Fig. 2(a) resembles the previous experimental data for the HOMO of coronene on Ag(111) and the corresponding theoretical simulation for the coronene HOMO [22]. However, while the main features in the momentum map of the (0-0) peak appear oval or slightly goggle shaped, these features develop an increasing triangular appearance in case of the (0-1) and (0-2) peaks.

Since the peaks of (0-1) and particularly (0-2) have relatively low intensities, adapting the intensity scale in Figs. 2(b) and 2(c) results in an increasing contribution of emission from the substrate. To verify that the substrate signal does not interfere with the molecular features in the momentum maps, we have simulated the intensity patterns

derived from the Au sp bands taking into account the backfolding on the 4×4 superstructure of the adsorbate. For this purpose, a momentum map recorded at the same energy as the (0-2) peak for a clean Au(111) sample (see Fig. S1 in Supplemental Material [18]) was shifted by $1/4$, $2/4$, and $3/4$ of the $\bar{\Gamma} - \bar{\Gamma}$ distance towards each of the six adjacent surface-Brillouin zones and then averaged. The resulting intensity pattern is given in Fig. 2(d) and allows identifying the substrate signals in the momentum maps recorded for the (0-1) and (0-2) peaks of coronene/Au(111). The backfolded sp bands contribute relatively sharp patterns such as the two hexagrams, which are most clearly visible in the (0-2) momentum map [Fig. 2(c)]. Also, the slight increase in intensity around $k_x = 1.45 \text{ \AA}^{-1}$, $k_y = 0 \text{ \AA}^{-1}$ and the intense lines along $k_x = 1.40 \text{ \AA}^{-1}$ (and symmetrically equivalent sites) have to be associated with crossing points of multiple Au bands.

The comparison of the momentum patterns recorded for the low-intensity vibronic sidebands to the simulated background thus allows identification of several contributions from Au sp bands. Although some of these signals coincide with the intensity pattern from the coronene HOMO, the overall change of the coronene features towards a triangular shape cannot be explained by a contribution from the substrate.

The changes in Figs. 2(a)–2(c) thus obviously have to be sought in a change of the coronene electronic wave function in momentum—and thus also in real space—upon vibronic excitation. A deviation of the intensity patterns recorded for vibronically excited molecular states was already observed for pentacene [23] as well as for several phthalocyanines ($X\text{-Pc}$, $X = \text{OTi, OV, ClAl, Pb, Cu, H}_2$) [24] and assigned to a breakdown of the sudden approximation in the photoionization process. In contrast to an instantaneous (vertical) transition, the photoemission process has to be rather described on a finite time scale, which is defined by the photohole lifetime. Photoemission thus bears information on a displacement of the nuclei on this very time scale.

Theoretical considerations can help to extract this information. Since the energy of the relevant vibrations is much larger than $k_B T$, the molecule is initially in its ground state [which is identical for the (0-0), (0-1), and (0-2) transitions]. Within the Born-Oppenheimer approximation, the electronic state of a system defines an energy surface, which acts as the potential for the motion of the nuclei. The change of the electronic potential that is caused by emission of an electron can trigger the vibronic excitation of the ionized system. While the common interpretation of angle-resolved PES based on ground-state single-particle orbitals can describe vertical processes well [19,25], it cannot capture structural changes of the molecular geometry caused by removing an electron. The latter, however, become accessible through the use of Dyson orbitals, defined by the projection of the $(N - 1)$ electron

ionized state $\Psi^+(N - 1)$ onto the molecular ground state $\Psi_0(N)$ [20,26]:

$$\Psi_D = \sqrt{N} \langle \Psi_0(N) | \Psi^+(N - 1) \rangle. \quad (1)$$

Viewing the PES process in terms of this overlap is ideally suited to our purpose, as the altering of the final molecular state's electronic structure due to the nuclei's vibrational displacement can easily be included explicitly. To identify possible vibrational modes, we perform a vibrational frequency analysis of positively charged isolated coronene using the density-functional theory with the Perdew-Burke-Ernzerhof exchange-correlation functional [27]. Nine modes are found in the energy range of interest between 185 and 250 meV (see Table I in Supplemental Material [18]). Since the vibronic excitations when time-averaged correspond to a displacement of the nuclei along normal coordinates, we calculated the electronic final state $\Psi^+(N - 1)$ for displacement amplitudes ranging from zero up to a reasonable mean displacement of 0.15 \AA [28]. In combination with the ground-state wave function of the neutral molecule, we evaluate the Dyson orbital according to Eq. (1) following the relaxed Slater determinant approach [20]. Approximating the photoelectron's state by a plane wave, which is justified for this class of materials [19,25], the photoelectron momentum maps can be simulated by a Fourier transform of the real-space Dyson orbitals into momentum space [20]. For the equilibrium position of the nuclei, i.e., the (0-0) transition, the corresponding momentum map is presented in Fig. 3(a) and resembles the single-particle molecular orbital case published earlier [22].

The overall agreement of Fig. 3(a) with its experimental counterpart in Fig. 2(a) is reasonable. However, the calculation does not reproduce the indicated goggle shape of the six main intensity maxima. Generally speaking, one possible explanation for this deviation could be a slight azimuthal tilt of the high-symmetry direction of coronene against the $[\bar{1}01]$ direction of the substrate surface. Taking into account different domains, this would lead to an azimuthal doubling of the intensity patterns in the experiment. However, based on such a multiplication of the calculated momentum map in Fig. 3(a), a simulation of the goggle features in Fig. 2(a) is not possible, thus rendering this explanation unlikely. An alternative explanation can be provided by the effect of lateral band dispersion. To reveal this, we have fitted the vibronic progression in the EDCs for all k_{\parallel} in analogy to Fig. 1(b). The energy of the (0-0) peak derived from this fit shows a lateral dispersion of about 20 meV, which is a reasonable value compared to similar systems [29,30]. Moreover, when plotted against k_{\parallel} , the energy position of the (0-0) peak mimics the goggle shaped features in Fig. 2(a) (see Fig. S2 in Supplemental Material [18]). Since the experimental momentum maps were recorded at constant energy, energy dispersion of the

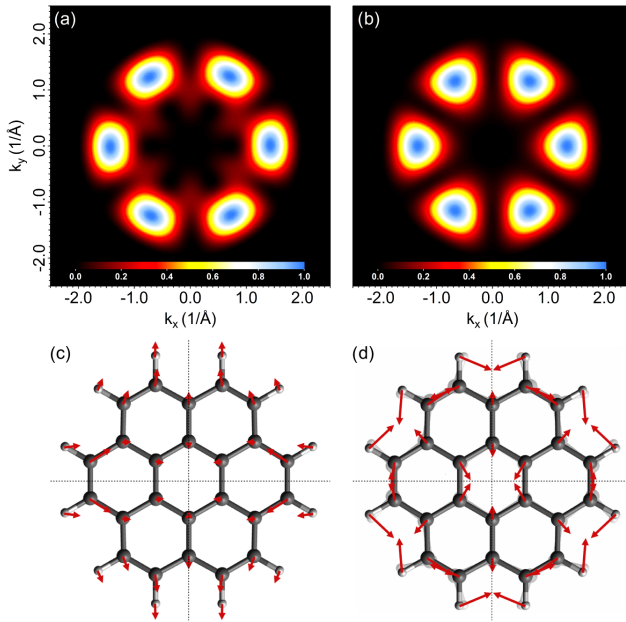


FIG. 3. Simulated photoelectron momentum maps derived for the Dyson orbital of (a) the coronene⁺ HOMO with the nuclei in equilibrium position and (b) the HOMO of the distorted coronene⁺ at a mean displacement amplitude of 0.15 Å according to the A_g mode at 196 meV. (c) Illustration of the geometric relaxation of an isolated coronene molecule upon ionization. The point group symmetry is reduced from D_{6h} to D_{2h} . Red arrows show the change in nuclear equilibrium positions enhanced by a factor of 50 for better visualization. The black dotted lines mark planes of symmetry, indicating an A_g symmetry of the distorted molecule. (d) Illustration of the respective A_g mode. The dark image indicates the undistorted molecule and is overlaid by a lighter image depicting the vibronic displacement. The associated force vectors are indicated as elongated red arrows.

(0-0) peak will directly translate to intensity variations, thus most likely accounting for the observed difference between the calculated and experimental momentum maps of the (0-0) peak.

For an increasing displacement of the nuclei, we find a change in the shape of the coronene features, depending on the displacement directions according to the individual vibrational modes. The momentum maps calculated for the nine vibrational modes between 180 and 250 meV at a mean displacement of 0.15 Å are depicted in Fig. S3 in Supplemental Material [18]. Interestingly, the modes show remarkable differences in the momentum maps. Only two modes show a change into a triangular pattern, which resembles the experimental finding for the vibronic sidebands in Figs. 2(a)–2(c).

Consequently, the changes in the photoemission data can be explained by changes of the molecular orbital density of the HOMO due to a deformation of the coronene molecule in a vibronically excited state. The gradual change from (0-0) over (0-1) to (0-2) is moreover plausible, since (0-1)

to (0-2) represent transitions into different overtones of the same vibration, which have different mean displacement amplitudes. The simulation of the respective orbital density allows identifying the corresponding vibronic modes, a B_{2u} mode at 195 meV and an A_g mode at 196 meV, which fit quite well to the experimentally determined energy of (206 ± 10) meV. Moreover, the momentum patterns of the other modes in Fig. S3 obviously do not contribute significantly to the experimental data in Fig. 2, thus ruling out a coupling of these modes. This agrees with earlier studies that also found a preferential coupling of selected modes for pentacene and perfluoropentacene [31].

Based on our experimental data alone, we cannot derive further restrictions on the coupled vibronic modes. However, our calculations show that upon photoionization the coronene molecular frame relaxes as illustrated by Fig. 3(c), reducing the point group symmetry from D_{6h} to D_{2h} . The displacement of the nuclei is indicated by red arrows and shows A_g symmetry, thus resembling the A_g mode at 196 meV, which is depicted in Fig. 3(d) together with the corresponding momentum pattern in Fig. 3(b).

In summary, we demonstrated that the angle-dependent intensity patterns of photoelectrons of molecular states show characteristic changes due to the vibronic distortion of the molecule. By a comparison to the simulated patterns, an assignment of the specific vibronic modes that preferentially couple to the electronic excitation is possible. In the example of the coronene HOMO, the experimental data agree with two in-plane modes with an energy of 195 and 196 meV, respectively. The latter mode is A_g symmetric and should be favored according to symmetry arguments. Our approach of orbital imaging by photoelectron momentum mapping with high energy resolution thus provides unique information and constitutes a novel route for the analysis of the coupling between electronic and vibronic excitation and allows unprecedented insight into the properties of molecular materials.

A. S. and F. R. acknowledge support by the Deutsche Forschungsgemeinschaft (DFG; Grants No. GRK1221, No. SCHO-1260/4-1, No. SCHO-1260/5-1, and No. RE1469/9-1). M. D. and S. K. acknowledge support by DFG Graduiertenkolleg 1640 and the Bavarian State Ministry of Science, Research, and the Arts for the Collaborative Research Network “Solar Technologies go Hybrid.” We thank J. Osterwalder, M. Hengsberger, and L. Castiglioni for fruitful discussion.

-
- [1] A. Devos and M. Lannoo, *Phys. Rev. B* **58**, 8236 (1998).
 - [2] O. Gunnarsson, H. Handschuh, P. S. Bechthold, B. Kessler, G. Ganteför, and W. Eberhardt, *Phys. Rev. Lett.* **74**, 1875 (1995).
 - [3] T. Kato and T. Yamabe, *J. Chem. Phys.* **115**, 8592 (2001).
 - [4] T. Brixner, J. Stenger, H. Vaswani, M. Cho, R. Blankenship, and G. Fleming, *Nature (London)* **434**, 625 (2005).

- [5] A. Mugarza, R. Robles, C. Krull, R. Korytár, N. Lorente, and P. Gambardella, *Phys. Rev. B* **85**, 155437 (2012).
- [6] J. Brédas, J. Calbert, D. da Silva Filho, and J. Cornil, *Proc. Natl. Acad. Sci. U.S.A.* **99**, 5804 (2002).
- [7] S. Kera, H. Yamane, and N. Ueno, *Prog. Surf. Sci.* **84**, 135 (2009).
- [8] J. Sukegawa, C. Schubert, X. Zhu, H. Tsuji, D. Guldi, and E. Nakamura, *Nat. Chem.* **6**, 899 (2014).
- [9] V. Coropceanu, J. Cornil, D. da Silva Filho, Y. Olivier, R. Silbey, and J. Brédas, *Chem. Rev.* **107**, 926 (2007).
- [10] N. Ueno and S. Kera, *Prog. Surf. Sci.* **83**, 490 (2008).
- [11] R. Boschi, J. N. Murrell, and W. Schmidt, *Faraday Discuss. Chem. Soc.* **54**, 116 (1972).
- [12] D. Hudgins and L. Allamandola, *J. Phys. Chem.* **99**, 3033 (1995).
- [13] A. Schöll, Y. Zou, L. Kilian, D. Hübner, D. Gador, C. Jung, S. G. Urquhart, T. Schmidt, R. Fink, and E. Umbach, *Phys. Rev. Lett.* **93**, 146406 (2004).
- [14] A. Schöll, D. Hübner, T. Schmidt, S. Urquhart, R. Fink, and E. Umbach, *Chem. Phys. Lett.* **392**, 297 (2004).
- [15] B. Koel, J. Crowell, C. Mate, and G. Somorjai, *J. Phys. Chem.* **88**, 1988 (1984).
- [16] C. Seidel, R. Ellerbrake, L. Gross, and H. Fuchs, *Phys. Rev. B* **64**, 195418 (2001).
- [17] C. Tusche, A. Krasnyuk, and J. Kirschner, *Ultramicroscopy* **159**, 520 (2015).
- [18] See Supplemental Material at <http://link.aps.org/supplemental/10.1103/PhysRevLett.116.147601> for details on experiment and theory, experimental data on the back-folding of Au-bands, dispersion of the coronene HOMO, and the photoelectron momentum maps of the relevant vibronic modes.
- [19] P. Puschnig, S. Berkebile, A. Fleming, G. Koller, K. Emtsev, T. Seyller, J. Riley, C. Ambrosch-Draxl, F. Netzer, and M. Ramsey, *Science* **326**, 702 (2009).
- [20] M. Dauth, M. Wiessner, V. Feyer, A. Schöll, P. Puschnig, F. Reinert, and S. Kümmel, *New J. Phys.* **16**, 103005 (2014).
- [21] J. Gadzuk, *Phys. Rev. B* **10**, 5030 (1974).
- [22] M. Wießner, N. Lastra, J. Ziroff, F. Forster, P. Puschnig, L. Dössel, K. Müllen, A. Schöll, and F. Reinert, *New J. Phys.* **14**, 113008 (2012).
- [23] H. Yamane, S. Nagamatsu, H. Fukagawa, S. Kera, R. Friedlein, K. K. Okudaira, and N. Ueno, *Phys. Rev. B* **72**, 153412 (2005).
- [24] N. Ueno, S. Kera, K. Sakamoto, and K. Okudaira, *Appl. Phys. A* **92**, 495 (2008).
- [25] M. Dauth, T. Körzdörfer, S. Kümmel, J. Ziroff, M. Wießner, A. Schöll, F. Reinert, M. Arita, and K. Shimada, *Phys. Rev. Lett.* **107**, 193002 (2011).
- [26] M. Walter and H. Häkkinen, *New J. Phys.* **10**, 043018 (2008).
- [27] J. P. Perdew, K. Burke, and M. Ernzerhof, *Phys. Rev. Lett.* **77**, 3865 (1996).
- [28] G. Hagen and S. Cyvin, *J. Phys. Chem.* **72**, 1446 (1968).
- [29] M. Wießner, J. Ziroff, F. Forster, M. Arita, K. Shimada, P. Puschnig, A. Schöll, and F. Reinert, *Nat. Commun.* **4**, 1514 (2013).
- [30] M. Wießner, J. Kübert, V. Feyer, P. Puschnig, A. Schöll, and F. Reinert, *Phys. Rev. B* **88**, 075437 (2013).
- [31] S. Kera, S. Hosoumi, K. Sato, H. Fukagawa, S. Nagamatsu, Y. Sakamoto, T. Suzuki, H. Huang, W. Chen, A. Wee, V. Coropceanu, and N. Ueno, *J. Phys. Chem. C* **117**, 22428 (2013).

SUPPLEMENTAL MATERIAL

TECHNICAL DETAILS

All experiments were performed with a home-built momentum microscope [1] at the Max-Planck Institute of Microstructure Physics in Halle, Germany. All samples were prepared *in situ* in an attached preparation chamber. The Au(111) substrate was cleaned by repeated cycles of 30 min Ar-sputtering and annealing for 5 min at 870 K. Commercially available coronene was cleaned twice by sublimation in a home-built system. Coronene films were prepared onto the substrate at room temperature by molecular beam deposition from a home-made evaporator at a temperature of 450 K, resulting in a rate of two monolayers per hour. The coverage was calibrated by low energy electron diffraction (LEED), monitoring the well known 4x4 superstructure [2]. With increasing coronene coverage the LEED spots become sharper due to increasing domain size and the sharpest spots occur for a coverage of one complete monolayer (1 ML).

Photoelectron momentum mapping (PMM) experiments were performed at a base pressure in the low 10^{-11} mbar regime and at a sample temperature of about 15 K with unpolarized He-I excitation (Specs UVS 300). Photoelectrons were detected with a momentum microscope, adjusted to a momentum resolution of 0.005 \AA^{-1} and an energy resolution of 20 meV [1]. The detection energy was changed in steps of 25 meV and the acquisition time per picture was set to 15 sec.

Darkcurrent subtraction and flat-field correction were made to account for the inhomogeneities in the microchannel plate response and hotpixels. The camera images were averaged to a size of 512x512 to further improve statistics. The energy aberration of the imaging energy filter, resulting in a curvature of the energy over the image in the order of less than 100 meV, was corrected by calibrating the energy distribution curves (EDC) at every pixel to the Fermi energy, resulting in an accuracy of the energy axis of better than ± 10 meV over the full hemisphere. All presented PMM data were symmetrized sixfold according to the symmetry of the adsorbate system. This also accounts for the effect of the $A \times k$ factor as described by Puschnig *et al.* [3].

For our DFT calculations we use the PBE exchange correlation functional [4]. Geometry optimization and the vibrational analysis have been performed with the Gaussian09 code [5] and the 6-31G(d,p) basis set. The ground-state electronic structure necessary for determining the Dyson orbitals was calculated with the Bayreuth version [6] of the parsec real-space code [7] following the procedure outlined in Ref. 8. We here use a grid spacing of $0.3 a_0$ and PBE based norm conserving Troullier-Martins pseudopotentials with cutoff radii of $1.53 a_0$ and $1.40 a_0$ for carbon and hydrogen, respectively [9].

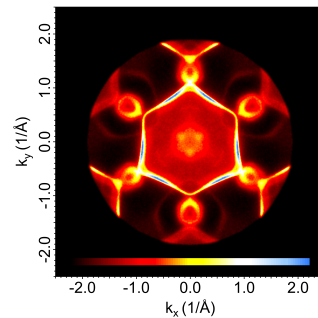


FIG. 1. Photoelectron momentum map recorded for the clean Au(111) substrate at a binding energy of $E_B=1.95$ eV with a photon energy of 21.22 eV and a sample temperature of 15 K.

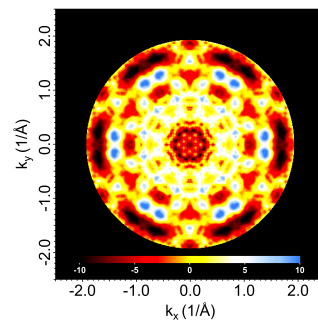


FIG. 2. Dispersion of the (0-0) peak derived from a fit of the EDCs at different $k_{||}$. The colorscale is given in meV and shows a molecular dispersion of around 20 meV. The dispersion pattern reflects the goggle shape of the (0-0) intensity shown in Fig. 2a) of the main article.

energy(meV)	symmetry
185	B_{1u}
187	B_{2u}
189	B_{3g}
190	B_{1u}
191	B_{3g}
195	B_{2u}
196	A_g
198	B_{1u}
200	A_g

TABLE I. Energy and symmetry of the vibrational modes of coronene between 185 eV and 250 eV calculated with the Gaussian09 code, using a PBE functional and a 6-31G(d,p) basis set.

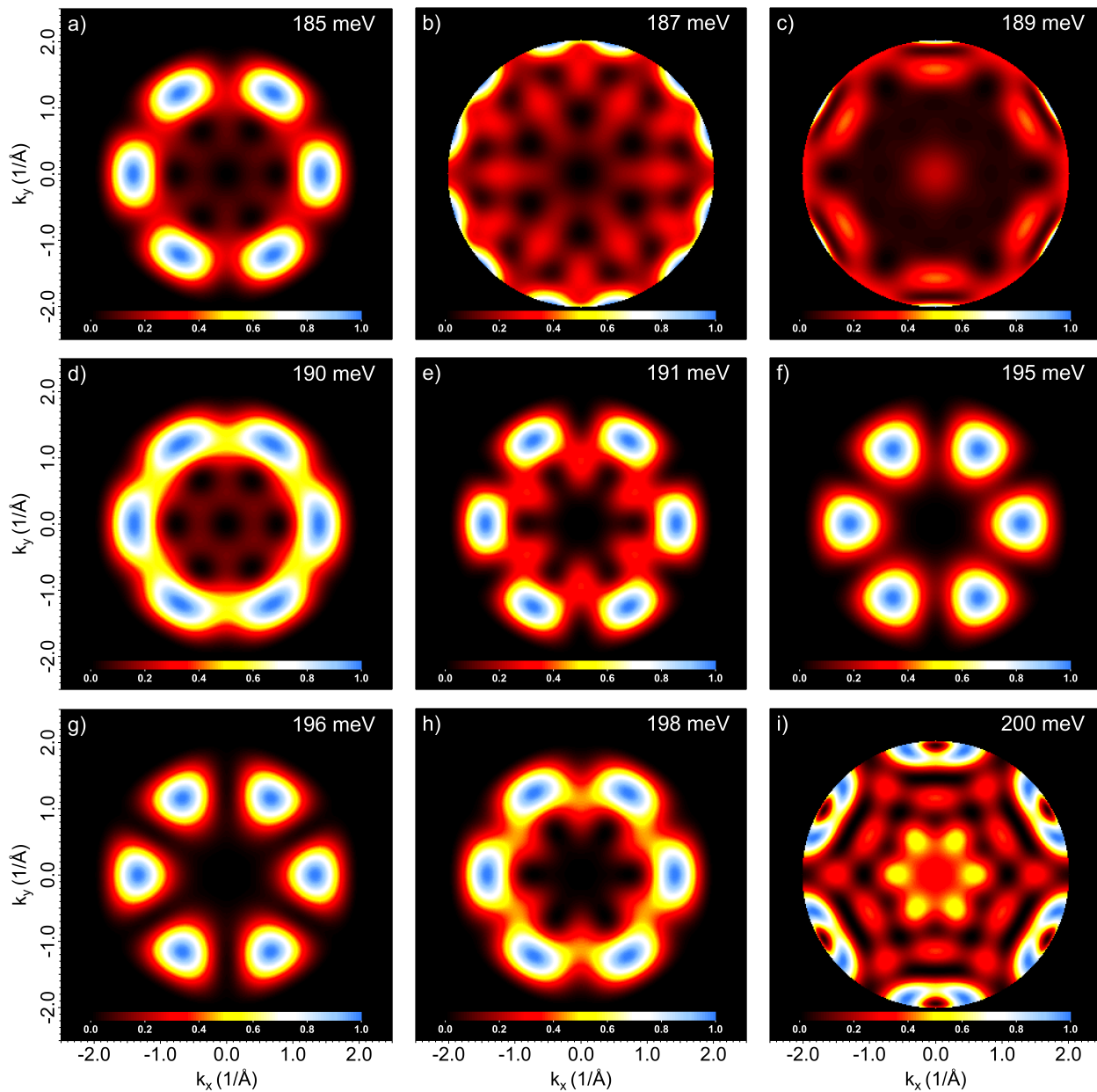


FIG. 3. Simulated photoelectron momentum maps derived for the Dyson orbital of the HOMO of distorted coronene⁺ for the different vibrational modes listed in TABLE I. The patterns were derived for a mean displacement amplitude of 0.15 Å and after sixfold symmetrization. Independent of amplitude, the triangular features observed in experiment can only be explained by the modes at 195 meV and at 196 meV.

-
- [1] C. Tusche, A. Krasnyuk, and J. Kirschner, *Ultramic.* **159**, 520 (2015).
- [2] C. Seidel, R. Ellerbrake, L. Gross, and H. Fuchs, *Phys. Rev. B* **64**, 195418 (2001).
- [3] P. Puschnig, S. Berkebile, A. Fleming, G. Koller, K. Emtsev, T. Seyller, J. Riley, C. Ambrosch-Draxl, F. Netzer, and M. Ramsey, *Science* **326**, 702 (2009).
- [4] J. P. Perdew, K. Burke, and M. Ernzerhof, *Phys. Rev. Lett.* **77**, 3865 (1996).
- [5] M. Frisch, G. Trucks, H. Schlegel, G. Scuseria, M. Robb, J. Cheeseman, G. Scalmani, V. Barone, B. Mennucci, G. Petersson, H. Nakatsuji, M. Caricato, X. Li, H. Hratchian, A. Izmaylov, J. Bloino, G. Zheng, J. Sonnenberg, M. Hada, M. Ehara, K. Toyota, R. Fukuda, J. Hasegawa, M. Ishida, T. Nakajima, Y. Honda, O. Kitao, H. Nakai, T. Vreven, J. Montgomery, J. Peralta, F. Ogliaro, M. Bearpark, J. Heyd, E. Brothers, K. Kudin, V. Staroverov, R. Kobayashi, J. Normand, K. Raghavachari, A. Rendell, J. Burant, S. Iyengar, J. Tomasi, M. Cossi, N. Rega, J. Millam, M. Klene, J. Knox, J. Cross, V. Bakken, C. Adamo, J. Jaramillo, R. Gomperts, R. Stratmann, O. Yazyev, A. Austin, R. Cammi, C. Pomelli, J. Ochterski, R. Martin, K. Morokuma, V. Zakrzewski, G. Voth, P. Salvador, J. Dannenberg, S. Dapprich, A. Daniels, Ö. Farkas, J. Foresman, J. Ortiz, J. Cioslowski, and D. Fox, *Gaussian 09 Revision D.01*, Gaussian Inc. Wallingford CT 2009.
- [6] M. Mundt and S. Kümmel, *Phys. Rev. B* **76**, 035413 (2007).
- [7] L. Kronik, A. Makmal, M. L. Tiago, M. M. G. Alemany, M. Jain, X. Huang, Y. Saad, and J. R. Chelikowsky, *Phys. Stat. Sol. B* **243**, 1063 (2006).
- [8] M. Dauth, M. Wiessner, V. Feyer, A. Schöll, P. Puschnig, F. Reinert, and S. Kümmel, *New J. Phys.* **16**, 103005 (2014).
- [9] N. Troullier and J. L. Martins, *Phys. Rev. B* **43**, 1993 (1991).

Publication 3

Angle-resolved photoemission from outer valence states: approximate Dyson orbitals from time-dependent density functional theory

In preparation

M. Dauth and S. Kümmel

Theoretical Physics IV, University of Bayreuth, D-95440 Bayreuth, Germany

Publ.3

My contribution

I performed all calculations presented in the manuscript, implemented the algorithms to compute the Dyson orbitals, wrote a first draft of the manuscript, and lead the scientific discussion.

Publ.3

Angle-resolved photoemission from outer valence states: approximate Dyson orbitals from time-dependent density functional theory

Matthias Dauth, and Stephan Kümmel

Theoretical Physics IV, University of Bayreuth, 95440 Bayreuth, Germany

(Dated: June 8, 2016)

Photoemission spectroscopy is a primary technique for characterizing the electronic structure of condensed matter systems. The fundamental quantities for the interpretation of photoemission processes in wavefunction-based quantum mechanics are Dyson orbitals, i.e., the overlaps between N -electron and $N - 1$ -electron wavefunctions. However, today's electronic structure theory is often based on the density-functional theory (DFT) formulation of quantum mechanics. As there is no wavefunction in DFT, Dyson orbitals are, strictly speaking, beyond DFT. We here discuss how approximations to Dyson orbital can be calculated from linear-response time-dependent DFT. Studying the photoemission from adsorbed 3,4,9,10-perylene-tetracarboxylic-dianhydride (PTCDA) we explore the practical usefulness of the concept.

PACS numbers: 33.60.+q,31.15.E-,79.60.-i

I. INTRODUCTION

Photoemission is one of the cornerstones for characterizing physical and chemical properties of materials. Yet, the interpretation or accurate prediction of photoemission data is a non-trivial task. Most systems that are interesting to study from a fundamental or practical perspective are many-electron systems. One, thus, has to face the question of how to properly embed involved electron-electron interactions in theories that aim to describe photoemission. An intuitive view on the ejection of a single electron can be gained, for instance, from the quasiparticle picture. It provides a natural framework in which a quasihole (or quasidelectron for electron injection) is dressed by the interaction with its environment. Quasiparticle energies are directly related to photoemission energies, quasiholes and electrons are described by so-called Dyson orbitals. They are solutions to the identically named Dyson equation [1, 2]. Alternatively, Dyson orbitals can be viewed from a stringent many-body wavefunction perspective. They emerge as effective single particle orbitals which are formally defined as the projection of the – possibly excited – many-body wavefunction of an ionized system $\psi_I(N \pm 1)$ with $N \pm 1$ electrons onto its initial N electron ground-state wavefunction. Even without invoking formal arguments, it seems plausible from the definition of Dyson orbitals that they are related to photoemission. Due to the projection of the $N - 1$ onto the N electron state, the resulting Dyson orbitals can be interpreted as to describe the missing electron.

In practice, the most frequently applied realization of the quasiparticle ansatz is many-body perturbation theory in the GW approximation [1–3]. Typically, the GW method achieves a reliable description of ionization energies [4–6]. Likewise frequently used is density-functional theory (DFT). In common applications one assigns ground-state single particle eigenvalues to ionization energies [7–11]. This is exact for the highest occupied molecular orbital (HOMO) eigenvalues [12–15] but lacks a rigorous connection for eigenvalues that lie be-

neath the HOMO. Yet, Kohn-Sham (KS) and generalized KS eigenvalues can be tied to quasiparticle energies as they form the leading contributions in a perturbation expansion [16, 17]. Applying sophisticated exchange-correlation (xc) functionals, such as range-separated hybrids, the accuracy of generalized KS eigenvalues can even reach the GW level [18, 19].

Single particle molecular orbitals play a comparable role in DFT as Dyson orbitals do in many-body perturbation theory [20–22]. They share several formal similarities such as being solutions to effective single particle equations, reproducing the exact electron density, and having the same exponential decay [20]. Further, it has been argued that the exact KS xc potential is the variationally best local approximation to the exchange correlation self-energy in the Dyson equation [21]. Despite these facts, orbitals from DFT do not resemble all features of Dyson orbitals as the former would lead, for example, to infinite quasiparticle lifetimes. Further, Dyson orbitals are neither normalized nor orthogonal. The key differences between DFT orbitals and Dyson orbitals arise from the distinctly different nature of the KS, respectively Dyson equation. Whereas the former is a single particle equation for auxiliary particles, the latter is an exact many-body equation for charged excitations and probability amplitudes (Dyson orbitals). Nevertheless, the Dyson equation has the form of an effective single particle equation with all interactions embedded in the self-energy, which is in general non-local in space and time [1, 3].

That KS orbitals can still have an – admittedly approximate – physical interpretation has been underpinned by studies using angle-resolved photoemission spectroscopy (ARPES) [23–32]. These works are based on the notion that the photoemission process can be described as a transition of an electron from a molecular orbital (MO) into the state of an unbound photoelectron. Approximating the latter as completely unperturbed, i.e., assuming the emitted electron can be reasonably described by a plane wave (PW), a one-to-one relation between ARPES

intensities and orbitals φ_i has been established [23, 33],

$$J \propto |\langle e^{i\mathbf{k}\mathbf{r}} | \mathbf{A}\mathbf{p} | \varphi_i(\mathbf{r}) \rangle|^2 \delta(E_k + \hbar\omega - \varepsilon_i) \propto |\tilde{\varphi}_i(\mathbf{k})|^2. \quad (1)$$

The intriguing resemblance of certain experimental spectra with the ones obtained from MOs of planar organic molecules doubtlessly supports the physical interpretation of MOs as approximations to Dyson orbitals [23–25, 27, 28]. Yet, the interpretability is strongly coupled to the satisfaction of a few premises [23, 27]. Particularly the level of sophistication of the xc functional approximations has a major impact on the reliability of MOs because all many-body effects are ingrained in the xc functional. As the interpretability of KS orbitals is closely related to the quality of eigenvalues, a reliable description of eigenvalues is a necessary requirement for predicting the right orbitals in the right energetic order [17, 19, 27, 34, 35]. The prominent self-interaction error plays a major role in this instance [27, 34, 35]. One needs to be particularly cautious when considering deeper lying eigenvalues that are approximate even with the ultimate xc functional.

Further, effects that are beyond the molecular orbital interpretation have been reported in Ref. 30. A possibility to go one step beyond the mere MO interpretation while still resting on DFT calculations has been proposed for photoemission processes in which the ionized system remains in its ground state. In a nutshell, one constructs approximate Dyson orbitals from the ground-state KS Slater determinants of the neutral and ionized system [30, 36, 37]. As the resulting Dyson orbital emerges as a coherent superposition of all initially occupied orbitals, one breaks away from the single MO interpretation. This might be a useful concept for excited final states, too.

In this work we want to demonstrate how to calculate approximate Dyson orbitals from time-dependent DFT (TDDFT) that correspond to excited molecular final states. Therefore, we briefly review the connection of Dyson orbital and ARPES intensities in Sec. II. In Sec. III we propose a way to calculate approximate Dyson orbitals from TDDFT in the linear response limit. We begin the discussion of the results reviewing ARPES intensities obtained from the molecular orbital perspective and compare to measured intensities of PTCDA in Sec. IV. Subsequently, we contrast the Dyson orbitals from TDDFT with the experimental ARPES intensities of PTCDA in Sec. V. A conclusion is offered in Sec. VI.

II. PHOTOEMISSION IMAGING DYSON ORBITALS

To derive an approach for calculating ARPES using Dyson orbitals from DFT, we want to give an overview of the photoionization process expressed in terms of Dyson orbitals. Describing the vertical ionization process triggered by a photon with energy $\hbar\omega$ via Fermi's Golden

Rule in dipole approximation [38], the photoemission intensity writes

$$J \propto |\langle \Psi^I | \mathbf{A} \cdot \mathbf{P} | \Psi^0 \rangle|^2 \delta(\hbar\omega + E^0 - E^I). \quad (2)$$

It is proportional to the matrix element with the initial ground state Ψ^0 with N electrons, the dipole operator $\mathbf{A} \cdot \mathbf{P}$, and the final state Ψ^I . Here, \mathbf{A} is the vector potential of the electro-magnetic field and \mathbf{P} denotes the many-body momentum operator. We approximate Ψ^I as an antisymmetrized product of the state of the ionized molecule Ψ^{I+} (quantities of the ionized system are denoted by $+$) and the state of the emitted electron $\chi_{\mathbf{k}}$ under the assumption that correlation between both states can be neglected. Ψ^{I+} is either in the ground state $I = 0$ or in an excited state $I > 0$.

With the definition of Dyson orbitals

$$d^I(\mathbf{r}) = \sqrt{N} \langle \Psi^I(N-1) | \Psi^0(N) \rangle, \quad (3)$$

the many-body matrix element can be reduced to a effective single particle matrix element [30, 36],

$$J \propto |\langle \chi_{\mathbf{k}}(\mathbf{r}) | \Delta | d^I(\mathbf{r}) \rangle|^2 \delta(\hbar\omega + E^0 - E^{I+} - E_{\mathbf{k}}). \quad (4)$$

In our notation d^I is the Dyson orbital to the transition from the initial ground state to the final molecular state Ψ^{I+} .

Furthermore, applying the PW approximation simplifies the evaluation of the matrix element significantly, leading to a one-to-one relation of ARPES intensities to Dyson orbitals,

$$J \propto |d^I(\mathbf{k})|^2. \quad (5)$$

On a formal level one can deduce the intensity within the single particle interpretation given in Eq. (1) from Eq. (2) under a few assumptions. First, the initial and final states are approximated by Slater determinants, $\Psi \approx \Phi$. Usually this simplification is supposed to be well justified for organic systems with non-degenerate ground states [20, 39–41]. Second, electron relaxation effects have to be negligible [30]. Particularly for excited final states, there is a third approximation that has to be made in order to obtain Eq. (1). Instead of a sound treatment of the excited state, one assumes that the final molecular state emerges from the initial state Slater determinant by annihilating only one particle in a certain single particle state φ_i . It corresponds to the orbital which is depleted during the photoemission process. This approximation certainly depends on how dominant the single particle character of the considered excitation is.

III. EXCITED STATES FROM TDDFT

Despite being a ground-state theory in its original formulation, DFT can systematically be extended to describe excitations. Within TDDFT in the linear-response

limit, excited-state properties can be obtained by evaluating the first order density response to a small perturbation [42–45]. Applying common xc potential approximations (in their adiabatic formulation), respectively the corresponding xc kernels, usually yields reasonable estimates for excitation energies and oscillator strengths [46–49]. Pertinent to our purpose, TDDFT provides an approximate way to assign an excited-state wavefunction. Due to the superposition of different particle-hole excitations, which are mediated by the xc kernel, an approximate excited-state wavefunctions can be written in a configuration interaction form [50] (using the Tamm-Dancoff approximation [51]),

$$|\Phi^{I+}\rangle = \sum_{\alpha,l} X_{\alpha,l} a_l^\dagger a_\alpha |\Phi^{0+}\rangle. \quad (6)$$

Here, the index α denotes occupied ground-state orbitals, l virtual orbitals, and a^\dagger the creation, respectively a the annihilation operator.

To follow up with the Dyson orbital calculation, one needs to conduct the integration between the wavefunctions according to Eq. (3). For this purpose it is helpful to reformulate the N electron ground-state Slater determinant as an expansion by minors that reduces the number of coordinates of the determinant to $N - 1$ [36],

$$\Phi^0(N) = \frac{1}{\sqrt{N}} \sum_{i=1}^N \varphi_i^0(\mathbf{r}) (-1)^{i+N} \Phi_i^0(N-1). \quad (7)$$

The index i implies that orbital φ_i^0 is excluded from the $\Phi_i^0(N-1)$ determinant. Inserting Eqs. (7) and (6) in Eq. (3) allows for rewriting the Dyson orbitals as a coherent superposition of all N occupied orbitals of the initial state weighted by the remaining overlap,

$$d^I(\mathbf{r}) = \sum_{i=1}^N \varphi_i^0(\mathbf{r}) \frac{1}{\sqrt{N}} (-1)^{i+N} \langle \Phi^{I+} | \Phi_i^0 \rangle. \quad (8)$$

Here, each overlap accords with one weighting factor and we can simplify the Dyson orbital to

$$d^I(\mathbf{r}) = \sum_{i=1}^N \varphi_i^0(\mathbf{r}) w_i^{I*}. \quad (9)$$

Eventually, the Dyson orbital boils down to a superposition of the occupied ground-state orbitals of the neutral molecule weighted by the coefficients,

$$w_i^I = \frac{1}{\sqrt{N}} (-1)^{i+N} \langle \Phi_i^0 | \sum_{l,\alpha} X_{l,\alpha} a_l^\dagger a_\alpha | \Phi^{0+} \rangle. \quad (10)$$

IV. RELATING THE “HOMO-1” EMISSION PEAK OF PTCDA TO MOLECULAR ORBITALS

To probe the approach we draw on ARPES measurements on a 3,4,9,10-perylene-tetracarboxylic-dianhydride

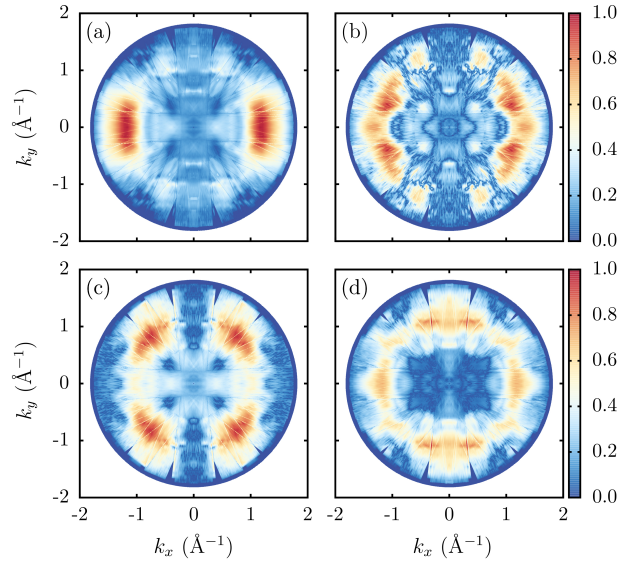


FIG. 1. Experimental momentum maps of PTCDA on Ag(110) from Ref. 27. Figures (a)-(d) show the four different contributions to the “HOMO-1” PTCDA emission band, obtained from a principle component analysis. The maps are ordered by increasing binding energies (relative to the Fermi level) of $E_B = 3.1$ eV (a), 3.2 eV (b), 3.3 eV (c), and 3.5 eV (d).

(PTCDA) monolayer absorbed on Ag(110) [27, 28]. This system has delivered unique insights because a principle component analysis of emission band beneath the “HOMO”-emission peak has revealed four distinct ARPES intensity patterns [27]. They lie within a range of just 0.4 eV, each originating from a different excited final state though. We refer to this emission band as the “HOMO-1” peak. Its four components are displayed in Fig. 1 (a)-(d), ordered by increasing binding energy.

Our aim in the following sections is to associate the four patterns with momentum maps of molecular orbitals and Dyson orbitals from the presented TDDFT approach to gain detailed insights which orbitals are needed to generate the measured intensities. We start the discussion from the individual molecular orbital perspective, i.e., assigning single molecular orbitals to the ARPES spectra according to their energetic order.

As an example, the commonly used PBE xc functional [52] predicts the four outermost valence orbitals (beneath the HOMO) to be of σ type. Their resulting momentum maps are displayed in Fig. 2. Neither of the PBE momentum maps can be doubtlessly associated with one of the experimentally recorded intensity patterns. More appropriate π type orbitals lie beneath the σ orbitals [28]. Apparently, PBE lacks the sensitivity to push down σ , respectively spatially more localized, orbitals in the energetic order which is one of the notorious deficiency of self-interaction affected functionals [34, 35]. This is in line with the argumentation in Ref. 27, where the presence of the self-interaction error is shown to have major

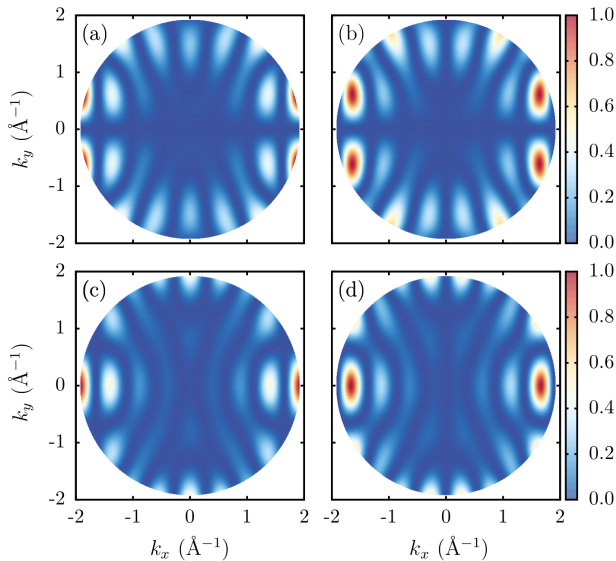


FIG. 2. Momentum maps of the four frontier valence orbitals beneath the HOMO from PBE ordered by increasing binding energy (a)-(d). The orbitals to (a) and (b), respectively (c) and (d) are each twofold degenerate in energy. The maps are evaluated at a kinetic photo electron energy of $E_k = 14.05$ eV.

impact on a physically sound interpretation of orbitals.

In analogy to the momentum maps obtained from the self-interaction corrected (SIC) KS orbitals in Ref. 27, we display the maps of the KS HOMO-1 to HOMO-4 from a refined SIC version [53] in Fig. 3. In Ref. 27 the variance under unitary orbital transformations of the Perdew and Zunger (PZ) [54] SIC expression gave reason to employ a real, localizing unitary transformations. Here, we want to exploit the PZ SIC in a more systematic and physical way. Vital to all electronic structure approaches and DFT in particular is the energy minimization principle. In the very same spirit, it seems promising to use a set of orbitals that minimizes the SIC energy. More detailed, we use a complex unitary orbital transformation that minimizes the PZ SIC energy based on LDA [53]. To stick to the realm of KS DFT we used the generalized [55] Krieger-Li-Iafrate approximation [56] to the generalized optimized effective potential equation (GOEP) that is an extension to the traditional OEP for unitarily variant functionals [55, 57].

We find four π orbitals located beneath the HOMO. The experimental intensity pattern in Fig. 1 (a) can easily be identified with the SIC HOMO-4 momentum map in Fig. 3 (d) due to the unique intensities around $k_x \approx 1.2 \text{ \AA}^{-1}$, $k_y \approx 0 \text{ \AA}^{-1}$. Next, we want to assign the maps displayed in Fig. 3 (a) and (c). As the main intensities in Fig. 3 (a), which stem from the SIC HOMO-1, are located at larger $k_y \approx 1.0 \text{ \AA}^{-1}$ compared to the ones in Fig. 3 (c) ($k_y \approx 0.6 \text{ \AA}^{-1}$), we associate the former with the measured ARPES intensity in Fig. 1 (c) and the latter with Fig. 1 (b), respectively. The momentum map of the HOMO-2 orbital in Fig. 1 (b) reproduces mainly the

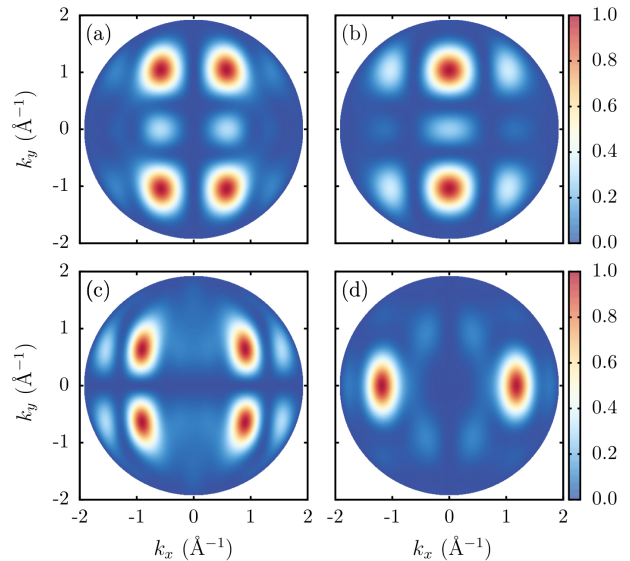


FIG. 3. Momentum maps of the HOMO-1 (a) to HOMO-4 (d) obtained from KS-SIC. The maps are evaluated at a kinetic photo electron energy of $E_k = 14.05$ eV. The maps (a)-(d) are ordered by increasing binding energy, respectively by their eigenvalue sequence.

blurred peaks around $k_x \approx 0.0 \text{ \AA}^{-1}$ and $k_y \approx \pm 1.1 \text{ \AA}^{-1}$ in Fig. 1 (b). However, it lacks the vertical intensity bands at $k_x \approx \pm 1.2 \text{ \AA}^{-1}$. Due to the discrepancies, it remains not completely clear whether the experimental pattern can be fully explained by this single orbital. A possible reason might be the influence of the silver substrate, as the corresponding experimental momentum map is energetically close to the Ag d band emission. Besides, we cannot exclude the possibility that the concept of just one orbital being responsible for the photoemission is stretched to its limits.

Although we have identified the presented SIC momentum maps and their MOs as possible origins for the ARPES intensities, they do not emerge in the correct energetic order. An explanation might be that we compare calculations of an isolated molecule with measurements on an adsorbed monolayer. This is plausible since the energetic differences between the individual contributions lie within a range of just 0.4 eV, which is on the scale where adsorption effects might tilt the energetic ordering with respect to the gas phase. Likewise, the SIC HOMO-1 until HOMO-4 orbitals are only separated by 0.3 eV. Predicting the correct order of states in such a small interval is certainly challenging for every DFT method and lies at the edge of capability of DFT and yet more the interpretation of the orbitals.

V. DYSON ORBITALS

We now proceed to the TDDFT model and raise the question whether a more stringent treatment of excita-

tions may lead to reliable results, especially with respect to the PBE momentum maps. Therefore, we evaluate the ARPES intensity in Eq. (5) with the Dyson orbitals of Eq. (9) for PBE using the QChem code [58] and the cc-pVTZ basis sets [59]. The most straightforward way to ascribe the calculated Dyson orbitals, respectively their momentum maps, to experiment is by successively increasing excitation energy. Following this strategy, the four Dyson orbitals corresponding to the four lowest excitation energies predominantly reproduce the spatial structure of the molecular orbitals predicted by PBE. Expressed in terms of the weighting coefficients in Eq. (9), there is one dominant contribution to each Dyson orbital that coincides with the corresponding molecular orbital (the Dyson orbital to the first excitation resembles the HOMO-1 orbital and so on). Subsequent weighting factors are negligible as they are at least one order of magnitude smaller. Note that ARPES intensities scale with the second power of the weighting coefficients. The momentum maps obtained from the first four excitations, respectively from the corresponding Dyson orbitals, hardly show differences to the momentum maps from the MOs presented in Fig. 2. From this perspective, it seems like the TDDFT approach is not able to make corrections to the deficiencies buried in the PBE approximation.

Despite being a straightforward approach for the assignment of experimental spectra to TDDFT excitations, it might lack a criterion for transition probabilities. To further distinguish between experimentally relevant excitations we suggest another ansatz.

Although oscillator strengths are formally related to optical transitions, they provide a proper criterion for the probability to find the cation in a certain excited state. In this sense, an oscillator strength close to zero indicates a dark final state that will not be seen in experiment. In contrast, high values are hallmarks of high transition probabilities. The second requirement follows directly from Fermi’s golden rule, respectively the transition matrix element in Eq. (4). Among the constituents of the matrix element are the Dyson orbital, the dipole operator, and the state of the emitted electron. The latter two parts are independent of the molecular system, but the Dyson orbital is not. It comprises all information about the overlap of the wavefunctions of the initial and the ionized system. The Dyson orbital is in general not normalized, $\langle d | d \rangle \leq 1$. Because the transition probability is proportional to the square of the matrix element, the norm of the Dyson orbital accordingly has to be proportional to the transition probability.

Both arguments suggest a qualitative ansatz to approximately assign the TDDFT excitations to the experimentally measured excitations: Beginning with the lowest TDDFT excitation in energy, we check whether the norm of the Dyson orbital and the oscillator strength is high (compared to other excitations), where we consider their product as the critical quantity. In the case of both attributes, respectively their product, having low values, the transition to this particular excited state will not be

	$\langle d d \rangle \cdot f_I$	E_{exc} (eV)	Dyson orbital $d \approx$
(a)	0.0008	1.44	$-0.88\varphi_{H-5} + 0.33\varphi_{H-8} + 0.25\varphi_{H-10}$
(b)	0.0005	1.51	$0.68\varphi_{H-6}$
(c)	0.01	1.78	$-0.89\varphi_{H-9} - 0.31\varphi_{H-5} + 0.12\varphi_{H-10}$
(d)	0.004	1.976	$-0.94\varphi_{H-10} + 0.15\varphi_{H-5}$

TABLE I. Data of the four relevant excitations calculated with TDDFT based on PBE. $\langle d^I | d^I \rangle \cdot f_I$ is the product of the Dyson orbital norm and the oscillator strength f_I where we display and consecutively label only excitation with a high product. Omitted excitation have an at least two orders of magnitude smaller product. E_{exc} denotes the excitation energy. The last column shows the orbital contributions to the Dyson orbital according to Eq. (9) with all weighting factors that are not more than ten times smaller than the highest one. The momentum maps (a)-(d) in Fig. 5 correspond to the excitations (a)-(d). The orbital in the last column are numbered by their energetic order from the HOMO (H) downwards. Note that degenerate orbitals are counted separately.

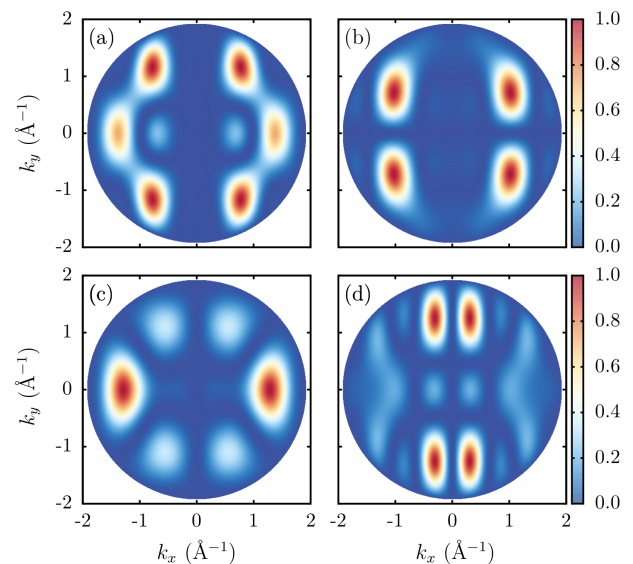


FIG. 4. Momentum maps from Dyson orbital calculations based on TDDFT with PBE evaluated at a kinetic photo electron energy of $E_k = 14.05$ eV. (a)-(d) shows the four different Dyson orbital momentum maps to the “HOMO-1” PTCDA emission ordered by increasing TDDFT excitation energy, respectively binding energy.

related to the measured intensities and we consider the state with the next higher excitation energy (within an adequate energy interval) and repeat the procedure. We apply this procedure consecutively to refer all measured spectra to a specific TDDFT excitation along with its Dyson orbital if possible.

A. Dyson orbitals from time-dependent DFT

Having established a scheme to relate TDDFT final-state excitations to ARPES, we discuss the results of this approach based on PBE.

The first distinct difference to the previous approach is that all Dyson orbitals (within the first 20 TDDFT excitations) that have σ -character originate from excitations with a vanishingly low oscillator strength ($f_I < 10^{-4}$). Thus, they do not meet the criterion of having a high product of the oscillator strength and Dyson orbital norm and hence will not be assigned to experiment. We present the details about the four relevant excitations in table I, in which we only label the relevant excitations according to their energetic position from (a) to (d). Additionally, the four TDDFT excitations lie in the right energy range although they do not coincide with the experimental ordering. In detail, the gap between the HOMO and the ‘‘HOMO-1’’ peak is with 1.4 eV close to the experimental one of 1.2 eV. All four excitations are located in an interval of about 0.5 eV (experiment 0.4 eV). However, the energetic ordering of the individual TDDFT momentum maps according to their excitation energies does not comply with experiment, just as in the case of the SIC orbitals. As we performed all calculations on the basis of PBE, this hardly comes as a surprise. The difference to the MO interpretation can further be emphasized as the Dyson orbitals now come as superpositions of molecular orbitals. Thus, the intensity patterns are generated by more than one orbital. The detailed composition of the Dyson orbitals is displayed in table I and the resulting momentum maps are shown in Fig. 4 (a)-(d). Taken as a whole, the measured maps in Fig. 4 match appreciably better with experiment than the maps of the frontier PBE molecular orbitals and the ones from the straightforward assignment within TDDFT based on PBE. In detail, the intensity pattern of the experimental map in Fig. 1 (a) is clearly reflected by the map of Fig. 4 (c). Note that the main features of Fig. 4 (c) around $k_y = 0 \text{ \AA}^{-1}$ and the four side intensities around $k_y = \pm 1 \text{ \AA}^{-1}$, which are present in experiment and theory, are generated by different orbital contributions. Similarly, the intensities in the momentum map of Fig. 4 (a) stem from multiple orbitals. The dominant features that are located at $k_x \approx \pm 0.8 \text{ \AA}^{-1}$ and $k_y \approx \pm 1.0 \text{ \AA}^{-1}$ are due to the HOMO-5 which has the largest weighting coefficient [60]. The less pronounced intensities at $k_y \approx 0 \text{ \AA}^{-1}$ originate from the two additional orbitals that are listed in table I. Contrasted to experiment, we find a possible counterpart with Fig. 1 (b), which in addition to the main intensities shows intensities around $k_y \approx 0 \text{ \AA}^{-1}$. Owing to the close resemblance of these maps, our first conclusion here is that the Dyson orbital can comprise additional features that go beyond the single molecular orbital interpretation. Particularly, intensities that are less pronounced stem from non trivial orbital superpositions.

To complete the assignment puzzle, we relate the four

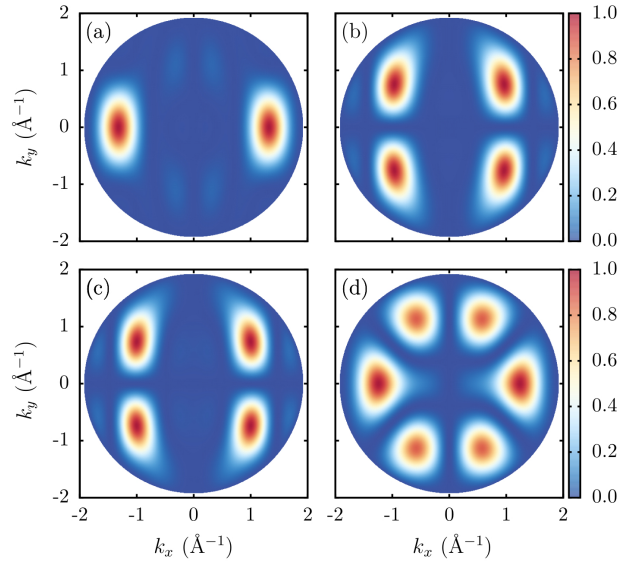


FIG. 5. Momentum maps from Dyson orbital calculations based on TDHF evaluated at a kinetic photo electron energy of $E_k = 14.05 \text{ eV}$. (a)-(d) shows the four different Dyson orbital momentum maps to the ‘‘HOMO-1’’ PTCDA emission ordered by increasing excitation energy, respectively binding energy.

distinct intensity peaks at $k_x \approx \pm 1.0 \text{ \AA}^{-1}$ and $k_y \approx 0.8 \text{ \AA}^{-1}$ in Fig. 4 (b) to Fig. 1 (c). Finally, the remaining momentum map of our analysis yields a new candidate to explain the intensity pattern of Fig. 1 (d). Inside the washed-out intensity at $k_y \approx \pm 1.0 \text{ \AA}^{-1}$ there is a finer structure present with two maxima at $k_x \approx \pm 0.3 \text{ \AA}^{-1}$. Thus, the peak might be pieced together by two separate intensities maxima as they are predicted by the TDDFT Dyson orbital in Fig. 4 (d). Additionally, the latter map shows an admittedly weak intensity band around $k_x \approx \pm 1 \text{ \AA}^{-1}$ that could reflect the intensity band in its experimental counterpart.

All in all, the TDDFT approach illustrates that, first, Dyson orbitals can deviate from the single molecular orbital interpretation and rather are composed of a superposition of MOs. Second, including the oscillator strength as a criterion for the selection of relevant excitations rejects Dyson orbitals that have σ -orbital character, which are not present in the experimental reference. This significantly improves the resemblance of the momentum maps compared to the mere MO interpretation.

B. Dyson orbitals from Hartree-Fock

Within our approach, one is not restricted to a description of photoemission with TDDFT but can, for instance, use the conceptually similar is time-dependent Hartree-Fock (TDHF). An advantage of Hartree-Fock is that it is free of self-interaction. This is particularly interesting because the requirement of the xc-kernel foils the use

	$\langle d d \rangle \cdot f_I$	E_{exc} (eV)	Dyson orbital $d \approx$
(a)	0.03	2.45	0.58 $\varphi_{\text{H}-4}$
(b)	0.18	3.39	0.57 $\varphi_{\text{H}-3}$
(c)	0.003	3.88	0.21 $\varphi_{\text{H}-3}$
(d)	0.007	4.48	$-0.12 \varphi_{\text{H}-1} + 0.11 \varphi_{\text{H}-4}$

TABLE II. Data of the four relevant excitations calculated with TDHF. $\langle d^I | d^I \rangle \cdot f_I$ is the product of the Dyson orbital norm and the oscillator strength F_I where we display and consecutively label only excitation with a high product. Omitted excitation have an at least two orders of magnitude smaller product. E_{exc} denotes the excitation energy. The last column shows the orbital contributions to the Dyson orbital according to Eq. (9) with all weighting factors that are not more than ten times smaller than the highest one. The momentum maps (a)-(d) in Fig. 5 correspond to the excitations (a)-(d).

of the SIC approach presented above as there is no kernel to xc-potentials constructed via the GOEP [55, 57], nor to its approximate generalized [55] Krieger-Li-Iafrate [56] counterpart known by now. Yet, one has to pay the price of passing on electron correlation when using HF. A closer look at the momentum maps of the frontier HF orbitals substantiates the use of HF, as the LUMO, HOMO until HOMO-4 spectra are very similar to the KS-SIC results with the same energetic ordering. The energetic positions with respect to the HOMO eigenvalue do not coincide, though. We therefore do not expect the energetic positions of TDHF excitations to improve significantly.

Within the first couple of excitations we find four contributions with a comparatively high product of the Dyson orbital norm and oscillator strength. All other contributions are at least two orders of magnitude smaller. These values, excitation energies, and the resulting Dyson orbitals are depicted in table II.

Going through the excitations (a) to (d), several interesting features occur. From an eigenvalue sequence point of view, one would expect that the Dyson orbital to the first relevant excitation should approximately coincide with the HOMO-1. This is, however, not necessarily the case as excitation (a) explicitly illustrates. Here, the Dyson orbital is mainly dominated by the HOMO-4. In this context we use "dominated" to highlight that there are other orbitals contributing to the Dyson orbitals. Yet, their weighting factors are at least one order smaller. As the intensity is proportional to the square of the weighting factors, their influence on the momentum maps is hardly recognizable. Comparing the momentum map from excitation (a) in Fig. 5 to the first experimental pattern, they are in good accordance. This is particularly remarkable, as in contrast to assigning the orbitals by their eigenvalue sequence to experiment, we find the matching Dyson orbital in the right order. The

situation is similar for excitation (b). Its Dyson orbital is set by the HOMO-3 and the resulting momentum map in Fig. 5 (b) approximately reflects the main features of the second experimental map in Fig. 1 (b). Yet, it misses the intensity present at $k_y = 0 \text{ \AA}^{-1}$. Turning towards excitation (c), our analysis predicts a momentum map akin to the one of excitation (b) as both show a similar Dyson orbital structure. Compared to its experimental counterpart in Fig. 5 (c) it shows a similar intensity pattern but with the main experimental peaks being at higher $|k_y|$. Having a closer look at excitation (d), we find a Dyson orbital with a new feature. By now, all TDHF calculations have yielded Dyson orbitals that are merely determined by one single orbital. Opposed to this, there are two equal contributions, i.e., the HOMO-1 and the HOMO-4. The corresponding momentum map is shown in Fig. 5 (d) and reveals six distinct intensity maxima. The four peaks at $k_x \approx \pm 0.5 \text{ \AA}^{-1}$ and $k_y \approx \pm 1.0 \text{ \AA}^{-1}$ can be associated with the experimental intensities of Fig. 1 (d) if one assumes that the experimental intensities are composed of four maxima. Furthermore, the intensities around $k_x \approx \pm 1.2 \text{ \AA}^{-1}$ and $k_y \approx 0.0 \text{ \AA}^{-1}$ are visible in both spectra. One may argue that the six intensities resemble the experimental data. However, the ratio of the intensity heights is reversed in contrast to experiment.

VI. CONCLUSION

In summary, the focus of our present work was to link ARPES intensities from outer valence band emission to Dyson orbitals, respectively molecular orbitals. With the deconvoluted "HOMO-1" emission band from PTCDA that reveals four different contributions we were able to underpin that a direct assignment of orbitals from DFT to the measured ARPES spectra according to their eigenvalue sequence is possible when using a high quality xc functional. An example is the self-interaction corrected approach we explained. From a fundamental point of view our analysis gives rise that high quality KS orbitals from DFT can be reliable approximations to Dyson orbital. This might, for instance, be beneficial for choosing a sound starting point for perturbative G_0W_0 calculations.

However, not all features of the experimental momentum maps can be unambiguously linked to one single orbital. To go beyond the mere orbital interpretation we constructed approximate Dyson orbitals from TDDFT. Thereby, we calculated the excitations of the ionized molecular state with TDDFT. Contrary to the single orbital interpretation the Dyson orbitals emerge as a coherent superposition of KS orbitals. By considering the norm of the Dyson orbitals and the oscillator strength as a qualitative criterion to assign excitations to ARPES intensities we found fairly good matching momentum maps with PBE. Although multi orbital contributions to one Dyson orbital can entail detailed features of the momentum maps, it is not possible to recognize all experimental

features. Further, the energetic ordering of the Dyson orbitals is wrong. The freedom of self-interaction of TDHF yields a correct ordering underlining the importance of an effective self-interaction correction within DFT.

ACKNOWLEDGMENTS

S.K. and M.D. acknowledge support by Deutsche Forschungsgemeinschaft Graduiertenkolleg 1640 and the Bavarian State Ministry of Science, Research, and the Arts for the Collaborative Research Network Soltech

-
- [1] L. Hedin, Phys. Rev. **139**, A796 (1965).
- [2] W. G. Aulbur, L. Jönsson, and J. W. Wilkins, Solid State Phys. **54**, 1 (1999).
- [3] M. S. Hybertsen and S. G. Louie, Phys. Rev. B **34**, 5390 (1986).
- [4] F. Bruneval and M. A. L. Marques, J. Chem. Theory Comput. **9**, 324 (2012).
- [5] N. Marom, F. Caruso, X. Ren, O. T. Hofmann, T. Körzdörfer, J. R. Chelikowsky, A. Rubio, M. Scheffler, and P. Rinke, Phys. Rev. B **86**, 245127 (2012).
- [6] F. Caruso, P. Rinke, X. Ren, M. Scheffler, and A. Rubio, Phys. Rev. B **86**, 081102 (2012).
- [7] N. Binggeli and J. R. Chelikowsky, Phys. Rev. Lett. **75**, 493 (1995).
- [8] J. Akola, M. Manninen, H. Häkkinen, U. Landman, X. Li, and L.-S. Wang, Phys. Rev. B **62**, 13216 (2000).
- [9] L. Kronik, T. Stein, S. Refaely-Abramson, and R. Baer, J. Chem. Theory Comput. **8**, 1515 (2012).
- [10] U. Salzner and R. Baer, J. Chem. Phys. **131**, 231101 (2009).
- [11] T. Körzdörfer and S. Kümmel, Phys. Rev. B **82**, 155206 (2010).
- [12] J. F. Janak, Phys. Rev. B **18**, 7165 (1978).
- [13] J. P. Perdew, R. G. Parr, M. Levy, and J. L. Balduz Jr, Phys. Rev. Lett. **49**, 1691 (1982).
- [14] C.-O. Almbladh and U. von Barth, Phys. Rev. B **31**, 3231 (1985).
- [15] M. Levy, J. P. Perdew, and V. Sahni, Phys. Rev. A **30**, 2745 (1984).
- [16] T. Körzdörfer and S. Kümmel, Phys. Rev. B **82**, 155206 (2010).
- [17] D. P. Chong, O. V. Gritsenko, and E. J. Baerends, J. Chem. Phys. **116**, 1760 (2002).
- [18] S. Refaely-Abramson, S. Sharifzadeh, N. Govind, J. Autschbach, J. B. Neaton, R. Baer, and L. Kronik, Phys. Rev. Lett. **109**, 226405 (2012).
- [19] D. Egger, S. Weissman, S. Refaely-Abramson, S. Sharifzadeh, M. Dauth, R. Baer, S. Kümmel, J. B. Neaton, E. Zojer, and L. Kronik, J. Chem. Theory Comput. **10**, 1934 (2014).
- [20] P. Duffy, D. P. Chong, M. E. Casida, and D. R. Salahub, Phys. Rev. A **50**, 4707 (1994).
- [21] M. E. Casida, Phys. Rev. A **51**, 2005 (1995).
- [22] G. Onida, L. Reining, and A. Rubio, Rev. Mod. Phys. **74**, 601 (2002).
- [23] P. Puschnig, S. Berkebile, A. J. Fleming, G. Koller, K. Emtsev, T. Seyller, J. D. Riley, C. Ambrosch-Draxl, F. P. Netzer, and M. G. Ramsey, Science **326**, 702 (2009).
- [24] S. Kera, S. Tanaka, H. Yamane, D. Yoshimura, K. K. Okudaira, K. Seki, and N. Ueno, Chem. Phys. **104**, 1 (2010).
- [25] J. Ziroff, F. Forster, A. Schöll, P. Puschnig, and F. Reinert, Phys. Rev. Lett. **104**, 1 (2010).
- [26] B. Stadtmüller, M. Willenbockel, E. M. Reinisch, T. Ules, F. C. Bocquet, S. Soubatch, P. Puschnig, G. Koller, M. G. Ramsey, F. S. Tautz, and C. Kumpf, Europhys. Lett. **100**, 26008 (2012).
- [27] M. Dauth, T. Körzdörfer, S. Kümmel, J. Ziroff, M. Wiessner, A. Schöll, F. Reinert, M. Arita, and K. Shimada, Phys. Rev. Lett. **107**, 193002 (2011).
- [28] P. Puschnig, E.-M. Reinisch, T. Ules, G. Koller, S. Soubatch, M. Ostler, L. Romaner, F. S. Tautz, C. Ambrosch-Draxl, and M. G. Ramsey, Phys. Rev. B **84**, 235427 (2011).
- [29] D. Lüftner, T. Ules, E. M. Reinisch, G. Koller, S. Soubatch, F. S. Tautz, M. G. Ramsey, and P. Puschnig, Proc. Natl. Acad. Sci. USA **111**, 605 (2013).
- [30] M. Dauth, M. Wießner, V. Feyer, A. Schöll, P. Puschnig, F. Reinert, and S. Kümmel, New J. Phys. **16**, 103005 (2014).
- [31] M. Wießner, D. Hauschild, C. Sauer, V. Feyer, A. Schöll, and F. Reinert, Nat. Commun. **5**, 4156 (2014).
- [32] S. Weiß, D. Lüftner, T. Ules, E. M. Reinisch, H. Kaser, a. Gottwald, M. Richter, S. Soubatch, G. Koller, M. G. Ramsey, F. S. Tautz, and P. Puschnig, Nat. Commun. **6**, 8287 (2015).
- [33] J. W. Gadzuk, Phys. Rev. B **10**, 5030 (1974).
- [34] T. Körzdörfer, S. Kümmel, N. Marom, and L. Kronik, Phys. Rev. B **79**, 201205(R) (2009).
- [35] T. Körzdörfer, S. Kümmel, N. Marom, and L. Kronik, Phys. Rev. B **82**, 129903(E) (2010).
- [36] M. Walter and H. Häkkinen, New J. Phys. **10**, 043018 (2008).
- [37] A. Humeniuk, M. Wohlgemuth, T. Suzuki, and R. Mitrić, J. Chem. Phys. **139**, 134104 (2013).
- [38] S. Hüfner, "Photoelectron spectroscopy," (Springer, Berlin, 2003).
- [39] E. J. Baerends and O. V. Gritsenko, J. Phys. Chem. A **101**, 5383 (1997).
- [40] E. J. Baerends, Theor. Chem. Acc. **103**, 265 (2000).
- [41] R. Stowasser and R. Hoffmann, J. Am. Chem. Soc. **121**, 3414 (1999).
- [42] E. Runge and E. K. U. Gross, Phys. Rev. Lett. **52**, 997 (1984).
- [43] R. Bauernschmitt and R. Ahlrichs, Chem. Phys. Lett. **256**, 454 (1996).
- [44] M. a. L. Marques and E. K. U. Gross, in *Annu. Rev. Phys. Chem.*, Vol. 55 (2004) p. 427.
- [45] M. A. L. Marques and E. K. U. Gross, "Time-dependent density functional theory," in *A primer in density functional theory*, edited by C. Fiolhais, F. Nogueira, and M. A. Marques (Springer, Berlin-Heidelberg, 2003) pp. 144–184.
- [46] D. Jacquemin, V. Wathelet, E. A. Perpète, and C. Adamo, J. Chem. Theory Comput. **5**, 2420 (2009).
- [47] S. S. Leang, F. Zaharieiev, and M. S. Gordon, J. Chem.

- Phys. **136**, 104101 (2012).
- [48] M. Miura, Y. Aoki, and B. Champagne, J. Chem. Phys. **127**, 084103 (2007).
- [49] M. Caricato, G. W. Trucks, M. J. Frisch, and K. B. Wiberg, J. Chem. Theor. Comput. **7**, 456 (2011).
- [50] M. E. Casida, "Time-dependent density functional response theory for molecules," in *Recent advances in density functional methods, part I*, edited by D. P. Chong (World Scientific, Berlin, 1995).
- [51] S. Hirata and M. Head-Gordon, Chem. Phys. Lett. **314**, 291 (1999).
- [52] J. P. Perdew, K. Burke, and M. Ernzerhof, Phys. Rev. Lett. **77**, 3865 (1996).
- [53] D. Hofmann, S. Klüpfel, P. Klüpfel, and S. Kümmel, Phys. Rev. A **85**, 062514 (2012).
- [54] J. P. Perdew and A. Zunger, Phys. Rev. B **23**, 5048 (1981).
- [55] T. Körzdörfer, M. Mundt, and S. Kümmel, J. Chem. Phys. **129**, 014110 (2008).
- [56] J. B. Krieger, Y. Li, and G. J. Iafrate, Phys. Rev. A **46**, 5453 (1992).
- [57] S. Kümmel and L. Kronik, Rev. Mod. Phys. **80**, 3 (2008).
- [58] Y. Shao and et al., Phys. Chem. Chem. Phys. **8**, 3172 (2006).
- [59] T. H. Dunning, J. Chem. Phys. **90**, 1007 (1989).
- [60] Regardless of their degree of degeneracy, we label each orbital individually. For example the PTCDA PBE HOMO-1 and HOMO-2 as well as the HOMO-3 and HOMO-4 are each twofold degenerate.

Publication 4

Predicting photoemission intensities and angular distributions with real-time density-functional theory

Physical Review A **93**, 022502 (2016)

M. Dauth and S. Kümmel

Theoretical Physics IV, University of Bayreuth, D-95440 Bayreuth, Germany

Publ.4

My contribution

I implemented the algorithms needed to evaluate the photoemission signal, the absorbing potentials, and the perturbing field. I performed all calculations presented in the paper, wrote a first draft of the manuscript, and lead the scientific discussion.

Publ.4

Predicting photoemission intensities and angular distributions with real-time density-functional theory

M. Dauth and S. Kümmel

Theoretical Physics IV, University of Bayreuth, D-95440 Bayreuth, Germany

(Received 11 December 2015; published 2 February 2016)

Photoemission spectroscopy is one of the most frequently used tools for characterizing the electronic structure of condensed matter systems. We discuss a scheme for simulating photoemission from finite systems based on time-dependent density-functional theory. It allows for the first-principles calculation of relative electron binding energies, ionization cross sections, and anisotropy parameters. We extract these photoemission spectroscopy observables from Kohn-Sham orbitals propagated in real time. We demonstrate that the approach is capable of estimating photoemission intensities, i.e., peak heights. It can also reliably predict the angular distribution of photoelectrons. For the example of benzene we contrast calculated angular distribution anisotropy parameters to experimental reference data. Self-interaction free Kohn-Sham theory yields meaningful outer valence single-particle states in the right energetic order. We discuss how to properly choose the complex absorbing potential that is used in the simulations.

DOI: [10.1103/PhysRevA.93.022502](https://doi.org/10.1103/PhysRevA.93.022502)

I. INTRODUCTION

Outer valence electrons determine a wide range of properties inherent to condensed matter systems that are relevant to physics, chemistry, and material science. A fundamental understanding of these properties can often be gained by analyzing the valence electrons' density of states. The primary technique for determining the density of states is photoemission spectroscopy (PES) [1]. With PES' growing sophistication, increasingly detailed insights have become possible. Even the spatial structure of outer valence molecular orbitals could recently be revealed by techniques such as angular resolved photoemission spectroscopy (ARPES) [2–8] and high-harmonic generation [9–12]. Yet, theoretically predicting photoemission observables with satisfying accuracy is still challenging for state-of-the-art computational methods. Density-functional theory (DFT) is one of the most frequently used electronic structure approaches because it offers a favorable ratio of computational cost to accuracy. The customary approach for predicting photoemission spectra from DFT calculations is to approximate ionization potentials (IPs) by Kohn-Sham (KS) or generalized KS eigenvalues from self-consistent ground-state calculations [13–17]. This is based on the—in exact DFT rigorously valid—relation that the highest occupied molecular orbital (HOMO) eigenvalue equals the first ionization potential [18–21]. In addition to this rigorous relation it has been demonstrated that exact KS eigenvalues can be decent approximations to higher IPs of outer valence electrons, with deviations to experiment on the order of 0.1 eV [22]. Furthermore, KS eigenvalues are connected to quasiparticle energies by a perturbation expansion in which the former are the leading contribution [17,22].

In practice the predictive power of DFT eigenvalues strongly depends on the approximation for the exchange-correlation (xc) functional that is used. Known deficiencies of common functionals, in particular with respect to an accurate description of photoemission, are for instance the self-interaction error (SIE), the absence of a derivative discontinuity, and the deviation from the correct asymptotic $\sim -1/r$ behavior of the xc potential [19,20,23–28]. Yet, it

has been demonstrated that, e.g., tuned-range separated hybrid functionals can predict IPs with an accuracy that matches that of many-body perturbation theory methods such as the *GW* approximation [26,29].

While ground-state DFT can thus make relevant contributions to the understanding of PES experiments, there are also important characteristics of PES spectra that cannot be captured by ground-state DFT for fundamental reasons. Dynamical effects such as the interaction of the ejected photoelectron with the remaining system are intrinsically beyond a ground-state approach. Furthermore, the “static eigenvalue approach” gives information about the relative photoemission intensities, i.e., the ratio of ionization cross sections at different binding energies, only in a very approximate way. For understanding this problem, one should recall that in a single-particle picture, the ionization cross section follows from Fermi's golden rule under the assumption that one electron is ejected from a specific single-particle orbital φ_i . However, calculating PES intensities from transition matrix elements (including the dipole operator $\mathbf{A}\mathbf{p}$),

$$I \propto |\langle \psi_k | \mathbf{A}\mathbf{p} | \varphi_i \rangle|^2 \delta(E_{\text{kin}} + \hbar\omega - \epsilon_i), \quad (1)$$

requires knowledge about the state of the emitted electron ψ_k . Finding a reliable approximation for this photoelectron wave function is a delicate task. Furthermore, using DFT orbitals in the evaluation of matrix elements assigns physical meaning to the orbitals, which rigorously taken are just auxiliary quantities. Hence, one usually does not explicitly evaluate any matrix element at all, but simply ascribes a normalized intensity to each eigenvalue [13,14,17,26,29,30]. With this simplistic approach the relative peak heights in a spectrum are determined just by the degeneracy of the eigenvalues. Investigating PES with time-dependent DFT (TD-DFT) in the linear response limit allows for including some dynamical effects, but also does not lead to a rigorous assessment of emission intensities [31–33].

Constructing (approximate) Dyson orbitals from KS Slater determinants [34,35] is yet another way of going beyond the purely static picture, but leads to a different level, both

conceptually and in terms of computational complexity. In this work, we discuss a way to evaluate PES observables directly from TD-DFT. In this way, dynamical effects, if desired also beyond the linear regime, are explicitly taken into account (Sec. II). We further show in Sec. III that one can obtain reasonable estimates for intensity heights and binding energies. Finally we demonstrate in Sec. IV that the approach is able to predict the angular distribution of photoelectrons. Conclusions and an outlook are offered in Sec. V.

II. PHOTOEMISSION FROM REAL-TIME PROPAGATION

When one wants to take into account the dynamical nature of the PES process and wants to assess PES intensities, it is natural to go over to an explicitly time-dependent description. TD-DFT [36] allows for realizing this idea by propagating a system's occupied KS orbitals in real time and real space using the time-dependent KS equations [32,36–40]. This ansatz is particularly interesting as the entire dynamics, *including* the dynamics of the ionized density, is captured. The key question, however, is how to obtain photoemission observables from the time-dependent electron density. By virtue of the Runge-Gross theorem [36], the existence of a density functional for the ionization probability is guaranteed, but so far an exact, explicit functional form has not been discovered. However, different approximate schemes have been suggested [32,41–44].

Giovannini *et al.* proposed a photoelectron density functional relying on a phase-space interpretation of photoemission [41]. At the heart of this method lies a Wigner transformation of the TD KS density matrix. It has been interpreted as an approximate, semiclassical probability distribution for finding a photoelectron with a certain momentum at a certain point in space.

An alternative approach that is attractive because of its transparency was suggested by Pohl *et al.* [42,45,46]. One records the occupied orbitals at a detection point \mathbf{R}_D as a function of time, i.e., one records $\varphi_j(\mathbf{R}_D, t)$ for $j = 1, \dots, N$, where N is the number of electrons. Each orbital can be interpreted as being a superposition of plane waves, i.e., $\varphi_j(\mathbf{R}_D, t) = \int d\omega c_j(\omega) \exp[i(\mathbf{k}\mathbf{R}_D - \omega t)]$. For R_D far away from the system, this superposition can be interpreted as an outgoing wave packet. Consequently, a Fourier transform of $\varphi_j(\mathbf{R}_D, t)$ from the time into the frequency domain reveals $|c_j(\omega)|^2$ as the probability with which a certain kinetic energy is found in the outgoing wave packet. Summing over all orbitals yields the total probability density for detecting the kinetic energy E_{kin} at space point \mathbf{R}_D ,

$$\begin{aligned} n(\mathbf{R}_D, E_{\text{kin}}/\hbar) &= \sum_{i=1}^N |\varphi_i(\mathbf{R}_D, E_{\text{kin}}/\hbar)|^2 \\ &= \sum_{i=1}^N |c_i(E_{\text{kin}}/\hbar)|^2, \end{aligned} \quad (2)$$

which is proportional to the probability of finding a photoelectron with kinetic energy E_{kin} at space point \mathbf{R}_D , i.e.,

$$I(\mathbf{R}_D, E_{\text{kin}}) \propto n(\mathbf{R}_D, E_{\text{kin}}/\hbar). \quad (3)$$

Equations (3) and (2) define an implicit density functional for the photoemission intensity. It avoids interpreting the

eigenvalues as removal energies, which is satisfying from a formal DFT perspective. A second and important advantage is that no *a priori* assumptions about the outgoing electron's (final) state have to be made—the outgoing electron's state emerges naturally during the propagation. A third advantage is that the scheme is ideally suited for obtaining the spatial distribution of emitted electrons by placing detection points on a spherical surface around the probed molecule (see the discussion further below).

On the fundamental level, there is one inherent approximation made in the derivation of Eqs. (3) and (2): By interpreting the TD KS orbitals at large R_D as outgoing wave packets, one implicitly identifies KS particles with electrons. A second approximation—inherent to almost all (TD-)DFT calculations—is of course that one has to rely on an approximate exchange-correlation functional. These two issues are somewhat related: Because the scheme identifies KS particles with electrons, it is clear that it can be expected to work best with exchange-correlation approximations that conform with this identification. The self-interaction correction (SIC) [47] used as a KS scheme meets this criterion, as discussed in Refs. [48,49].

In practice there is a third set of approximations which are of purely technical nature, but nevertheless very important. These are related to the choice of the detection point and the boundary conditions that are used in the simulation. The detection point \mathbf{R}_D should be placed as far as possible from the system's center to ensure that one only analyzes density that corresponds to detached electrons. Thus, the real-space grid on which we run our simulations should be chosen as large as possible (see Appendices A and B). A second reason for choosing a large grid is related to the boundary conditions: In order to prevent that outgoing density is reflected back when it reaches points on the grid boundaries (R_b) and interferes with outgoing waves, we do not use the zero boundary condition that is used in ground-state calculations [$\varphi(R_b) = 0$]. Instead we employ an imaginary absorbing potential [50,51]. In doing so it is important that the absorbing function is chosen to be very smooth and that the effective absorbing region is large enough to absorb all Fourier components of the outgoing wave packet [51]. These conditions can be fulfilled easier, the larger the grid is. Yet, the computational effort grows noticeably with increasing grid size, and one therefore has to optimize the numerical setup to obtain good accuracy at reasonable computational expense. We acquire our PES signals (as, for instance, displayed in Figs. 2 and 3) according to Eq. (3) without substantial numerical noise for benzene and pyridine by using a spherical simulation box with a radius of $R_b = 24a_0$ and an exponential function for the absorbing potential, which we add to the usual KS Hamiltonian (see Appendix A). The detection points have to be placed in a region where the absorbing potential is still small and the molecule's potential has (sufficiently) faded. We found that in the present calculations a radius of $R_D = 17.5a_0$ was a good choice. We further note that the potential created by the ionizing light is present at the detection point. As we use only moderate intensities of $8.8 \times 10^7 \text{ W/cm}^2$, we assume its impact to be small [43]. In Appendix A we discuss in detail how the choice of R_D affects the spectra.

III. GAS-PHASE PHOTOEMISSION FROM BENZENE AND PYRIDINE

In gas-phase photoemission spectroscopy the probed ensemble of molecules is confined in a cavity and the molecules are randomly oriented. The photoemission process is triggered by linear polarized light with a fixed photon energy, here $\hbar\omega = 21.2$ eV, incoming from a certain direction [1,52,53]. In order to simulate this experimental situation, we cannot restrict ourselves to one TD-DFT simulation run, because one run corresponds to one distinct alignment of the molecule with respect to the light polarization. To average over the different molecular orientations as in experiment, we simulate different alignments in separate runs. Instead of varying the molecule's orientation towards the fixed light polarization it is computationally more convenient (and equivalent) to keep the molecule fixed and to rotate the linear light polarization. We place the benzene, respectively, pyridine, ring in the x - y plane and sample over the polarization directions as illustrated (for the first octant) in Fig. 1. The polarization directions for the other octants are completely equivalent. Thus, due to the symmetry of benzene, we can reduce the number of actually needed TD-DFT runs to the ones displayed.

We compute the angle-integrated cross section for one single TD-DFT run by distributing about 3000 detection points on a spherical surface with radius R_D and by integrating over all individual intensities from the detection points.

In the first step of our analysis we focus on binding energy differences between the outer valence states. In order to obtain these reliably it is essential to correct for the self-interaction error that is present in commonly used xc functionals [5,24,25]. Therefore, we use the KS SIC, respectively, time-dependent SIC (TD-SIC) [48,49,54,55]. It is based on the seminal SIC energy functional of Perdew and Zunger [47]. However, contrary to the orbital-specific potential approach of Ref. [47], we here stay on the grounds of KS theory and construct a local multiplicative xc potential using the time-dependent [56] generalized [54] Krieger-Li-Iafrate [57] (TD-GKLI) approximation to the optimized effective potential equation with a complex Foster-Boys localizing unitary orbital transformation [49].

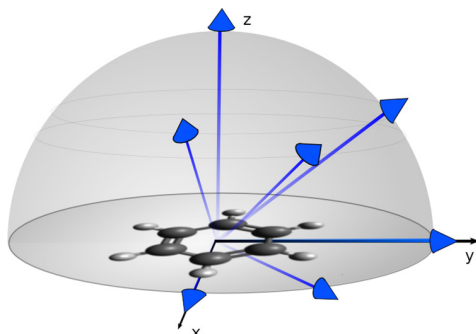


FIG. 1. Blue arrows indicate the seven different directions of the light polarization that were chosen to simulate the angularly averaged photoemission spectrum of the benzene molecule. In the chosen coordinate system shown in the figure, the polarization directions indicated by the blue arrows correspond to the vectors $(1, 0, 0)$, $(0, 1, 0)$, $(0, 0, 1)$, $(1, 1, 0)$, $(1, 1, 1)$, $(0, 1, 1)$, and $(1, 0, 1)$.

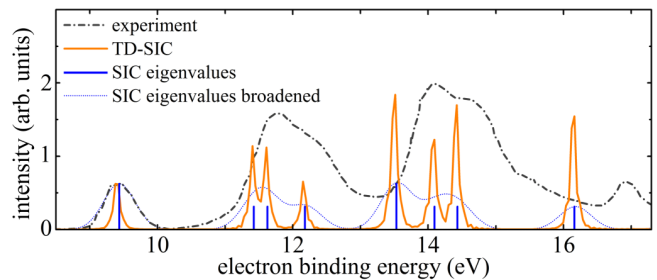


FIG. 2. Photoemission spectrum of benzene. Black dashed line: Experimental spectrum from Ref. [52]. Orange full line: Photoemission spectrum as predicted by TD-SIC. Dotted blue line: Ground-state SIC eigenvalues folded by Gaussian functions with a width of 0.4 eV. Blue bars indicate the positions of the SIC eigenvalues. The peak position and height at the smallest binding energy were scaled to match the corresponding experimental peak for all theoretical spectra.

Figures 2 and 3 show the resulting PES spectra for benzene and pyridine, respectively. In order to facilitate comparison with the experimental data we aligned all calculated eigenvalues and the spectrum obtained from the TD calculation such that the first peak in the theoretical spectra in each case coincides with the first experimental peak [58]. Consequently, we restrict our analysis to relative energy differences.

For benzene, the (shifted) first ground-state SIC eigenvalue corresponds to a binding energy of $E_B = 9.4$ eV, and the second eigenvalue corresponds to $E_B = 11.4$ eV. Their difference matches the difference between the first two experimental peaks reasonably well, deviating by 0.3 eV. Altogether, three eigenvalues are correctly found within the experimental emission band around $E_B \approx 12$ eV [26,59]. The next (lower) three eigenvalues (close to $E_B \approx 14$ eV) are located at slightly too low binding energies. The reason for discrepancies of this kind has been clarified in earlier work: KS eigenvalues are just lowest order approximations to ionization potentials, and higher order corrections lead to an effective “stretching” of the spectrum [17,22]. Nonlocal exchange can correct KS eigenvalues towards quasiparticle energies [15,17,22,26]. The same effect is seen even more pronouncedly for the eigenvalue at $E_B \approx 16$ eV.

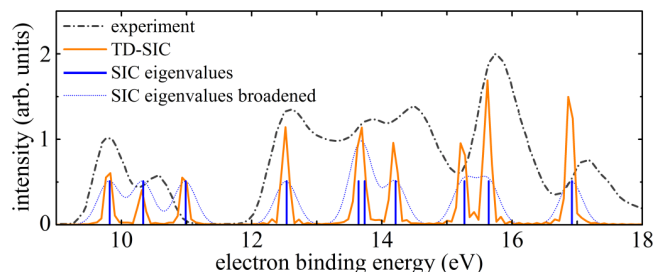


FIG. 3. Photoemission spectrum of pyridine. Black dashed line: Experimental spectrum from Ref. [52]. Orange full line: Photoemission spectrum as predicted by TD-SIC. Dotted blue line: Ground-state SIC eigenvalues folded by Gaussian functions with a width of 0.4 eV. Blue bars indicate the positions of the SIC eigenvalues. The peak position and height at the smallest binding energy were scaled to match the corresponding experimental peak for all theoretical spectra.

When we now turn towards the time-dependent description of PES by the real-time approach, our first observation is that the energetic positions of the PES intensities do not change significantly: The orange peaks are almost at the same positions as the blue lines that mark the eigenvalues. This shows that, at least with the chosen xc approximation, the positions of the photoemission peaks are primarily determined by the ground-state electronic structure and are hardly affected by dynamical interactions.

However, despite the similarity in the peak *positions*, the peak *heights* that are obtained in the time-dependent calculation differ significantly from the peak heights predicted by the ground-state calculation. In order to ease the comparison between the experimental data and the different calculations, we scaled the theoretical intensities plotted in Fig. 2 such that the peak height at the smallest binding energy in each case equals the height of the first experimental peak. Looking at the blue dotted curve that reflects the eigenvalue-based prediction for the intensities then shows that for the larger binding energies, i.e., for the three peaks around 12 eV and for the three around 14 eV, the intensity is severely underestimated: Based on the eigenvalues' degeneracies one would expect the peaks at 12 and 14 eV to have approximately the same heights as the first peak at 9.4 eV. Yet, in the experimental spectrum, the peaks around 12 and 14 eV are more than twice as high as the first peak.

This serious deficiency is to a large extent remedied when the photoemission spectrum is calculated with the real-time approach. The orange line that reflects the intensity from the TD-DFT calculation shows the same pattern of increasing peak heights as the experiment and captures the relative heights of the first three main emission bands (around $E_B \approx 9.4$, 12.0, and 14.0 eV) well. That this is a nontrivial finding is seen particularly well when looking at the TD-DFT peaks at binding energies of $E_B \approx 9.4$ eV and $E_B \approx 13.5$ eV (see Fig. 2). Both correspond to doubly degenerate Kohn-Sham states, yet the intensities from the TD-DFT calculation differ by a factor of about 3. Thus, in the real-time approach it is not the degeneracy that governs the intensity, but the dynamics and final state effects. TDDFT thus captures effects that are intrinsically beyond a ground-state-based interpretation of photoemission and leads to a much better agreement with the experimental observation.

Finally, we note that deviations between experiment and the real-time results occur for the emission peaks corresponding to more strongly bound electrons (from 16 eV onwards for benzene, from 17 eV onwards for pyridine, not shown in the figures). In an orbital-based interpretation, the origin of these peaks can be traced back to the HOMO-9 and further down. Whether these discrepancies are a consequence of the employed xc approximation or of the implicit identification of KS particles with electrons remains to be investigated in future work.

Similar findings as the one just discussed for benzene are also made for other systems, e.g., pyridine, as shown in Fig. 3. Again we display the binding energies as obtained from the eigenvalues and as found in the real-time approach (both rigidly shifted by $\Delta = 2.8$ eV). Again the relative energetic positions found in the two approaches are very similar and are overall in good agreement with experiment. The positions

of emission peaks above $E_B = 12$ eV are even closer to the experimental reference than for the case of benzene. We note, however, that the first two peaks around $E_B = 10$ eV should be quasidegenerate [26,59], i.e., the separation of about 0.4 eV that we find here is too large. This affects the scaling of the theoretical spectra, which we again want to do such that the first peak height matches the first experimental peak height. We account for the overestimation of the peak separation by scaling the added intensities of the first two calculated peaks to the first experimental peak height. With a common basis for the comparison of relative peak heights thus established, it becomes obvious that the ground-state eigenvalue approach (blue line in Fig. 3) again considerably underestimates the intensity of the emission peaks that correspond to binding energies of about 12 eV and more. Yet, as in the case of benzene, the real-time approach cures this deficiency and predicts considerably higher intensity for the more strongly bound electrons, in agreement with experiment. As a specific example one may look at the emission peaks at about $E_B = 12.5$ and 15.7 eV: The considerable increase in intensity that is seen in the experiment is well reproduced by the real-time approach, yet missed completely by the eigenvalue-based interpretation of photoemission. We thus conclude that the real-time approach to photoemission can capture what commonly is called “matrix element effects” [31] without explicitly evaluating any matrix elements.

IV. ORBITAL CHARACTERIZATION

Photoemission can reveal much more about a system's electronic structure than what can be inferred from peak positions and peak heights. Of particular interest is the spatial distribution of the electronic density. Measurements that have been interpreted as showing single-particle orbitals or orbital densities, respectively, have become possible with the techniques of high-harmonic generation [9–12] or ARPES [2–5,7,8]. However, the number of systems which can be studied in this way is limited for various reasons. ARPES, e.g., requires an aligned molecular monolayer to prevent averaging over emission directions. This restricts the repertoire of molecules that can be studied. Although gas-phase PES provides no immediate access to data that can be interpreted as reflecting orbitals, such information can be extracted from the specific emission behavior at different binding energies. When one realizes PES without any preferred direction, the photoelectron angular distribution from a randomly oriented ensemble is strictly uniform. Yet, one can take advantage of the typical gas-phase PES experimental setup that has one distinguished direction, namely, the spatially fixed linear light polarization. As a result the photoemission intensity can vary with respect to the polarization direction. If one defines θ as the angle between the photoelectron emission direction and the light polarization ($\theta = 0^\circ$ and $\theta = 180^\circ$ parallel; $\theta = 90^\circ$ perpendicular), the photoemission intensity for spherical systems is given by [45,60–62]

$$I(E, \theta) \propto 1 + \beta(E)P_2(\cos \theta). \quad (4)$$

Here, P_2 is the Legendre polynomial of second order. The angular dependence (i.e., deviation from a spatially uniform emission) introduced by $P_2(\cos \theta)$ is weighted by

the factor β , called the anisotropy parameter. The largest possible value of the anisotropy parameter, determined by dipole selection rules [60], is $\beta = 2$. It corresponds to an emission maximally parallel to the light polarization with $I(\theta) \propto \cos^2 \theta$. An emission that is primarily perpendicular to the polarization is indicated by $\beta = -1$, which leads to $I(\theta) \propto \sin^2 \theta$.

Typically, individual photoemission bands show different emission characteristics, and β can vary between the two limiting cases. When the photoemission signal is interpreted in terms of molecular orbitals, i.e., when each emission peak is assigned to electron ejection from one specific orbital as in Eq. (1), the variation in β as a function of energy can be ascribed to probing different molecular orbitals with different spatial structure. However, there is another ingredient to the transition matrix element in Fermi's golden rule in Eq. (1), namely, the final state of the ejected electron. It can also affect the emission characteristics. A direct evaluation of Fermi's golden rule was, for example, realized by approximating the photoelectron's state with the aid of multiple scattering X_α approaches [53,63]. However, the real-time propagation approach is an elegant and parameter-free way to bypass the need for explicitly specifying the ejected electron's state. It allows for connecting orbitals and emission peaks in an unbiased way. Separately evaluating the emission from the individual orbital densities $n_i(E)$ as discussed in Sec. II, then calculating $\beta_i(E)$ and comparing these values to the anisotropy parameters that were experimentally recorded for the individual emission bands, allows us to check the *orbital assignment* in a straightforward way. Closely linked to the orbital assignment question is the finding that different xc-functional approximations can predict different orbital orderings [5,17,24,64]. This raises the question of which theoretical approach gives the "correct" energetic ordering of orbitals. The self-interaction error plays a prominent role in determining the orbital ordering [24]. In the following we show that anisotropy parameters calculated for individual emission peaks based on the KS SIC orbital ordering match the experimentally measured anisotropy parameters well.

To calculate the anisotropy parameter for benzene, we record, similar to Wopperer *et al.*, who calculated β for sodium clusters [45,46], the PES signal angle and energy resolved. We again use the alignment scheme for the gas-phase PES calculation from Sec. III including the variation of the light polarization instead of the molecule's orientation. However, a smooth angular signal requires a denser discretization of light polarization to molecule alignment directions. Furthermore, we have to transform all individual spectra from the molecular frame (with the spatially fixed molecule and varying light polarization) into the laboratory frame where the light polarization is spatially fixed, i.e., is pointing into the z direction. Afterwards we sum the individual spectra up to obtain the total, angle-resolved photoemission spectrum. As the only distinguished direction is that of the light polarization, we integrate the intensity over the azimuthal angle which lies in planes perpendicular to the light polarization (in the laboratory frame). We provide further details regarding the calculation of β in Appendix C.

Figure 4 shows two examples for the resulting angle-resolved emission intensity for the case of benzene. The

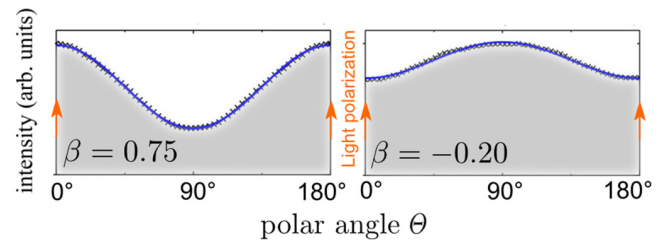


FIG. 4. Left: Angle-resolved photoemission intensity from the benzene HOMO as predicted by TD-SIC. The direction of the light polarization is indicated by the orange arrows. Photoemission parallel to the light polarization corresponds to $\theta = 0^\circ$ and 180° ; $\theta = 90^\circ$ corresponds to perpendicular emission. The calculated intensity (black crosses) was fitted with the help of Eq. (4), resulting in $\beta = 0.75$ (blue line). Emission occurs predominantly parallel to the light polarization. Right: Angle-resolved photoemission intensity from the benzene HOMO-7 (green-white orbital in Fig. 5). Here the emission is predominantly perpendicular to the light polarization, with $\beta = -0.20$.

left panel depicts the angle-resolved emission intensity solely from the two degenerate HOMOs. Thus, instead of taking the entire electron density into account as in Eq. (3), we exclusively calculated the intensity ejected from the HOMOs, $I_{\text{HOMO}} \propto n_{\text{HOMO}}$. This angle-resolved signal was evaluated at the HOMOs' electron binding energy. A polar angle θ equal to 0° or 180° indicates emission parallel to the light polarization (marked by the arrows in Fig. 4). We have fitted the intensity profile of the calculated data according to Eq. (4). The resulting β value amounts to $\beta = 0.75$, which indicates an emission primarily towards the polarization direction. As an example for perpendicular emission we show in the right part of Fig. 4 the angle-resolved intensity profile which corresponds to the most negative anisotropy parameter, $\beta = -0.20$ (this value corresponds to the emission at $E_B = 14.6$ eV in Fig. 5).

Figure 5 shows the shapes of the benzene orbitals at the very top, in the upper panel the experimentally recorded β values for benzene from Refs. [52,53,65,66], and the measured and calculated photoemission spectra in the lower panel. In order to compare measured and calculated β values in a meaningful way, the scales for the binding energies must match. Therefore, we enhance the resemblance of the two spectra by stretching the calculated spectrum by a constant factor of $s = 1.11$. With this stretching factor, the first (lowest binding energy) and last (highest binding energy) calculated peak in Fig. 5 coincide exactly with the corresponding experimental peaks. This *a posteriori* stretching procedure can be understood as imitating a first order correction of the KS eigenvalues towards quasiparticle energies [17,22].

We now discuss the data going through the spectrum, starting at the lowest binding energy of 9.4 eV. For this first peak we calculated $\beta = 0.75$, as indicated by the leftmost triangle in the upper panel of Fig. 5. We see that the experimentally measured values of β in this energy range show quite some scatter, but are generally of quite similar magnitude (though the theoretical value admittedly lies at the lower end of the experimental scatter). Going to higher binding energies the experimental emission characteristic changes significantly

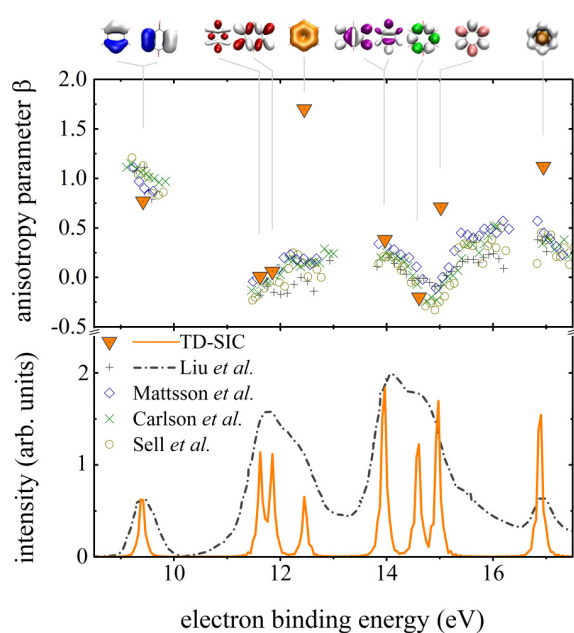


FIG. 5. Lower panel: Experimentally recorded photoemission spectrum for benzene from Ref. [52] (black) and photoemission spectrum from TD-SIC (orange). In difference to Fig. 2, we here stretched the theoretical spectrum by a factor of $s = 1.11$ to ease comparison to experiment. Top panel: Anisotropy parameter β as a function of energy. Triangles depict the calculated values obtained for the emission from individual orbitals, i.e., corresponding to the peaks shown right below in the lower panel. Different experimental β values are designated by small symbols as designated in the plot, with the data taken from Liu *et al.* [52], Carlson *et al.* [53], Mattsson *et al.* [65], and Sell and Kuppermann [66].

and becomes uniform, with values of β that are close to zero. This is correctly reflected by the TD-DFT calculation, which yields $\beta = 0.01$ at $E_B = 11.7$ eV. Similar, the transition of β from positive over slightly negative and back to positive values in the binding energy region from 14.0 to 15.5 eV is accurately reproduced. This characteristic transition enables a decomposition of the rather broad emission band in terms of the origins of the photoelectrons. As we obtained the β values from the individual orbital densities separately, it allows us to draw conclusions about the responsible orbitals, as indicated at the top of Fig. 5.

The only severe discrepancy between theory and experiment is seen for the anisotropy parameter at $E_B = 12.2$ eV. It corresponds to the π orbital that is completely delocalized over the whole benzene ring. While the calculated value of $\beta = 1.70$ suggests an electron emission mostly along the polarization, measurements observe a rather uniform electron emission. A possible explanation is the natural broadening of the emission peaks. The only sparsely pronounced shoulder at around $E_B = 12.5$ eV testifies a strong mixing of the emission from the neighboring states with the ring-shaped one. Probably, the experimental anisotropy parameter is thus notably suppressed by the nearby states showing a uniform emission with $\beta = 0.01$. Moreover, the ring orbital is predicted to be slightly overbound by SIC, most likely due to a lack of beyond (semi-)local correlation [26]. It thus should be even closer to

the states with the next lower binding energy than seen in our spectrum in Fig. 5. We are therefore inclined to believe that the value of β which we calculated for the ring orbital and find to be noticeably larger than zero, is not an artifact. Yet, the precise theoretical value may be influenced by electron-electron interaction effects that are beyond our xc-functional approximation, and the experimental data may suffer from orbital near degeneracy. Therefore, we presently cannot draw a final conclusion.

Yet, the overall agreement between theory and experiment for β is quite good, and we can therefore return to the question of assigning orbitals to emission peaks. Since the orbital is a noninteracting particle concept, while true electrons are interacting, this assignment is of course an approximation. However, in line with the results of Carlson *et al.* [53] our results confirm that, at least for the present systems, the interpretation that individual emission bands stem from individual orbitals is a reasonable one and is confirmed by the directional-specific emission behavior. Along with earlier works on the interpretability of molecular orbitals [2,5,22,34,67,68] we can further corroborate the assertion that KS orbitals can be attributed physical significance, i.e., KS orbitals have more meaning than just being auxiliary quantities that reproduce the electron density.

V. CONCLUSION

We simulated photoemission from organic molecules using self-interaction-free KS TD-DFT. Doing so we go beyond the static, ground-state approach to photoemission which interprets the eigenvalues as ionization potentials and infers relative peak heights just from degeneracies. The TD-DFT approach explicitly includes dynamical effects and allows for the first-principles calculation of gas-phase PES with angular resolution. We demonstrated for benzene and pyridine that a strength of the approach lies in yielding reasonable estimates for photoemission intensities. This improvement is a consequence of including dynamical effects and of not relying on the evaluation of Fermi's golden rule which necessitates, e.g., an approximation for the ejected electron's state. The real-time approach makes a straightforward evaluation of PES intensities possible via Eq. (3). We have used the method for calculating angle-resolved photoemission from benzene. Assessing the photoemission anisotropy with respect to a spatially fixed light polarization, expressed in terms of the anisotropy parameter β , and comparing β values calculated for individual orbital emissions to measured values of β , showed that associating individual photoemission peaks with individual orbitals is a very useful concept for the systems studied here. We are convinced that this approach is promising also for other systems and applications. In particular, the description of situations which require one to go beyond stationary or simple final state approximations will benefit from the accurate, first-principles approach in which the final state emerges naturally without *a priori* assumptions. For example, the prediction of circular dichroism in the photoelectron angular distribution is a challenge in which we expect valuable contributions from our method.

ACKNOWLEDGMENTS

S.K. and M.D. acknowledge support by Deutsche Forschungsgemeinschaft Graduiertenkolleg 1640 and the Bavarian State Ministry of Science, Research, and the Arts for the Collaborative Research Network ‘‘Solar Technologies go Hybrid’’.

APPENDIX A: DETECTION POINT DEPENDENCE

In this section, we discuss details of our technical setup regarding the choice of the absorbing potential and the detection point. These are rather technical issues. They are important, however, because the interplay of quite a number of factors is important for obtaining reliable results with bearable computational effort. Among the things that one has to take into account are the choice of the detection point, the choice of the shape of the absorbing imaginary potential, its strength, the radial extension of the volume in which the absorbing potential acts, and the size of the simulation box (which one would like to be as small as possible to minimize the computational effort).

We start by discussing the absorbing potential. As stated in Sec. II we have chosen an exponential function,

$$-iv(r) = -i \exp \frac{r - R_b}{1.39a_0}. \quad (\text{A1})$$

We tested several other potential shapes. Polynomial functions of second order and transmission-free absorbing potentials [51] led to similar results, but overall we found that the potential of Eq. (A1) performed best. It has the advantage of being continuous and very smooth, thus being very unlike a steplike structure that causes quantum-mechanical reflections. However, the price that has to be paid is that the potential is not vanishing at any point in the simulation box. Therefore, it in principle absorbs some probability density also in the central molecular region. However, this amount can be kept extremely small in practice and utterly negligible with a proper choice of parameters. In our experience it is mainly the effective length (effective absorbing region) that is crucial for efficiently absorbing all Fourier components (respectively, all wavelengths) of the outgoing density. In Fig. 6 we contrast three different effective absorption lengths, where the detection point was held fixed. We have changed the radius of the spherical numerical box from $R_b = 24a_0$ to $22a_0$, and $20a_0$ and hence decreased the effective length of the potential according to Eq. (A1). This results in a dramatically increasing width

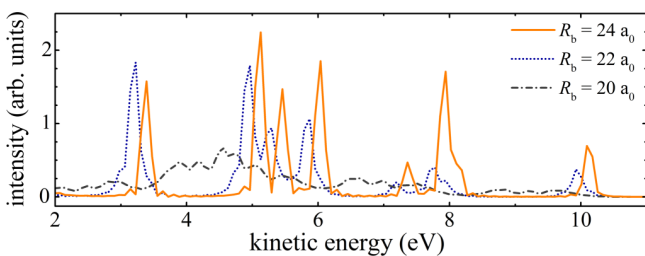


FIG. 6. PES spectra obtained using absorbing potentials with different effective length. We show the kinetic energy of photoelectrons from benzene for one relative orientation of light polarization and molecule.

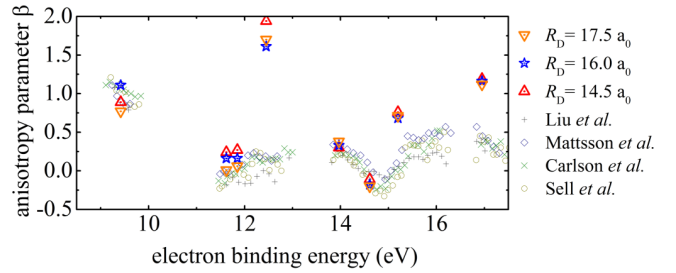


FIG. 7. Anisotropy parameter for three different choices of the detector radius: $R_D = 14.5a_0$ (red triangles), $16.0a_0$ (blue stars), and $17.5a_0$ (orange triangles). Positions of the TD-SIC β values are aligned and scaled by $s = 1.11$. The experimental data is taken from Liu *et al.* [52], Carlson *et al.* [53], Mattsson *et al.* [65], and Sell and Kuppermann [66].

of the emission peaks as depicted in Fig. 6. Therefore, with decreasing effective absorption length the spectrum is increasingly contaminated by signals from quantum-mechanical reflections. An absorption region that is too small can easily wipe out the relevant signal.

The next parameter we discuss is the detection point R_D . For the potential (A1) with a box size of $24a_0$, we set R_D to $17.5a_0$, $16.0a_0$, and $14.5a_0$ [as measured from the center of the simulation box. For comparison: the H atom furthest away from the coordinate origin (the origin is also the center of mass of the benzene molecule) is located at $R \approx 4.7a_0$]. To demonstrate the influence, we show the anisotropy parameters in Fig. 7 evaluated in exactly the same way as described in the main text in Sec. IV, just using the different values for R_D . The resulting differences are visible, but are not huge and lie within the experimental uncertainty range.

In contrast to the minor influence on the anisotropy parameter, the difference is more pronounced for the PES intensities, i.e., peak heights. Figures 8 and 9 show the PES spectra for benzene and pyridine for all three observation distances. Yet, we find moderate deviations in the intensity heights at, e.g., $E_B = 13.5$ and 14.5 eV for benzene (Figs. 2 and 8).

Finally, we show the spectra that result without correcting for the one-electron SIE. The PES in Fig. 10 is evaluated in exactly the same way as for TD-SIC except for the difference in the xc approximation. We here used the local density approximation (LDA) which is strongly influenced by SIE. The TD-LDA PES spectrum does not resemble the experimental spectrum very much.

APPENDIX B: TECHNICAL DETAILS

For all our simulations we used the Bayreuth version of the PARSEC real-time and real-space code [40,69], which uses norm-conserving Troullier-Martins pseudopotentials [70,71].

Our simulations for benzene and pyridine were performed with a grid spacing of $0.38a_0$ in the space and 0.001 fs in the time domain. The propagation time for benzene was 50 fs for the photoemission spectra and 25 fs for the TD-DFT runs necessary to calculate β . For pyridine we propagated the system for 30 fs. The ionizing laser pulse was simulated by a classical time-dependent electric field.

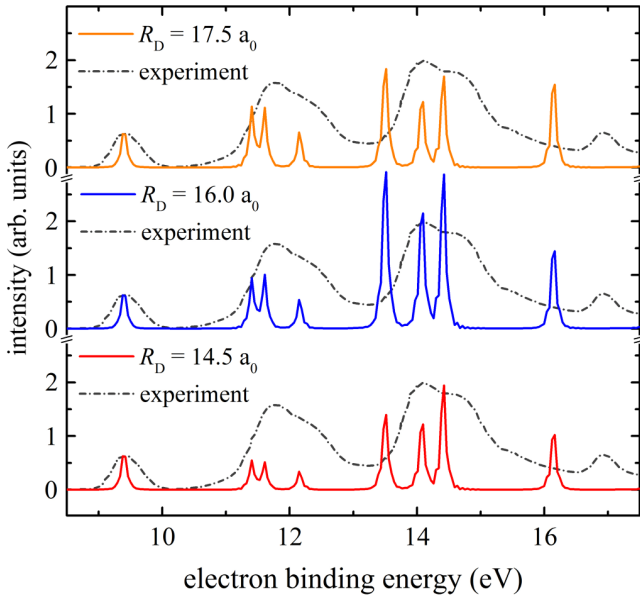


FIG. 8. Photoemission spectrum of benzene, predicted by TD-SIC, for three different choices of the detector radii: $R_D = 17.0a_0$ (orange), $16.0a_0$ (blue), and $14.5a_0$ (red). Experimental spectrum taken from Ref. [52].

This electric field was chosen as a sine with a frequency of $\hbar\omega = 21.2$ eV that was linearly ramped to its maximal intensity of $8.8 \times 10^7 \text{ W/cm}^2$ within 1 fs and then remained constant throughout the propagation time. The chosen spatial grid spacing is on the coarse side for the chosen elements and pseudopotentials. We went into this limit in order to keep the numerical burden for the time propagation with the TD-SIC approach manageable. (Changes in the real-space grid spacing relate approximately quadratically to the time step spacing, i.e., doubling the real-space grid spacing allows for

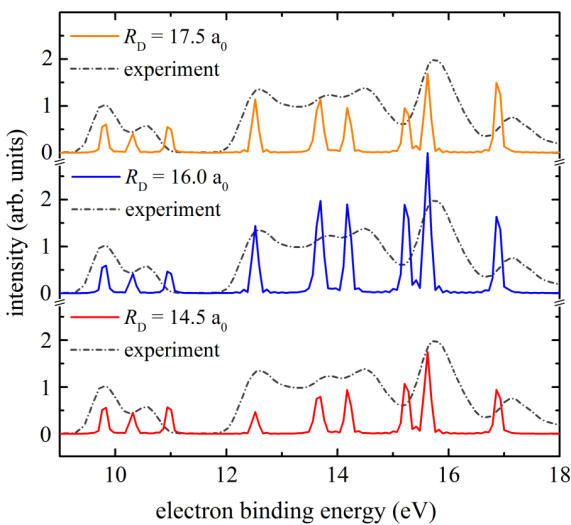


FIG. 9. Photoemission spectrum of pyridine, predicted by TD-SIC, for three different choices of the detector radii: $R_D = 17.0a_0$ (orange), $16.0a_0$ (blue), and $14.5a_0$ (red). Experimental spectrum taken from Ref. [52].

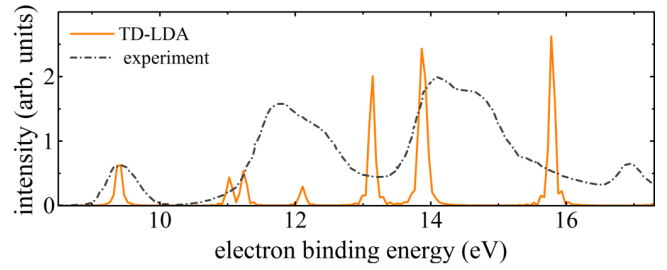


FIG. 10. Orange: Photoelectron spectrum of benzene as predicted by TD-LDA. Black: Experimental photoemission spectrum from Ref. [52]. The position and height of the TD-LDA peak corresponding to the smallest binding energy was aligned to its experimental counterpart. The agreement between TD-LDA and experiment is not good.

taking an about four times larger time step.). With respect to a calculation that uses a grid spacing that is tightened to convergence, the grid spacing of $0.38a_0$ leads to uncertainties in the eigenvalues of up to 0.2 eV. This tolerance is acceptable for the present purposes, but it does affect, e.g., the two benzene emission peaks at a binding energy of about 11.5 eV in Fig. 8. These are closer together when a smaller grid spacing is used. The convergence threshold for the localizing Foster-Boys unitary orbital transformation, which is described in Ref. [55], Eq. (B18), was set to 1×10^{-5} .

APPENDIX C: SAMPLING OF MOLECULE ORIENTATIONS

In order to calculate the intensity in a way that corresponds to experimental gas-phase PES setups, we need to sample over many molecule to light polarization directions. As discussed in Sec. IV, we varied the light polarization instead of the orientation of benzene (it lies in the x - y plane). The polarization vector directions— $(1, 0, 0)$, $(0, 1, 0)$, $(0, 0, 1)$, $(1, 1, 0)$, $(1, 1, 1)$, $(0, 1, 1)$, and $(1, 0, 1)$ —are displayed in Fig. 1 and as red pentagons in Fig. 11 for the first octant in the case of benzene. In the case of pyridine, the nitrogen on one site of the ring lowers the symmetry compared to benzene.

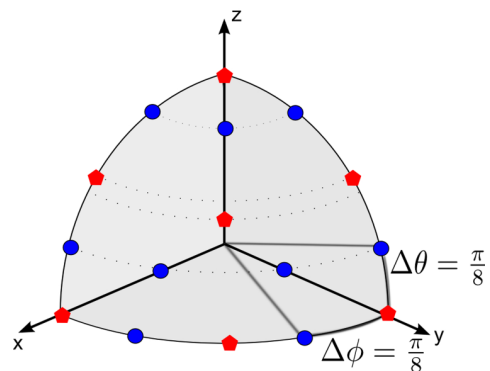


FIG. 11. Directions of the light polarization in the first octant with respect to benzene that is lying in the x - y plane. The red pentagons correspond to the directions chosen for calculating the PES spectra of benzene. For calculating β we additionally ran the TD-DFT simulations with the orientations corresponding to the blue dots.

To account for this, we additionally performed TD-DFT runs with the polarization orientations (1,−1,0) and (1,−1,1). The polarization directions for the octants that are not shown explicitly are analogous.

For recording the angular-resolved photoemission data for β from benzene we had to increase the number of discrete

sampling directions in order to get a smooth angular signal. The additional polarization directions are displayed in Fig. 11 for the first octant. The polarization directions for the other octants are equivalent. The 16 directions for which we actually performed TD-DFT runs to calculate β are the ones shown in Fig. 11.

-
- [1] S. Hüfner, *Photoelectron Spectroscopy* (Springer, Berlin, 2003), pp. 10–19.
- [2] P. Puschnig, S. Berkebile, A. J. Fleming, G. Koller, K. Emtsev, T. Seyller, J. D. Riley, C. Ambrosch-Draxl, F. P. Netzer, and M. G. Ramsey, *Science* **326**, 702 (2009).
- [3] S. Kera, S. Tanaka, H. Yamane, D. Yoshimura, K. K. Okudaira, K. Seki, and N. Ueno, *Chem. Phys.* **325**, 113 (2006).
- [4] J. Ziroff, F. Forster, A. Schöll, P. Puschnig, and F. Reinert, *Phys. Rev. Lett.* **104**, 233004 (2010).
- [5] M. Dauth, T. Körzdörfer, S. Kümmel, J. Ziroff, M. Wiessner, A. Schöll, F. Reinert, M. Arita, and K. Shimada, *Phys. Rev. Lett.* **107**, 193002 (2011).
- [6] D. Lüftner, T. Ules, E. M. Reinisch, G. Koller, S. Soubatch, F. S. Tautz, M. G. Ramsey, and P. Puschnig, *Proc. Natl. Acad. Sci. USA* **111**, 605 (2013).
- [7] M. Wießner, D. Hauschild, C. Sauer, V. Feyer, A. Schöll, and F. Reinert, *Nat. Commun.* **5**, 4156 (2014).
- [8] S. Weiß, D. Lüftner, T. Ules, E. M. Reinisch, H. Kaser, A. Gottwald, M. Richter, S. Soubatch, G. Koller, M. G. Ramsey, F. S. Tautz, and P. Puschnig, *Nat. Commun.* **6**, 8287 (2015).
- [9] J. Itatani, J. Levesque, D. Zeidler, H. Niikura, H. Pépin, J. C. Kieffer, P. B. Corkum, and D. M. Villeneuve, *Nature (London)* **432**, 867 (2004).
- [10] B. K. McFarland, J. P. Farrell, P. H. Bucksbaum, and M. Gühr, *Science* **322**, 1232 (2008).
- [11] S. Haessler, J. Caillat, W. Boutu, C. Giovanetti-Teixeira, T. Ruchon, T. Auguste, Z. Diveki, P. Breger, A. Maquet, B. Carré, R. Taïb, and P. Salieres, *Nat. Phys.* **6**, 200 (2010).
- [12] M. Lein, *J. Phys. B* **40**, R135 (2007).
- [13] N. Binggeli and J. R. Chelikowsky, *Phys. Rev. Lett.* **75**, 493 (1995).
- [14] J. Akola, M. Manninen, H. Häkkinen, U. Landman, X. Li, and L.-S. Wang, *Phys. Rev. B* **62**, 13216 (2000).
- [15] L. Kronik, T. Stein, S. Refaely-Abramson, and R. Baer, *J. Chem. Theory Comput.* **8**, 1515 (2012).
- [16] U. Salzner and R. Baer, *J. Chem. Phys.* **131**, 231101 (2009).
- [17] T. Körzdörfer and S. Kümmel, *Phys. Rev. B* **82**, 155206 (2010).
- [18] J. F. Janak, *Phys. Rev. B* **18**, 7165 (1978).
- [19] J. P. Perdew, R. G. Parr, M. Levy, and J. L. Balduz, Jr., *Phys. Rev. Lett.* **49**, 1691 (1982).
- [20] C.-O. Almbladh and U. von Barth, *Phys. Rev. B* **31**, 3231 (1985).
- [21] M. Levy, J. P. Perdew, and V. Sahni, *Phys. Rev. A* **30**, 2745 (1984).
- [22] D. P. Chong, O. V. Gritsenko, and E. J. Baerends, *J. Chem. Phys.* **116**, 1760 (2002).
- [23] S. Kümmel and L. Kronik, *Rev. Mod. Phys.* **80**, 3 (2008).
- [24] T. Körzdörfer, S. Kümmel, N. Marom, and L. Kronik, *Phys. Rev. B* **79**, 201205 (2009).
- [25] T. Körzdörfer, S. Kümmel, N. Marom, and L. Kronik, *Phys. Rev. B* **82**, 129903(E) (2010).
- [26] D. Egger, S. Weissman, S. Refaely-Abramson, S. Sharifzadeh, M. Dauth, R. Baer, S. Kümmel, J. B. Neaton, E. Zojer, and L. Kronik, *J. Chem. Theory Comput.* **10**, 1934 (2014).
- [27] A. J. Cohen, P. Mori-Sánchez, and W. Yang, *Science* **321**, 792 (2008).
- [28] T. Schmidt, E. Kraisler, L. Kronik, and S. Kümmel, *Phys. Chem. Chem. Phys.* **16**, 14357 (2014).
- [29] S. Refaely-Abramson, S. Sharifzadeh, N. Govind, J. Autschbach, J. B. Neaton, R. Baer, and L. Kronik, *Phys. Rev. Lett.* **109**, 226405 (2012).
- [30] M. Mundt, S. Kümmel, B. Huber, and M. Moseler, *Phys. Rev. B* **73**, 205407 (2006).
- [31] M. Walter and H. Häkkinen, *New J. Phys.* **10**, 043018 (2008).
- [32] M. Mundt and S. Kümmel, *Phys. Rev. B* **76**, 035413 (2007).
- [33] L. Kronik and S. Kümmel, in *First Principle Approaches to Spectroscopic Properties of Complex Materials*, edited by C. D. Valentin, S. Botti, and M. Cococcioni, Topics in Current Chemistry (Springer, Berlin-Heidelberg, 2014).
- [34] M. Dauth, M. Wießner, V. Feyer, A. Schöll, P. Puschnig, F. Reinert, and S. Kümmel, *New J. Phys.* **16**, 103005 (2014).
- [35] A. Humeniuk, M. Wohlgemuth, T. Suzuki, and R. Mitrić, *J. Chem. Phys.* **139**, 134104 (2013).
- [36] E. Runge and E. K. U. Gross, *Phys. Rev. Lett.* **52**, 997 (1984).
- [37] K. Yabana and G. F. Bertsch, *Phys. Rev. B* **54**, 4484 (1996).
- [38] F. Calvayrac, P.-G. Reinhard, and E. Suraud, *Ann. Phys. (NY)* **255**, 125 (1997).
- [39] A. Castro, H. Appel, M. Oliveira, C. Rozzi, X. Andrade, F. Lorenzen, M. Marques, E. Gross, and A. Rubio, *Phys. Status Solidi B* **243**, 2465 (2006).
- [40] M. Mundt, *J. Theor. Comput. Chem.* **08**, 561 (2009).
- [41] U. De Giovannini, D. Varsano, M. A. L. Marques, H. Appel, E. K. U. Gross, and A. Rubio, *Phys. Rev. A* **85**, 062515 (2012).
- [42] A. Pohl, P.-G. Reinhard, and E. Suraud, *Phys. Rev. Lett.* **84**, 5090 (2000).
- [43] P. M. Dinh, P. Romaniello, P.-G. Reinhard, and E. Suraud, *Phys. Rev. A* **87**, 032514 (2013).
- [44] V. Véniard, R. Taïeb, and A. Maquet, *Laser Phys.* **13**, 465 (2003).
- [45] P. Wopperer, B. Faber, P. M. Dinh, P.-G. Reinhard, and E. Suraud, *Phys. Rev. A* **82**, 063416 (2010).
- [46] P. Wopperer, P. M. Dinh, E. Suraud, and P.-G. Reinhard, *Phys. Rev. A* **85**, 015402 (2012).
- [47] J. P. Perdew and A. Zunger, *Phys. Rev. B* **23**, 5048 (1981).
- [48] T. Körzdörfer, M. Mundt, and S. Kümmel, *J. Chem. Phys.* **129**, 014110 (2008).
- [49] D. Hofmann and S. Kümmel, *J. Chem. Phys.* **137**, 064117 (2012).
- [50] A. Goldberg and B. W. Shore, *J. Phys. B: Atom. Molec. Phys.* **11**, 3339 (1978).
- [51] D. E. Manolopoulos, *J. Chem. Phys.* **117**, 9552 (2002).

- [52] S.-Y. Liu, K. Alnama, J. Matsumoto, K. Nishizawa, H. Kohguchi, Y.-P. Lee, and T. Suzuki, *J. Phys. Chem. A* **115**, 2953 (2011).
- [53] T. Carlson, P. Gerard, M. O. Krause, F. A. Grimm, and B. P. Pullen, *J. Chem. Phys.* **86**, 6918 (1987).
- [54] D. Hofmann, T. Körzdörfer, and S. Kümmel, *Phys. Rev. Lett.* **108**, 146401 (2012).
- [55] D. Hofmann, S. Klüpfel, P. Klüpfel, and S. Kümmel, *Phys. Rev. A* **85**, 062514 (2012).
- [56] C. A. Ullrich, U. J. Gossmann, and E. K. U. Gross, *Phys. Rev. Lett.* **74**, 872 (1995).
- [57] J. B. Krieger, Y. Li, and G. J. Iafrate, *Phys. Rev. A* **46**, 5453 (1992).
- [58] For benzene the magnitude of the shift was 1.6 eV, and for pyridine it was 2.8 eV.
- [59] N. Marom, F. Caruso, X. Ren, O. T. Hofmann, T. Körzdörfer, J. R. Chelikowsky, A. Rubio, M. Scheffler, and P. Rinke, *Phys. Rev. B* **86**, 245127 (2012).
- [60] H. A. Bethe, *Handbuch der Physik* (Springer, Berlin, 1933), Vol. 24, p. 483.
- [61] J. Cooper and R. N. Zare, *J. Chem. Phys.* **48**, 942 (1968).
- [62] J. Cooper and R. N. Zare, *J. Chem. Phys.* **49**, 4252 (1968).
- [63] Y.-i. Suzuki and T. Suzuki, *J. Phys. Chem. A* **112**, 402 (2008).
- [64] N. Dori, M. Menon, L. Kilian, M. Sokolowski, L. Kronik, and E. Umbach, *Phys. Rev. B* **73**, 195208 (2006).
- [65] L. Mattsson, L. Karlsson, R. Jadrny, and K. Siegbahn, *Phys. Scr.* **16**, 221 (1977).
- [66] J. A. Sell and A. Kuppermann, *Chem. Phys.* **33**, 367 (1978).
- [67] W. H. E. Schwarz, *Angew. Chem.* **45**, 1508 (2006).
- [68] P. Duffy, D. P. Chong, M. E. Casida, and D. R. Salahub, *Phys. Rev. A* **50**, 4707 (1994).
- [69] L. Kronik, A. Makmal, M. L. Tiago, M. M. G. Alemany, M. Jain, X. Huang, Y. Saad, and J. R. Chelikowsky, *Phys. Status Solidi B* **243**, 1063 (2006).
- [70] N. Troullier and J. L. Martins, *Phys. Rev. B* **43**, 1993 (1991).
- [71] We use LDA pseudopotentials with cutoff radii of $r_c = 1.09a_0$ for C, $r_c = 1.50a_0$ for N, and $r_c = 0.15a_0$ for H.

Publication 5

Perpendicular emission, dichroism, and energy dependence in angle-resolved photoemission: the importance of the final state

Physical Review Letters **117**, 183001 (2016)

M. Dauth¹, M. Graus², I. Schelter¹, M. Wießner², A. Schöll², F. Reinert², and S. Kümmel¹

¹ Theoretical Physics IV, University of Bayreuth, D-95440 Bayreuth, Germany ² Experimental Physics VII, University of Würzburg, D-97074 Würzburg, Germany

My contribution

I implemented the algorithms needed to evaluate the photoemission signal, the absorbing potentials, and the perturbing field. I performed all calculations presented in the paper, wrote a first draft of the manuscript, and lead the scientific discussion.

Publ.5

Publ.5

Perpendicular Emission, Dichroism, and Energy Dependence in Angle-Resolved Photoemission: The Importance of The Final State

M. Dauth,¹ M. Graus,² I. Schelter,¹ M. Wießner,² A. Schöll,² F. Reinert,² and S. Kümmel¹

¹Theoretical Physics IV, University of Bayreuth, D-95440 Bayreuth, Germany

²Experimental Physics VII, University of Würzburg, D-97074 Würzburg, Germany

(Received 24 February 2016; published 24 October 2016)

Angle-resolved photoemission spectroscopy has been developed to a very high accuracy. However, effects that depend sensitively on the state of the emitted photoelectron were so far hard to compute for real molecules. We here show that the real-time propagation approach to time-dependent density functional theory allows us to obtain final-state effects consistently from first principles and with an accuracy that allows for the interpretation of experimental data. In a combined theoretical and experimental study we demonstrate that the approach captures three hallmark effects that are beyond the final-state plane-wave approximation: emission perpendicular to the light polarization, circular dichroism in the photoelectron angular distribution, and a pronounced energy dependence of the photoemission intensity.

DOI: 10.1103/PhysRevLett.117.183001

Photoelectron spectroscopy is one of the most important techniques for characterizing condensed matter systems [1,2]. With rapidly increasing experimental accuracy, increasingly precise insights into the electronic structure have become possible [3,4]. In addition to conventional applications such as the band mapping of solids [5,6], angle-resolved photoemission spectroscopy (ARPES) has become an invaluable tool for studying organic semiconductors and their interfaces [7–9]. It can, e.g., quantify hybridization and band dispersion effects of adsorbed molecular films and can reveal the structure of molecular orbitals [10–19]. Yet, as photoemission is an involved many-body process [2,20–22], the interpretation of experiments relies on theoretical models. Evaluating the commonly assumed one step Fermi's golden rule transition [21,22] requires the initial and the final state. For many prototype organic semiconductors, the initial state has successfully been approximated under the assumption that the photoelectron stems from a single molecular orbital [10,11,13,14,19,22]. Assuming the final state of the emitted electron to be a plane wave (PW) is not only computationally straightforward but under certain conditions [11,23] also leads to a fascinating interpretation of ARPES experiments: The transition matrix element reduces to the Fourier transform $\tilde{\varphi}_i(\mathbf{k})$ of the molecular orbital $\varphi_i(\mathbf{r})$ from which the electron is emitted. Thus, the photoemission intensity,

$$I(k_x, k_y) \propto |\mathbf{A} \cdot \mathbf{k}|^2 |\tilde{\varphi}_i(\mathbf{k})|_{k=\text{const}}^2, \quad (1)$$

finds a powerful interpretation [11]: It reveals the structure of orbital densities on a hemisphere of constant kinetic energy in momentum space [11]. Here, \mathbf{k} denotes the momentum of the photoelectron and \mathbf{A} the vector potential of the ionizing electromagnetic field which also determines

the polarization direction of the field. Equation (1) has been used with great success for organic molecular films in the past years [10–19].

Yet, it is well known that important photoemission effects are beyond the PW approximation [18,19,24,25]. A more accurate description of final state effects can be achieved, for instance, with the independent atomic center approximation, (continuum) multiple scattering X_α approaches, frozen-core Hartree-Fock final states, and time reversed low-energy-electron-electron-diffraction (LEED) states [11,20,23,26–33]. Many approaches of this type rely on combining a static single particle concept—often ground-state density functional theory (DFT)—with a model description of the final state.

In this paper we show that simulating the photoemission process in real time within the framework of time-dependent density functional theory (TDDFT) incorporates very important experimentally observed final-state effects. The approach avoids model assumptions about initial and final state and leads to a consistent DFT-based description of photoemission. The emission dynamics emerges naturally including interaction effects between the outgoing electron and the remaining molecule. In this way the need for explicitly evaluating transition matrix elements, which would require a quasiparticle initial state and a fully interacting final state [22,34], is sidestepped.

Specifically, we demonstrate that the real-time description captures three important effects: First, photoemission perpendicular to the light polarization direction, second, circular dichroism in the angular distribution (CDAD) of photoelectrons, and third, the dependence of the emission pattern on the energy of the photoelectron. These effects are missed by the PW approximation: The polarization factor in Eq. (1) strictly forbids intensity in planes perpendicular to the light polarization, a fixed parallel alignment $\mathbf{A} \parallel \mathbf{k}$ as

preferred by Eq. (1) is not possible for circularly polarized light, and the energy dependence obtained from Eq. (1) is typically much too weak, as it only stems from evaluating the Fourier transform of the orbital on hemispheres of different radii [35].

However, a reliable description of beyond-PW effects is decisive, as exemplified by the following example: In orbital density mapping, one tries to associate the experimentally observed ARPES intensity to one [10,11] or several [13,14] orbitals. As shown in Fig. 1 and discussed in detail below, the PW ansatz can completely miss pronounced spots of intensity. Based on the PW ansatz one would thus associate the wrong orbital with the observed intensity or would wrongly assume contributions from several orbitals in order to explain the intensity pattern. Thus, one would grossly mispredict the studied system's electronic structure. In order to avoid such mistakes, a theoretically consistent approach that allows us to go beyond the PW ansatz, yet is computationally feasible enough to be applicable to true systems, is of great conceptual and practical importance. TDDFT offers the distinct advantage of a favorable ratio of accuracy to computational efficiency.

Different suggestions for simulating photoemission with TDDFT have been made [36–41]. The technique that we rely on here has been pioneered by Pohl *et al.* [38]. Propagating a system's Kohn-Sham (KS) orbitals in real-time on a real-space grid is an established powerful technique [40,42–44]. In our calculations the electronic dynamics is driven by an external electrical dipole field that corresponds to a specific photon energy, polarization, and incidence direction. When the field is large enough it can ionize the system. A fraction of the electron density, represented by the occupied TD KS orbitals, is then traveling away from the molecule. This outgoing density can be understood as originating from a superposition of plane waves. A Fourier transform of the KS orbitals $\varphi_i(\mathbf{R}_D, t)$ recorded at an observation point \mathbf{R}_D far away from the system's center from time t to frequency ω renders a spectral decomposition of the outgoing kinetic energy components. Detecting a photoelectron emitted from a certain state at \mathbf{R}_D is proportional to the probability amplitude [38,45]

$$I_i \propto |\varphi_i(\mathbf{R}_D, E_{\text{kin}} = \hbar\omega)|^2. \quad (2)$$

The total intensity can be calculated by summing up the contributions from all occupied orbitals. By distributing many detection points on a hemisphere, the scheme can record ARPES signals. We recently [45,46] were able to go beyond earlier work on small sodium clusters [38,47,48] and implemented this technique in combination with non-local norm-conserving pseudopotentials [49,50], a diligent choice of the required absorbing boundary conditions [51] and an efficient real-space grid parallelization [46]. These aspects are crucial for the present study in order to achieve the very high accuracy that is needed in the computations. They allow us to study the same complex molecules as in recent ARPES experiments and we can capture electron dynamics over extended regions of space. For the perylene-3,4,9,10-tetracarboxylic dianhydride (PTCDA) calculations we in practice used an equally spaced real-space grid with a spacing of $\Delta r = 0.38a_0$ and a radius of $R = 40a_0$. A timestep of $\Delta t = 0.002$ fs was employed with a Crank-Nicholson propagator [52]. The intensity of the incoming light was ramped to a constant intensity of 10^9 W/cm² within 0.5 fs and remained constant throughout the total propagation time of $T = 50$ fs. The photoemission signals were evaluated at a detection radius of $R_D = 27a_0$. Further technical details can be found in the Supplemental Material [51], which includes Refs. [53–55], and Ref. [45].

In the following we show that the real-time approach remedies all of the three major restrictions of the PW approximation. In a first step we demonstrate that it can describe electron emission that is not parallel to the field vector. The experimental geometry was in this case chosen such that the light polarization is purely parallel to the long molecular axis, denoted as x axis, of the PTCDA molecules, which are azimuthally aligned in the so-called brick wall monolayer on Ag(110) [56–59]. We refer to the short axis in the molecular plane as the y axis. With this setup, the $\mathbf{A} \parallel \mathbf{k}$ condition is fulfilled for emission along the x direction and the PW approximation cannot yield any photoemission intensity at $k_x \approx 0$ Å⁻¹. This is reflected in the momentum map on the left of Fig. 1 which we calculated using the PW approximation, the HOMO in the local-density approximation (LDA), and a photoelectron momentum of $|\mathbf{k}| = 2.0$ Å⁻¹. Turning towards our experimentally recorded ARPES spectrum, shown in the middle of Fig. 1, however, reveals that there is significant emission perpendicular to the light polarization: Two bright spots of intensity occur around $k_x \approx 0$ Å⁻¹ and $k_y \approx \pm 1.5$ Å⁻¹. The PW approximation completely misses these spots. The ARPES pattern from the real-time approach is displayed on the right of Fig. 1. It was obtained by propagating the KS orbitals of an isolated PTCDA molecule under the influence of an ionizing field with a polarization vector aligned in the x direction and a frequency corresponding to a photon energy of $\hbar\omega = 27$ eV [51], i.e., consistent

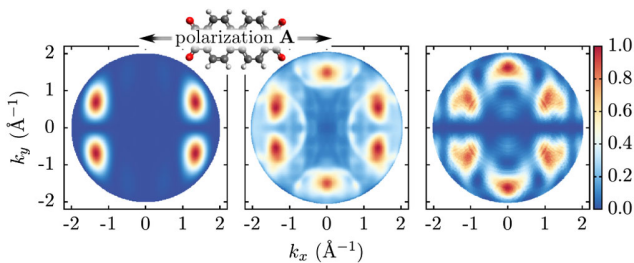


FIG. 1. ARPES maps corresponding to the PTCDA highest occupied molecular orbital (HOMO). Left: plane-wave result; middle: experiment; right: real-time propagation result.

with experiment. We again used the LDA and evaluated Eq. (2) for the HOMO. Clearly, the real-time approach captures the emission perpendicular to the light polarization: All six of the experimentally recorded spots of bright intensity are reproduced, and specifically the ones at $k_x \approx 0 \text{ \AA}^{-1}$, $k_y \approx \pm 1.5 \text{ \AA}^{-1}$. The comparison also reveals that there are differences in some of the smaller features: the experimental data include additional arc-shaped features stemming from the sp bands of the silver substrate, and the shape of the spots is not identical. These differences reflect that both experimentally and computationally, obtaining the accuracy for such detailed comparisons is a challenge. For instance, small reflections from the boundary can remain in the calculations and can slightly distort the low intensity regions. However, there is no doubt that in both theory and experiment, pronounced emission perpendicular to the light polarization is observed.

Encouraged by this success we look at a yet more challenging effect, namely differences in the photoemission signal that result from different circular light polarizations. Studies on adsorbed diatomic molecules suggest that here the photoelectron angular distribution is largely governed by interference effects of partial-wave components of the final state [60–62]. Yet, constructing an appropriate final-state approximation for extended molecules is technically and conceptually challenging. Nonetheless there is an urgent need for theoretical access to photon helicity driven ARPES due to the fascinating insights that can be obtained in this way. For instance, dichroism experiments revealed information about the phase symmetry of molecular orbitals [18], and circular dichroism is one of the candidates for explaining the origin of the homochirality of organic molecules which is relevant for the development of life [63].

A necessary criterion for observing CDAD in photoemission is a definite handedness of the entire system.

Whereas chiral molecules, with amino acids and further biomolecules as prominent examples, inherently provide a handedness [63–65], the required breaking of inversion symmetry can be implemented by the overall experimental geometry also for nonchiral molecules [60]. Thereby, the ordered monolayer structure of the molecular semiconductors provides a first distinct axis, while the other directions are determined by the photon incidence and the photoemission direction.

In this spirit we probe PTCDA with right circularly polarized (RCP) light and left circularly polarized (LCP) light with an energy of $\hbar\omega = 20 \text{ eV}$. We set the incidence direction of the photons in the yz plane with an angle of 65° counted from the surface plane normal as displayed in Fig. 2(b). The polarization vector rotates in a plane perpendicular to the incidence direction. Our first observation (both in experiment and calculation) is an increased intensity for photoelectrons emitted in the direction of the polarization plane with $k_y > 0 \text{ \AA}^{-1}$ as seen in Figs. 2(a) and 2(c). While this finding is also predicted by the PW approach, the latter results in identical ARPES patterns for LCP and RCP which are symmetrical to $k_x = 0 \text{ \AA}^{-1}$ [51]. In contrast, the emission obtained in the real-time propagation has its strongest intensity at about $k_x = 1.4 \text{ \AA}^{-1}$ and $k_y = 0.7 \text{ \AA}^{-1}$ for LCP, as seen in the upper left part of Fig. 2(a), and when switching the polarization to RCP, as shown in the upper right part of Fig. 2(a), this feature changes sides to $k_x = -1.4 \text{ \AA}^{-1}$ and $k_y = 0.7 \text{ \AA}^{-1}$: The whole LCP spectrum equals the RCP one mirrored at the $k_x = 0$ axis. Comparing this to the experimental situation, displayed in the lower row of Fig. 2(a), shows that again the real-time approach captures the relevant experimental features: There are four spots of preferred emission, each one with a different intensity, and upon reversing the helicity, the

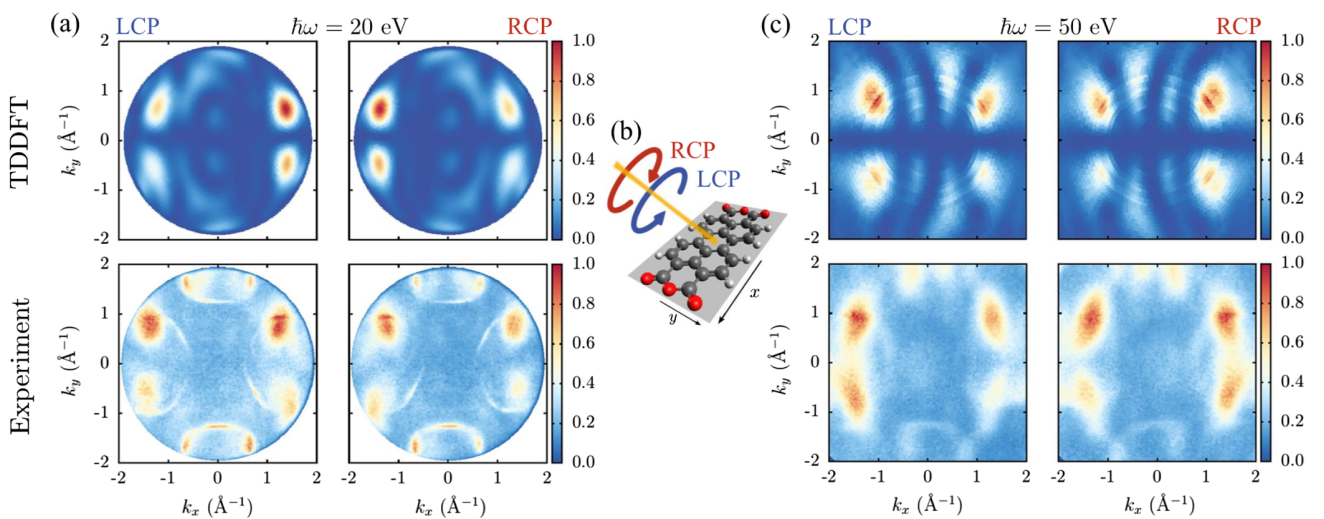


FIG. 2. ARPES maps corresponding to the PTCDA HOMO at $\hbar\omega = 20 \text{ eV}$ (a) and 50 eV (c). Upper row: real-time propagation. Lower row: experiment. Within each panel, LCP spectra are on the left and RCP on the right. Middle panel (b): geometry.

observed pattern is mirrored at the $k_x = 0 \text{ \AA}^{-1}$ axis. Note that the LCP and RCP data were obtained in separate, independent calculations and experiments, respectively. That the panels in the upper row in Figs. 2(a) and 2(c) look like pairwise mirror images is a result of the calculations and attests their numerical accuracy. Comparing theory and experiment in detail we note that the intensity difference between the spots at $k_x = 1.4 \text{ \AA}^{-1}$, $k_y = 0.7 \text{ \AA}^{-1}$ and $k_x = -1.4 \text{ \AA}^{-1}$, $k_y = 0.7 \text{ \AA}^{-1}$ in Fig. 2(a) is more pronounced in the calculations than in the experiment. The influence of the Ag substrate, which is again visible in the experiment, may explain such differences. However, given that recording a subtle observable like dichroism from a monolayer of medium sized molecules is a serious challenge; the qualitative agreement of theory and experiment is noteworthy.

When changing the energy of the incident photons from 20 to 50 eV, we observe a distinct change in the observed ARPES pattern. This pronounced dependence on the kinetic energy of the photoelectron is the third important final-state effect. The lower part of Fig. 2(c) shows the experimental ARPES intensities for a photon energy of $\hbar\omega = 50 \text{ eV}$, i.e., at considerably higher photoelectron energy than in Fig. 2(a). The upper two panels show the corresponding result from the real-time propagation approach. For computing the latter, the change of the photoelectron energy was easily achieved by simply changing the frequency of the applied external field.

Comparing, e.g., the top left panels of Figs. 2(c) and 2(a) shows that the change of photon energy reverses the observed intensity pattern: The two bright spots that appear on the right side (i.e., $k_x > 0 \text{ \AA}^{-1}$) in the LCP part of Fig. 2(a) appear on the left side (i.e., $k_x < 0 \text{ \AA}^{-1}$) in the LCP part of Fig. 2(c). The same pattern reversal is also seen in the RCP signals. The ability to theoretically predict changes in the intensity patterns—within the accuracy limits of TDLDA—upon varying the photoelectron energy is a consequence of the “automatic” adaption of the photoelectron’s state within the real-time approach. As shown in the Supplemental Material [51], this effect is missed completely in the plane-wave approximation. There we also show that the circular dichroism observed experimentally for a different photon incident direction and for the (partially) filled lowest unoccupied molecular orbital of PTCDA is captured by the real-time approach; i.e., the agreement is found not only for the HOMO.

Close inspection of Fig. 2(c) shows that theory and experiment again somewhat differ for some of the less intense features. As mentioned previously, we expect certain differences due to influences of the Ag substrate and finite resolution in the experiment, and remaining quantum mechanical reflections or LDA limitations in the calculations. Therefore, in order to demonstrate the accuracy and generality of the real-time approach beyond the

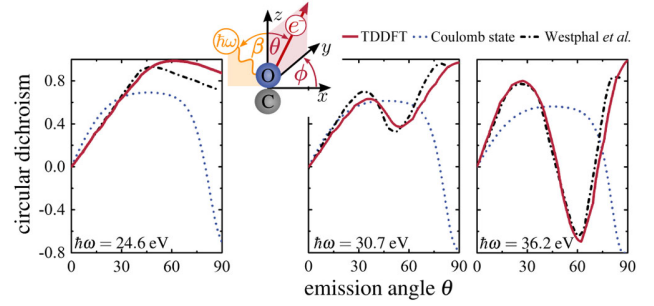


FIG. 3. CDAD intensities for the CO molecule for $\beta = 50^\circ$ and $\phi = 90^\circ$; the black dash-dotted line shows the data [66] from Westphal *et al.*

PTCDA molecule, we compare to established reference results for a completely different system: For adsorbed CO molecules, a significant energy dependence of the circular dichroism has been reported [60,61,66,67].

Figure 3 compares the normalized CDAD intensities, $I_{\text{CDAD}} = (I_{\text{LCP}} - I_{\text{RCP}})/(I_{\text{LCP}} + I_{\text{RCP}})$, of the 4σ orbital of a single CO molecule from the real-time propagation with calculations using frozen-core Hartree-Fock final states [30,61,66], which were calculated by iteratively solving the Lippmann-Schwinger equation. Also shown are results for continuum final states of the bare Coulomb potential corresponding to a single positive charge. The setup is displayed in the inset of Fig. 3 and has been adopted from Ref. [66]. The real-time approach is close to the reference results for all three photon energies, and we presently cannot tell which approach’s limitations are responsible for the small deviations seen for large angles in the left panel. The Coulomb final state results, on the other hand, disagree noticeably, demonstrating that the final state question here is a nontrivial one.

In conclusion, we have demonstrated that the real-time approach to DFT allows us to go beyond the PW final-state approximation in a consistent manner. It opens up theoretical access to important ARPES features. In particular we have shown that three prominent effects are correctly described: emission perpendicular to the light polarization, circular dichroism in the photoelectron angular distribution, and a pronounced energy dependence of the photoemission intensity. Our work indicates that final state properties may also be relevant in several observations in photoemission [33,68] which cannot be described by first principle calculations of the initial state alone.

S. K., I. S., and M. D. acknowledge support by Deutsche Forschungsgemeinschaft (DFG) Graduiertenkolleg 1640 and the Bavarian State Ministry of Science, Research, and the Arts for the Collaborative Research Network “Solar Technologies go Hybrid.” A. S. and F. R. thank the DFG (Grants No. GRK1221, No. SCHO-1260/4-1, No. SCHO-1260/5-1, and No. RE1469/9-1) for support. We acknowledge support during the experiments by V. Feyer and P. Nigge.

- [1] F. Reinert and S. Hüfner, *New J. Phys.* **7**, 97 (2005).
- [2] L. Kronik and S. Kümmel, in *Topics in Current Chemistry*, edited by C. D. Valentin, S. Botti, and M. Cococcioni (Springer, Berlin-Heidelberg, 2014).
- [3] S.-M. Huang, S.-Y. Xu, I. Belopolski, C.-C. Lee, G. Chang, B. Wang, N. Alidoust, G. Bian, M. Neupane, C. Zhang, S. Jia, A. Bansil, H. Lin, and M. Z. Hasan, *Nat. Commun.* **6**, 7373 (2015).
- [4] T. Kondo *et al.*, *Nat. Commun.* **6**, 10042 (2015).
- [5] P. Aebi, R. Fasel, D. Naumovic, J. Hayoz, T. Pillo, M. Bovet, R. Agostino, L. Patthey, L. Schlapbach, F. Gil, H. Berger, T. Kreutz, and J. Osterwalder, *Surf. Sci.* **402–404**, 614 (1998).
- [6] A. Damascelli, H. Zahid, and S. Zhi-Xun, *Rev. Mod. Phys.* **75**, 473 (2003).
- [7] N. Ueno and S. Kera, *Prog. Surf. Sci.* **83**, 490 (2008).
- [8] S. Braun, W. R. Salaneck, and M. Fahlman, *Adv. Mater.* **21**, 1450 (2009).
- [9] A. Kahn, *Mater. Horiz.* **3**, 7 (2016).
- [10] S. Kera, S. Tanaka, H. Yamane, D. Yoshimura, K. K. Okudaira, K. Seki, and N. Ueno, *Chem. Phys.* **325**, 113 (2006).
- [11] P. Puschnig, S. Berkebile, A. J. Fleming, G. Koller, K. Emtsev, T. Seyller, J. D. Riley, C. Ambrosch-Draxl, F. P. Netzer, and M. G. Ramsey, *Science* **326**, 702 (2009).
- [12] J. Ziroff, F. Forster, A. Schöll, P. Puschnig, and F. Reinert, *Phys. Rev. Lett.* **104**, 233004 (2010).
- [13] M. Dauth, T. Körzdörfer, S. Kümmel, J. Ziroff, M. Wiessner, A. Schöll, F. Reinert, M. Arita, and K. Shimada, *Phys. Rev. Lett.* **107**, 193002 (2011).
- [14] P. Puschnig, E.-M. Reinisch, T. Ules, G. Koller, S. Soubatch, M. Ostler, L. Romaner, F. S. Tautz, C. Ambrosch-Draxl, and M. G. Ramsey, *Phys. Rev. B* **84**, 235427 (2011).
- [15] B. Stadtmüller, M. Willenbockel, E. M. Reinisch, T. Ules, F. C. Bocquet, S. Soubatch, P. Puschnig, G. Koller, M. G. Ramsey, F. S. Tautz, and C. Kumpf, *Europhys. Lett.* **100**, 26008 (2012).
- [16] M. Wießner, J. Kübert, V. Feyer, P. Puschnig, A. Schöll, and F. Reinert, *Phys. Rev. B* **88**, 075437 (2013).
- [17] D. Lüftner, T. Ules, E. M. Reinisch, G. Koller, S. Soubatch, F. S. Tautz, M. G. Ramsey, and P. Puschnig, *Proc. Natl. Acad. Sci. U.S.A.* **111**, 605 (2014).
- [18] M. Wießner, D. Hauschild, C. Sauer, V. Feyer, A. Schöll, and F. Reinert, *Nat. Commun.* **5**, 4156 (2014).
- [19] S. Weiß, D. Lüftner, T. Ules, E. M. Reinisch, H. Kaser, A. Gottwald, M. Richter, S. Soubatch, G. Koller, M. G. Ramsey, F. S. Tautz, and P. Puschnig, *Nat. Commun.* **6**, 8287 (2015).
- [20] P. J. Feibelman and D. E. Eastman, *Phys. Rev. B* **10**, 4932 (1974).
- [21] J. B. Pendry, *Surf. Sci.* **57**, 679 (1976).
- [22] M. Dauth, M. Wießner, V. Feyer, A. Schöll, P. Puschnig, F. Reinert, and S. Kümmel, *New J. Phys.* **16**, 103005 (2014).
- [23] W. D. Grobman, *Phys. Rev. B* **17**, 4573 (1978).
- [24] N. Richardson, *Chem. Phys. Lett.* **102**, 390 (1983).
- [25] A. M. Bradshaw and D. P. Woodruff, *New J. Phys.* **17**, 013033 (2015).
- [26] J. W. Gadzuk, *Phys. Rev. B* **10**, 5030 (1974).
- [27] D. Dill and J. L. Dehmer, *J. Chem. Phys.* **61**, 692 (1974).
- [28] A. Liebsch, *Phys. Rev. Lett.* **32**, 1203 (1974).
- [29] Y.-i. Suzuki and T. Suzuki, *J. Phys. Chem. A* **112**, 402 (2008).
- [30] R. R. Lucchese, G. Raseev, and V. McKoy, *Phys. Rev. A* **25**, 2572 (1982).
- [31] P. Krüger, F. DaPieve, and J. Osterwalder, *Phys. Rev. B* **83**, 115437 (2011).
- [32] A. X. Gray, C. Papp, S. Ueda, B. Balke, Y. Yamashita, L. Plucinski, J. Minár, J. Braun, E. R. Ylvisaker, C. M. Schneider, W. E. Pickett, H. Ebert, K. Kobayashi, and C. S. Fadley, *Nat. Mater.* **10**, 759 (2011).
- [33] M. R. Scholz, J. Sanchez-Barriga, J. Braun, D. Marchenko, A. Varykhalov, M. Lindroos, Y. J. Wang, H. Lin, A. Bansil, J. Minár, H. Ebert, A. Volykhov, L. V. Yashina, and O. Rader, *Phys. Rev. Lett.* **110**, 216801 (2013).
- [34] M. Walter and H. Häkkinen, *New J. Phys.* **10**, 043018 (2008).
- [35] Many valence orbitals are rather smooth in the relevant parts of \mathbf{k} space.
- [36] C. A. Ullrich, P.-G. Reinhard, and E. Suraud, *J. Phys. B* **30**, 5043 (1997).
- [37] U. De Giovannini, D. Varsano, M. A. L. Marques, H. Appel, E. K. U. Gross, and A. Rubio, *Phys. Rev. A* **85**, 062515 (2012).
- [38] A. Pohl, P.-G. Reinhard, and E. Suraud, *Phys. Rev. Lett.* **84**, 5090 (2000).
- [39] P. M. Dinh, P. Romaniello, P.-G. Reinhard, and E. Suraud, *Phys. Rev. A* **87**, 032514 (2013).
- [40] M. Mundt and S. Kümmel, *Phys. Rev. B* **76**, 035413 (2007).
- [41] V. Vénier, R. Taïeb, and A. Maquet, *Laser Phys.* **13**, 465 (2003).
- [42] K. Yabana and G. F. Bertsch, *Phys. Rev. B* **54**, 4484 (1996).
- [43] F. Calvayrac, P.-G. Reinhard, and E. Suraud, *Ann. Phys. (N.Y.)* **255**, 125 (1997).
- [44] A. Castro, H. Appel, M. Oliveira, C. Rozzi, X. Andrade, F. Lorenzen, M. A. L. Marques, E. K. U. Gross, and A. Rubio, *Phys. Status Solidi B* **243**, 2465 (2006).
- [45] M. Dauth and S. Kümmel, *Phys. Rev. A* **93**, 022502 (2016).
- [46] I. Schelter and S. Kümmel (unpublished).
- [47] P. Wopperer, B. Faber, P. M. Dinh, P.-G. Reinhard, and E. Suraud, *Phys. Rev. A* **82**, 063416 (2010).
- [48] P. Wopperer, P. M. Dinh, E. Suraud, and P.-G. Reinhard, *Phys. Rev. A* **85**, 015402 (2012).
- [49] N. Troullier and J. L. Martins, *Phys. Rev. B* **43**, 1993 (1991).
- [50] The cutoff radii of our LDA-consistent pseudopotentials were $r_c = 1.39a_0$ for H, $1.09a_0$ for C, and $1.10a_0$ for O.
- [51] See Supplemental Material at <http://link.aps.org/supplemental/10.1103/PhysRevLett.117.183001> for details.
- [52] A. Castro, M. A. L. Marques, and A. Rubio, *J. Chem. Phys.* **121**, 3425 (2004).
- [53] D. E. Manolopoulos, *J. Chem. Phys.* **117**, 9552 (2002).
- [54] T. Gonzalez-Lezana, E. J. Rackham, and D. E. Manolopoulos, *J. Chem. Phys.* **120**, 2247 (2004).
- [55] P. Schaffhauser and S. Kümmel, *Phys. Rev. B* **93**, 035115 (2016).
- [56] C. Seidel, C. Awater, X. Liu, R. Ellerbrake, and H. Fuchs, *Surf. Sci.* **371**, 123 (1997).
- [57] K. Glöckler, C. Seidel, A. Soukopp, M. Sokolowski, E. Umbach, M. Bohringer, R. Berndt, and W. Schneider, *Surf. Sci.* **405**, 1 (1998).

- [58] Y. Zou, L. Kilian, A. Schöll, T. Schmidt, R. Fink, and E. Umbach, *Surf. Sci.* **600**, 1240 (2006).
- [59] M. Wießner, D. Hauschild, A. Schöll, F. Reinert, V. Feyer, K. Winkler, and B. Krömker, *Phys. Rev. B* **86**, 045417 (2012).
- [60] G. Schönhense, *Phys. Scr.* **T31**, 255 (1990).
- [61] R. L. Dubs, S. N. Dixit, and V. McKoy, *Phys. Rev. Lett.* **54**, 1249 (1985).
- [62] I. Dreissigacker and M. Lein, *Phys. Rev. A* **89**, 053406 (2014).
- [63] N. Böwering, T. Lischke, B. Schmidtke, N. Müller, T. Khalil, and U. Heinzmann, *Phys. Rev. Lett.* **86**, 1187 (2001).
- [64] B. Ritchie, *Phys. Rev. A* **13**, 1411 (1976).
- [65] I. Powis, *J. Chem. Phys.* **112**, 301 (2000).
- [66] C. Westphal, J. Bansmann, M. Getzlaff, G. Schönhense, N. A. Cherepkov, M. Braunstein, V. McKoy, and R. L. Dubs, *Surf. Sci.* **253**, 205 (1991).
- [67] C. Westphal, J. Bansmann, M. Getzlaff, and G. Schönhense, *Phys. Rev. Lett.* **63**, 151 (1989).
- [68] H. Maaß, H. Bentmann, C. Seibel, C. Tusche, S. V. Eremeev, T. R. Peixoto, O. E. Tereshchenko, K. A. Kokh, E. V. Chulkov, J. Kirschner, and F. Reinert, *Nat. Commun.* **7**, 11621 (2016).

Supplemental Material to: Perpendicular Emission, Dichroism, and Energy Dependence in Angle-Resolved Photoemission: The Importance of the Final State

M. Dauth¹, M. Graus², I. Schelter¹, M. Wießner², A. Schöll², F. Reinert², and S. Kümmel¹

¹ *Theoretical Physics IV, University of Bayreuth, D-95440 Bayreuth, Germany and*

² *Experimental Physics VII, University of Würzburg, D-97074 Würzburg, Germany*

In the calculations that we refer to in the article *Perpendicular Emission, Dichroism, and Energy Dependence in Angle-Resolved Photoemission: The Importance of The Final State* we suppress reflections at the numerical boundaries by adding a complex absorbing potential to the usual Kohn-Sham Hamiltonian. Specifically, we use $h'_{\text{KS}} = h_{\text{KS}} - iv$ with

$$v(r) = \frac{4\hbar^2}{2mc^2} \left(\frac{2\pi}{\Delta R} \right)^2 \left[\left(\frac{\Delta R}{R_E - 2R_S + r} \right)^2 + \left(\frac{\Delta R}{R_E - r} \right)^2 - 2 \right] \quad (1)$$

that is based on the absorbing potentials presented in Refs. 1–3. Here, R_S denotes the radius where the potential starts acting ($R_S = 28a_0$ for PTCDA and $R_S = 14a_0$ for CO calculations). For $r < R_S$ the absorbing potential is set to zero. $R_E = R_B + \Delta$ is the radius of our numerical box ($R_B = 40a_0$ for PTCDA and $R_B = 26a_0$ for CO) plus a shift $\Delta = 3a_0$ that is needed to prevent the potential from diverging at the numerical boundary. $\Delta R = R_B - R_S$ is the “active length” of the potential. During the total simulation time the norm of the electron density was typically reduced by approximately $1 \cdot 10^{-2}$ due to absorption at the boundaries. Thus, a charge equivalent to approximately $1 \cdot 10^{-2}e$ was absorbed. Under the used conditions, it made almost no difference whether Eq. (2) of the main paper was evaluated for just the HOMO or summed over all orbitals. Furthermore we found that qualitatively, the HOMO ARPES signal stays the same when we propagate only the HOMO and keep all other orbitals frozen.

The frequency of the pulse was chosen as in the experiment. We ran the simulations once with a pulse that was switched on (linearly ramped up over 0.5 fs) and then kept on for the whole time of the simulation (50 fs), and once with a pulse that was ramped up over 0.5 fs, kept on for 24 fs, and then ramped down for 0.5 fs. In both cases, the ARPES signal that we obtained was very similar. We generally find that neither the time to ramp up the laser, nor the time to ramp it down have influence on the spectra for sufficiently long propagation times.

To give an example for the type of results that are found with the plane-wave approximation and circular polarized light we show the momentum maps of the PTCDA HOMO corresponding to $\hbar\omega = 20$ eV (upper row) and 50 eV (lower) with LCP (left) and RCP (right) in Fig. 1. In contrast to experiment and our TDDFT calculations, the PW results are completely symmetric to the $k_x = 0 \text{ \AA}^{-1}$ axis and, thus, miss the major characteristic of the circular dichroism. The results for LCP and RCP are completely identical. This can also be shown analytically. For the example of circular polarization in the xy -plane $\mathbf{A}_{\pm} = (1, \pm i, 0)$, the sign that determines LCP or RCP vanishes in the polarization dependent scaling factor $|\mathbf{A}_{\pm} \mathbf{k}|^2 = (k_x)^2 + (k_y)^2$. Furthermore, increasing the photon energy from 20 to 50 eV does not lead to any significant difference in the momentum maps, contrary to what is observed in the experiment and the real-time approach.

As mentioned in the main paper, we present results for the PTCDA HOMO for another photon incidence direction

FIG. 1. ARPES momentum maps corresponding to the PTCDA HOMO at $\hbar\omega = 20$ eV (upper row) and 50 eV (lower row) calculated with the PW approximation and LCP (left) and RCP (right). The momenta of the photoelectrons at which the spectra are evaluated are $k = 1.9 \text{ \AA}^{-1}$ (left) and $k = 3.4 \text{ \AA}^{-1}$ (right). These values correspond to the energy of the photon minus the HOMO binding energy as predicted by LDA for an isolated PTCDA molecule. To ease comparison, we only display k values up to 2.0 \AA^{-1} for the maps at the bottom.

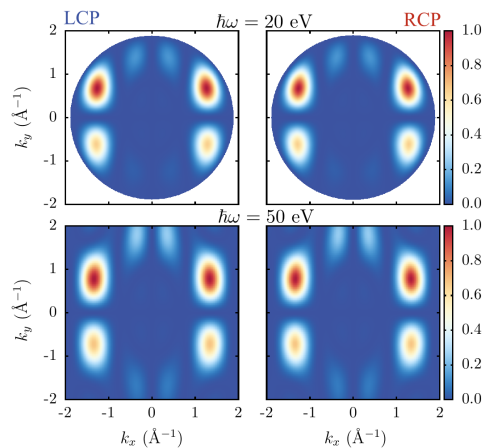


FIG. 2. ARPES momentum maps corresponding to the PTCDA HOMO at $\hbar\omega = 27$ eV. Photon incident direction is 65° towards the surface normal and the xz -plane, i.e., the incidence direction is changed by 90° with regards to the yz -plane incidence in the spectra of Fig. 2 of the main paper. The molecular orientation and the numerical setups are identical. Left: TDDFT. Right: experiment. Upper row: LCP. Lower row: RCP.

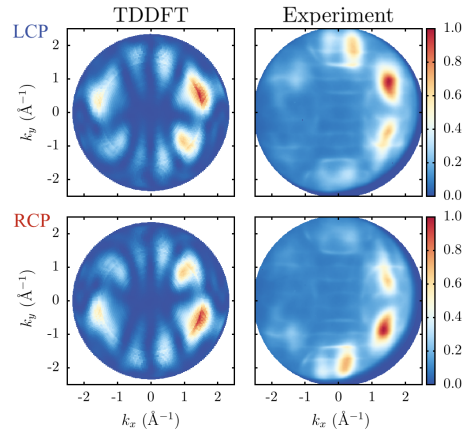
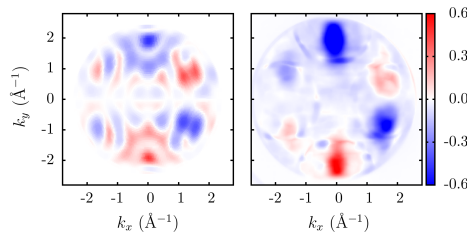


FIG. 3. CDAD intensity from the PTCDA LUMO. Left: real-time propagation. Right: Experiment. In red (blue) colored areas the RCP (LCP) intensity is higher than the LCP (RCP) intensity.



in Fig. 2. Further, we demonstrate that the approach can also be applied to describe ARPES corresponding to other orbitals. Figure 3 shows the results for the lowest unoccupied molecular orbital (LUMO) of PTCDA, which is (partially) filled by electrons from the metal substrate and appears close to the Fermi level [4, 5].

In Fig. 2 PTCDA is probed with photons incoming in the xz -plane. We observe a pronounced dichroism of the HOMO, which manifests in a mirroring of the dominant intensities at $k_x \approx 1.5 \text{ \AA}^{-1}$, $k_y \approx 0.7 \text{ \AA}^{-1}$ (for LCP) to $k_x \approx 1.5 \text{ \AA}^{-1}$, $k_y \approx -0.7 \text{ \AA}^{-1}$ (for RCP) in the real-time propagation results as well as in experiment. The circular dichroism intensity for the LUMO is shown as the difference of the RCP and LCP intensities, $I_{\text{CDAD}} = I_{\text{RCP}} - I_{\text{LCP}}$. To evaluate the CDAD, we normalized each LCP and RCP spectrum to unity before subtracting them. The left panel of Fig. 3 shows the CDAD signal obtained by propagating all orbitals and evaluating the ARPES signal for the unoccupied time-dependent LDA LUMO following Eq. (2) of the main paper. The right panel shows the experimental CDAD signal. We observe that also the LUMO, which is here probed with photons of 27 eV incident in the xz -plane, reveals a strong dichroism signal. CDAD patterns are in general extremely sensitive to the exact positioning and heights of the intensities, therefore this test is extremely challenging and perfect agreement can hardly be expected. Yet, we find that the theoretical and experimental CDAD spectra show the same characteristic pattern of increased and decreased intensity, with distinct blue areas at $k_x \approx 0 \text{ \AA}^{-1}$, $k_y \approx 2 \text{ \AA}^{-1}$ and $k_x \approx 1.5 \text{ \AA}^{-1}$, $k_y \approx -1 \text{ \AA}^{-1}$ and distinct red areas at $k_x \approx 1 \text{ \AA}^{-1}$, $k_y \approx 1 \text{ \AA}^{-1}$ and $k_x \approx 0 \text{ \AA}^{-1}$, $k_y \approx -2 \text{ \AA}^{-1}$.

For the CO calculations we use the same pseudopotentials, the same grid spacing, and the same active length, i.e., the same form, of the imaginary potential as for PTCDA. The radius of the numerical grid could be reduced to $26a_0$ due to the significantly smaller molecule size, resulting in reduced computational effort. The emission signal is recorded at a radius of $14.5a_0$, the propagation time is $T = 40$ fs, and the laser intensity is 10^8 W/cm^2 .

Experiments were performed with a momentum microscope (Omicron NanoESCA) at the ELETTRA synchrotron in Trieste, Italy. All presented data was recorded for samples of perylene-3,4,9,10-tetracarboxylic dianhydride (PTCDA) on Ag(110) in the so-called brick-wall monolayer, where all molecules are aligned with their long axis along the [100]-direction of the substrate. The Ag(110) substrate was cleaned *in situ* by thermal flashing to 400°C , followed by cycles of 45 min Ar^+ ion-sputtering (acceleration voltage 1000V, sample current 15 μA) and annealing (525°C and 480°C , 5 min each). The PTCDA powder was sublimated twice in a home-build system and deposited onto the substrate at room temperature by thermal evaporation from a glass crucible at a temperature of 365°C resulting in a rate of about 0.25 monolayer per min. Coverage was checked by low energy electron diffraction by the occurrence of the well-known $\begin{pmatrix} 2 & 3 \\ -2 & 3 \end{pmatrix}$ superstructure [6, 7].

The momentum maps were recorded with an energy resolution of $\approx 150 \text{ meV}$ and a momentum resolution of $\approx \pm 0.05 \text{ \AA}$ and corrected for darkcurrent and flat-field. The energy aberration of the imaging double hemispherical energy analyzer was compensated by calibration of each energy distribution curve to the Fermi energy. Data recorded

with circular polarized light and dichroism data are plotted as measured, whereas the data recorded with s-polarization in Fig. 1 of the main article is twofold symmetrized to improve statistics.

The calculated and experimental spectra in Fig. 1 and Fig. 2 of the main article and Fig. 1 and Fig. 2 of the Supplemental Material are normalized to unity. For Fig. 1 of the main text we further subtracted a constant background from the experimental intensities and we chose a maximal k -radius of 2.0 \AA^{-1} to accord with the experimental photoemission horizon. In the right panel of Fig. 1 of the main article we reduced the displayed k -range to $k = 2.0 \text{ \AA}^{-1}$ in order to ease comparison to experiment because additional features occur at larger k .

-
- [1] D. E. Manolopoulos, *J. Chem. Phys.* **117**, 9552 (2002).
 - [2] T. Gonzalez-Lezana, E. J. Rackham, and D. E. Manolopoulos, *J. Chem. Phys.* **120**, 2247 (2004).
 - [3] P. Schaffhauser and S. Kümmel, *Phys. Rev. B* **93**, 035115 (2016).
 - [4] J. Ziroff, F. Forster, A. Schöll, P. Puschnig, and F. Reinert, *Phys. Rev. Lett.* **104**, 233004 (2010).
 - [5] Y. Zou, L. Kilian, A. Schöll, T. Schmidt, R. Fink, and E. Umbach, *Surf. Sci.* **600**, 1240 (2006).
 - [6] C. Seidel, C. Awater, X. Liu, R. Ellerbrake, and H. Fuchs, *Surf. Sci.* **371**, 123 (1997).
 - [7] M. Wießner, D. Hauschild, a. Schöll, F. Reinert, V. Feyer, K. Winkler, and B. Krömker, *Phy. Rev. B* **86**, 045417 (2012).

Publication 6

Outer-valence electron spectra of prototypical aromatic heterocycles from an optimally tuned range-separated hybrid functional

Journal of Chemical Theory and Computation **10**, 1934 (2014)

David A. Egger^{1,2}, Shira Weissman², Sivan Refaely-Abramson², Sahar Sharifzadeh³, **Matthias Dauth**⁴, Roi Bear⁵, Stephan Kümmel⁴, Jeffrey B. Neaton³, Egbert Zojer¹, and Leeor Kronik²

¹Institute of Solid State Physics, Graz University of Technology, 8010 Graz, Austria

²Department of Materials and Interfaces, Weizmann Institute of Science, Rehovoth 76100, Israel

³Molecular Foundry, Lawrence Berkeley National Laboratory, Berkeley, California 94720, United States

⁴Theoretical Physics IV, University of Bayreuth, D-95440 Bayreuth, Germany

⁵Fritz Haber Center for Molecular Dynamics, Institute of Chemistry, Hebrew University, 91904 Jerusalem, Israel

⁶Department of Physics and Kavli Energy Nanosciences Institute, University of California, Berkeley, California 94720, United States

Publ.6

My contribution

I implemented the hybrid calculations within the KS scheme into PARSEC. I performed the GSIC and KS hybrid calculations, was part of the scientific discussion, and wrote a draft for the section explaining the GSIC and KS hybrid calculations.

Publ.6

Outer-valence Electron Spectra of Prototypical Aromatic Heterocycles from an Optimally Tuned Range-Separated Hybrid Functional

David A. Egger,^{†,‡,∇} Shira Weissman,^{‡,∇} Sivan Refaely-Abramson,^{*,‡} Sahar Sharifzadeh,[§] Matthias Dauth,^{||} Roi Baer,[⊥] Stephan Kümmel,^{||} Jeffrey B. Neaton,^{§,#} Egbert Zojer,[†] and Leor Kronik^{*,‡}

[†]Institute of Solid State Physics, Graz University of Technology, 8010 Graz, Austria

[‡]Department of Materials and Interfaces, Weizmann Institute of Science, Rehovoth 76100, Israel

[§]Molecular Foundry, Lawrence Berkeley National Laboratory, Berkeley, California 94720, United States

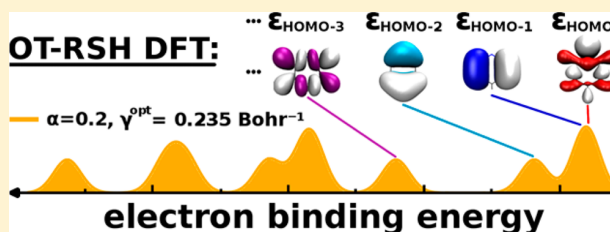
^{||}Theoretical Physics IV, University of Bayreuth, 95440 Bayreuth, Germany

[⊥]Fritz Haber Center for Molecular Dynamics, Institute of Chemistry, Hebrew University, 91904 Jerusalem, Israel

[#]Department of Physics and Kavli Energy Nanosciences Institute, University of California, Berkeley, California 94720, United States

Supporting Information

ABSTRACT: Density functional theory with optimally tuned range-separated hybrid (OT-RSH) functionals has been recently suggested [Refaely-Abramson et al. *Phys. Rev. Lett.* 2012, 109, 226405] as a nonempirical approach to predict the outer-valence electronic structure of molecules with the same accuracy as many-body perturbation theory. Here, we provide a quantitative evaluation of the OT-RSH approach by examining its performance in predicting the outer-valence electron spectra of several prototypical gas-phase molecules, from aromatic rings (benzene, pyridine, and pyrimidine) to more complex organic systems (terpyrimidinethiol and copper phthalocyanine). For a range up to several electronvolts away from the frontier orbital energies, we find that the outer-valence electronic structure obtained from the OT-RSH method agrees very well (typically within ~ 0.1 – 0.2 eV) with both experimental photoemission and theoretical many-body perturbation theory data in the GW approximation. In particular, we find that with new strategies for an optimal choice of the short-range fraction of Fock exchange, the OT-RSH approach offers a balanced description of localized and delocalized states. We discuss in detail the sole exception found—a high-symmetry orbital, particular to small aromatic rings, which is relatively deep inside the valence state manifold. Overall, the OT-RSH method is an accurate DFT-based method for outer-valence electronic structure prediction for such systems and is of essentially the same level of accuracy as contemporary GW approaches, at a reduced computational cost.



I. INTRODUCTION

Many electronic properties of molecules and materials are determined by and understood through the energetics of the valence electrons, which are often probed experimentally using photoemission spectroscopy (PES).¹ Via measurement of the kinetic energy of photoemitted electrons, PES provides direct experimental access to the electron ejection energies, the smallest of which is the ionization potential (IP). Calculating PES data from first principles is a long-standing challenge to modern electronic structure methods.^{2,3} A state-of-the-art method for obtaining ionization spectra theoretically is many-body perturbation theory (MBPT), which calculates quasi-particle excitation energies via solving the Dyson equation, typically within the GW approximation (where G is the Green function and W is the dynamically screened Coulomb potential).^{4–7} However, GW calculations can be computationally demanding. Moreover, in particular for gas-phase computations that are at the center of this work, results can

be sensitive to details of the specific GW scheme employed^{8–13} and can also be challenging to converge.^{11,14}

Density functional theory (DFT),^{15,16} in which the ground-state electron density, rather than the many-electron wave function, is the fundamental quantity,¹⁷ is a computationally efficient first principles method for calculating the electronic structure of many-electron systems. DFT is often made practical via the Kohn–Sham (KS) scheme,¹⁸ in which the original many-electron problem is mapped uniquely into a fictitious noninteracting electron system yielding the same electron density. This mapping leads to effective single-particle equations that provide a significant conceptual and computational simplification of the original many-electron problem. However, due to the fictitious nature of the noninteracting electrons, the correspondence of KS eigenvalues with ionization

Received: October 31, 2013

Published: March 25, 2014

energies measured in an experiment is not at all straightforward.^{3,19} It can be shown that for the exact KS potential, the energy of the highest occupied molecular orbital (HOMO) equals the negative of the IP, a result known as the IP theorem.^{20–23} Lower-lying eigenvalues do not strictly correspond to electron removal energies.¹⁹ For outer-valence electrons, however, exact DFT eigenvalues may still serve as a useful and even quantitative approximation to electron removal energies.^{3,24} We note that in general the simulation of photoemission spectra also requires that the photoionization cross-section is addressed.¹ Its calculation is outside the scope of the present manuscript, which focuses on the correct description of the energetics. Our comparison between the calculated density of states and the photoelectron spectra concentrates, therefore, on peak positions rather than peak intensities. We note, however, that for gas-phase ultraviolet photoemission spectroscopy (UPS)—the standard choice for probing molecular outer-valence states—angle-dependent cross-section effects are irrelevant, owing to orientational averaging, and orbital-dependent cross-section effects are relatively weak.²⁵ Therefore, their neglect is not expected to have serious consequences.

The KS mapping scheme relies on an exchange-correlation energy-functional of the density, the exact form of which is generally unknown and must be approximated. Common approximate exchange-correlation functionals used within the KS scheme are the local density approximation (LDA) and the generalized gradient approximation (GGA).^{15,16} In the former, one assumes that at each point in space the exchange-correlation energy per particle is given by its value for a homogeneous electron gas. In the latter, information on deviations from homogeneity is partly accounted for by considering gradients of the charge density. Unfortunately, for gas-phase molecules, KS eigenvalues obtained through the use of these approximations are not in good agreement with experimental ionization spectra.^{3,26} First, the IP theorem is grossly disobeyed and the negative of the HOMO energy usually underestimates the IP severely.^{27–30} Even if this difference is accounted for by rigidly shifting the theoretical eigenvalue spectrum,^{31,32} the calculated eigenvalue spectrum may still exhibit qualitative failures, notably an erroneous ordering of the electronic levels (see, e.g., refs 33–41).

These two drawbacks can be traced back to two different (yet not unrelated) deficiencies of the above-described approximations: lack of a derivative discontinuity (DD) and orbital self-interaction errors (SIE).^{3,26,28,42} The DD is a uniform “jump” in the KS potential, when approaching the integer electron number either from above or from below. This “jump” helps to account for the discontinuity of the chemical potential at integer electron numbers, i.e., for the fact that the electron removal energy is not the same as the electron insertion energy.¹⁶ Part of the discontinuity in the chemical potential is accounted for by the KS kinetic energy term.^{20,23} But the kinetic energy contribution to the discontinuity in the chemical potential is generally insufficient, and the remaining discontinuity must be provided by the DD. Because the electron–ion and Hartree energies are continuous in the electron density, the remaining discontinuity can only be attained by a jump in the exchange-correlation potential. However, in standard LDA or GGA functionals, the exchange-correlation potential explicitly depends on the electron density and does not incorporate any orbital dependence (in contrast to, e.g., Fock exchange). As a result, calculations based on these approximations cannot

exhibit any DD in the exchange-correlation part of the potential.⁴³ Instead, they approximately average over it, and as a consequence the KS-HOMO energy is strongly underbinding with respect to the “true” ionization potential.^{31,44,45}

The SIE⁴⁶ arises from the fact that the classical electron–electron repulsion term (Hartree potential) in the KS equation means that each electron is repelled from the total charge in the system, including a spurious repulsion from itself. Because KS theory is, in principle, exact, whatever error one makes in the Hartree term must then be completely canceled out by the exact exchange-correlation term. Unfortunately, only partial error cancellation is obtained in either LDA or GGA. For strongly localized orbitals, self-interaction may be significant and spuriously destabilize electron energies.²⁶

The situation can be improved, if one uses “hybrid” DFT, i.e., functionals that contain exact exchange based expressions employed using a nonlocal Fock operator.²⁶ We emphasize that while such functionals do not fall within the KS scheme, they are still very much within the DFT framework^{3,26,47} through the generalized Kohn–Sham (GKS) scheme.⁴⁸ In the KS scheme, many-body effects are incorporated entirely in a multiplicative potential (which is the sum of the Hartree and exchange-correlation potentials). In contrast, in the GKS scheme, many-body effects are incorporated in a combination of a multiplicative potential and a nonlocal operator (nonmultiplicative potential). This is achieved via mapping to a partially interacting electron gas. Generally, in the GKS scheme, the additional nonlocal operator can mitigate the need for a DD in the multiplicative potential.²⁶ This may reduce errors associated with averaging over the DD in practical approximations. Most hybrid functionals in everyday use are of the global type, i.e., they contain a fixed fraction of Fock exchange.^{49–51} In practice, one typically observes that HOMO energies extracted from such hybrid functionals are closer to experimental ionization energies than those obtained from LDA or GGA but still significantly underestimate those observables.^{9,32,52} Spectral distortions (including the possibility of an erroneous ordering of the electronic levels) are often mitigated, as the fraction of Fock exchange reduces the SIE.^{3,26,33,34} However, the quantitative details of the eigenvalue spectrum typically still depend on the specific choice of the approximate hybrid functional.⁵³

One reason for the failure of conventional hybrid functionals to obey the IP theorem is the presence of only a fraction of exact exchange. Because of this, they do not yield the correct $\sim 1/r$ asymptotic potential that should be “felt” by an electron at large distances from the molecule, which is especially relevant for describing the ionization process. However, when using the full Fock exchange to correct for that, the delicate balance between exchange and correlation is disrupted, which is highly detrimental—especially for short-range electron–electron interactions that govern chemical bonding.²⁶ A promising strategy for tackling that problem is offered by the more recent class of range-separated hybrid (RSH) DFT functionals,⁵⁴ pioneered by Savin and co-workers.⁵⁵ In these functionals, the interelectron Coulomb repulsion term is separated into long-range (LR) and short-range (SR) components via a range-separation parameter γ . The LR term is mapped using full Fock exchange, thereby establishing the correct asymptotic potential. The SR term is (typically) mapped using a GGA approach, maintaining the compatibility between the exchange and correlation expressions. In this approach, one still needs to determine the range-separation parameter, γ .

Both formal considerations⁵⁶ and practical simulations show that aiming at accurate results for a broad range of systems, one typically needs significantly different values of γ . This is taken care of by using optimally tuned RSH (OT-RSH) functionals.^{32,47} There, instead of using one and the same range-separation parameter for all systems, γ is tuned for each system such that physically motivated tuning conditions are fulfilled without introducing any empirical parameters. In particular, it has been shown for gas phase molecules that insisting on the HOMO energy being equal to the negative of the IP (i.e., fulfilling the IP theorem) for the neutral and anion species yields highly accurate HOMO energies and HOMO–LUMO gaps when compared to experimentally measured fundamental gaps or to the results of GW calculations.^{52,57} More recently, some of us have shown that in addition to the IP and the fundamental gap, the entire higher-lying part of the valence-electron spectrum of gas-phase molecules and molecular solids can be accurately described by the eigenvalues of OT-RSH ground-state DFT calculations.^{58,59} In particular, it has been suggested that a more general OT-RSH functional that introduces a fraction of Fock exchange in the SR and simultaneously maintains the full Fock exchange in the LR⁶⁰ allows for a more flexible treatment of differently localized molecular orbitals, resulting in an accurate description of more complex organic molecules relevant for applications in organic electronics.⁵⁸

In the present contribution, we further investigate the capabilities of such more general OT-RSH functionals for predicting outer-valence electron spectra of organic molecules in the gas phase. First, we study the prototypical aromatic building blocks—benzene, pyridine, and pyrimidine (see Figure 1a). This choice is motivated by the fact that for such simple

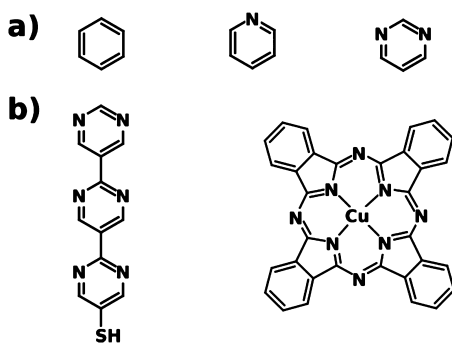


Figure 1. Molecules studied in this article. (a) Prototypical aromatic rings—benzene, pyridine, and pyrimidine. (b) More complex representative systems—terpyrimidinethiol and copper phthalocyanine.

systems, existing high-level experimental PES data can serve as useful benchmarks for theory. Moreover, the nitrogen heteroatoms in the azabenzenes can be expected to result in differently localized molecular orbitals in the higher-lying part of the valence electron system and, in particular, close-lying σ and π states.³⁰ For their accurate description, the OT-RSH approach would need to attain a quantitatively satisfactory balance of self-interaction errors for both.⁵⁸ Moreover, these prototypical systems were recently identified as a challenge for both the GW⁶¹ and the OT-RSH⁶² methods. Here, we perform both OT-RSH and GW calculations for these systems and find that they overall yield similar (to ~ 0.2 eV) eigenvalue energies,

both being highly accurate compared to PES experiments. We suggest that a simultaneous reliable prediction of both π and σ orbital energies is indeed within the realm of the OT-RSH functional applied here. Still, we identify one specific molecular orbital that is peculiar to ring-type molecules, which in the OT-RSH calculations displays a significant deviation from experimental results and GW calculations. We analyze the origin of this discrepancy by further computing the spectra of the same systems using conventional hybrid calculations, as well as explicitly self-interaction corrected (SIC) calculations.

With the obtained overall very encouraging results at hand, we proceed toward larger and more complex systems, here chosen to be terpyrimidinethiol and copper phthalocyanine (3N-thiol and CuPc, see Figure 1b). These molecules, which also contain N as a heteroatom, are interesting for novel applications in organic electronics^{63–68} but at the same time challenging to assess theoretically due to pronounced differences in SIE among the high-lying orbitals in the valence electron spectrum.^{34,68,69} Through a comparison to GW calculations and/or PES experiments, we show that OT-RSH can provide accurate valence-electron spectra also for these more complex organic systems, with an optimal choice for the short-range Fock exchange that is guided by conventional hybrid functional calculations. Our results clearly demonstrate that OT-RSH functionals are a highly promising, state-of-the-art approach for predicting ionization spectra of gas-phase organic molecules.

II. THEORETICAL AND METHODOLOGICAL DETAILS

A. Formalism. As mentioned in the Introduction, we examine a generalized RSH form, which allows for different amounts of Fock exchange in the short range and in the long range.⁷⁰ We use the range-partitioning expression of Yanai et al., given by⁷¹

$$\frac{1}{r} = \frac{\alpha + \beta \operatorname{erf}(\gamma r)}{r} + \frac{1 - [\alpha + \beta \operatorname{erf}(\gamma r)]}{r} \quad (1)$$

("HF") ("GGA")

Here, r is the interelectron coordinate and α , β , and γ are adjustable parameters. Naturally, this partition is not unique, but the choice of the error function is computationally convenient when using a Gaussian basis for expanding the wave functions of finite systems.⁵⁵ Equation 1 defines the range-separation procedure, where the Coulomb operator, $1/r$, in the exchange-part of the xc potential is replaced by two complementary terms, which are treated differently. As suggested by the “HF” and “GGA” delimiters in the equation, the first term is treated using Hartree–Fock exchange, the second term is treated using GGA semilocal exchange. Specifically, using the Perdew–Burke–Ernzerhof (PBE)⁷² form for the GGA exchange–correlation leads to the following expression for the exchange–correlation energy⁷³

$$E_{xc}^{\text{RSH}} = \alpha E_{x,\text{HF}}^{\text{SR},\gamma} + (1 - \alpha) E_{x,\text{PBE}}^{\text{SR},\gamma} + (\alpha + \beta) E_{x,\text{HF}}^{\text{LR},\gamma} + (1 - \alpha - \beta) E_{x,\text{PBE}}^{\text{LR},\gamma} + E_{c,\text{PBE}} \quad (2)$$

where the superscripts LR and SR denote that the full Coulomb repulsion, $1/r$, has been substituted by the LR and SR Coulomb repulsions, $\operatorname{erf}(\gamma r)/r$ and $\operatorname{erfc}(\gamma r)/r$, respectively. PBE correlation is used for the entire range. Yanai et al. viewed α , β , and γ as semiempirical parameters and determined “universal” values for them based on benchmark thermochemistry data. Here, we wish to determine these parameters based on the satisfaction of

inherent constraints on the exchange-correlation density functional, without recourse to experimental data.

From eq 2 it is clear that for full long-range Fock exchange, which guarantees the correct asymptotic potential, one condition is that $\alpha + \beta = 1$ (note that the fit to thermochemistry data performed by Yanai et al. leads to $\alpha + \beta = 0.65$, i.e., to a potential that is not asymptotically correct and will, therefore, run into problems when trying to associate eigenvalues with ionization energies or electron affinities). Equation 2 further shows that α controls the fraction of SR Fock exchange. We restrict the current investigation to α values between 0 and 0.2. This is because in the former limit, the SR behavior is expected to be GGA-like; in the latter limit, the SR behavior is expected to resemble that of a conventional hybrid functional.^{58,74} For example, in the PBE0 hybrid functional, which is based on the PBE semilocal functional, a global exact-exchange fraction of 25% is used.⁵¹ In a RSH functional, the SR Fock exchange fraction is indeed expected to be somewhat smaller than in a conventional hybrid functional, because the LR Fock exchange is 100% in the former but only a finite fraction in the latter. The remaining parameter, γ , controls the range-separation. As mentioned in the Introduction, we do not seek a universal value for γ . Instead, we rely on a nonempirical tuning procedure, where γ is adjusted on a per-system basis. One possibility to determine the optimal gamma, γ^{opt} , is to choose it such that the IP theorem is satisfied:^{32,75}

$$\varepsilon_{\text{H}}^{\gamma^{\text{opt}}}(N) = -\text{IP}^{\gamma^{\text{opt}}}(N) \quad (3)$$

$\varepsilon_{\text{H}}(N)$ is the HOMO energy of the N -electron system and $\text{IP}(N)$ is the ionization potential of the N -electron system, determined from total energy difference of the N - and $(N - 1)$ -electron systems. In general, as emphasized by the superscript notation, both $\varepsilon_{\text{H}}(N)$ and $\text{IP}(N)$ display a strong γ dependence.

It is often useful to invoke the IP theorem not only for the molecule in its neutral state but also in certain charged states. The condition which then needs to be fulfilled is that the target function J^2 , given by³²

$$J^2(\gamma; \alpha) = \sum_i (\varepsilon_{\text{H}}^{\gamma; \alpha}(N + i) + \text{IP}^{\gamma; \alpha}(N + i))^2 \quad (4)$$

is minimized. In eq 4, i can in principle adopt any integer number, and one can observe the effect of adding further terms on the residual J value (*vide infra*). In practice, only values of i that are close to zero are of interest to avoid information from highly charged radical species—a point elaborated below. In particular, including the anion has been found to be highly beneficial for the prediction of fundamental gaps and the energies of charge-transfer excited states.^{52,76,77} Note that when restricting i to 0 in eq 4, which we do here if the electron affinity is negative and the molecule does not bind an extra electron, then eq 3 is recovered. In agreement with previous work,^{32,52,57–60,78–80} it was repeatedly found that the optimal γ strongly changes from one system to the other, showing that our “per system” tuning approach is indeed necessary.

The above-mentioned optimal-tuning of γ can, in principle, be performed for any choice of the SR Fock exchange parameter, α . In fact, various strategies can be employed to determine α . These are discussed below in detail, along with their pros and cons, in the context of specific computational results.

B. Computational Details. All PBE calculations (within the KS scheme) and PBE0 and RSH calculations (within the

GKS scheme) presented in this article were obtained within the QChem⁸¹ and NWChem⁸² codes, using cc-PVTZ⁸³ basis functions. All geometries were optimized using the PBE functional. As the above-described tuning scheme is based on components taken from well-established density functionals (cf. eq 2) and range-separation is available in many different electronic structure codes, optimal tuning of γ via eq 4 is straightforward to perform. Moreover, the tuning strategy is computationally efficient, as it relies on a series of standard total-energy DFT calculations. We note, however, that when charging the gas-phase molecule as part of the above-explained tuning procedure, the configuration of the cation and/or anion must be identified carefully, as it may affect the results of the calculation.⁸⁴

We illustrate the possible complications associated with different ion configurations by considering pyridine—one of the molecules of Figure 1, which is discussed extensively in the results section. When tuning γ using the above-described approach, it is important to ensure that the character of the HOMO (related to the left-hand term in eq 3) corresponds to the “hole density,” defined as the charge-density difference of the neutral and charged states (and, consequently, related to the right-hand term in eq 3). For pyridine, the self-consistent solution of the GKS equation with the RSH functional was found to lead to two different doublet configurations of the cation, depending on the initial guess used in the procedure. These two configurations correspond to two qualitatively different hole densities (see Figure 2, left part). As shown in the

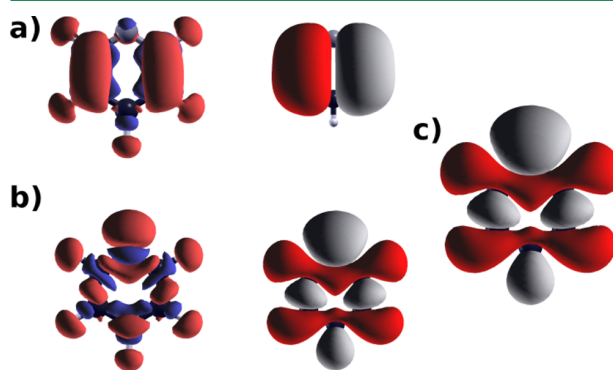


Figure 2. Charge-density difference between neutral and cation (left) and LUMO of cation (right), obtained using two different doublet configurations (a and b) of the pyridine cation. The configuration denoted by b is the energetically more stable one. In the charge-density difference plots, red (blue) regions denote areas of electron density depletion (accumulation) as a consequence of the ionization process. (c) HOMO of the neutral pyridine molecule.

right part of Figure 2, the reason for the different hole densities is that the two cation configurations possess two different LUMO orbitals; i.e., the two cationic ground states represent two different ionization processes. The main difference is that the electron “loss” is, in one case, from a π orbital and, in the other case, from a σ orbital. These two cationic configurations are energetically close, which is consistent with the observation that the HOMO and the HOMO–1 of pyridine are very close in energy (*vide infra*). Importantly, however, only the “hole density” depicted in Figure 2b—which is associated with the configuration lower in energy, i.e., the true ground state predicted for the cation—corresponds to the HOMO of pyridine (see Figure 2c). Therefore, one has to ensure that the

cationic state shown in Figure 2b is indeed the one entering the tuning procedure, in order to retain consistency for the orbital energies and total energies required in eq 3.

For our analysis of the OT-RSH results, we also performed comparative GW calculations, as well as self-interaction-corrected calculations and KS-PBE0 calculations (the latter are defined and explained below). Our GW calculations are based on a standard G_0W_0 scheme,¹⁴ where quasi-particle energies are computed via a first-order correction to DFT eigenvalues, with no self-consistent update of the starting wave functions. The starting quasi-particle wave function for the G_0W_0 corrections was obtained from the PBE functional.⁷² The static dielectric function is computed within the random-phase approximation and extended to finite frequency via the generalized plasmon-pole (GPP) model of Hybertsen and Louie.⁵

Our G_0W_0 calculations were performed using the BerkeleyGW package,⁸⁵ which employs a plane-wave basis set to compute the dielectric function and self-energy, using a PBE starting point. DFT-PBE calculations were performed within the Quantum Espresso package,⁸⁶ which is compatible with BerkeleyGW. The nuclei and core electrons were described by Troullier–Martins relativistic norm-conserving pseudopotentials,⁸⁷ which are part of the Quantum Espresso pseudopotential library. Here, one, four, five, and six electrons were explicitly considered as valence electrons for H, C, N, and S, respectively, with cutoff radii (in Bohr) of 1.3, 0.5, 1.0, and 1.7, respectively. We used a plane-wave basis cutoff of 80 Ry for benzene and 120 Ry for pyridine, pyrimidine, and 3N-thiol. These values lead to a total DFT energy converged to <1 meV/atom. To avoid spurious interactions with periodic images, we used a supercell with lattice vectors twice the size necessary to contain 99% of the charge density and, when computing the GW self-energy, the Coulomb interaction was truncated at distances larger than half of the unit cell size. The supercell dimensions, in atomic units, were $35 \times 39 \times 24$; $30 \times 20 \times 32$, $19 \times 30 \times 30$; and $64 \times 26 \times 15.5$ for benzene, pyridine, pyrimidine, and 3N-thiol, respectively.

Our static dielectric function and self-energy were constructed from 4914, 5515, 5071, and 3598 unoccupied states, respectively, for benzene, pyridine, pyrimidine, and 3N-thiol. For the former three prototypical small molecules, this energy range corresponds to 90 eV above the vacuum energy, while for 3N-thiol, it corresponds to 50 eV above the vacuum energy. Fewer states were included for 3N-thiol due to the greater computational expense associated with this rather large system. A static remainder approach was applied to the self-energy to approximately complete the unoccupied subspace.⁸⁸ The plane-wave cutoff for the dielectric function was 30 Ry for pyridine and pyrimidine and 24 Ry for 3N-thiol and benzene. We find that these parameters converge the HOMO energies of the prototypical small molecules to less than 0.1 eV. On the basis of the convergence behavior of these molecules and the residual differences that we find for GW and OT-RSH HOMO energies (vide infra), we extrapolate the errors associated with eigenvalues of the 3N-thiol calculation to be less than 0.2 eV.

All SIC calculations were based on the seminal SIC concept of Perdew and Zunger.⁴⁶ However, we constructed a spatially local, multiplicative exchange-correlation potential identical for all orbitals in the system, which ensures that the SIC remains within the KS realm.^{89,90} This is based on the generalized optimized effective potential (OEP) equation, which extends the original OEP equation to the case of unitarily variant

functionals. It is solved using the generalized Krieger–Li–Iafrate (KLI) approximation.^{89,91} Unlike the KLI approximation to the standard OEP equation, which can introduce significant deviations for the SIC,⁹² the generalized KLI approximation used here has been shown to be an excellent approximation to the generalized OEP. The additional degree of freedom arising from the variance inherent to our procedure can be used to construct a set of orbitals that minimize the total SIC energy of the system, where we applied a complex-valued energy minimizing unitary orbital transformation.⁹⁰ For additional insights, we also used the PBE0 functional in conjunction with a local multiplicative potential, constructed—in contrast to traditional GKS schemes—via the KLI⁹¹ approximation for the exact exchange part of the functional. We refer to these calculations as PBE0^{KS}.

All SIC and PBE0^{KS} calculations were performed with the Bayreuth version⁹³ of the PARSEC real-space code,⁹⁴ where we employed a grid-spacing of 0.2 Bohr and Troullier–Martins norm-conserving pseudopotentials.⁸⁷

Finally, for a meaningful comparison between the results of different functionals and/or computational approaches, we tested explicitly that eigenvalues obtained from different codes and basis-set expansions (Gaussian, planewave, real-space) do not differ by more than 0.1 eV for the same underlying functional. Furthermore, we verified by visual inspection^{95,96} that eigenvalues calculated from different methods correspond to the same molecular orbitals.

III. PROTOTYPICAL AROMATIC RINGS—RESULTS AND DISCUSSION

We start our analysis by considering the prototypical aromatic gas-phase molecules of Figure 1a. The computed peak positions in the eigenvalue spectra (neglecting differences of the photoionization cross sections) should correspond to those in the photoemission spectra (in arbitrary units, denoted as a.u. or arb. units) and are shown in Figure 3. The computed spectra are obtained from OT-RSH eigenvalues with SR Fock exchange fractions of $\alpha = 0$ and $\alpha = 0.2$ for (a) benzene, (b) pyridine, and (c) pyrimidine. The results are compared to gas-phase PES spectra from refs 97–99 and to the results of our GW calculations. Importantly, the spectra are plotted on an absolute energy scale; i.e., the calculated eigenvalue spectra shown in Figure 3 have *not* been shifted so as to align the theoretical data with experimental results. To facilitate a visual comparison with the experimental spectra, we broadened the calculated eigenvalue spectra via convolution with a Gaussian (with a standard deviation of 0.4 eV for benzene and 0.2 eV for pyridine and pyrimidine). For all three systems, we find an overall excellent agreement between OT-RSH, our GW calculations, and experimental results. In particular, the HOMO energies calculated from the OT-RSH approach correspond very well to the first peak in the experimental spectrum, indicating the success of the tuning procedure. In addition, the shape of the experimental spectra at higher binding energies is very well reproduced by the OT-RSH spectra. Note that the comparison extends over a relatively large energy range of ~ 8 eV below the first IP (much more than the ~ 3 eV in previous work on somewhat larger aromatic-based organic molecules⁵⁸). The agreement over such a wide energy range is remarkable, considering that the correspondence between DFT eigenvalues and photoemission energies is expected, on general theoretical grounds, to deteriorate for lower-lying states.^{3,24,100} Interestingly, the shape of the OT-

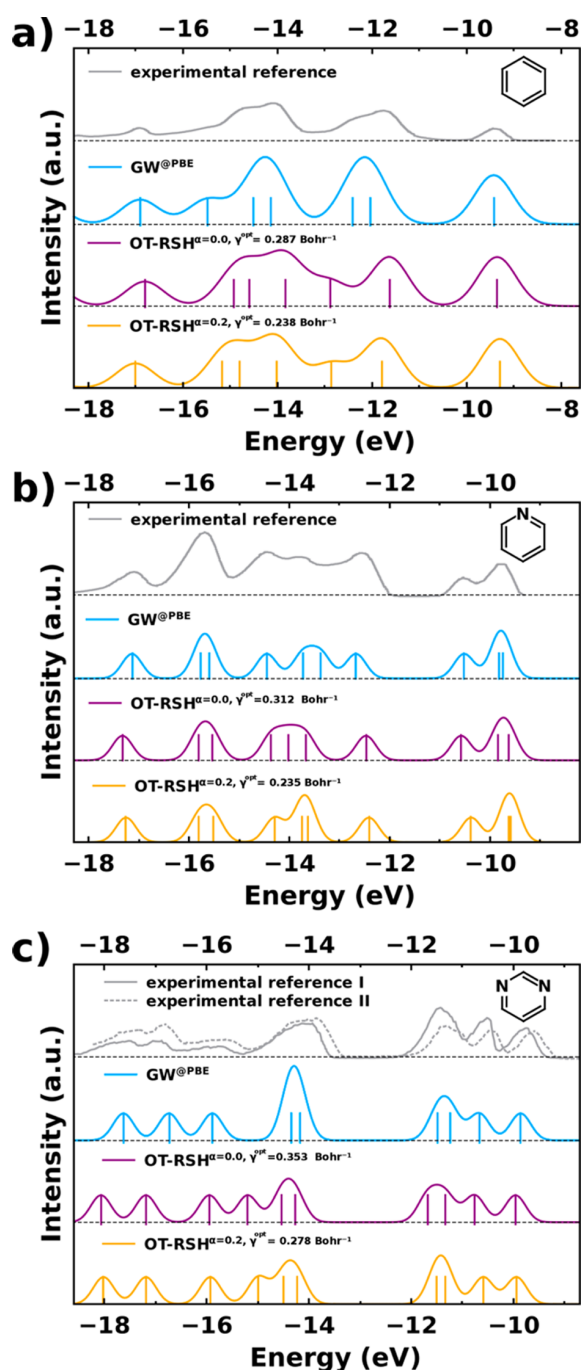


Figure 3. Valence electron spectra for (a) benzene, (b) pyridine, (c) pyrimidine, as obtained from experiment (benzene and pyridine, ref 97; pyrimidine, refs 99 and 98, reference I and II in the figure), compared with simulated data obtained from GW and OT-RSH calculations (with two different amounts of SR Fock exchange, α), broadened with Gaussians of widths 0.4, 0.2, and 0.2 eV, respectively, to facilitate comparison with experimental results.

RSH spectra for these molecules is only mildly sensitive to the choice of α (which is not always the case—see below).

Despite the overall agreement, there is one particular feature which does not agree with experimental results for each of the three molecules: For benzene, the pronounced intensity in the OT-RSH spectra around -13 eV is in contrast to the very low

intensity seen in the experiment. For pyridine and pyrimidine, mismatches occur around -13 eV and -15 eV, respectively. These discrepancies, discussed in more detail below, are observed for both considered SR choices ($\alpha = 0$ and $\alpha = 0.2$). The main deviation between our GW calculations and experiments is found for the benzene molecule, where the feature that in the experiment occurs around -11.5 eV is shifted to higher binding energies. A similar discrepancy (as well as some additional ones for the other rings) has previously been pointed out by Marom et al.⁶¹

A precise quantitative comparison between theory and experiment beyond the above statements is complicated by several aspects: (i) The peaks in the experiments are not well separated; i.e., to determine peak maxima and, correspondingly, vertical ionization energies, one would need to perform extensive fitting. (ii) While important information on orbital symmetry and localization can be obtained directly from experimental results, it is common practice to provide a detailed assignment of orbital shape and ordering based on comparisons to theory, as was done in, e.g., ref 97. (iii) There are also some deviations between different experimental reports, e.g., for pyrimidine, where the two experimental spectra from refs 98 and 99 (shown in Figure 3c) appear to be shifted with respect to each other by ~ 0.2 eV. Therefore, in the following, we choose to compare theoretical data only to the original experimental spectra and avoid the extraction of vertical ionization series from the experiments. Nevertheless, in the interest of putting our OT-RSH results for these prototypical systems into perspective with previous literature findings,⁶² we adopt the extracted experimental values for the ionization energies reported by Marom et al.⁶¹ We can then perform a straightforward statistical analysis of mean absolute differences (MADs) between theory and experiment. This yields MADs of ~ 0.1 eV for our GW calculations and MADs of ~ 0.2 eV for the OT-RSH ($\alpha = 0.2$) calculations. Ref 62 can be understood to suggest that the accuracy of the OT-RSH method falls short of that of GW. In fact, the MADs of the OT-RSH calculations differ from those of our GW calculations by an extent which is marginal and on par with the experimental resolution. Furthermore, the MAD between OT-RSH and GW results is ~ 0.2 eV, i.e., in the same range. Similar conclusions hold for the 3,4,9,10-perylene-tetracarboxylic-dianhydride (PTCDA) and 1,4,5,8-naphthalene-tetracarboxylic-dianhydride (NTCDA) molecules discussed in detail in refs 58 and 62.

For a deeper analysis of the remaining differences between theory and experiment and their origin, we turn to a detailed comparison between the OT-RSH and GW eigenvalues, given in Figure 4. For each eigenvalue, the figure also provides the corresponding single-electron orbital.

It has been recently implied⁶² that the satisfactory agreement between OT-RSH and GW results, reported in ref 58, worsens if the comparison is made to a GW calculation based on a hybrid-functional DFT starting point, rather than on a PBE starting point. To examine this, the first two columns in Figure 4 show PBE- and PBE0-based G_0W_0 valence-electron energies computed by Marom et al.⁶¹ for the small aromatic systems. Our PBE-based G_0W_0 calculations, based on the scheme presented in ref 14 and already shown in Figure 3 to agree well with experiment results, are given in the third column in Figure 4. They are followed by our two ($\alpha = 0$ and $\alpha = 0.2$) OT-RSH results. As in Figure 3, all eigenvalues are shown on an absolute energy scale, with no shifting of the computed data. For all three prototypical rings, our PBE-based G_0W_0 calculations,

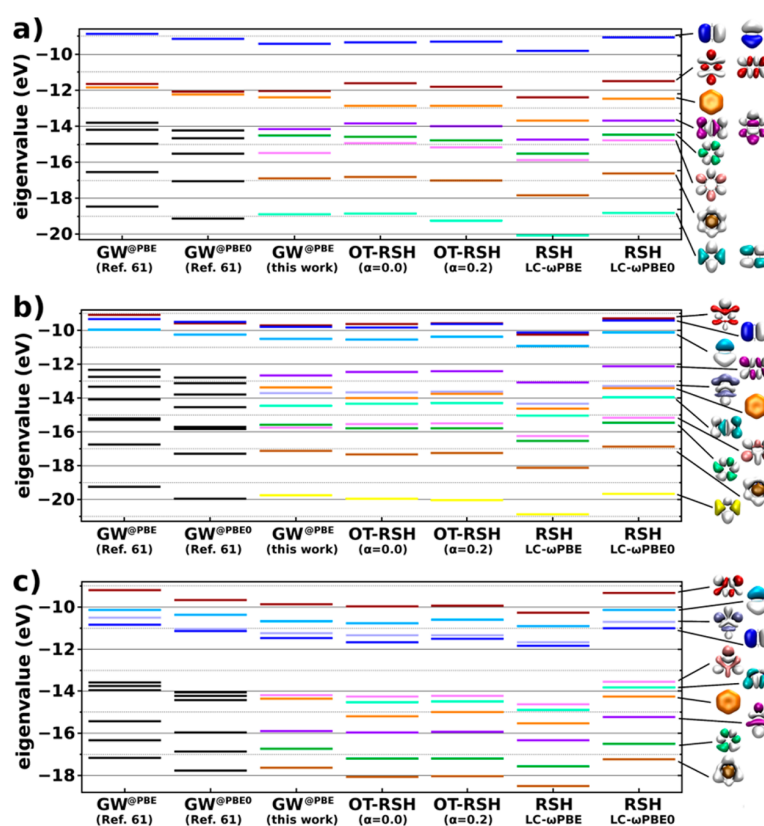


Figure 4. Valence eigenvalue spectra of (a) benzene, (b) pyridine, and (c) pyrimidine, obtained from GW, OT-RSH, and the nonoptimally tuned LC- ω PBE and LC- ω PBE0 RSH functionals. The GW spectra shown were obtained from literature data (scanned in with corresponding color coding from ref 61) with two different starting points, and from our own work. The OT-RSH data were obtained from two different choices for the amount of SR Fock exchange, α .

within a plasmon-pole approximation,⁵ are closer to the PBE0-based “full frequency”¹⁰¹ G_0W_0 calculations of Marom et al.⁶¹ than to their PBE-based ones. Specifically, the MAD between our PBE-based G_0W_0 results and the literature ones (averaged over outer valence orbitals of all three molecules) is 0.56 eV. The MAD is reduced to only 0.22 eV upon comparison with the G_0W_0 results based on PBE0. The difference stems from the fact that these two non-self-consistent, “one-shot” G_0W_0 results are calculated using different approximations within the GW scheme itself. Here, we use a plasmon-pole approximation, pseudopotentials, and a plane-wave basis, an approach that yields good agreement with measured IPs for small gas-phase molecules;^{12,14} ref 61 reports all-electron calculations, with a fully frequency-dependent dielectric function and a finite localized basis. Indeed, the outcome of a GW calculation can depend on more than just the starting point,^{9,12,14,102,103} and more specifically, plasmon-pole models have been seen, in other classes of systems such as simple oxides,^{104,105} to enhance the magnitude of GW corrections. A detailed discussion of the relative accuracy and precision and the pros and cons of different G_0W_0 approaches for molecular systems is well outside the scope of this manuscript and will be taken up elsewhere. Here, the only salient point is that the similarity between the second and third columns of Figure 4 validates the comparison made here and in ref 58, to the PBE-based GW methodology of ref 14 (simply referred to as GW hereafter). Generally, differences of 0.1–0.2 eV, owing to numerical precision, are expected in present-day GW approaches. As mentioned above,

uncertainties of similar magnitude are expected in many of the experiments relevant in the present context. Beyond numerical precision, owing to the physical approximations inherent in any choice of DFT functional, as well as in a G_0W_0 or GW approximation to the self energy, energy differences smaller than ~ 0.1 – 0.2 eV are beyond the accuracy of these approaches.

Turning to the detailed comparison between OT-RSH and our GW calculation, given in Figure 4, the following picture emerges. First, the OT-RSH HOMO energies for all three systems are in very good (<0.15 eV) agreement with the respective lowest quasi-hole energy computed from GW. Excellent agreement of OT-RSH HOMO values with reference theoretical or experimental IPs has been previously reported for a variety of systems—see, e.g., refs 52, 57, and 78. Nevertheless, this finding is still not trivial, because the HOMO of benzene consists of degenerate π orbitals, whereas the HOMO of pyridine and pyrimidine is of σ character (n , to be precise). We emphasize the importance of the tuning procedure for obtaining this level of accuracy for the HOMO energy. For comparison, consider the LC- ω PBE¹⁰⁶ or LC- ω PBE0⁷⁴ functionals. Both are PBE-based RSH functionals just like the one used here, with (α, γ) pairs of $(\alpha = 0, \gamma = 0.4 \text{ Bohr}^{-1})$ and $(\alpha = 0.2, \gamma = 0.2 \text{ Bohr}^{-1})$, respectively; i.e., they employ a fixed nontuned value of γ . The outer-valence energies obtained from these two functionals are shown in the two right-most columns of Figure 4. For the LC- ω PBE functional, the fixed- γ value is much larger than the optimally tuned one at $\alpha = 0$ (cf. Figure 3; $\gamma^{\text{opt}} = 0.287 \text{ Bohr}^{-1}$, $\gamma^{\text{opt}} = 0.312 \text{ Bohr}^{-1}$, and $\gamma^{\text{opt}} = 0.353$

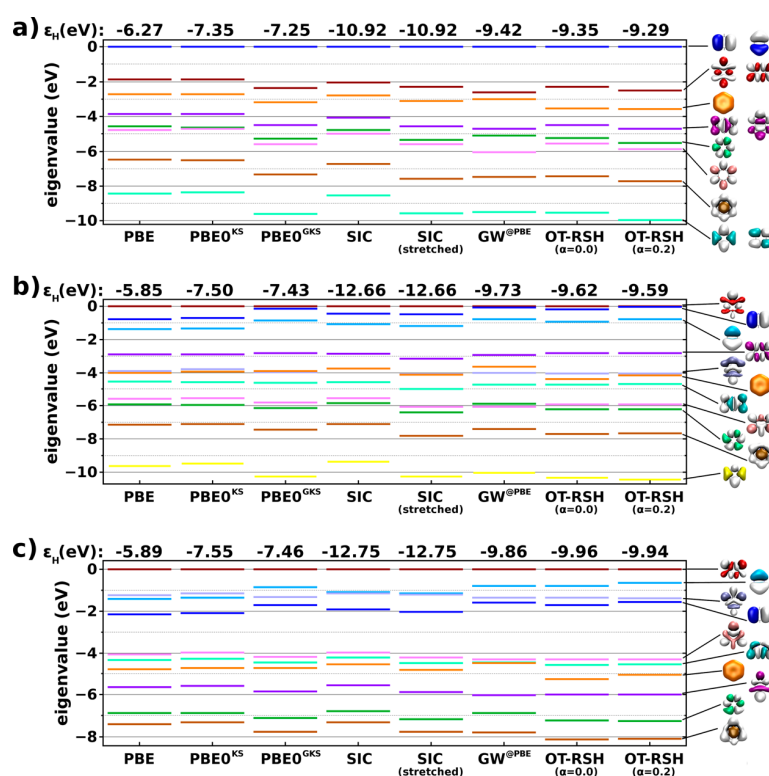


Figure 5. Shifted eigenvalue spectra of (a) benzene, (b) pyridine, and (c) pyrimidine obtained from different theoretical schemes: a semilocal functional (PBE), a conventional hybrid functional (PBE0) in both the Kohn–Sham (KS) and generalized Kohn–Sham (GKS) scheme, a self-interaction-corrected (SIC) calculation, with and without additional “stretching” of the energy axis, GW calculations based on a PBE starting point, and optimally tuned range-separated hybrid (OT-RSH) calculations with two different short-range exchange parameters, $\alpha = 0$ and $\alpha = 0.2$. See text for further details on the computational approaches. The absolute HOMO energy, in electronvolts, is given at the top of each column.

Bohr⁻¹ for benzene, pyridine, and pyrimidine, respectively), and consequently, the LC- ω PBE spectrum is too low in energy. Complementarily, the LC- ω PBE0 fixed- γ value is smaller than that obtained with optimal γ tuning at $\alpha = 0.2$ (cf. Figure 3; $\gamma^{\text{opt}} = 0.238$ Bohr⁻¹, $\gamma^{\text{opt}} = 0.235$ Bohr⁻¹, and $\gamma^{\text{opt}} = 0.278$ Bohr⁻¹ for benzene, pyridine, and pyrimidine, respectively), and the spectrum is too high in energy. Even for benzene, where this is a smaller effect, the LC- ω PBE0 are shifted by ~ 0.35 eV from our GW data and by ~ 0.25 eV from the OT-RSH ($\alpha = 0.2$) data. For pyrimidine, the effect is more pronounced and the shifts amount to ~ 0.55 eV and ~ 0.6 eV, respectively. This observation is fully consistent with the discussion of ref 32 (especially Figure 6 therein) and underscores once again the importance of optimal tuning.

With the optimally tuned functional, the predicted deeper-lying parts of the spectra (with one exception, mentioned previously and discussed in more detail below) are in overall excellent agreement with our GW calculations in spite of the large energy range and the fact that for all systems both σ and π orbitals are present. Increasing α from 0 to 0.2 slightly improves the agreement between OT-RSH and GW, but the effect is overall minor for this kind of system; shifts in orbital energy amount to up to ~ 0.2 eV, as shown in the Supporting Information (SI)). The reasons for this minor impact of α are discussed below.

One may question the accuracy of the OT-RSH functional for describing states with higher binding-energies because of the absence of piecewise linearity⁶² (discussed in more detail below) for highly charged species of the studied system. Such

piecewise linearity should indeed be obtained with the exact DFT functional. However, it should be kept in mind that a highly charged radical is much less stable and undergoes considerable charge density relaxation and orbital reordering with respect to the neutral or cationic molecule. As shown above for the case of the pyridine molecule, even for the (only singly charged) cation, it can be difficult to obtain a meaningful ground state, and this issue can be expected to be more severe for more highly charged molecules. Therefore, while indeed piecewise linearity in principle should be observed with the exact functional also for highly charged species, we believe that other issues are more relevant for describing accurately the excited states of the singly charged cation, which are the ones essential for describing the photoemission process.^{3,93,107,108}

The one discrepancy between the GW and OT-RSH data (vide supra) involves a particular ring-shaped π orbital (orange-colored in Figure 4), which is specific to cyclic compounds. In the OT-RSH, this orbital appears significantly below its GW position (by ~ 0.4 eV for benzene and pyridine and an even worse ~ 0.7 eV for pyrimidine, almost independently of α). For all three molecules, this orbital is primarily responsible for the remaining disagreement between the OT-RSH calculations and the experimental spectra in Figure 3.

To understand the OT-RSH results in more detail, and to explore the possible origins of this remaining discrepancy, we performed additional DFT calculations with several different functionals. Of all DFT functionals studied here, the OT-RSH one is the only one capable of obeying the ionization potential theorem of eq 3 and, consequently, providing HOMO energies

that are close to the experimental IP.^{3,32} Therefore, in the following comparison, all energies are reported relative to the HOMO energy of the respective calculation (which is set to zero). The resulting shifted eigenvalue spectra for the three prototypical aromatic molecules are shown in Figure 5, with the original HOMO energies shown on top.

First, we compare our OT-RSH results to those obtained with their “parent” semilocal functional—PBE—and those obtained from PBE0, the most popular “conventional” hybrid functional based on PBE. In the latter functional, semilocal PBE exchange is mixed with 25% nonlocal Fock exchange for the entire interaction range. This leads to an orbital-dependent functional for the exchange-correlation energy,²⁶ which can then be used within DFT in two different ways. If one wishes to remain within the KS framework, one must take the variational derivative of the exchange-correlation energy with respect to the density, so as to determine the *multiplicative* KS potential. This can be achieved for an implicit density-functional by solving the (integro-differential) optimized effective potential (OEP) equation.^{26,109–111} Here, we solve this equation within the KLI approximation⁹¹ (for details, see the “Computational Details” section) and refer to the result as PBE0^{KS}. Alternatively, one can minimize the total energy with respect to the orbitals. This is the almost universal practice with hybrid functionals, which (as explained in the Introduction) is rigorously justified within the generalized Kohn–Sham scheme. We refer to this result as PBE0^{GKS}.

A first observation is that the shifted PBE0^{KS} eigenvalues are virtually identical to the shifted PBE ones for all systems. This is in agreement with similar observations reported in ref 53. One notable difference between the PBE and PBE0^{KS} results is that the shift needed to align the PBE0^{KS} HOMO energy to the experimental IP energy is substantially smaller than in PBE, albeit still significant. More profound differences occur between the PBE0^{GKS} and the PBE0^{KS} data. While the amount of shift needed for alignment of the HOMO with experimental results is essentially the same for PBE0^{GKS} and PBE0^{KS}, the PBE0^{GKS} eigenvalues are overall “stretched” (= energy rescaled) with respect to the PBE0^{KS} data—as seen most clearly for the case of benzene. For pyridine and pyrimidine, some additional orbital reordering is found, especially in the upper part of the valence band, due to mitigation of self-interaction errors, as discussed below. Such a “stretching” of the energy scale has been observed previously (see, e.g., refs 53, 112, and 113): Körzdörfer and Kümmel⁵³ have rationalized it by arguing that, if the differences in the shapes of the KS and GKS orbitals are ignored, then the difference between GKS and corresponding KS eigenvalue can be viewed in terms of first-order perturbation theory involving the difference between Fock and semilocal exchange. They suggested that this first-order correction mimics successfully the first-order correction between KS values and ionization energies, which is known to dominate for outer-valence electrons.^{3,24,100} Indeed, the shifted PBE0^{GKS} eigenvalues are in much better agreement with GW than the PBE0^{KS} ones. This underscores the beneficial effect of the nonlocal potential operator that is inherent to the GKS scheme but absent in the KS schemes.

As a next step, the role played by the self-interaction error (SIE) in the description of these systems shall be assessed, also in order to understand whether orbital SIE considerations may explain the discrepancy found above for the ring-shaped π orbital. In order to examine that, we have performed SIC calculations within the KS scheme (for details, see the

“Computational Details” section), which results in SIE-free orbitals and eigenvalues. Generally speaking, the shifted SIC spectra are quite similar (but not identical) to the shifted PBE0^{KS} spectra for all systems, although some eigenvalue differences between the two spectra (up to ~ 0.3 eV for benzene and ~ 0.4 eV for pyridine and pyrimidine) are found. This leads to the above-mentioned orbital reordering found for pyridine and pyrimidine once the SIE is mitigated. We furthermore find that SIC modifies PBE eigenvalues differently for π and σ orbitals, by an average of 0.2 eV, which in particular leads to a reordering of the close-lying HOMO–1 and HOMO–2 of pyrimidine. Notably, these differences in the SIC corrections for π and σ PBE orbital energies are rather similar for all three systems, meaning that the relative differences of SIEs in the σ and π orbitals of benzene are similar to the ones in pyridine and pyrimidine. We further note that, for these particular systems, the magnitude of the SIC modifications is moderate, suggesting a moderate SIE in these systems.

Comparison of the SIC data to our GW calculations reveals immediately that, just like the PBE0^{KS} data, they would benefit from further “stretching.” This is fully consistent with the fact that both SIC and PBE0^{KS} spectra arise from a KS, rather than a GKS, calculation. We can simulate the effect of such “stretching” on the SIC spectrum by multiplying the shifted SIC eigenvalues with a constant (a procedure that is, in fact, often performed heuristically in the comparison of KS data with experimental spectra—see, e.g., refs 114 and 115). For each SIC spectrum, we chose this stretching factor such that the lowest-energy PBE0^{GKS} and SIC eigenvalues agree. For all three prototypical systems, the resulting stretched SIC eigenvalue spectra are in overall better agreement with the PBE0^{GKS} spectra than the regular (unstretched) SIC spectra and, furthermore, are in very good agreement with the OT-RSH data and with GW. For a few of the pyridine and pyrimidine orbitals, we find some remaining deviations of the stretched SIC from the PBE0^{GKS} and OT-RSH results, which is, however, expected as the three approaches are very different. This agreement shows that a (range-separated or conventional) hybrid can be highly effective in the quantitative mitigation of SIEs, even though it is not rigorously self-interaction free because only a fraction of exact exchange is employed in the short range. Indeed, similar observations have been made for many other molecular systems,^{33–35,39,53,58,61,112,116} often by comparison to experimental results, but also by comparison to SIC.^{36,68} This rules out that the poor description of the “ring-shaped” (orange-colored) π orbital by OT-RSH is due to a general lack of balance in the description of π and σ orbitals owing to the SIE.

Instead, we attribute the incorrect description of this highly delocalized orbital to the absence of beyond-PBE (and possibly nonlocal) correlation. This is supported by the observation that this π orbital is also overbound in the shifted PBE0^{GKS} data, albeit by a lesser amount of ~ 0.2 to ~ 0.35 eV. As semilocal exchange is known to mimic static correlation,^{117,118} it stands to reason that further removal of some of it, as in the OT-RSH scheme, would worsen the situation. From this point of view, the error in this orbital is then yet one more issue of compatibility between exact exchange and correlation, especially a static one.²⁶ However, one cannot rule out that even if the correlation issue is overcome, an error would still remain, owing to further dynamic relaxation which is not captured in any eigenvalue-based and thus static description. Indications for such effects have been reported in the literature

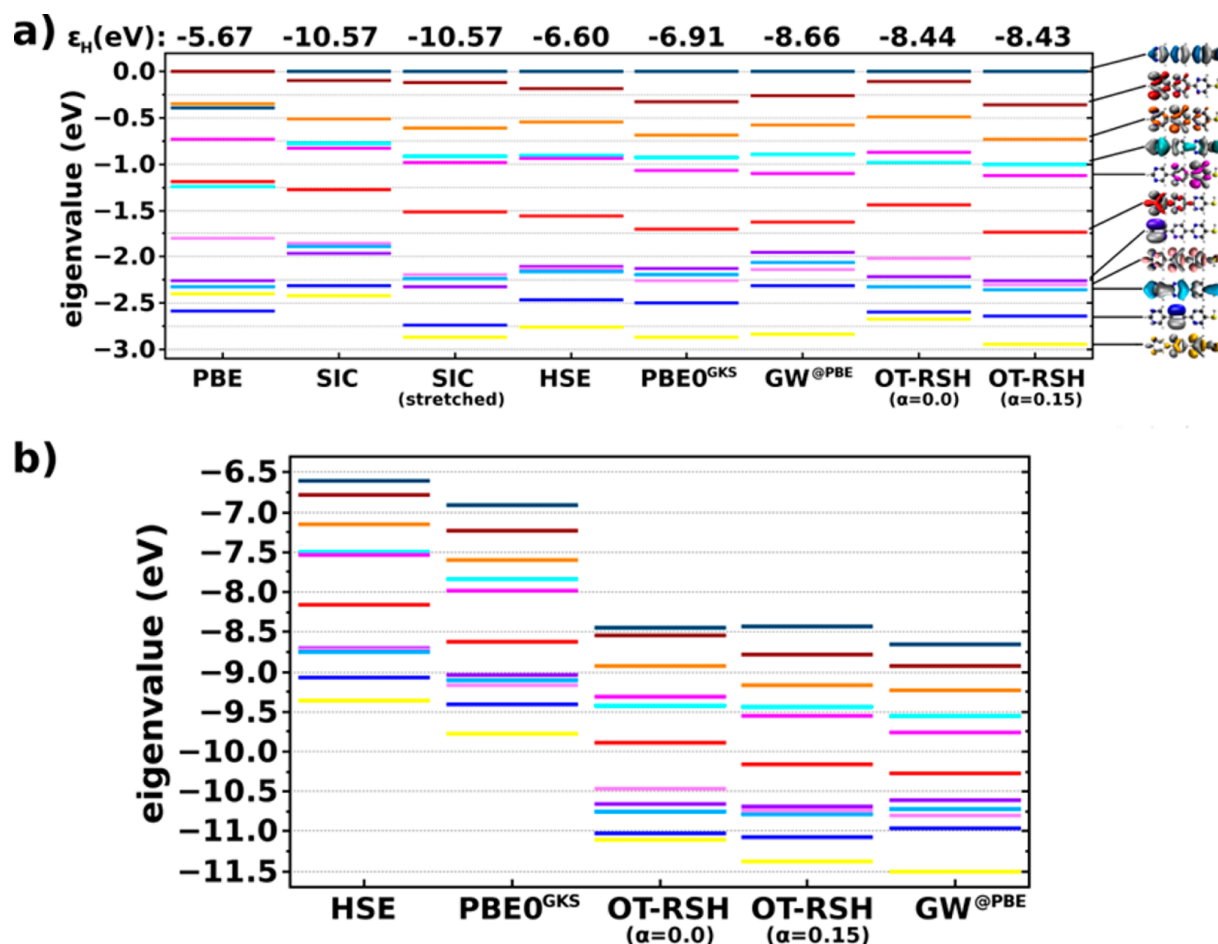


Figure 6. (a) Shifted eigenvalue spectra of 3N-thiol as obtained from different theoretical schemes (see text for details). PBE, SIC, and HSE values were taken from ref 68. For the OT-RSH calculations, the optimal γ value was 0.217 and 0.187 (in Bohr⁻¹) for $\alpha = 0$ and $\alpha = 0.15$, respectively. The absolute HOMO energy, in electronvolts, is given at the top of each column. (b) Unshifted eigenvalue spectra of the same system, as calculated from HSE, PBE0^{GKS}, OT-RSH calculations with the two different α values, and GW.

for small metal clusters,¹¹⁹ and the response of a very delocalized orbital may be “metallic like.” Overcoming this drawback, e.g., by examining more advanced correlation functionals is, therefore, a challenge for future work.

IV. MORE COMPLEX AROMATIC HETEROCYCLES—RESULTS AND DISCUSSION

Encouraged by the overall success of the OT-RSH approach for the prototypical aromatic rings, we now turn to examining the performance of the OT-RSH method for more complex organic molecules: terpyrimidinethiol (3N-thiol) and copper phthalocyanine (CuPc)—see Figure 1b.

Pyrimidinethiols such as 3N-thiol are known to form self-assembled monolayers (SAMs),¹²⁰ and they were shown to display a number of interesting phenomena; e.g., they exhibit diode-type current–voltage characteristics in molecular-scale electronic devices.^{66,121} In the context of 3N-thiol SAMs, some of us have predicted theoretically that the electronic structure is significantly altered due to collective electrostatic effects in the SAM, leading to a localization of the frontier molecular orbitals and a concomitant pronounced reduction in the HOMO–LUMO gap.⁶⁸ 3N-thiols were also suggested as SAMs to strongly reduce or enhance the work function of an underlying metal.⁶⁷ These appealing findings render 3N-thiols an

interesting candidate for applications in organic and molecular electronics. 3N-thiols are also interesting from a methodological perspective, as they pose a serious challenge to semilocal KS schemes:⁶⁸ By means of SIC calculations analogous to the ones performed here, it was shown that close-lying π and σ orbitals in the outer-valence region of 3N-thiol have markedly different SIEs and, as a consequence, are wrongly ordered in (semi)local DFT functionals such as PBE. It was additionally found that the Heyd–Scuseria–Ernezerhof (HSE) SR hybrid functional^{122,123} to a large extent reproduces the SIC corrections to the PBE outer-valence eigenvalues. In HSE, the SR components are the same as in PBE0, but in the LR there is no nonlocal exchange. From the photoemission spectroscopy point of view, the behavior of HSE is known to be similar to that of conventional hybrid functionals.^{34,124–128}

The above-mentioned findings are supported by the data in Figure 6a, which shows the *shifted* eigenvalue spectra of 3N-thiol, i.e., aligning all HOMO levels to zero, starting with the literature data⁶⁸ for PBE, SIC, and HSE. Here, we focus on the range of ~ 3 eV below the HOMO, which we have previously identified for molecules of a similar size as a useful range of accuracy for the RSH-derived eigenvalues.⁵⁸ Generally, PBE tends to produce σ orbitals that are underbound owing to significant SIE.^{33,34,58,68} Because the HOMO obtained from

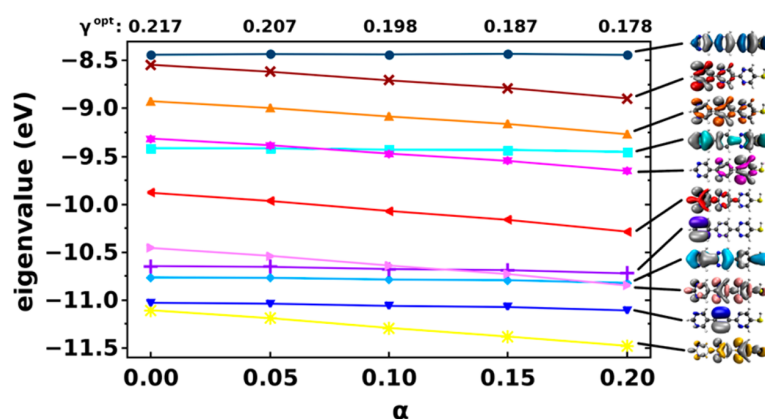


Figure 7. Eigenvalues of 3N-thiol, obtained from optimally tuned range-separated hybrid (OT-RSH) calculations, as a function of the short-range exchange fraction, α , with the optimal value of the range-separation parameter, γ^{opt} (in Bohr⁻¹) determined for each choice of α .

PBE is of σ nature, shifting according to its energy results in π orbitals that appear to be overbound. The SIC calculations (as above, the spectrum is shown both “as calculated” and “stretched”) correct the SIE and, as discussed above, strongly shift the σ orbitals down in energy with respect to the π ones, leading to extensive reordering of the eigenvalue spectrum. This effect also applies to the HSE spectrum, which needs no stretching as it originates from a GKS calculation. We additionally performed PBE0^{GKS} calculations, also shown in Figure 6a,¹²⁹ and found an overall very good agreement with the HSE spectrum and with the “stretched” SIC with an average deviation of the shifted eigenvalues around ~ 0.1 eV. This is consistent with the above-mentioned findings, namely that HSE is comparable to conventional hybrid functionals as far as photoemission spectra are concerned.

To the best of our knowledge, an experimental PES spectrum of 3N-thiol is not available in the literature. Therefore, we performed reference GW calculations for which the (again shifted) eigenvalue spectrum is also given in Figure 6a. As seen above for the prototypical aromatic rings, the agreement of the shifted GW spectrum with the shifted hybrid functional (PBE0 or HSE) spectrum is very good. Some discrepancy is observed between ~ -2.0 to ~ -2.5 eV, but in this context it should be kept in mind that here the plotted energy range is much smaller than for the aromatic rings in Figures 4 and 5. In fact, in the present case, the errors do not exceed 0.2 eV, which is within the expected level of agreement between the two methods (*vide supra*). This confirms the conclusion drawn already from the data of the “prototypical” molecules that the partial correction of SIE and a “stretching” of the spectrum are the essential effects of a hybrid functional.

Despite the excellent agreement of the shifted conventional hybrid (and stretched SIC) data with the GW results, the two differ by a large rigid energy shift. This can be gleaned even from Figure 6a, where the HOMO eigenvalue obtained from each method is given at the top of each column, but is made obvious by Figure 6b, which shows *unshifted* spectra on an absolute energy scale. This discrepancy is removed by the OT-RSH results, also shown in Figure 6a and b (again with two different choices of SR exact exchange— $\alpha = 0$ and $\alpha = 0.15$ —the motivation for this particular selection of α values is discussed below). As with the simpler systems, the IPs deduced from our computed OT-RSH and GW eigenvalues are very close in energy (~ 0.2 eV) for both choices of α . Consequently, the OT-RSH scheme produces quantitatively meaningful

spectra also on an *absolute* energy scale. This is in sharp contrast to all other DFT methods presented in Figure 6.

A remaining and important issue is the best choice for the short-range Fock-exchange fraction, α . In contrast to the case of the small aromatic rings, where different choices for α have had no qualitative effect and only a small quantitative effect, for the 3N-thiol system the differences between the OT-RSH spectra for the two choices of α are more pronounced. As shown in Figure 6, these differences include qualitative deviations, e.g., a reordering of the HOMO–3 and HOMO–4 orbitals. In particular, we observe that, while the position of the π orbitals is similar in both spectra, the σ orbitals are systematically underbound in the $\alpha = 0$ calculation, in comparison to the $\alpha = 0.15$ or the GW calculations. The different dependence of π and σ orbitals on α is underscored in Figure 7, which shows the dependence of orbital eigenvalues on α in the entire range of $\alpha = 0$ to 0.2, with the range-separation parameter, γ , optimized individually for each choice of α . We relate the underbinding of the σ orbitals at small α to the fact that the spatial extent of the σ and π orbitals within the molecular plane is significantly different; i.e., the σ orbitals are clearly more localized than π states and, therefore, should suffer from a larger SIE.⁶⁸ The finding that the agreement with our GW calculations is significantly improved for $\alpha = 0.15$ underscores that, as suggested in ref 58 and discussed in the Introduction, a fraction of Fock exchange in the SR together with full Fock exchange in the LR allows for a mitigation of SIE and therefore a balanced treatment of differently localized molecular orbitals, while retaining the correct absolute position of the energy levels. In principle, a similar statement applies for the small aromatic rings as well. However, there the difference in degree of localization is not the same and, perhaps more importantly, the energy differences between individual eigenvalues are much larger. Therefore, the practical importance of α is smaller in the prototypical small (hetero)cycles, as shown in Figure 4 and in the SI.

These considerations raise the question of whether an optimal α can be chosen *a priori*. Srebro and Autschbach⁶⁰ have suggested that it can be achieved by tuning α . Specifically, they sought the value of α that minimizes the curvature of the ideally piecewise-linear total energy versus particle number curve for the addition and removal of one charge from the neutral molecule. This was done while simultaneously determining the optimal γ for each choice of α obtained from eq 4 (with i restricted to 0 and 1). As discussed in ref 58, some of the

present authors successfully employed a similar approach to determine an optimal value of α also for the purpose of obtaining an outer-valence eigenvalue spectra, but only if it also involved the removal of a second electron. Specifically, α^{opt} was found to equal 0.2 for PTCDA and NTCDA. This value agrees well with the above considerations. Recently, Stein et al. established a rigorous quantitative equality between deviations from piecewise linearity and deviations from the IP theorem.¹³⁰ Therefore, one can equivalently seek α directly by minimizing the target function J from eq 4 without an explicit consideration of fractional densities. Indeed, if this procedure is applied to PTCDA and NTCDA, the same optimal α value is found (see SI). Therefore, we discuss these two tuning procedures (by piecewise linearity and by the IP theorem) together in the following.

Indeed, in cases where an optimal α can be clearly identified, several properties, including the eigenvalue spectrum, have been found to be predicted satisfactorily.^{58,60,131} However, in the case of 3N-thiol, we could not employ that strategy: With i restricted to 0 and 1, a similar minimal value of the target function J of eq 4 is obtained across a large range of α values: the residual J only changed by 0.01 eV from $\alpha = 0.00$ to $\alpha = 0.60$, and no minimum of J occurred. Removal of the second electron resulted in orbital reordering (see SI for more details).

In the absence of viable alternatives, a possible strategy would be to resort to the generally recommended value⁷⁴ of $\alpha = 0.2$, which indeed has been shown to yield very good results, for the prototypes studied above as well as for other systems.⁵⁹ This would also be the case here; i.e., the MAD between the absolute eigenenergies from our GW calculations and OT-RSH with $\alpha = 0.2$, for the states shown in Figure 7, is ~ 0.1 eV. However, as the 3N-thiol results do depend more sensitively on α , it is still interesting, if possible, to determine an optimal α value from additional considerations. In this context, a useful practical observation is that the *shifted* results of the conventional hybrid functional PBE0 are in good agreement with experimental and/or theoretical reference data for the systems discussed here, as well as for many other cases.^{35,58,59,132} Therefore, a pragmatic approach would be to simply tune α so as to obtain agreement between splitting of eigenvalues in the OT-RSH and in the PBE0 spectra. Specifically, one should seek a balance in the relative description of delocalized π and localized σ states. The easiest way to achieve that is to tune α such that the π - σ energy difference between the HOMO and HOMO-1 states is the same in the OT-RSH and the PBE0^{GKS} calculations. This allows us to obtain the same useful level of SIE mitigation as in a conventional hybrid functional, without the need for spectral shifting. It is this approach which has led to the value of $\alpha = 0.15$ for which the data shown in Figure 6 have been obtained.

Comparing our unshifted GW and OT-RSH ($\alpha = 0.15$) calculations of Figure 6b, one, indeed, observes a very good agreement between the two methods. The only clear difference is some orbital reordering around ~ -10.8 eV. One should, however, note that the eigenvalues clustered there are very close in energy and that this reordering does not involve deviations greater than ~ 0.1 eV between corresponding eigenvalues of the two methods. Overall, the MAD between the GW and OT-RSH ($\alpha = 0.15$) calculations is a satisfying ~ 0.1 eV, with the largest deviation being ~ 0.2 eV for the HOMO. For comparison, with OT-RSH ($\alpha = 0$) the MAD is ~ 0.25 eV, with the largest deviation being ~ 0.45 eV, where the reduced level of agreement is mostly due to the less accurate description of the σ orbitals.

Encouraged by this further success, we now turn to an even more complex system—copper phthalocyanine (CuPc—see Figure 1b). In molecular-solid form, CuPc is a highly stable organic semiconductor with a broad range of applications, including light-emitting diodes, solar cells, gas sensors, and thin-film transistors.¹³³ Owing to these applications, there is considerable interest in investigating its electronic structure (see ref 69 and additional references therein). In the present context, CuPc mainly serves as a test case that poses several additional challenges for the OT-RSH method: First, it is an open shell molecule ($s = 1/2$). Second, the interaction between the d orbitals of the copper atom and the s and p orbitals of the embedding macrocycle result in a highly nontrivial set of localized and delocalized orbitals—an issue elaborated below.

For the CuPc molecule, Marom et al. have previously established that: (1) semilocal functionals, such as PBE, result in eigenvalue spectra that are strongly distorted by severe SIE;³⁴ (2) these errors are mitigated substantially, though not completely, by the use of hybrid functionals such as PBE0 or HSE;^{34,69} (3) severe SIE distortions at the DFT level are partly carried over to GW calculations building on the DFT densities.⁶⁹

To better understand the above claims, consider Figure 8a, which provides a scheme containing the computed frontier eigenvalues and orbitals. We illustrate the severe SIE (claim 1) by considering several selected frontier orbitals. Whereas the a_{1u} orbital and the doubly degenerate e_g orbitals are highly delocalized on the macrocycle, the spin-split b_{1g} orbitals are quite strongly localized around the copper atom. Configuration 1 (left side of Figure 8a) was obtained from the OT-RSH calculations discussed below but is equivalent to the one obtained from the GW calculations of ref 69. It identifies the delocalized a_{1u} and e_g orbitals as the HOMO and LUMO, respectively, and places the spin-split $b_{1g\uparrow}$ and $b_{1g\downarrow}$ orbitals as HOMO-1 and LUMO+1, respectively. PBE calculations, however, predict configuration 2 (right side of Figure 8a), in which the spin-split $b_{1g\uparrow}$ and $b_{1g\downarrow}$ are identified as HOMO and LUMO, respectively. Clearly, the localized $b_{1g\uparrow}$ orbital is spuriously pushed to higher energies by the SIE, the effect being strong enough to make the $b_{1g\uparrow}$ orbital become the HOMO. This forces the unoccupied $b_{1g\downarrow}$ orbital to be spuriously shifted to lower energies in order to maintain the spin-splitting symmetry, to the point of it becoming the LUMO. PBE0 or HSE strongly mitigate this error (claim 2) and yield configuration 1.

To understand the manifestation of the SIE (and its mitigation) in the simulated photoelectron data, spectra computed with different computational methods are compared to experimental photoemission data in Figure 9. Importantly, in this figure we compare occupied-state eigenvalues to the gas-phase photoelectron spectrum as before, but further compare unoccupied-state eigenvalues to experimental *inverse* photoemission spectroscopy (IPES). In IPES, photons are emitted from a sample due to its irradiation with fixed-energy electrons, and the energy distribution of the emitted photons is measured, yielding experimental information on virtual states.¹ CuPc is the first system in this article for which such comparison is possible, because for the small aromatic rings the virtual states are unbound and because for 3N-thiol no (regular or inverse) experimental PES data are available. In fact, gas-phase inverse photoemission spectroscopy is nonexistent in general. Therefore, the comparison is to experimental data obtained from thin CuPc films. Due to polarization effects,^{59,134,135} the electron

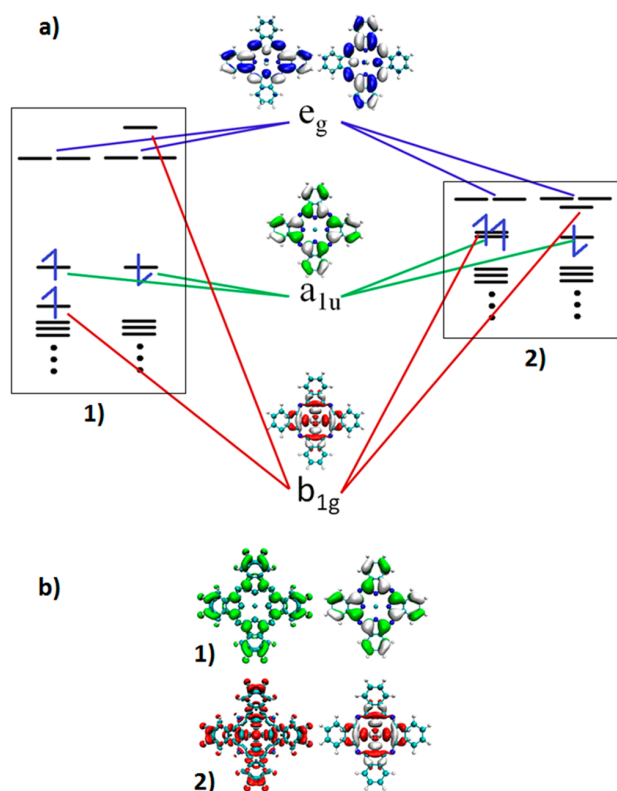


Figure 8. (a) Schematic diagram of selected frontier eigenvalues and orbitals for the CuPc molecule, as obtained from an OT-RSH calculation (configuration 1, left) and from a PBE calculation (configuration 2, right). (b) OT-RSH charge-density differences between neutral and cation (left) and LUMO of cation (right), obtained from the “open-shell singlet” configuration of the CuPc cation, corresponding to ionization of neutral configuration 1 (in green), and from the “closed-shell singlet” configuration of the CuPc cation, corresponding to ionization of configuration 2 (in red). In the charge density difference plots, green or red (blue) regions denote areas of electron density depletion (accumulation) as a consequence of the ionization process.

affinity of a film is much smaller than that of an isolated molecule, and the computed empty state energies and the measured inverse photoemission spectroscopy data can be compared only up to a rigid shift. Therefore, to allow comparison to experimental results without modifying the computational gas-phase data, the experimental IPES spectra were shifted so as to align the lowest-energy peak with the GW spectrum shown at the topmost computed spectrum in Figure 9.

As discussed above, it is well-known that for either PBE or PBE0 the HOMO and LUMO do not correspond to the ionization potential or the electron affinity, respectively (see, e.g., refs 26 and 32). This causes an uncontrolled rigid shift of the simulated photoemission curve. To facilitate a meaningful comparison also for these functionals, the PBE and PBE0 spectra of Figure 9 are additionally shown in shifted form. To determine the required rigid shift, the ionization potential is computed as the total energy difference between the neutral species and the cation, and the filled-state eigenvalue spectrum is rigidly shifted such that the HOMO energy coincides with the computed ionization potential. An equivalent procedure is applied to the unoccupied-state eigenvalue spectrum, which is

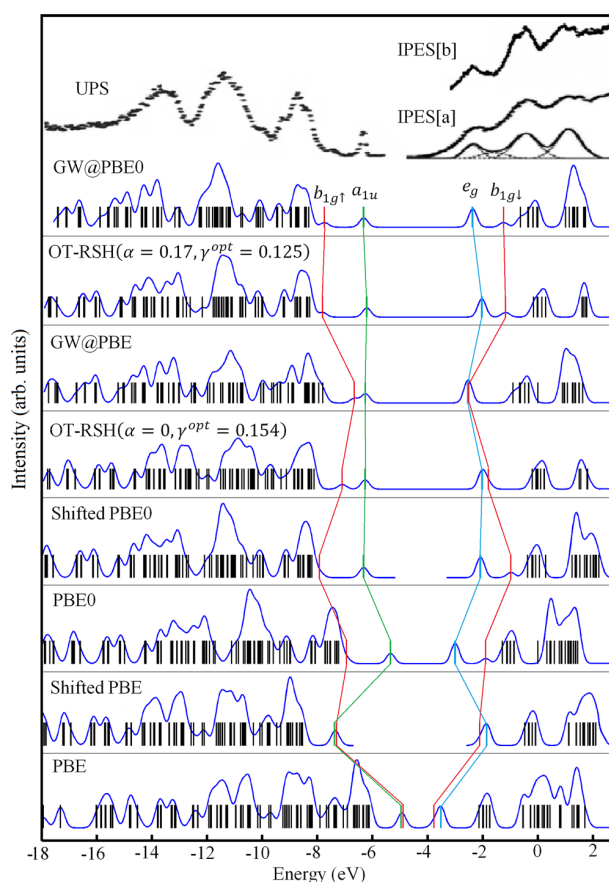


Figure 9. Simulated DFT and GW spectra (see text for details), obtained from computed energy levels (shown as sticks) by broadening via convolution with a 0.15-eV-wide Gaussian. PBE, PBE0, and GW data were taken from ref 69. Theoretical data are compared to the experimental gas phase photoemission data of Evangelista et al.¹⁴¹ and to the thin film inverse photoemission data of (a) Murdey et al.¹⁴² (shown with curve fitting results) and (b) Hill et al.¹⁴³ The experimental inverse photoemission spectra were shifted so as to align the LUMO peak with the computed GW@PBE0 LUMO peak. On the OT-RSH data, optimal γ values are given in Bohr⁻¹. Eigenvalues corresponding to the e_g , a_{1u} , and b_{1g} orbitals are designated by the same color scheme as in Figure 8.

rigidly shifted such that the LUMO energy coincides with the computed electron affinity. Comparison of the PBE- and PBE0-based simulated spectra in Figure 9 (taken from ref 69) with the experimental data reveals that whereas the shifted PBE spectrum is in poor agreement with experiment for both filled and empty states, the shifted PBE0 spectrum provides for a much improved agreement with experimental results. This highlights both the severe SIE in the PBE calculation and its mitigation by the PBE0 calculation. Better agreement yet, including an accurate placement of the spin-split filled $b_{1g\uparrow}$ and empty $b_{1g\downarrow}$ orbitals, is afforded by GW calculations of Marom et al.,⁶⁹ based on a PBE0 starting point. It is in significantly better agreement with experimental results than their GW calculations based on a PBE starting point (at least with the particular flavor of GW used in ref 69, which, as discussed earlier, is different from the one we used above for benzene, pyridine, and pyrimidine; we refrained from conducting such GW calculations also for CuPc, because of the computational cost involved). This improved description of the electronic structure

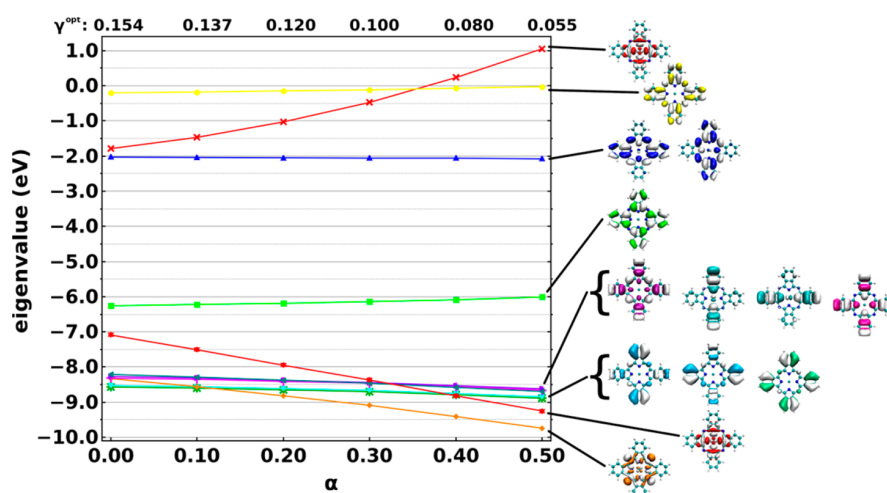


Figure 10. Eigenvalues of CuPc, obtained from optimally tuned range-separated hybrid (OT-RSH) calculations, as a function of the short-range exchange fraction, α , with the optimal value of the range-separation parameter, γ^{opt} (in Bohr⁻¹), determined for different choices of α .

of CuPc by the PBE0 based GW calculations substantiates the third above claim, i.e., the possible carry-over of severe SIE to the GW calculation.

It is intriguing to determine how well the OT-RSH approach performs in this more complicated scenario. As for the case of pyridine (see Figure 2), it is important to choose the correct cationic configuration for the tuning procedure. Two cationic configurations can be obtained from the OT-RSH calculation. One is an “open shell singlet,” with a single spin in the b_{1g} orbital and in the a_{1u} orbital, which corresponds to removal of an electron from the a_{1u} HOMO of configuration 1 in Figure 8a. The other is a “closed-shell singlet” cation, which corresponds to removal of an electron from the b_{1g} HOMO of configuration 2 in Figure 8a. Importantly, only for the “open-shell singlet” configuration (which is lower in total energy) is the LUMO consistent with the character of the neutral HOMO, and with the “hole density,” as shown in Figure 8b. Just like in the pyridine example of Figure 2, all tuning must be performed solely with this configuration. We note that multiple stable configurations are well-known to occur in metal-phthalocyanines,¹³² which is why we strongly stress the need for correct identification and usage of compatible neutral and ionic configurations in the tuning procedure.¹³⁶

Having ascertained the validity of our tuning procedure, we turn to the spectra simulated using the OT-RSH method, also shown in Figure 9. As for the case of 3N-thiol, the obtained spectra (second and fourth theoretical curves in the figure) are strongly α -dependent. This is shown explicitly in Figure 10, which shows the dependence of orbital eigenvalues on α , with the range-separation parameter, γ , again optimized individually for each choice of α . It is particularly striking that the orbitals most sensitive to α are the highly localized spin-split b_{1g} pair, which is fully consistent with our above discussion on the relation between orbital localization and sensitivity to short-range Fock exchange. Unfortunately, here direct tuning of α based on eq 4, even with $i = 0, 1, -1$, was not useful because the minimal value of the target function J was very small and very weakly dependent on α within the numerical accuracy of our work (see SI). Thus, while the procedure of ref 58 did not fail, in the sense of providing an incorrect value for α , it did not succeed either. Therefore, we determined α as for the case of 3N-thiol, i.e., based on the success of the shifted PBE0

spectrum. As discussed above, a crucial aspect in the theoretical description of the CuPc spectrum is the energy separation between the delocalized a_{1u} orbital and the filled localized b_{1g} orbital of Figure 8. Therefore, we tune the value of α so as to agree with the PBE0-calculated separation between the eigenvalues for the a_{1u} and b_{1g} orbitals. This yields $\alpha = 0.17$, which is again close to the “default” value of 0.2, further supporting the latter as a useful choice even without any α -tuning. $\alpha = 0.17$ was then used to calculate the second theoretical curve in Figure 9. It yields excellent agreement with prior GW@PBE0 calculations (shown in the figure) and the experimental data in both the top valence (i.e., occupied) states and the bottom conduction (i.e., unoccupied) states. In particular, the OT-RSH alignment of the a_{1u} , b_{1g} , and e_g states of Figure 8 agrees very well with the prior GW calculations. As orbitals above and below these frontier ones tend to be “clustered” for these larger molecule, we do not discuss them individually. However, it is clear that the agreement between GW and OT-RSH gradually deteriorates as one goes further down or up in the valence or conduction states, respectively. In particular, it appears that agreement of the lower valence states with the GW results could be further assisted by some “stretching” of the energy scale—an observation consistent with the generally expected differences between nonlocal exchange and self-energy operators,³ as well as with our general guideline of restricting our attention to states within a few electronvolts of the frontier orbitals. Nevertheless, in the absence of detailed orbital information, at the level of the given experimental resolution, the OT-RSH results can be viewed as agreeing with experimental results as well as the GW ones, possibly even relatively deep into the valence band.

As an additional observation, we note that the HOMO and LUMO eigenvalues obtained from the OT-RSH ($\alpha = 0.17$) calculation (as is, without any rigid shifting of the data) are in excellent agreement with the lowest quasi-hole and quasi-electron excitations, respectively, obtained from GW@PBE0. This is fully consistent with the work of Stein et al.,⁵² who suggested that OT-RSH gaps can be identified with quasi-particle gaps—an observation that has since been confirmed for a large variety of systems by ourselves, as well as by several other groups.^{58,59,78,137–140} A related interesting observation is that the OT-RSH ($\alpha = 0$) data are rather similar to the GW@

PBE calculations from ref 69 (again, for that particular flavor of GW): Both are far better than the PBE data, but in both spectra, the $a_{1u}-b_{1g}$ and e_g-b_{1g} separations are not large enough. This highlights yet again the positive role of SR exchange in mitigating SIEs where they are significant.⁵⁸

V. CONCLUSIONS

In conclusion, we examined the performance of optimally tuned range-separated hybrid functionals for predicting the photoemission spectra of several challenging prototypical (benzene, pyridine, and pyrimidine) and complex (3N-thiol and CuPc) (hetero)cyclic organic molecules. Overall, the resulting spectra agree very well (typically within $\sim 0.1-0.2$ eV) with experimental data and our GW calculations, even for states several electronvolts away from the frontier orbitals. We performed several additional hybrid DFT calculations in both the KS and GKS schemes and found that the inclusion of a nonlocal operator strongly benefits the calculated spectrum. Moreover, our SIC calculations confirmed that self-interaction errors can be efficiently mitigated in OT-RSH functionals, which shows that, with a PBE0-based optimal choice of the short-range fraction of Fock exchange, the OT-RSH method can offer an excellent balance in the description of localized and delocalized states. The sole exception found in the studied systems is a high-symmetry orbital, particular to small aromatic rings. We conclude that the OT-RSH method is a highly accurate DFT method for outer-valence PES prediction for such systems, and its accuracy is comparable to state-of-the-art GW schemes. This success comes at the price of increased computational and conceptual cost that is inherent to the parameter tuning. While this increase in effort is notable compared to standard, nontuned DFT calculations, it is not overwhelming and still lower than the cost of a GW calculation.

■ ASSOCIATED CONTENT

Supporting Information

This material is available free of charge via the Internet at <http://pubs.acs.org>.

■ AUTHOR INFORMATION

Corresponding Authors

*E-mail: sivan.abramson@weizmann.ac.il.

*E-mail: leor.kronik@weizmann.ac.il.

Author Contributions

These authors contributed equally to this work.

Notes

The authors declare no competing financial interest.

■ ACKNOWLEDGMENTS

D.A.E. was partially supported through a DOC fellowship by the Austrian Academy of Sciences. S.R.A. is supported by an Adams fellowship of the Israel Academy of Sciences and Humanities. Portions of this work were supported by the European Research Council, the Israel Science Foundation, the United States-Israel Binational Science Foundation, the Germany-Israel Foundation, the Wolfson Foundation, the Hemsley Foundation, the Austrian Science Fund (FWF): P24666-N20, the German Science Foundation (DFG/GRK 1640) and the Molecular Foundry. J.B.N. was supported by the U.S. Department of Energy, Office of Basic Energy Sciences, Division of Materials Sciences and Engineering (Theory FWP) under Contract No. DE-AC02-05CH11231. S.S. was partially

supported by the Scientific Discovery through Advanced Computing (SciDAC) Partnership program funded by U.S. Department of Energy, Office of Science, Advanced Scientific Computing Research and Basic Energy Sciences. Work performed at the Molecular Foundry was also supported by the Office of Science, Office of Basic Energy Sciences, of the U.S. Department of Energy. We thank the National Energy Research Scientific Computing center for computational resources.

■ REFERENCES

- (1) Hüfner, S. *Photoelectron Spectroscopy: Principles and Applications*, 3rd ed.; Springer: Berlin, 2003; Advanced Texts in Physics.
- (2) Martin, R. M. *Electronic Structure: Basic Theory and Practical Methods*; Cambridge University Press: Cambridge, U. K., 2004.
- (3) Kronik, L.; Kümmel, S. Gas-Phase Valence-Electron Photoemission Spectroscopy Using Density Functional Theory. *Top. Curr. Chem.* In press.
- (4) Hedin, L. New Method for Calculating the One-Particle Green's Function with Application to the Electron-Gas Problem. *Phys. Rev.* **1965**, *139*, A796–A823.
- (5) Hybertsen, M.; Louie, S. Electron Correlation in Semiconductors and Insulators: Band Gaps and Quasiparticle Energies. *Phys. Rev. B* **1986**, *34*, 5390–5413.
- (6) Aulbur, W. G.; Jönsson, L.; Wilkins, J. W. Quasiparticle Calculations in Solids. In *Solid State Physics*; Elsevier: Amsterdam, 1999; Vol. 54, pp 1–218.
- (7) Onida, G.; Reining, L.; Rubio, A. Electronic Excitations: Density-Functional versus Many-Body Green's-Function Approaches. *Rev. Mod. Phys.* **2002**, *74*, 601–659.
- (8) Grossman, J.; Rohlfing, M.; Mitas, L.; Louie, S.; Cohen, M. High Accuracy Many-Body Computational Approaches for Excitations in Molecules. *Phys. Rev. Lett.* **2001**, *86*, 472–475.
- (9) Blase, X.; Attaccalite, C.; Olevano, V. First-Principles GW Calculations for Fullerenes, Porphyrins, Phtalocyanine, and Other Molecules of Interest for Organic Photovoltaic Applications. *Phys. Rev. B* **2011**, *83*, 115103.
- (10) Blase, X.; Attaccalite, C. Charge-Transfer Excitations in Molecular Donor-Acceptor Complexes within the Many-Body Bethe-Salpeter Approach. *Appl. Phys. Lett.* **2011**, *99*, 171909.
- (11) Qian, X.; Umari, P.; Marzari, N. Photoelectron Properties of DNA and RNA Bases from Many-Body Perturbation Theory. *Phys. Rev. B* **2011**, *84*, 075103.
- (12) Sharifzadeh, S.; Biller, A.; Kronik, L.; Neaton, J. B. Quasiparticle and Optical Spectroscopy of the Organic Semiconductors Pentacene and PTCDA from First Principles. *Phys. Rev. B* **2012**, *85*, 125307.
- (13) Körzdörfer, T.; Marom, N. Strategy for Finding a Reliable Starting Point for G_0W_0 Demonstrated for Molecules. *Phys. Rev. B* **2012**, *86*, 041110(R).
- (14) Sharifzadeh, S.; Tamblyn, I.; Doak, P.; Darancet, P. T.; Neaton, J. B. Quantitative Molecular Orbital Energies within a G_0W_0 Approximation. *Eur. Phys. J. B* **2012**, *85*.
- (15) Parr, R. G.; Yang, W. *Density-Functional Theory of Atoms and Molecules*; Oxford University Press; Clarendon Press: New York, 1989.
- (16) Dreizler, R. M.; Gross, E. K. U. *Density Functional Theory: An Approach to the Quantum Many-Body Problem*; Springer-Verlag: Berlin, 1990.
- (17) Hohenberg, P.; Kohn, W. Inhomogeneous Electron Gas. *Phys. Rev.* **1964**, *136*, B864–B871.
- (18) Kohn, W.; Sham, L. J. Self-Consistent Equations Including Exchange and Correlation Effects. *Phys. Rev.* **1965**, *140*, A1133–A1138.
- (19) Sham, L.; Kohn, W. One-Particle Properties of an Inhomogeneous Interacting Electron Gas. *Phys. Rev.* **1966**, *145*, 561–567.
- (20) Perdew, J. P.; Parr, R. G.; Levy, M.; Balduz, J. L. Density-Functional Theory for Fractional Particle Number: Derivative Discontinuities of the Energy. *Phys. Rev. Lett.* **1982**, *49*, 1691–1694.

- (21) Levy, M.; Perdew, J.; Sahni, V. Exact Differential Equation for the Density and Ionization Energy of a Many-Particle System. *Phys. Rev. A* **1984**, *30*, 2745–2748.
- (22) Almladh, C.-O.; von Barth, U. Exact Results for the Charge and Spin Densities, Exchange–Correlation Potentials, and Density-Functional Eigenvalues. *Phys. Rev. B* **1985**, *31*, 3231–3244.
- (23) Perdew, J.; Levy, M. Comment on “Significance of the Highest Occupied Kohn-Sham Eigenvalue”. *Phys. Rev. B* **1997**, *56*, 16021–16028.
- (24) Chong, D. P.; Gritsenko, O. V.; Baerends, E. J. Interpretation of the Kohn–Sham Orbital Energies as Approximate Vertical Ionization Potentials. *J. Chem. Phys.* **2002**, *116*, 1760.
- (25) Trzhaskovskaya, M. B.; Nefedov, V. I.; Yarzhevsky, V. G. Photoelectron Angular Distribution Parameters for Elements $Z=1$ to $Z=54$ in the Photoelectron Energy Range 100–5000 eV. *At. Data Nucl. Data Tables* **2001**, *77*, 97–159.
- (26) Kümmel, S.; Kronik, L. Orbital-Dependent Density Functionals: Theory and Applications. *Rev. Mod. Phys.* **2008**, *80*, 3.
- (27) Baerends, E. J.; Ros, P. Self-Consistent Molecular Hartree–Fock–Slater Calculations II. The Effect of Exchange Scaling in Some Small Molecules. *Chem. Phys.* **1973**, *2*, 52–59.
- (28) Perdew, J. P. Orbital Functional for Exchange and Correlation: Self-Interaction Correction to the Local Density Approximation. *Chem. Phys. Lett.* **1979**, *64*, 127–130.
- (29) Salzner, U.; Baer, R. Koopmans’ Springs to Life. *J. Chem. Phys.* **2009**, *131*, 231101.
- (30) Faber, C.; Attacalite, C.; Olevano, V.; Runge, E.; Blase, X. First-Principles GW Calculations for DNA and RNA Nucleobases. *Phys. Rev. B* **2011**, *83*, 115123.
- (31) Teale, A. M.; De Proft, F.; Tozer, D. J. Orbital Energies and Negative Electron Affinities from Density Functional Theory: Insight from the Integer Discontinuity. *J. Chem. Phys.* **2008**, *129*, 044110.
- (32) Kronik, L.; Stein, T.; Refaely-Abramson, S.; Baer, R. Excitation Gaps of Finite-Sized Systems from Optimally Tuned Range-Separated Hybrid Functionals. *J. Chem. Theory Comput.* **2012**, *8*, 1515–1531.
- (33) Dori, N.; Menon, M.; Kilian, L.; Sokolowski, M.; Kronik, L.; Umbach, E. Valence Electronic Structure of Gas-Phase 3,4,9,10-Perylene Tetracarboxylic Acid Dianhydride: Experiment and Theory. *Phys. Rev. B* **2006**, *73*, 195208.
- (34) Marom, N.; Hod, O.; Scuseria, G. E.; Kronik, L. Electronic Structure of Copper Phthalocyanine: A Comparative Density Functional Theory Study. *J. Chem. Phys.* **2008**, *128*, 164107.
- (35) Marom, N.; Kronik, L. Density Functional Theory of Transition Metal Phthalocyanines, I: Electronic Structure of NiPc and CoPc—self-Interaction Effects. *Appl. Phys. A: Mater. Sci. Process.* **2008**, *95*, 159–163.
- (36) Körzdörfer, T.; Kümmel, S.; Marom, N.; Kronik, L. When to Trust Photoelectron Spectra from Kohn-Sham Eigenvalues: The Case of Organic Semiconductors. *Phys. Rev. B* **2009**, *79*, 201205.
- (37) Körzdörfer, T.; Kümmel, S.; Marom, N.; Kronik, L. Erratum: When to Trust Photoelectron Spectra from Kohn-Sham Eigenvalues: The Case of Organic Semiconductors [Phys. Rev. B *79*, 201205 (2009)]. *Phys. Rev. B* **2010**, *82*, 129903.
- (38) Puschnig, P.; Reinisch, E.-M.; Ules, T.; Koller, G.; Soubatch, S.; Ostler, M.; Romaner, L.; Tautz, F. S.; Ambrosch-Draxl, C.; Ramsey, M. G. Orbital Tomography: Deconvoluting Photoemission Spectra of Organic Molecules. *Phys. Rev. B* **2011**, *84*, 235427.
- (39) Brena, B.; Puglia, C.; de Simone, M.; Coreno, M.; Tarafder, K.; Feyrer, V.; Banerjee, R.; Göthelid, E.; Sanyal, B.; Oppeneer, P. M.; Eriksson, O. Valence-Band Electronic Structure of Iron Phthalocyanine: An Experimental and Theoretical Photoelectron Spectroscopy Study. *J. Chem. Phys.* **2011**, *134*, 074312.
- (40) Vogel, M.; Schmitt, F.; Sauther, J.; Baumann, B.; Altenhof, A.; Lach, S.; Ziegler, C. Photoionization Cross-Section Weighted DFT Simulations as Promising Tool for the Investigation of the Electronic Structure of Open Shell Metal-Phthalocyanines. *Anal. Bioanal. Chem.* **2011**, *400*, 673–678.
- (41) Dauth, M.; Körzdörfer, T.; Kümmel, S.; Ziroff, J.; Wiessner, M.; Schöll, A.; Reinert, F.; Arita, M.; Shimada, K. Orbital Density Reconstruction for Molecules. *Phys. Rev. Lett.* **2011**, *107*, 193002.
- (42) Cohen, A. J.; Mori-Sanchez, P.; Yang, W. Insights into Current Limitations of Density Functional Theory. *Science* **2008**, *321*, 792–794.
- (43) But Note Recent Work on Non-Standard LDA and GGA Expressions That Allows a DD to Emerge Naturally Even within These Approximations: Kraissler, E.; Kronik, L. *Phys. Rev. Lett.* **2013**, *110*, 126403. Armiento, R.; Kümmel, S. *Phys. Rev. Lett.* **2013**, *111*, 036402.
- (44) Perdew, J.; Levy, M. Physical Content of the Exact Kohn-Sham Orbital Energies: Band Gaps and Derivative Discontinuities. *Phys. Rev. Lett.* **1983**, *51*, 1884–1887.
- (45) Borgoo, A.; Teale, A. M.; Tozer, D. J. Effective Homogeneity of the Exchange–correlation and Non-Interacting Kinetic Energy Functionals under Density Scaling. *J. Chem. Phys.* **2012**, *136*, 034101.
- (46) Perdew, J. P.; Zunger, A. Self-Interaction Correction to Density-Functional Approximations for Many-Electron Systems. *Phys. Rev. B* **1981**, *23*, 5048–5079.
- (47) Baer, R.; Livshits, E.; Salzner, U. Tuned Range-Separated Hybrids in Density Functional Theory. *Annu. Rev. Phys. Chem.* **2010**, *61*, 85–109.
- (48) Seidl, A.; Görling, A.; Vogl, P.; Majewski, J.; Levy, M. Generalized Kohn-Sham Schemes and the Band-Gap Problem. *Phys. Rev. B* **1996**, *53*, 3764–3774.
- (49) Becke, A. D. A New Mixing of Hartree–Fock and Local Density-Functional Theories. *J. Chem. Phys.* **1993**, *98*, 1372.
- (50) Stephens, P. J.; Devlin, F. J.; Chabalowski, C. F.; Frisch, M. J. Ab Initio Calculation of Vibrational Absorption and Circular Dichroism Spectra Using Density Functional Force Fields. *J. Phys. Chem.* **1994**, *98*, 11623–11627.
- (51) Perdew, J. P.; Ernzerhof, M.; Burke, K. Rationale for Mixing Exact Exchange with Density Functional Approximations. *J. Chem. Phys.* **1996**, *105*, 9982.
- (52) Stein, T.; Eisenberg, H.; Kronik, L.; Baer, R. Fundamental Gaps in Finite Systems from Eigenvalues of a Generalized Kohn-Sham Method. *Phys. Rev. Lett.* **2010**, *105*, 266802.
- (53) Körzdörfer, T.; Kümmel, S. Single-Particle and Quasiparticle Interpretation of Kohn-Sham and Generalized Kohn-Sham Eigenvalues for Hybrid Functionals. *Phys. Rev. B* **2010**, *82*, 155206.
- (54) Iikura, H.; Tsuneda, T.; Yanai, T.; Hirao, K. A Long-Range Correction Scheme for Generalized-Gradient-Approximation Exchange Functionals. *J. Chem. Phys.* **2001**, *115*, 3540.
- (55) Leininger, T.; Stoll, H.; Werner, H.-J.; Savin, A. Combining Long-Range Configuration Interaction with Short-Range Density Functionals. *Chem. Phys. Lett.* **1997**, *275*, 151–160.
- (56) Baer, R.; Neuhauser, D. Density Functional Theory with Correct Long-Range Asymptotic Behavior. *Phys. Rev. Lett.* **2005**, *94*, 043002.
- (57) Refaely-Abramson, S.; Baer, R.; Kronik, L. Fundamental and Excitation Gaps in Molecules of Relevance for Organic Photovoltaics from an Optimally Tuned Range-Separated Hybrid Functional. *Phys. Rev. B* **2011**, *84*, 075144.
- (58) Refaely-Abramson, S.; Sharifzadeh, S.; Govind, N.; Autschbach, J.; Neaton, J. B.; Baer, R.; Kronik, L. Quasiparticle Spectra from a Nonempirical Optimally Tuned Range-Separated Hybrid Density Functional. *Phys. Rev. Lett.* **2012**, *109*, 226405.
- (59) Refaely-Abramson, S.; Sharifzadeh, S.; Jain, M.; Baer, R.; Neaton, J. B.; Kronik, L. Gap Renormalization of Molecular Crystals from Density Functional Theory. *Phys. Rev. B* **2013**, *88*, 081204(R).
- (60) Srebro, M.; Autschbach, J. Does a Molecule-Specific Density Functional Give an Accurate Electron Density? The Challenging Case of the CuCl Electric Field Gradient. *J. Phys. Chem. Lett.* **2012**, *3*, 576–581.
- (61) Marom, N.; Caruso, F.; Ren, X.; Hofmann, O. T.; Körzdörfer, T.; Chelikowsky, J. R.; Rubio, A.; Scheffler, M.; Rinke, P. Benchmark of GW Methods for Azabenzene. *Phys. Rev. B* **2012**, *86*, 245127.

- (62) Körzdörfer, T.; Parrish, R. M.; Marom, N.; Sears, J. S.; Sherrill, C. D.; Brédas, J.-L. Assessment of the Performance of Tuned Range-Separated Hybrid Density Functionals in Predicting Accurate Quasiparticle Spectra. *Phys. Rev. B* **2012**, *86*, 205110.
- (63) Van den Brink, J.; Morpurgo, A. F. Materials Science: Magnetic Blue. *Nature* **2007**, *450*, 177–178.
- (64) Heutz, S.; Mitra, C.; Wu, W.; Fisher, A. J.; Kerridge, A.; Stoneham, M.; Harker, A. H.; Gardener, J.; Tseng, H.-H.; Jones, T. S.; Renner, C.; Aeppli, G. Molecular Thin Films: A New Type of Magnetic Switch. *Adv. Mater.* **2007**, *19*, 3618–3622.
- (65) Mugarza, A.; Lorente, N.; Ordejón, P.; Krull, C.; Stepanow, S.; Bocquet, M.-L.; Fraxedas, J.; Ceballos, G.; Gambardella, P. Orbital Specific Chirality and Homochiral Self-Assembly of Achiral Molecules Induced by Charge Transfer and Spontaneous Symmetry Breaking. *Phys. Rev. Lett.* **2010**, *105*, 115702.
- (66) Díez-Pérez, I.; Hihath, J.; Lee, Y.; Yu, L.; Adamska, L.; Kozhushner, M. A.; Oleynik, I. L.; Tao, N. Rectification and Stability of a Single Molecular Diode with Controlled Orientation. *Nat. Chem.* **2009**, *1*, 635–641.
- (67) Egger, D. A.; Rissner, F.; Rangger, G. M.; Hofmann, O. T.; Wittwer, L.; Heimel, G.; Zojer, E. Self-Assembled Monolayers of Polar Molecules on Au(111) Surfaces: Distributing the Dipoles. *Phys. Chem. Chem. Phys.* **2010**, *12*, 4291.
- (68) Rissner, F.; Egger, D. A.; Natan, A.; Körzdörfer, T.; Kümmel, S.; Kronik, L.; Zojer, E. Collectively Induced Quantum-Confined Stark Effect in Monolayers of Molecules Consisting of Polar Repeating Units. *J. Am. Chem. Soc.* **2011**, *133*, 18634–18645.
- (69) Marom, N.; Ren, X.; Moussa, J. E.; Chelikowsky, J. R.; Kronik, L. Electronic Structure of Copper Phthalocyanine from G_0W_0 Calculations. *Phys. Rev. B* **2011**, *84*, 195143.
- (70) Even more general range-separation schemes can be devised, e.g., to include a middle-range as well. See, e.g. Lucero, M. J.; Henderson, T. M.; Scuseria, G. E. *J. Phys.: Condens. Matter* **2012**, *24*, 145504.
- (71) Yanai, T.; Tew, D. P.; Handy, N. C. A New Hybrid Exchange–correlation Functional Using the Coulomb-Attenuating Method (CAM-B3LYP). *Chem. Phys. Lett.* **2004**, *393*, 51–57.
- (72) Perdew, J. P.; Burke, K.; Ernzerhof, M. Generalized Gradient Approximation Made Simple. *Phys. Rev. Lett.* **1996**, *77*, 3865–3868.
- (73) This is obtained by replacing the $1/r$ terms in the exchange-part of the potential according to eq 1 and using the identity $\operatorname{erf}(\gamma r) + \operatorname{erfc}(\gamma r) = 1$.
- (74) Rohrdanz, M. A.; Martins, K. M.; Herbert, J. M. A Long-Range-Corrected Density Functional That Performs Well for Both Ground-State Properties and Time-Dependent Density Functional Theory Excitation Energies, Including Charge-Transfer Excited States. *J. Chem. Phys.* **2009**, *130*, 054112.
- (75) Livshits, E.; Baer, R. A Well-Tempered Density Functional Theory of Electrons in Molecules. *Phys. Chem. Chem. Phys.* **2007**, *9*, 2932.
- (76) Stein, T.; Kronik, L.; Baer, R. Reliable Prediction of Charge Transfer Excitations in Molecular Complexes Using Time-Dependent Density Functional Theory. *J. Am. Chem. Soc.* **2009**, *131*, 2818–2820.
- (77) Stein, T.; Kronik, L.; Baer, R. Prediction of Charge-Transfer Excitations in Coumarin-Based Dyes Using a Range-Separated Functional Tuned from First Principles. *J. Chem. Phys.* **2009**, *131*, 244119.
- (78) Körzdörfer, T.; Sears, J. S.; Sutton, C.; Brédas, J.-L. Long-Range Corrected Hybrid Functionals for Π -Conjugated Systems: Dependence of the Range-Separation Parameter on Conjugation Length. *J. Chem. Phys.* **2011**, *135*, 204107.
- (79) Pandey, L.; Doiron, C.; Sears, J. S.; Brédas, J.-L. Lowest Excited States and Optical Absorption Spectra of Donor–acceptor Copolymers for Organic Photovoltaics: A New Picture Emerging from Tuned Long-Range Corrected Density Functionals. *Phys. Chem. Chem. Phys.* **2012**, *14*, 14243.
- (80) Sun, H.; Autschbach, J. Influence of the Delocalization Error and Applicability of Optimal Functional Tuning in Density Functional Calculations of Nonlinear Optical Properties of Organic Donor–Acceptor Chromophores. *ChemPhysChem* **2013**, *14*, 2450–2461.
- (81) Shao, Y.; Molnar, L. F.; Jung, Y.; Kussmann, J.; Ochsenfeld, C.; Brown, S. T.; Gilbert, A. T. B.; Slipchenko, L. V.; Levchenko, S. V.; O'Neill, D. P.; DiStasio, R. A., Jr.; Lochan, R. C.; Wang, T.; Beran, G. J. O.; Besley, N. A.; Herbert, J. M.; Yeh Lin, C.; Van Voorhis, T.; Hung Chien, S.; Sodt, A.; Steele, R. P.; Rassolov, V. A.; Maslen, P. E.; Korambath, P. P.; Adamson, R. D.; Austin, B.; Baker, J.; Byrd, E. F. C.; Dachsel, H.; Doerksen, R. J.; Dreuw, A.; Dunietz, B. D.; Dutoi, A. D.; Furlani, T. R.; Gwaltney, S. R.; Heyden, A.; Hirata, S.; Hsu, C.-P.; Kedziora, G.; Khalliulin, R. Z.; Klunzinger, P.; Lee, A. M.; Lee, M. S.; Liang, W.; Lotan, I.; Nair, N.; Peters, B.; Proynov, E. I.; Pieniazek, P. A.; Min Rhee, Y.; Ritchie, J.; Rosta, E.; David Sherrill, C.; Simmonett, A. C.; Subotnik, J. E.; Lee Woodcock, H., III; Zhang, W.; Bell, A. T.; Chakraborty, A. K.; Chipman, D. M.; Keil, F. J.; Warshel, A.; Hehre, W. J.; Schaefer, H. F., III; Kong, J.; Krylov, A. I.; Gill, P. M. W.; Head-Gordon, M. Advances in Methods and Algorithms in a Modern Quantum Chemistry Program Package. *Phys. Chem. Chem. Phys.* **2006**, *8*, 3172.
- (82) Valiev, M.; Bylaska, E. J.; Govind, N.; Kowalski, K.; Straatsma, T. P.; Van Dam, H. J. J.; Wang, D.; Nieplocha, J.; Apra, E.; Windus, T. L.; de Jong, W. A. NWChem: A Comprehensive and Scalable Open-Source Solution for Large Scale Molecular Simulations. *Comput. Phys. Commun.* **2010**, *181*, 1477–1489.
- (83) Dunning, T. H. Gaussian Basis Sets for Use in Correlated Molecular Calculations. I. The Atoms Boron through Neon and Hydrogen. *J. Chem. Phys.* **1989**, *90*, 1007.
- (84) Karolewski, A.; Kronik, L.; Kümmel, S. Using Optimally Tuned Range Separated Hybrid Functionals in Ground-State Calculations: Consequences and Caveats. *J. Chem. Phys.* **2013**, *138*, 204115.
- (85) Deslippe, J.; Samsonidze, G.; Strubbe, D. A.; Jain, M.; Cohen, M. L.; Louie, S. G. BerkeleyGW: A Massively Parallel Computer Package for the Calculation of the Quasiparticle and Optical Properties of Materials and Nanostructures. *Comput. Phys. Commun.* **2012**, *183*, 1269–1289.
- (86) Giannozzi, P.; Baroni, S.; Bonini, N.; Calandra, M.; Car, R.; Cavazzoni, C.; Ceresoli, D.; Chiarotti, G. L.; Cococcioni, M.; Dabo, I.; Dal Corso, A.; de Gironcoli, S.; Fabris, S.; Fratesi, G.; Gebauer, R.; Gerstmann, U.; Gougoussis, C.; Kokalj, A.; Lazzeri, M.; Martin-Samos, L.; Marzari, N.; Mauri, F.; Mazzarello, R.; Paolini, S.; Pasquarello, A.; Paulatto, L.; Sbraccia, C.; Scandolo, S.; Sclauzero, G.; Seitsonen, A. P.; Smogunov, A.; Umari, P.; Wentzcovitch, R. M. QUANTUM ESPRESSO: A Modular and Open-Source Software Project for Quantum Simulations of Materials. *J. Phys.: Condens. Matter* **2009**, *21*, 395502.
- (87) Troullier, N.; Martins, J. L. Efficient Pseudopotentials for Plane-Wave Calculations. *Phys. Rev. B* **1991**, *43*, 1993–2006.
- (88) Deslippe, J.; Samsonidze, G.; Jain, M.; Cohen, M. L.; Louie, S. G. Coulomb-Hole Summations and Energies for GW Calculations with Limited Number of Empty Orbitals: A Modified Static Remainder Approach. *Phys. Rev. B* **2013**, *87*, 165124.
- (89) Körzdörfer, T.; Kümmel, S.; Mundt, M. Self-Interaction Correction and the Optimized Effective Potential. *J. Chem. Phys.* **2008**, *129*, 014110.
- (90) Hofmann, D.; Klüpfel, S.; Klüpfel, P.; Kümmel, S. Using Complex Degrees of Freedom in the Kohn-Sham Self-Interaction Correction. *Phys. Rev. A* **2012**, *85*, 062514.
- (91) Krieger, J. B.; Li, Y.; Iafate, G. J. Derivation and Application of an Accurate Kohn-Sham Potential with Integer Discontinuity. *Phys. Lett. A* **1990**, *146*, 256–260.
- (92) Körzdörfer, T.; Mundt, M.; Kümmel, S. Electrical Response of Molecular Systems: The Power of Self-Interaction Corrected Kohn-Sham Theory. *Phys. Rev. Lett.* **2008**, *100*, 133004.
- (93) Mundt, M.; Kümmel, S. Photoelectron Spectra of Anionic Sodium Clusters from Time-Dependent Density-Functional Theory in Real Time. *Phys. Rev. B* **2007**, *76*, 035413.
- (94) Kronik, L.; Makmal, A.; Tiago, M. L.; Alemany, M. M. G.; Jain, M.; Huang, X.; Saad, Y.; Chelikowsky, J. R. PARSEC – the Pseudopotential Algorithm for Real-Space Electronic Structure

Calculations: Recent Advances and Novel Applications to Nano-Structures. *Phys. Status Solidi B* **2006**, *243*, 1063–1079.

(95) Humphrey, W.; Dalke, A.; Schulten, K. VMD: Visual Molecular Dynamics. *J. Mol. Graphics* **1996**, *14*, 33–38.

(96) Kokalj, A. XCrySDen—a New Program for Displaying Crystalline Structures and Electron Densities. *J. Mol. Graphics Modell.* **1999**, *17*, 176–179.

(97) Liu, S.-Y.; Alnama, K.; Matsumoto, J.; Nishizawa, K.; Kohguchi, H.; Lee, Y.-P.; Suzuki, T.; He, I. Ultraviolet Photoelectron Spectroscopy of Benzene and Pyridine in Supersonic Molecular Beams Using Photoelectron Imaging. *J. Phys. Chem. A* **2011**, *115*, 2953–2965.

(98) Kishimoto, N.; Ohno, K. Collision Energy Resolved Penning Ionization Electron Spectroscopy of Azines: Anisotropic Interaction of Azines with He*(2³S) Atoms and Assignments of Ionic States. *J. Phys. Chem. A* **2000**, *104*, 6940–6950.

(99) Potts, A. W.; Holland, D. M. P.; Trofimov, A. B.; Schirmer, J.; Karlsson, L.; Siegbahn, K. An Experimental and Theoretical Study of the Valence Shell Photoelectron Spectra of Purine and Pyrimidine Molecules. *J. Phys. B: At., Mol. Opt. Phys.* **2003**, *36*, 3129–3143.

(100) Jones, R. O.; Gunnarsson, O. The Density Functional Formalism, Its Applications and Prospects. *Rev. Mod. Phys.* **1989**, *61*, 689–746.

(101) Ren, X.; Rinke, P.; Blum, V.; Wieferink, J.; Tkatchenko, A.; Sanfilippo, A.; Reuter, K.; Scheffler, M. Resolution-of-Identity Approach to Hartree–Fock, Hybrid Density Functionals, RPA, MP2 and GW with Numeric Atom-Centered Orbital Basis Functions. *New J. Phys.* **2012**, *14*, 053020.

(102) Bruneval, F.; Marques, M. A. L. Benchmarking the Starting Points of the GW Approximation for Molecules. *J. Chem. Theory Comput.* **2013**, *9*, 324–329.

(103) Caruso, F.; Rinke, P.; Ren, X.; Scheffler, M.; Rubio, A. Unified Description of Ground and Excited States of Finite Systems: The Self-Consistent GW Approach. *Phys. Rev. B* **2012**, *86*, 081102(R).

(104) Kang, W.; Hybertsen, M. S. Quasiparticle and Optical Properties of Rutile and Anatase TiO₂. *Phys. Rev. B* **2010**, *82*, 085203.

(105) Stankovski, M.; Antonius, G.; Waroquiers, D.; Miglio, A.; Dixit, H.; Sankaran, K.; Giantomasi, M.; Gonze, X.; Côté, M.; Rignanese, G.-M. G₀W₀ Band Gap of ZnO: Effects of Plasmon-Pole Models. *Phys. Rev. B* **2011**, *84*, 241201(R).

(106) Vydrov, O. A.; Scuseria, G. E. Assessment of a Long-Range Corrected Hybrid Functional. *J. Chem. Phys.* **2006**, *125*, 234109.

(107) Ehrler, O.; Weber, F.; Furche, F.; Kappes, M. Photoelectron Spectroscopy of C₈₄ Dianions. *Phys. Rev. Lett.* **2003**, *91*, 113006.

(108) Walter, M.; Häkkinen, H. Photoelectron Spectra from First Principles: From the Many-Body to the Single-Particle Picture. *New J. Phys.* **2008**, *10*, 043018.

(109) Sharp, R.; Horton, G. A Variational Approach to the Unipotent Many-Electron Problem. *Phys. Rev.* **1953**, *90*, 317–317.

(110) Talman, J.; Shadwick, W. Optimized Effective Atomic Central Potential. *Phys. Rev. A* **1976**, *14*, 36–40.

(111) Sahni, V.; Gruenebaum, J.; Perdew, J. Study of the Density-Gradient Expansion for the Exchange Energy. *Phys. Rev. B* **1982**, *26*, 4371–4377.

(112) Marom, N.; Tkatchenko, A.; Scheffler, M.; Kronik, L. Describing Both Dispersion Interactions and Electronic Structure Using Density Functional Theory: The Case of Metal–Phthalocyanine Dimers. *J. Chem. Theory Comput.* **2010**, *6*, 81–90.

(113) Stowasser, R.; Hoffmann, R. What Do the Kohn-Sham Orbitals and Eigenvalues Mean? *J. Am. Chem. Soc.* **1999**, *121*, 3414–3420.

(114) Segev, L.; Salomon, A.; Natan, A.; Cahen, D.; Kronik, L.; Amy, F.; Chan, C.; Kahn, A. Electronic Structure of Si(111)-Bound Alkyl Monolayers: Theory and Experiment. *Phys. Rev. B* **2006**, *74*, 165323.

(115) Hwang, J.; Kim, E.-G.; Liu, J.; Bredas, J.-L.; Duggal, A.; Kahn, A. Photoelectron Spectroscopic Study of the Electronic Band Structure of Polyfluorene and Fluorene-Arylamine Copolymers at Interfaces. *J. Phys. Chem. C* **2007**, *111*, 1378–1384.

(116) Palumbo, M.; Hogan, C.; Sottile, F.; Bagalá, P.; Rubio, A. Ab Initio Electronic and Optical Spectra of Free-Base Porphyrins: The Role of Electronic Correlation. *J. Chem. Phys.* **2009**, *131*, 084102.

(117) Mok, D. K. W.; Neumann, R.; Handy, N. C. Dynamical and Nondynamical Correlation. *J. Phys. Chem.* **1996**, *100*, 6225–6230.

(118) Gritsenko, O. V.; Schipper, P. R. T.; Baerends, E. J. Exchange and Correlation Energy in Density Functional Theory: Comparison of Accurate Density Functional Theory Quantities with Traditional Hartree–Fock Based Ones and Generalized Gradient Approximations for the Molecules Li₂, N₂, F₂. *J. Chem. Phys.* **1997**, *107*, 5007.

(119) Mundt, M.; Kümmel, S.; Huber, B.; Moseler, M. Photoelectron Spectra of Sodium Clusters: The Problem of Interpreting Kohn-Sham Eigenvalues. *Phys. Rev. B* **2006**, *73*, 205407.

(120) Sek, S. EC-STM Study of Potential-Controlled Adsorption of Substituted Pyrimidinethiol on Au(111). *Langmuir* **2009**, *25*, 13488–13492.

(121) Lörtscher, E.; Gotsmann, B.; Lee, Y.; Yu, L.; Rettner, C.; Riel, H. Transport Properties of a Single-Molecule Diode. *ACS Nano* **2012**, *6*, 4931–4939.

(122) Heyd, J.; Scuseria, G. E.; Ernzerhof, M. Hybrid Functionals Based on a Screened Coulomb Potential. *J. Chem. Phys.* **2003**, *118*, 8207–8215.

(123) Heyd, J.; Scuseria, G. E.; Ernzerhof, M. Erratum: “Hybrid Functionals Based on a Screened Coulomb Potential” [*J. Chem. Phys.* **118**, 8207 (2003)]. *J. Chem. Phys.* **2006**, *124*, 219906.

(124) Janesko, B. G.; Henderson, T. M.; Scuseria, G. E. Screened Hybrid Density Functionals for Solid-State Chemistry and Physics. *Phys. Chem. Chem. Phys.* **2009**, *11*, 443.

(125) Ren, J.; Meng, S.; Wang, Y.-L.; Ma, X.-C.; Xue, Q.-K.; Kaxiras, E. Properties of Copper (fluoro-)phthalocyanine Layers Deposited on Epitaxial Graphene. *J. Chem. Phys.* **2011**, *134*, 194706.

(126) Bisti, F.; Stroppa, A.; Picozzi, S.; Ottaviano, L. Fingerprints of the Hydrogen Bond in the Photoemission Spectra of Croconic Acid Condensed Phase: An X-Ray Photoelectron Spectroscopy and Ab-Initio Study. *J. Chem. Phys.* **2011**, *134*, 174505.

(127) Bisti, F.; Stroppa, A.; Donarelli, M.; Picozzi, S.; Ottaviano, L. Electronic Structure of tris(8-hydroxyquinolinato)aluminum(III) Revisited Using the Heyd-Scuseria-Ernzerhof Hybrid Functional: Theory and Experiments. *Phys. Rev. B* **2011**, *84*, 195112.

(128) Bisti, F.; Stroppa, A.; Perrozzi, F.; Donarelli, M.; Picozzi, S.; Coreno, M.; de Simone, M.; Prince, K. C.; Ottaviano, L. The Electronic Structure of Gas Phase Croconic Acid Compared to the Condensed Phase: More Insight into the Hydrogen Bond Interaction. *J. Chem. Phys.* **2013**, *138*, 014308.

(129) The HOMO-10 and HOMO-11 are degenerate in the case of the PBE0^{GKS} calculation. We do not show both orbital energies for clarity.

(130) Stein, T.; Autschbach, J.; Govind, N.; Kronik, L.; Baer, R. Curvature and Frontier Orbital Energies in Density Functional Theory. *J. Phys. Chem. Lett.* **2012**, *3*, 3740–3744.

(131) Moore, B.; Srebro, M.; Autschbach, J. Analysis of Optical Activity in Terms of Bonds and Lone-Pairs: The Exceptionally Large Optical Rotation of Norbornenone. *J. Chem. Theory Comput.* **2012**, *8*, 4336–4346.

(132) Marom, N.; Kronik, L. Density Functional Theory of Transition Metal Phthalocyanines, II: Electronic Structure of MnPc and FePc—symmetry and Symmetry Breaking. *Appl. Phys. A: Mater. Sci. Process.* **2008**, *95*, 165–172.

(133) *The Porphyrin Handbook*; Academic Press: San Diego, CA, 2000; Vol 19: Applications of Phthalocyanines.

(134) Sato, N.; Seki, K.; Inokuchi, H. Polarization Energies of Organic Solids Determined by Ultraviolet Photoelectron Spectroscopy. *J. Chem. Soc., Faraday Trans. 2* **1981**, *77*, 1621.

(135) Neaton, J. B.; Hybertsen, M. S.; Louie, S. G. Renormalization of Molecular Electronic Levels at Metal-Molecule Interfaces. *Phys. Rev. Lett.* **2006**, *97*, 216405.

(136) We have observed that with a smaller basis set, multiple stable configurations were obtained even for the CuPc neutral. However, this spurious phenomenon vanished when using a sufficiently large basis set.

(137) Risko, C.; Brédas, J.-L. *Top. Curr. Chem.* In press; DOI: 10.1007/128_2013_459.

(138) Sini, G.; Sears, J. S.; Brédas, J.-L. Evaluating the Performance of DFT Functionals in Assessing the Interaction Energy and Ground-State Charge Transfer of Donor/Acceptor Complexes: Tetrathiafulvalene–Tetracyanoquinodimethane (TTF–TCNQ) as a Model Case. *J. Chem. Theory Comput.* **2011**, *7*, 602–609.

(139) Phillips, H.; Zheng, S.; Hyla, A.; Laine, R.; Goodson, T.; Geva, E.; Dunietz, B. D. Ab Initio Calculation of the Electronic Absorption of Functionalized Octahedral Silsesquioxanes via Time-Dependent Density Functional Theory with Range-Separated Hybrid Functionals. *J. Phys. Chem. A* **2012**, *116*, 1137–1145.

(140) Foster, M. E.; Wong, B. M. Nonempirically Tuned Range-Separated DFT Accurately Predicts Both Fundamental and Excitation Gaps in DNA and RNA Nucleobases. *J. Chem. Theory Comput.* **2012**, *8*, 2682–2687.

(141) Evangelista, F.; Carravetta, V.; Stefani, G.; Jansik, B.; Alagia, M.; Stranges, S.; Ruocco, A. Electronic Structure of Copper Phthalocyanine: An Experimental and Theoretical Study of Occupied and Unoccupied Levels. *J. Chem. Phys.* **2007**, *126*, 124709.

(142) Murdey, R.; Sato, N.; Bouvet, M. Frontier Electronic Structures in Fluorinated Copper Phthalocyanine Thin Films Studied Using Ultraviolet and Inverse Photoemission Spectroscopies. *Mol. Cryst. Liq. Cryst.* **2006**, *455*, 211–218.

(143) Hill, I. G.; Kahn, A.; Soos, Z. G.; Pascal, R. A., Jr. Charge-Separation Energy in Films of Π -Conjugated Organic Molecules. *Chem. Phys. Lett.* **2000**, *327*, 181–188.

Publication 7

Piecewise linearity in the *GW* approximation for accurate quasiparticle energy predictions

Physical Review B Rapid Communications **93**, 121115 (2016)

M. Dauth^{1,2}, F. Caruso³, S. Kümmel¹, and P. Rinke²

¹ Theoretical Physics IV, University of Bayreuth, D-95440 Bayreuth, Germany

² COMP/Department of Applied Physics, Aalto University, P.O. Box 11100, Aalto FI-00076, Finland

³ Department of Materials, University of Oxford, Parks Road, Oxford OX1 3PH, United Kingdom

My contribution

I performed all calculations presented in the paper and wrote a first draft of the manuscript. I contributed to the scientific discussion significantly.

Publ.7

Piecewise linearity in the GW approximation for accurate quasiparticle energy predictions

Matthias Dauth,^{1,2} Fabio Caruso,³ Stephan Kümmel,¹ and Patrick Rinke²

¹Theoretical Physics IV, University of Bayreuth, D-95440 Bayreuth, Germany

²COMP Department of Applied Physics, Aalto University, P.O. Box 11100, Aalto FI-00076, Finland

³Department of Materials, University of Oxford, Parks Road, Oxford OX1 3PH, United Kingdom

(Received 7 December 2015; revised manuscript received 15 February 2016; published 31 March 2016)

We identify the *deviation from the straight-line error* (DSLE)—i.e., the spurious nonlinearity of the total energy as a function of fractional particle number—as the main source for the discrepancy between experimental vertical ionization energies and theoretical quasiparticle energies, as obtained from the GW and GW +SOSEX approximations to many-body perturbation theory (MBPT). To check whether a DSLE is present in GW , we propose an indicator that only invokes observables at integer particle numbers. For self-consistent calculations, we show that GW suffers from a small DSLE. Conversely, for perturbative G_0W_0 and G_0W_0 +SOSEX calculations the DSLE depends on the starting point. We exploit this starting point dependence to reduce (or completely eliminate) the DSLE. We find that the agreement with experiment increases as the DSLE reduces. DSLE-minimized schemes thus emerge as promising avenues for future developments in MBPT.

DOI: 10.1103/PhysRevB.93.121115

Electronic structure theory has developed into an essential tool in materials science because it offers a parameter-free, quantum mechanical description of solids, molecules, and nanostructures. This success is due to the continuous development of electronic structure methods such as density-functional theory (DFT) [1] and many-body perturbation theory (MBPT) in the GW approximation [2]. This development is guided in part by comparisons with experimental reference data and in part by exact constraints, imposed by the theoretical framework itself. We will demonstrate in this Rapid Communication that invaluable insight into the GW approach can be gained from such an exact constraint. The GW method has long been heralded as the method of choice for band gaps and band structures of solids and quasiparticle spectra of molecules and nanostructures [3–5]. Yet, its accuracy is not always satisfying and the starting point dependence in the perturbative G_0W_0 variant can be very pronounced [5–7]. Here, we will show that the accuracy of GW is closely related to the exact constraint that the ionization energy of the neutral system must equal the electron affinity of the cation, which is a direct consequence of the piecewise linearity of the total energy [8]. Its violation gives rise to the *deviation from the straight-line error* (DSLE), which has been extensively studied in DFT [9–14]. The starting point dependence in G_0W_0 can then be exploited to minimize the DSLE, which uniquely defines the optimal starting point.

In 1982 Perdew *et al.* showed that the total energy of a quantum mechanical system has to change linearly with respect to the fractional removal (or addition) of an electron [8],

$$E(f) = (1 - f)E(N_0 - 1) + fE(N_0). \quad (1)$$

Here, N_0 is the number of electrons in the neutral system and $E(N_0)$ the associated total energy. $E(N_0 - 1)$ is the total energy of the singly ionized system and f varies in the interval [0,1]. This piecewise linearity condition was initially derived in the context of DFT, but applies to any total energy method.

In the following, we introduce a formal definition of the deviation from linearity at fractional occupation numbers that

employs only quantities directly accessible by quasiparticle energy calculations, that is, the ionization potential (IP) and the electron affinity (EA). The linearity condition in Eq. (1) implies that the first derivative of the total energy with respect to the fractional occupation number f (i.e., $\partial E/\partial f$) should be constant and that it exhibits discontinuities at integer occupations ($f = 0$ and $f = 1$). Additionally, $\partial E/\partial f$ equals the electron removal energy $E(N_0) - E(N_0 - 1)$ or, equivalently, the energy for adding an electron to the positively charged system. Therefore, the vertical IP of the neutral system with N_0 electrons can be expressed as

$$\left. \frac{\partial E(f)}{\partial f} \right|_1 = E(N_0) - E(N_0 - 1) = -\text{IP}(N_0). \quad (2)$$

A similar relation holds for the electron affinity of the cation (EA_c):

$$\left. \frac{\partial E(f)}{\partial f} \right|_0 = E(N_0) - E(N_0 - 1) = -\text{EA}_c(N_0 - 1). \quad (3)$$

Equations (2) and (3) illustrate that $\text{IP} = \text{EA}_c$ in an exact theory. We thus define the difference between IP and EA_c as the DSLE,

$$\Delta_{\text{DSLE}} = \text{EA}_c(N_0 - 1) - \text{IP}(N_0). \quad (4)$$

$\Delta_{\text{DSLE}} = 0$ is a necessary condition for piecewise linearity. However, in an approximate treatment of electronic exchange and correlation, as, e.g., in GW , IP and EA_c may differ. A nonvanishing Δ_{DSLE} indicates a curvature in the total energy versus fractional electron number curve, as illustrated in Fig. 1, causing an erroneous deviation from the straight line [15,16].

The DSLE is most easily seen in the deviation from the straight line

$$\Delta E(f) = E(f) - E_{\text{lin}}(f), \quad (5)$$

where, following Eq. (1), $E_{\text{lin}}(f)$ is the straight line between $E(N_0)$ and $E(N_0 - 1)$. We will first examine the DSLE and Eq. (5) for different DFT functionals before proceeding to our GW analysis [17]. In DFT, common (semi)local functionals typically exhibit a convex curvature and suffer from a large

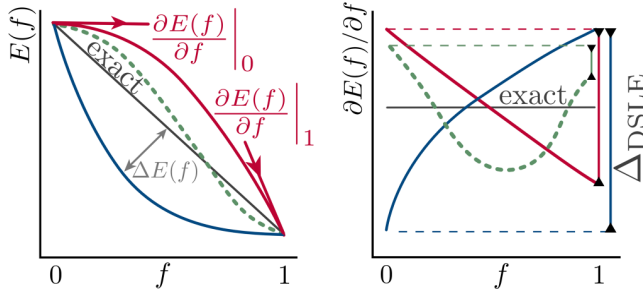


FIG. 1. Schematic representation of the DSLE for total energies E (left) and their derivatives $\partial E/\partial f$ (right) as a function of the occupation number f .

DSLE, whereas Hartree-Fock (HF) is concave with a moderate DSLE [9–14]. We show this tendency in terms of $\Delta E(f)$ for the examples of the O_2 and the benzene molecule in Fig. 2.

To quantify the DSLE by means of Eq. (4) we use the eigenvalue of the highest molecular orbital (HOMO) of the neutral system ($\epsilon_{N_0}^H$) for $IP(N_0)$ and the eigenvalue of the lowest unoccupied molecular orbital (LUMO) of the cation ($\epsilon_{N_0-1}^L$) for $EA_c(N_0 - 1)$ [8,18–20]. For O_2 , the Perdew-Burke-Ernzerhof (PBE) functional gives $\Delta_{DSLE} = \epsilon_{N_0}^H - \epsilon_{N_0-1}^L = 11.6$ eV, which agrees with the pronounced convexity observed in Fig. 2. For benzene, the DSLE in PBE reduces to half the size ($\Delta_{DSLE} = 5.9$ eV), which is also apparent from the maximal extent of $\Delta E(f)$ in Fig. 2. Conversely, HF exhibits a concave DSLE manifested in $\Delta_{DSLE} = -3.5$ eV for O_2 and $\Delta_{DSLE} = -2.5$ eV for benzene. All in all, the magnitude of Δ_{DSLE} can be taken as a measure for the severity of the DSLE, whereas the sign indicates the curvature. A positive value of Δ_{DSLE} corresponds to a concave and a negative sign to a convex curvature. Convexity gives rise to a delocalization of the electron density and concavity to an overlocalization [9].

We now move on to discuss the DSLE in the GW approximation. In GW , the total energy is only available at integer occupation numbers because a rigorous ensemble

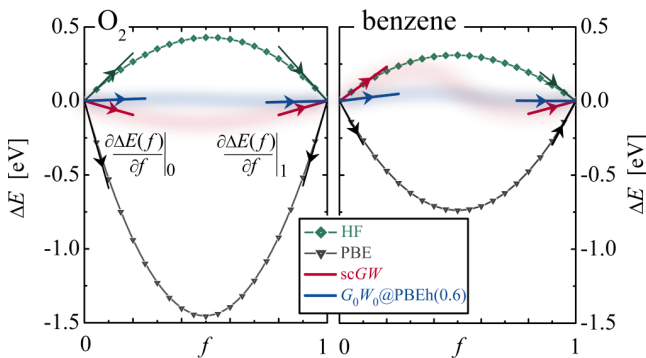


FIG. 2. Deviation from the straight line $\Delta E(f)$ for O_2 (left) and benzene (right). The slopes of ΔE are indicated by arrows obtained by evaluating Eq. (6) with an $scGW$ quasiparticle and total energies or RPA@PBEh($\alpha = 0.6$) total and G_0W_0 @PBEh($\alpha = 0.6$) quasiparticle energies. α defines the fraction of HF exchange in the PBEh(α) hybrid. The blurred curves qualitatively show how $\Delta E(f)$ could behave (see main text for a discussion).

generalization of G to fractional particle numbers has not yet been achieved and might give rise to additional self-energy diagrams at fractional particle numbers [21]. For the exact Green's function our analysis is warranted, because it satisfies Eqs. (2) and (3) and $\Delta_{DSLE} = 0$. Even if diagrams beyond GW would change $\partial E/\partial f$ so that it does not equal the quasiparticle energies at the integer end points of an approximate theory such as GW , $E(f)$ can still not be a straight line if Δ_{DSLE} , as defined by the quasiparticle energy difference in Eq. (4), is not equal to zero. It therefore makes sense to anticipate the severity of the deviation from the straight line by Δ_{DSLE} , which we will discuss for GW in the following.

Another reason for inspecting Δ_{DSLE} is related to the self-screening problem in GW . In the calculation for the $N - 1$ particle system, the screening in W will be that of $N - 1$ electrons and thus typically less than that in the N particle system. This is most evidently seen for one-electron systems such as the hydrogen (H) atom where the calculation for the proton gives the correct screening, i.e., zero, whereas the calculation for the neutral H atom already includes screening [22]. Thus, deviations between $EA_c(N - 1)$ and $IP(N)$ also measure the severity of the self-screening.

Among the different GW flavors only fully self-consistent GW ($scGW$), in which the Dyson equation is solved iteratively, gives results that are independent of the starting point [23,24]. Therefore, $scGW$ provides an unbiased assessment of the DSLE. Most importantly, in $scGW$ also the ground state is treated at the GW level and the $scGW$ density does not inherit the (de)localization error of the starting point, as is the case in G_0W_0 calculations. First, we evaluate Eq. (4) with the $scGW$ quasiparticle HOMO and LUMO energies and obtain $\Delta_{DSLE} = 0.9$ eV for O_2 . This clearly indicates that self-screening and a DSLE is present in $scGW$ calculations. Making the analogy to the DSLE in DFT, $\Delta_{DSLE} = 0.9$ eV would indicate convexity in the GW total energy curve, however, much less pronounced than in PBE.

Extending the DFT DSLE analogy, we would like to estimate how the GW total energy would behave if it could be calculated for fractional particle numbers. For this we assume that an ensemble generalization of GW exists and that potential additional diagrams yield only a negligible contribution near integer particle numbers. The slopes of ΔE then are

$$\partial \Delta E / \partial f = \partial E / \partial f - \partial E_{lin} / \partial f. \quad (6)$$

For the reference straight line we use $\partial E_{lin} / \partial f = E(N_0 - 1) - E(N_0)$. Identifying the GW quasiparticle energies with the electron affinity, respectively, the ionization potential, allows us to connect $\partial E / \partial f$ with the GW quasiparticle energies according to Eqs. (2) and (3). Equation (6) then becomes

$$\frac{\partial \Delta E}{\partial f} = \begin{cases} \epsilon_{N_0}^H + E(N_0 - 1) - E(N_0) & \text{for } N_0, \\ \epsilon_{N_0-1}^L + E(N_0 - 1) - E(N_0) & \text{for } N_0 - 1, \end{cases} \quad (7a)$$

$$(7b)$$

where we calculate the total energies $E(N_0 - 1)$ and $E(N_0)$ with $scGW$ [23,24]. The resulting slopes are displayed as arrows in Fig. 2. For the example of O_2 , the slopes at the two end points of the $scGW$ curve confirm the convex behavior predicted by Δ_{DSLE} , because they are pointing in different

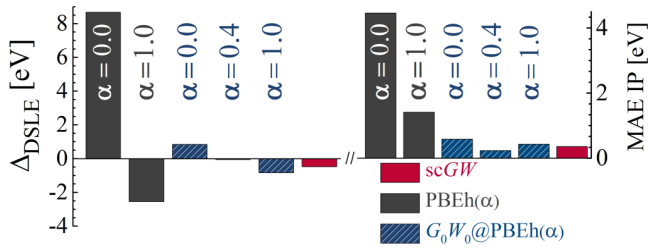


FIG. 3. Left panel: Average Δ_{DSLE} for the $G2_{\text{ip}}$ set. Right panel: Mean average error (MAE) of the ionization potential.

directions, i.e., they have different signs. The behavior between the end points can be schematically illustrated in the spirit of DFT total energies. Since we cannot calculate intermediate points at fractional particle numbers, we indicate a possible behavior schematically by the blurred curves. For our second example, benzene, the behavior is markedly different. The signs of $\partial\Delta E/\partial f$ are equal at both ends of the occupation interval. To connect both end points—again schematically sketched by the blurred curve in Fig. 2— ΔE inevitably has to cross zero at some point. Hence, we expect the ΔE curve to be divided into two regimes. Beginning from the cation, the positive slope at $N_0 - 1$ gives rise to a concave DSLE. When we approach the N_0 electron limit, the positive slope at N_0 requires a convex curvature. For benzene, the absolute value of the slope at $N_0 - 1$ is higher than at the other end of the interval. As a result, we expect the concave deviation on the $N_0 - 1$ side to be more pronounced than the convex part. This is also reflected by a negative Δ_{DSLE} of -0.7eV , which we associate with a concave DSLE.

To provide a comprehensive assessment of the DSLE in the GW approximation, we have further performed calculations for a benchmark set consisting of 48 atoms and molecules selected from the quantum chemical G2 ion test set [25,26] based on the availability of experimental vertical IPs—referred to as $G2_{\text{ip}}$ in the following [27]. For $scGW$ we find a mean DSLE of $\bar{\Delta}_{\text{DSLE}} = -0.5\text{eV}$. The average over the absolute $\bar{\Delta}_{\text{DSLE}}$ amounts to 0.9eV . The $scGW$ DSLE is thus much smaller than that of PBE and HF (Figs. 2 and 3). Our results suggest that $scGW$ predominantly exhibits a concave DSLE and thus has the tendency to overlocalize electron density, which is consistent with previous work [16] on the quasiparticle self-consistent GW approach [28].

Most commonly, GW is not carried out fully self-consistently, but applied in first-order perturbation theory (G_0W_0). This introduces a dependence on the reference ground state encoded in G_0 . Logically, also the DSLE should depend on the chosen starting point.

For O_2 , G_0W_0 calculations based on orbitals and eigenvalues from PBE ($G_0W_0@PBE$) yield an IP of -11.6eV , which differs from the EA_c of the cation (-13.0eV). Thus, $G_0W_0@PBE$ also violates the straight-line condition, as quantified through Eq. (4), which yields $\Delta_{\text{DSLE}} = 1.4\text{eV}$. The positive value of Δ_{DSLE} indicates a convex total energy at fractional particle numbers as in PBE, albeit an order of magnitude smaller than in PBE. Conversely, we find $\Delta_{\text{DSLE}} = -0.6\text{eV}$ with opposite sign if we use G_0W_0 based on the PBE hybrid functional $PBEh(\alpha)$ with $\alpha = 1$. $PBEh(\alpha)$ mixes

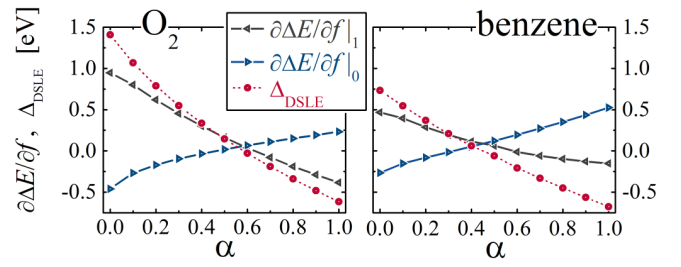


FIG. 4. Δ_{DSLE} (red), $\partial\Delta E/\partial f$ for O_2 , and benzene at $N_0 - 1$ (blue) and N_0 (black) particles for $G_0W_0@PBEh(\alpha)$ and $RPA@PBEh(\alpha)$ total energies.

PBE exchanges with HF exchange according to $E_{\text{xc}}^{\text{PBEh}(\alpha)} = E_c^{\text{PBE}} + (1 - \alpha)E_x^{\text{PBE}} + \alpha E_x^{\text{HF}}$ [29,30].

Now one could ask if our DSLE definition may prove useful for the design of novel DSLE-free approaches for quasiparticle energy calculations. Since in our two examples Δ_{DSLE} changes sign for $\alpha = 0$ and $\alpha = 1$, it is conceivable to postulate that an intermediate, optimal α exists for which the DSLE in G_0W_0 is eliminated or at least considerably reduced. To test this postulate, we evaluate the DSLE for several α values in the range $[0, 1]$. As illustrated in the lower panel of Fig. 4, an increasing α gradually decreases Δ_{DSLE} for O_2 and benzene. At an optimal α of ≈ 0.4 for benzene and ≈ 0.6 for O_2 , the DSLE vanishes. Beyond this point, Δ_{DSLE} becomes increasingly negative with a further increase in α , indicating an increasingly concave total energy curve.

We can support the G_0W_0 Δ_{DSLE} results by examining the slopes of ΔE as defined in Eq. (6). Within an approximate ensemble generalization of the noninteraction Green's function G_0 [31,32], G_0W_0 quasiparticle energies become equivalent to the derivative of the total energy in the random phase approximation (RPA) with respect to the particle number [31]. We show $\partial\Delta E/\partial f$ for $N_0 - 1$ and N_0 as a function of α for O_2 and benzene in Fig. 4. Both molecules show the trend expected from the Δ_{DSLE} calculations. Beginning at small α , the slopes support convexity because ΔE falls away from $N_0 - 1$ and rises again approaching N_0 . Conversely, for large α , the signs of the slopes are reversed, implying concavity. Both slopes approach zero around $\alpha = 0.6$ for O_2 and $\alpha = 0.4$ for benzene, which is consistent with the α values for which Δ_{DSLE} vanishes. Figure 2 shows the expected behavior of the total energy for $\alpha = 0.6$.

Next, we return to our benchmark set of 48 molecules. As illustrated in the upper panel of Fig. 5, G_0W_0 exhibits the largest DSLE, when starting from PBE. The DSLE decreases for increasing α and approaches a negative DSLE in the limit of 100% HF exchange that is almost as large in absolute value as for $G_0W_0@PBE$. The optimal α that eliminates the DSLE again amounts to ≈ 0.4 . We also determined the optimal α values for each molecule, individually. Here, too, the optimal α amounts to $\alpha \approx 0.4$ on average.

We now establish a correlation between the DSLE and the agreement with experimental reference data for ionization potentials. For all M molecules of the $G2_{\text{ip}}$ test set, we evaluated the $G_0W_0@PBEh(\alpha)$ HOMO energies for different α and calculated the mean absolute error (MAE $\equiv \sum_{i=1}^M |\epsilon_i^H - IP_i^{\text{exp}}|/M$) with respect to the experimental

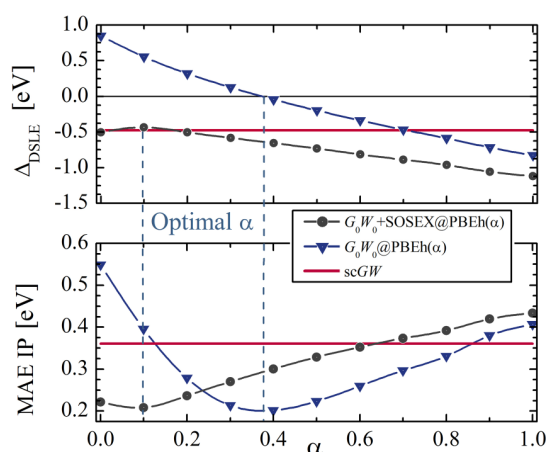


FIG. 5. Upper panel: Average Δ_{DSLE} for the $G_{2\text{ip}}$ set computed with $scGW$, G_0W_0 , and $G_0W_0 + \text{SOSEX}$, as a function of the HF exchange parameter α employed in the $PBEh(\alpha)$ starting point. Lower panel: MAE of the predicted ionization potential depending on the starting point.

vertical IPs [33]. As shown in the lower panel of Fig. 5, the MAE exhibits a minimum at $\alpha \approx 0.4$ when $G_0W_0@PBEh(\alpha)$ becomes DSLE minimized. At this point, the MAE amounts to 0.20 eV [34], which can be seen as the intrinsic accuracy of G_0W_0 based on global hybrid functionals. With increasing DSLE we observe a concomitant increase of the MAE.

As the minimum in the G_0W_0 MAE curve is rather shallow, hybrid functional starting points with 30%–50% HF exchange produce reasonable MAEs. This is consistent with the empirical findings of Bruneval [35], Marom *et al.* [7], and the work of Körzdörfer *et al.* [36].

Consistent with the analysis above, the MAE of $scGW$ (0.36 eV) is slightly higher than for DSLE-minimized G_0W_0 . However, the MAE of the IPs from the total energy difference, in $scGW$ amounts to only 0.22 eV, and is thus comparable to DSLE-minimized G_0W_0 . Our results strongly suggest that the DSLE is largely responsible for the discrepancies between GW quasiparticle energies and experimental ionization energies.

Finally, we illustrate that the concept of DSLE-minimized quasiparticle calculations is generally applicable and can be transferred to other self-energy approximations. Motivated by the good results of renormalized second-order perturbation theory (rPT2) for electron correlation energies [37], Ren and co-workers recently proposed a beyond- GW scheme [38] that combines GW with a second-order screened exchange self-energy ($G_0W_0+\text{SOSEX}$). In the following, we apply our DSLE analysis to $(G_0W_0+\text{SOSEX})@PBEh(\alpha)$ calculations for the $G_{2\text{ip}}$ test set. In the upper panel of Fig. 5 we display the corresponding DSLE and in the lower panel the MAE as a function of α . Compared to G_0W_0 , the starting point dependence is weaker and the DSLE is always negative. Also, the DSLE and the MAE are minimized at smaller α values. This confirms our previous, heuristic findings, that rPT2 and $G_0W_0+\text{SOSEX}$ perform best for starting points that are close to PBE. The smallest MAE amounts to 0.21 eV, which is comparable to G_0W_0 .

In conclusion, we have shown that the DSLE is a prominent source of discrepancy between experimental and theoretical vertical IPs. Through a formal definition of the DSLE for quasiparticle calculations, we show that the GW approach has an intrinsic DSLE of -0.5 eV and a tendency towards concavity, i.e., localization of electrons. We then establish a correlation between the DSLE and the deviation from experimental ionization energies. This allowed us to propose a recipe for obtaining DSLE-minimized approximations to many-body perturbation theory. The DSLE-minimized G_0W_0 and $G_0W_0+\text{SOSEX}$ schemes give the best agreement with experimental data, as illustrated for the 48 molecules of the $G_{2\text{ip}}$ test set.

We thank Xinguo Ren for supporting us with the SOSEX calculations and Christoph Friedrich for fruitful discussions. This work was supported by the Academy of Finland through its Centres of Excellence Programme under Projects No. 251748 and No. 284621. S.K. and M.D. acknowledge support by Deutsche Forschungsgemeinschaft Graduiertenkolleg 1640 and the Bavarian State Ministry of Sciences, Research, and the Arts for the Collaborative Research Network Soltech

- [1] W. Kohn and L. J. Sham, *Phys. Rev.* **140**, A1133 (1965).
- [2] L. Hedin, *Phys. Rev.* **139**, A796 (1965).
- [3] W. G. Aulbur, L. Jönsson, and J. W. Wilkins, *Solid State Phys.* **54**, 1 (1999).
- [4] G. Onida, L. Reining, and A. Rubio, *Rev. Mod. Phys.* **74**, 601 (2002).
- [5] P. Rinke, A. Qteish, J. Neugebauer, C. Freysoldt, and M. Scheffler, *New J. Phys.* **7**, 126 (2005).
- [6] F. Fuchs, J. Furthmüller, F. Bechstedt, M. Shishkin, and G. Kresse, *Phys. Rev. B* **76**, 115109 (2007).
- [7] N. Marom, F. Caruso, X. Ren, O. T. Hofmann, T. Körzdörfer, J. R. Chelikowsky, A. Rubio, M. Scheffler, and P. Rinke, *Phys. Rev. B* **86**, 245127 (2012).
- [8] J. P. Perdew, R. G. Parr, M. Levy, and J. L. Balduz, Jr., *Phys. Rev. Lett.* **49**, 1691 (1982).
- [9] A. J. Cohen, P. Mori-Sánchez, and W. Yang, *Science* **321**, 792 (2008).
- [10] A. Ruzsinszky, J. P. Perdew, G. I. Csonka, O. A. Vydrov, and G. E. Scuseria, *J. Chem. Phys.* **125**, 194112 (2006).
- [11] P. Mori-Sánchez, A. J. Cohen, and W. Yang, *J. Chem. Phys.* **125**, 201102 (2006).
- [12] Y. Zhang and W. Yang, *J. Chem. Phys.* **109**, 2604 (1998).
- [13] E. Kraisler and L. Kronik, *Phys. Rev. Lett.* **110**, 126403 (2013).
- [14] V. Vlček, H. R. Eisenberg, G. Steinle-Neumann, L. Kronik, and R. Baer, *J. Chem. Phys.* **142**, 034107 (2015).
- [15] V. Atalla, P. Rinke, I. Zhang, O. T. Hofmann, and M. Scheffler (unpublished).
- [16] F. Bruneval, *Phys. Rev. Lett.* **103**, 176403 (2009).
- [17] See Supplemental Material at <http://link.aps.org/supplemental/10.1103/PhysRevB.93.121115> for computational details.

- [18] C.-O. Almbladh and U. von Barth, *Phys. Rev. B* **31**, 3231 (1985).
- [19] J. F. Janak, *Phys. Rev. B* **18**, 7165 (1978).
- [20] W. Yang, A. J. Cohen, and P. Mori-Sánchez, *J. Chem. Phys.* **136**, 204111 (2012).
- [21] R. van Leeuwen and G. Stefanucci, *Phys. Rev. B* **85**, 115119 (2012).
- [22] W. Nelson, P. Bokes, P. Rinke, and R. W. Godby, *Phys. Rev. A* **75**, 032505 (2007).
- [23] F. Caruso, P. Rinke, X. Ren, M. Scheffler, and A. Rubio, *Phys. Rev. B* **86**, 081102 (2012).
- [24] F. Caruso, P. Rinke, X. Ren, A. Rubio, and M. Scheffler, *Phys. Rev. B* **88**, 075105 (2013).
- [25] L. A. Curtiss, K. Raghavachari, P. C. Redfern, and J. A. Pople, *J. Chem. Phys.* **106**, 1063 (1997).
- [26] X. Ren, P. Rinke, V. Blum, J. Wieferink, A. Tkatchenko, A. Sanfilippo, K. Reuter, and M. Scheffler, *New J. Phys.* **14**, 053020 (2012).
- [27] See Supplemental Material at <http://link.aps.org/supplemental/10.1103/PhysRevB.93.121115> for the systems and the corresponding numerical values of the G_{2ip} test set.
- [28] M. van Schilfgaarde, T. Kotani, and S. Faleev, *Phys. Rev. Lett.* **96**, 226402 (2006).
- [29] C. Adamo and V. Barone, *J. Chem. Phys.* **110**, 6158 (1999).
- [30] J. P. Perdew, K. Burke, and M. Ernzerhof, *Phys. Rev. Lett.* **77**, 3865 (1996).
- [31] L.-W. Wang, *Phys. Rev. B* **82**, 115111 (2010).
- [32] W. Yang, P. Mori-Sánchez, and A. J. Cohen, *J. Chem. Phys.* **139**, 104114 (2013).
- [33] Reference vertical ionization energies are taken from <http://cccbdb.nist.gov>.
- [34] At the optimal starting point for each system, we observe the same MAE for the G_{2ip} set.
- [35] F. Bruneval and M. A. L. Marques, *J. Chem. Theory Comput.* **9**, 324 (2012).
- [36] T. Körzdörfer and N. Marom, *Phys. Rev. B* **86**, 041110(R) (2012).
- [37] X. Ren, P. Rinke, G. E. Scuseria, and M. Scheffler, *Phys. Rev. B* **88**, 035120 (2013).
- [38] X. Ren, N. Marom, F. Caruso, M. Scheffler, and P. Rinke, *Phys. Rev. B* **92**, 081104(R) (2015).

Supplemental Material to: Piecewise linearity in the GW approximation for accurate quasiparticle energy predictions

Matthias Dauth^{1,2}, Fabio Caruso³, Stephan Kümmel¹, and Patrick Rinke²

¹ *Physics Institute, University of Bayreuth, D-95440 Bayreuth, Germany*

² *COMP Department of Applied Physics, Aalto University, P.O. Box 11100, Aalto FI-00076, Finland and*

³ *Department of Materials, University of Oxford, Parks Road, Oxford OX1 3PH, United Kingdom*

In the following we present a detailed listing of the relevant data that sets the foundation for the figures in the article *Piecewise linearity in the GW approximation for accurate quasiparticle energy predictions*. We list the molecules from the $G2_{ip}$ test set together with the corresponding experimental vertical ionization energies taken from <http://cccbdb.nist.gov>. Additionally we show the quasiparticle energies of the highest occupied molecular orbital $\epsilon_{N_0}^H$, the deviation from the straight line error Δ_{DSLE} , and the deviation from the experimental ionization energy $|\Delta IP|$. Representative for all G_0W_0 calculations we list numerical values for the starting points $G_0W_0@PBE$, $G_0W_0@PBEh(0.4)$, and $G_0W_0@PBEh(1.0)$. Further, we show the data obtained from fully self-consistent GW and from $G_0W_0+SOSEX@PBEh(0.1)$.

TABLE I: List of molecules from the $G2_{ip}$ test set. The second column show the experimental vertical ionization energies IP_{exp} taken from <http://cccbdb.nist.gov>. Calculated values for the quasiparticle energy of the highest occupied molecular orbital $\epsilon_{N_0}^H$, the deviation from the straight line error Δ_{DSLE} , and the deviation from the experimental ionization energy $|\Delta IP|$ are given in eV.

	IP_{exp}	$G_0W_0@PBE$			$G_0W_0@PBEh(0.4)$			$G_0W_0@PBEh(1.0)$		
		$\epsilon_{N_0}^H$	Δ_{DSLE}	$ \Delta IP $	$\epsilon_{N_0}^H$	Δ_{DSLE}	$ \Delta IP $	$\epsilon_{N_0}^H$	Δ_{DSLE}	$ \Delta IP $
Al	5.98	-5.85	0.32	0.13	-6.08	-0.01	0.10	-6.21	-0.26	0.23
Ar	15.76	-14.83	0.83	0.93	-15.27	0.02	0.49	-15.54	-0.68	0.22
B	8.30	-7.70	1.30	0.60	-8.33	0.21	0.03	-8.67	-0.27	0.37
BCl ₃	11.64	-11.09	0.60	0.55	-11.69	-0.04	0.05	-12.09	-0.55	0.45
Be	9.32	-8.96	0.05	0.36	-9.12	-0.25	0.20	-9.12	-0.41	0.20
BF ₃	15.96	-14.94	0.68	1.02	-15.81	-0.35	0.15	-16.34	-1.19	0.38
C	11.26	-10.37	1.21	0.89	-11.18	0.19	0.08	-11.61	-0.53	0.35
C ₂ H ₂	11.49	-11.06	0.74	0.43	-11.43	-0.07	0.06	-11.62	-0.80	0.13
C ₂ H ₄	10.68	-10.32	0.64	0.36	-10.59	-0.13	0.09	-10.70	-0.83	0.02
C ₂ H ₄ S	9.05	-8.74	0.92	0.31	-9.10	-0.02	0.05	-9.31	-0.87	0.26
C ₂ H ₅ OH	10.64	-10.18	2.23	0.46	-10.84	0.15	0.20	-11.34	-1.66	0.70
C ₆ H ₆	9.25	-9.05	0.73	0.20	-9.35	0.06	0.10	-9.49	-0.68	0.24
CH ₂ CCH ₂	10.20	-9.91	0.76	0.29	-10.32	-0.11	0.12	-10.58	-1.04	0.38
CH ₂ S	9.38	-8.97	0.95	0.41	-9.38	-0.03	0.00	-9.58	-0.86	0.20
CH ₃	9.84	-9.21	0.91	0.63	-9.76	0.00	0.08	-10.10	-0.78	0.26
CH ₃ Cl	11.29	-10.92	1.21	0.37	-11.33	0.13	0.04	-11.59	-0.81	0.30
CH ₃ F	13.04	-12.72	1.00	0.32	-13.35	-0.05	0.31	-13.90	-1.38	0.86
CH ₃ SH	9.44	-9.08	0.97	0.36	-9.43	0.02	0.01	-9.64	-0.76	0.20
CH ₄	13.60	-13.94	0.62	0.34	-14.43	-0.19	0.83	-14.74	-0.91	1.14
CHO	9.31	-9.11	1.00	0.20	-9.87	0.14	0.56	-10.48	-0.57	1.17

Continued on next page

TABLE I – *Continued from previous page*

	IP _{exp}	$G_0W_0@PBE$			$G_0W_0@PBEh(0.4)$			$G_0W_0@PBEh(1.0)$		
		$\epsilon_{N_0}^H$	Δ_{DSLE}	$ \Delta IP $	$\epsilon_{N_0}^H$	Δ_{DSLE}	$ \Delta IP $	$\epsilon_{N_0}^H$	Δ_{DSLE}	$ \Delta IP $
Cl	12.97	-12.42	0.69	0.55	-12.80	-0.06	0.17	-13.02	-0.70	0.05
Cl ₂	11.49	-11.06	0.73	0.43	-11.48	0.09	0.01	-11.80	-0.51	0.31
ClF	12.77	-12.22	0.94	0.55	-12.73	0.13	0.04	-11.35	-0.63	0.40
CO	14.01	-13.37	1.19	0.64	-14.18	-0.06	0.17	-14.87	-1.22	0.86
CO ₂	13.78	-13.30	1.11	0.48	-13.91	-0.07	0.13	-14.35	-1.55	0.57
CS ₂	10.09	-9.79	0.81	0.30	-10.14	0.02	0.05	-10.39	-0.92	0.30
F	17.42	-16.15	1.15	1.27	-16.90	-0.27	0.52	-17.24	-1.43	0.18
FH	16.12	-14.99	1.35	1.13	-15.76	-0.28	0.36	-16.11	-1.70	0.01
Li	5.39	-5.76	-0.56	0.37	-5.77	-0.49	0.38	-5.71	-0.39	0.32
Mg	7.65	-7.45	0.05	0.20	-7.58	-0.20	0.07	-7.58	-0.32	0.07
N	14.54	-13.44	1.43	1.10	-14.31	0.20	0.23	-14.79	-0.72	0.25
N ₂	15.58	-14.90	1.03	0.68	-15.75	0.07	0.17	-17.21	-1.50	1.63
Na	5.14	-5.28	-0.51	0.14	-5.32	-0.38	0.18	-5.28	-0.25	0.14
NaCl	9.80	-8.15	1.40	1.65	-9.02	-0.05	0.78	-9.26	-0.86	0.54
Ne	21.56	-19.61	1.33	1.95	-20.34	-0.23	1.22	-20.64	-1.56	0.92
NH ₃	10.82	-10.23	1.06	0.59	-10.88	-0.20	0.06	-11.24	-1.29	0.42
O	13.61	-12.84	0.92	0.77	-13.54	-0.32	0.07	-13.83	-1.27	0.22
O ₂	12.30	-11.64	1.41	0.66	-12.64	0.34	0.34	-13.52	-0.62	1.22
OCS	11.19	-10.96	0.83	0.23	-11.35	0.03	0.16	-11.65	-0.86	0.46
OH	13.02	-12.33	1.10	0.69	-13.05	-0.31	0.03	-13.37	-1.49	0.35
P	10.49	-9.98	0.77	0.51	-10.40	0.12	0.09	-10.65	-0.37	0.16
P ₂	10.62	-10.24	0.71	0.38	-10.49	0.10	0.13	-10.60	-0.43	0.02
PH ₃	10.59	-10.27	0.64	0.32	-10.60	-0.07	0.01	-10.79	-0.69	0.20
S	10.36	-10.06	0.53	0.30	-10.40	-0.14	0.04	-10.58	-0.68	0.22
S ₂	9.55	-9.06	0.87	0.49	-9.58	0.23	0.03	-10.02	-0.35	0.47
SH ₂	10.50	-10.06	0.69	0.44	-10.39	-0.03	0.11	-10.57	-0.68	0.07
Si	8.15	-7.81	0.58	0.34	-8.15	0.05	0.00	-8.34	-0.34	0.19
SiH ₄	12.30	-12.33	0.71	0.03	-12.88	-0.05	0.58	-13.24	-0.62	0.94

TABLE II: List of molecules from the $G2_{ip}$ test set. The second column show the experimental vertical ionization energies IP_{exp} taken from <http://cccbdb.nist.gov>. Calculated values for the quasiparticle energy of the highest occupied molecular orbital $\epsilon_{N_0}^H$, the deviation from the straight line error Δ_{DSLE} , and the deviation from the experimental ionization energy $|\Delta IP|$ are given in eV.

	IP_{exp}	$G_0W_0+SOSEX@PBEh(0.1)$			scGW		
		$\epsilon_{N_0}^H$	Δ_{DSLE}	$ \Delta IP $	$\epsilon_{N_0}^H$	Δ_{DSLE}	$ \Delta IP $
Al	5.98	-6.13	-0.42	0.15	-5.72	0.42	0.26
Ar	15.76	-15.54	-0.48	0.22	-15.41	0.14	0.35
B	8.30	-8.64	-0.64	0.34	-8.12	0.62	0.18
BCl ₃	11.64	-11.65	-0.23	0.01	-11.43	-0.47	0.21
Be	9.32	-9.34	-0.39	0.02	-8.56	0.30	0.76
BF ₃	15.96	-16.07	-0.59	0.11	-16.23	-1.70	0.27
C	11.26	-11.51	-0.60	0.25	-11.12	0.51	0.14
C ₂ H ₂	11.49	-11.40	-0.21	0.09	-10.99	-1.33	0.50
C ₂ H ₄	10.68	-10.61	-0.21	0.07	-10.16	0.62	0.52
C ₂ H ₄ S	9.05	-9.18	-0.36	0.13	-8.75	0.46	0.30
C ₂ H ₅ OH	10.64	-10.97	-0.61	0.33	-10.81	-2.61	0.17
C ₆ H ₆	9.25	-9.45	-0.33	0.20	-8.79	-0.72	0.46
CH ₂ CCH ₂	10.20	-10.19	-0.24	0.01	-9.91	-1.67	0.29
CH ₂ S	9.38	-9.47	-0.38	0.09	-9.03	0.43	0.35
CH ₃	9.84	-10.11	-0.69	0.27	-9.70	-0.02	0.14
CH ₃ Cl	11.29	-11.40	-0.70	0.11	-11.17	-1.66	0.12
CH ₃ F	13.04	-13.47	-0.68	0.43	-13.48	-1.91	0.44
CH ₃ SH	9.44	-9.51	-0.40	0.07	-9.12	0.25	0.32
CH ₄	13.60	-14.39	-0.57	0.79	-14.34	-1.75	0.74
CHO	9.31	-9.77	-0.30	0.46	-9.73	0.68	0.42
Cl	12.97	-12.95	-0.43	0.02	-12.61	0.52	0.36
Cl ₂	11.49	-11.52	-0.18	0.03	-11.24	-0.70	0.25
ClF	12.77	-12.86	-0.28	0.09	-12.59	-1.38	0.18
CO	14.01	-14.28	-0.64	0.27	-13.93	-1.35	0.08
CO ₂	13.78	-13.98	-0.44	0.20	-13.71	-2.18	0.07
CS ₂	10.09	-10.07	-0.06	0.02	-9.59	-0.73	0.50
F	17.42	-17.41	-0.83	0.01	-17.39	-0.17	0.03
FH	16.12	-16.26	-0.82	0.14	-16.30	-4.47	0.18
Li	5.39	-5.78	-0.58	0.39	-5.44	-0.13	0.05
Mg	7.65	-7.67	-0.23	0.02	-7.14	0.21	0.51
N	14.54	-14.69	-0.36	0.15	-14.44	0.05	0.10
N ₂	15.58	-15.89	-0.31	0.31	-15.57	-0.06	0.01

Continued on next page

TABLE II – *Continued from previous page*

	IP _{exp}	$G_0W_0+\text{SOSEX}@PBEh(0.1)$			scGW		
		$\epsilon_{N_0}^H$	Δ_{DSLE}	$ \Delta \text{IP} $	$\epsilon_{N_0}^H$	Δ_{DSLE}	$ \Delta \text{IP} $
Na	5.14	-5.36	-0.56	0.22	-5.17	-0.06	0.03
NaCl	9.80	-8.99	-0.10	0.81	-9.02	-1.65	0.78
Ne	21.56	-21.05	-0.98	0.51	-21.40	-1.13	0.16
NH ₃	10.82	-11.21	-0.66	0.39	-10.88	0.13	0.06
O	13.61	-13.99	-0.83	0.38	-15.47	-1.81	1.86
O ₂	12.30	-12.48	-0.29	0.18	-12.65	0.95	0.35
OCS	11.19	-11.35	-0.19	0.16	-10.88	-0.95	0.31
OH	13.02	-13.44	-0.73	0.42	-14.10	-0.75	1.08
P	10.49	-10.58	-0.18	0.09	-10.19	0.43	0.30
P ₂	10.62	-10.54	-0.16	0.08	-9.86	-0.54	0.76
PH ₃	10.59	-10.66	-0.23	0.07	-10.32	0.36	0.27
S	10.36	-10.41	-0.37	0.05	-10.99	-0.43	0.63
S ₂	9.55	-9.39	-0.07	0.16	-9.24	1.11	0.31
SH ₂	10.50	-10.55	-0.33	0.05	-10.10	0.58	0.40
Si	8.15	-8.27	-0.40	0.12	-7.87	0.61	0.28
SiH ₄	12.30	-12.82	-0.47	0.52	-12.75	0.09	0.45

Publication 8

Benchmark of *GW* approaches for the *GW100* testset

Journal of Chemical Theory and Computation **12**, 5076 (2016)

F. Caruso¹, **M. Dauth**², M. J. van Setten³, and P. Rinke²

¹ Department of Materials, University of Oxford, Parks Road, Oxford OX1 3PH, United Kingdom

² Theoretical Physics IV, University of Bayreuth, D-95440 Bayreuth, Germany

³ Nanoscopic Physics, Institute of Condensed Matter and Nanosciences, Université Catholique de Louvain, 1348 Louvain-la-Neuve, Belgium

⁴ COMP/Department of Applied Physics, Aalto University, P.O. Box 11100, Aalto FI-00076, Finland

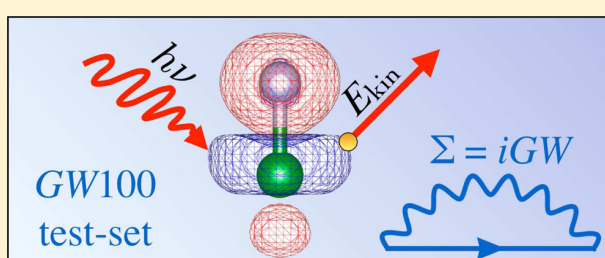
My contribution

I performed the $G_0W_0@PBE$, $G_0W_0@HF$, and DSLE calculations presented in the paper. I wrote a draft for the part of the manuscript that explains the DSLE concept and that discusses the DSLE results. I was part of the scientific discussion.

Benchmark of GW Approaches for the GW100 Test Set

Fabio Caruso,[†] Matthias Dauth,[‡] Michiel J. van Setten,[¶] and Patrick Rinke^{*,§}[†]Department of Materials, University of Oxford, Parks Road, Oxford OX1 3PH, United Kingdom[‡]Theoretical Physics IV, University of Bayreuth, D-95440 Bayreuth, Germany[¶]Nanoscope Physics, Institute of Condensed Matter and Nanosciences, Université Catholique de Louvain, 1348 Louvain-la-Neuve, Belgium[§]COMP/Department of Applied Physics, Aalto University, P.O. Box 11100, Aalto FI-00076, Finland

ABSTRACT: For the recent GW100 test set of molecular ionization energies, we present a comprehensive assessment of different GW methodologies: fully self-consistent GW (scGW), quasiparticle self-consistent GW (qsGW), partially self-consistent G_0W_0 (sc G_0W_0), perturbative GW (G_0W_0), and optimized G_0W_0 based on the minimization of the deviation from the straight-line error (DSLE-min GW). We compare our GW calculations to coupled-cluster singles, doubles, and perturbative triples [CCSD(T)] reference data for GW100. We find scGW and qsGW ionization energies in excellent agreement with CCSD(T), with discrepancies typically smaller than 0.3 eV (scGW) and 0.2 eV (qsGW), respectively. For sc G_0W_0 and G_0W_0 the deviation from CCSD(T) is strongly dependent on the starting point. We further relate the discrepancy between the GW ionization energies and CCSD(T) to the deviation from straight line error (DSLE). In DSLE-minimized GW calculations, the DSLE is significantly reduced, yielding a systematic improvement in the description of the ionization energies.



1. INTRODUCTION

Many-body perturbation theory provides an ideal framework for the first-principles study of electronic excitations in molecules and solids.¹ At variance with approaches based on density-functional theory (DFT),^{2,3} the description of electronic many-body interactions through the electron self-energy facilitates a seamless account of exact exchange and screening, which are essential to predict electronic excitations with quantitative accuracy.^{4–7} The GW approximation^{8,9} provides an ideal compromise between accuracy and computational cost, and it has, thus, evolved into the state-of-the-art technique for the computation of ionization energies and band gaps in molecules and solids.⁵

GW calculations are typically based on first-order perturbation theory (G_0W_0),⁹ a procedure that introduces a spurious dependence of the results on the starting point, that is, the initial reference ground state the perturbation is applied to.^{6,10–13} The starting-point dependence may be reduced by resorting to partial self-consistent approaches,^{11,14} such as eigenvalue self-consistent GW or self-consistent G_0W_0 (sc G_0W_0), and it is completely eliminated in the self-consistent GW method (scGW)^{15,16} – in which the Dyson equation is solved fully iteratively – and in quasi-particle self-consistent GW (qsGW).^{17–19} While scGW implementations are still relatively rare,^{15,16,20–27} qsGW is now widely used.^{19,28–32} Moreover, with rare exceptions,²⁵ scGW and qsGW are typically not implemented in the same code and have therefore not been systematically compared.

Given the various flavors of the self-consistent GW methodology, benchmark and validation are important instruments to (i) quantify the overall accuracy of GW calculations; (ii) reveal the effects of different forms of self-consistency; and (iii) identify new ways to improve over existing techniques for quasiparticle calculations. The GW100 set provides an ideal test case for addressing these challenges.³³ This benchmark set is specifically designed to target the assessment of ionization energies, and it is composed of 100 molecules of different bonding types, chemical compositions, and ionization energies.

In this manuscript, we present the ionization energies for the molecules of the GW100 test set calculated with G_0W_0 , sc G_0W_0 , scGW, and qsGW. We analyze their behavior in terms of the change in the electron density, the screening properties, and the treatment of the kinetic energy. The accuracy of different GW approaches is established based on the comparison with coupled-cluster singles, doubles, and perturbative triples [CCSD(T)] energies obtained for the same geometries and basis sets.³⁷ Our study reveals that scGW and qsGW ionization energies differ on average by 0.3 and 0.15 eV from the CCSD(T) reference data, respectively. The discrepancy of G_0W_0 and sc G_0W_0 from CCSD(T), on the other hand, is contingent on the starting point. For the GW100 set, we report an average starting-point dependence of 1.0 and 0.4 eV for G_0W_0 and sc G_0W_0 , respectively. Correspondingly, the starting point introduces an additional degree of freedom that allows

Received: August 4, 2016

Published: September 15, 2016

one to improve the agreement with CCSD(T), e.g., by imposing the satisfaction of exact physical constraints. One such constraint is the linearity of the total energy at fractional particle numbers.³⁸ The deviation from straight line error (DSLE) has been shown to lead to systematic errors in DFT, such as the tendency to overly localize or delocalize the electron density.^{39,40} Within the context of GW calculations, the DSLE may be minimized by varying the starting point. This procedure we refer to as the DSLE-minimized GW approach (DSLE-min).⁴¹ We show here that DSLE-min GW reduces the discrepancy with CCSD(T) for the GW100 set as compared to scGW with an average absolute deviation slightly larger than that of qsGW (0.26 eV, based on the def2-TZVPP basis set). Overall, our results provide a comprehensive assessment of the starting-point dependence, the accuracy of G_0W_0 and self-consistent GW methods, and suggest that the DSLE minimization may provide a strategy to improve the accuracy of the GW method at the cost of G_0W_0 calculations.

The manuscript is organized as follows. In Section 2 we review the basics of the GW method and self-consistency. Computational details are reported in Section 3. The ionization energies for the GW100 test set are reported in Section 4 and discussed in Section 5. DSLE-min GW results are discussed in Section 6. Conclusions and final remarks are presented in Section 7.

2. METHODS

In the following, we give a brief introduction to the GW methodology employed throughout the manuscript: scGW, scGW₀, qsGW, perturbative G_0W_0 , and DSLE-min GW.

In the scGW approach, the interacting Green's function G is determined through the iterative solution of Dyson's equation

$$G^{-1} = G_0^{-1} - [\Sigma - v_0 + \Delta v_H] \quad (1)$$

Δv_H denotes the change of the Hartree potential, which accounts for the density difference between G_0 and G , and v_0 is the exchange-correlation potential of the preliminary calculation.

The noninteracting Green's function G_0 may be expressed as

$$G_0^\sigma(\mathbf{r}, \mathbf{r}', \omega) = \sum_n \frac{\psi_{n\sigma}(\mathbf{r})\psi_{n\sigma}^*(\mathbf{r}')}{\omega - (\epsilon_{n\sigma} - \mu) - i\eta \operatorname{sgn}(\mu - \epsilon_{n\sigma})} \quad (2)$$

where μ is the Fermi energy, and η is a positive infinitesimal. $\psi_{n\sigma}$ and $\epsilon_{n\sigma}$ denote a set of single-particle orbitals and eigenvalues determined from an independent-particle calculation (e.g., Hartree–Fock or DFT) for spin-channel σ . In the GW approximation, the self-energy Σ is given by

$$\Sigma_\sigma(\mathbf{r}, \mathbf{r}', \omega) = i \int \frac{d\omega'}{2\pi} G_\sigma(\mathbf{r}, \mathbf{r}', \omega + \omega') W(\mathbf{r}, \mathbf{r}', \omega') e^{i\omega\tau} \quad (3)$$

The screened Coulomb interaction W , in turn, is also determined from the solution of a Dyson-like equation

$$W(\mathbf{r}, \mathbf{r}', \omega) = v(\mathbf{r}, \mathbf{r}') + \int d\mathbf{r}_1 d\mathbf{r}_2 v(\mathbf{r}, \mathbf{r}_1) \chi_0(\mathbf{r}_1, \mathbf{r}_2, \omega) W(\mathbf{r}_2, \mathbf{r}', \omega) \quad (4)$$

where $v(\mathbf{r}, \mathbf{r}') = |\mathbf{r} - \mathbf{r}'|^{-1}$ is the bare Coulomb interaction. The polarizability χ_0 is most easily expressed on the time axis τ

$$\chi_0(\mathbf{r}, \mathbf{r}', \tau) = -i \sum_\sigma G_\sigma(\mathbf{r}, \mathbf{r}', \tau) G_\sigma(\mathbf{r}', \mathbf{r}, -\tau) \quad (5)$$

and is Fourier transformed to the frequency axis before it is used in eq 4.

The structure of eqs 1–5 reveals the self-consistent nature of the GW approximation. Due to the interdependence of G , χ_0 , W , and Σ , eqs 1–5 need to be solved iteratively until the satisfaction of a given convergence criterion.¹⁶ We denote the procedure in which eqs 1–5 are solved fully self-consistently as scGW. Recent studies have revealed that Hedin's equations may exhibit multiple-solution behavior.^{42–47} For closed shell molecules we have not yet observed multiple solutions. Moreover, it has been shown that, if self-consistency is achieved through the solution of the Dyson equation, as in this work, the self-consistent loop converges to the unique physical solution.⁴⁶

In scGW₀ the screened interaction W is evaluated only once using orbitals and eigenvalues from an independent-particle calculation. The Dyson equation is thus solved iteratively updating G and Σ at each step but keeping W_0 fixed. In scGW and scGW₀, the physical properties of the system – such as, e.g., the total energy,^{20,21,48–50} the electron density,⁵¹ and the ionization energy^{15,23} – may be extracted directly from the self-consistent Green's function by means of the spectral function

$$A(\omega) = -\frac{1}{\pi} \int d\mathbf{r} \lim_{\mathbf{r}' \rightarrow \mathbf{r}} \operatorname{Im} G(\mathbf{r}, \mathbf{r}', \omega) \quad (6)$$

As an example, we report in Figure 1 the spectral function of the adenine nucleobase ($C_5H_5N_5O$) evaluated using scGW,

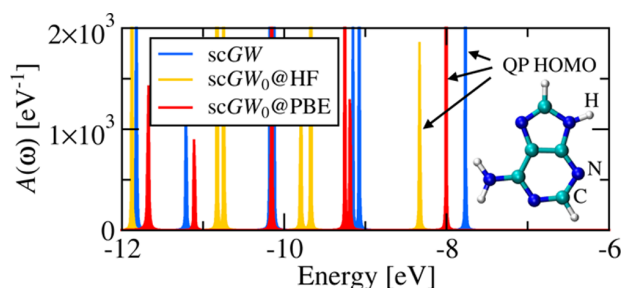


Figure 1. Spectral function of the adenine nucleobase, for which the molecular geometry is shown, obtained from scGW, scGW₀@HF, and scGW₀@PBE using the def2-TZVPP basis set.⁵² The quasiparticle HOMO is indicated by arrows.

scGW₀@HF, and scGW₀@PBE. For each approach, the energy of the quasiparticle highest occupied molecular orbital (HOMO) is given by the position of the highest energy peak, indicated by arrows in Figure 1. We note that scGW₀ still exhibits a dependence on the starting point, which stems from the nonself-consistent treatment of W , whereas scGW is completely independent of the initial reference calculation.¹⁵

In the G_0W_0 approach, the quasiparticle energies $\epsilon_{n\sigma}^{\text{QP}}$ are evaluated as a first-order perturbative correction to a set of single-particle (SP) eigenvalues $\epsilon_{n\sigma}^{\text{SP}}$ [obtained, for instance, from DFT]

$$\epsilon_{n\sigma}^{\text{QP}} = \epsilon_{n\sigma}^{\text{SP}} + \langle \psi_n^\sigma | \Sigma(\epsilon_{n\sigma}^{\text{QP}}) - v_0 | \psi_n^\sigma \rangle \quad (7)$$

Owing to the perturbative nature of eq 7, one would expect a pronounced dependence of $\epsilon_{n\sigma}^{\text{QP}}$ on the starting point, that is, on the set of eigenvalues $\epsilon_{n\sigma}^{\text{SP}}$ and orbitals $\psi_{n\sigma}$. To benchmark the starting point dependence for the GW100 test set we consider hereafter two different starting points: Hartree–Fock and the Perdew–Burke–Ernzerhof⁵³ (PBE) generalized gradient approximation to DFT. We explicitly denote the starting-point

dependence by adopting the notation *method@starting point* (e.g., $G_0W_0@PBE$).

In qsGW the Green's function keeps the analytic structure of a noninteracting Green's function (omitting spin indices for brevity)

$$G_0^{\text{qsGW}}(\mathbf{r}, \mathbf{r}', \omega) = \sum_n \frac{\psi_n^{\text{QP}}(\mathbf{r})\psi_n^{*\text{QP}}(\mathbf{r}')}{\omega - (\epsilon_n^{\text{QP}} - \mu) - i\eta \operatorname{sgn}(\mu - \epsilon_n^{\text{QP}})} \quad (8)$$

The quasi-particle orbitals and energies are iteratively updated solving the quasi-particle equation applying a linear mixing scheme.^{17–19} The QP-orbitals of the $(i+1)$ th iteration $\psi_n^{(i+1)}(\mathbf{r})$ are expressed in terms of the orbitals of the previous iteration

$$\psi_n^{(i+1)}(\mathbf{r}) = \sum_n \mathcal{A}_{n_n}^{(i+1)} \psi_n^{(i)}(\mathbf{r}) \quad (9)$$

In the reference basis $\psi_n^{(i)}(\mathbf{r})$ eq 7 takes the form of an eigenvalue problem

$$\sum_n \mathcal{A}_{n_n}^{(i+1)} \left[\int d\mathbf{r} d\mathbf{r}' \psi_n^{(i)}(\mathbf{r}) (H_0[G_0^{(i)}] \delta(\mathbf{r} - \mathbf{r}') + \tilde{\Sigma}(\mathbf{r}, \mathbf{r}')) \psi_n^{(i)}(\mathbf{r}') \right] = \epsilon_n^{\text{QP}(i+1)} \mathcal{A}_{n_n}^{(i+1)} \quad (10)$$

where $H_0[G_0^{\text{qsGW}}]$ is the single-particle part of the Hamiltonian evaluated with the electron density generated by G_0^{qsGW} . The self-energy matrix is approximated as static and Hermitian

$$\tilde{\Sigma}_{m'm'} = \frac{1}{2} (\Sigma_{m'm}(\epsilon_n) + \Sigma_{m'm}(\epsilon_n')) \quad (11)$$

The diagonalization of eq 10 updates $\epsilon_n^{\text{QP}(i+1)}$ and $\mathcal{A}_{n_n}^{(i+1)}$. With these new orbitals, the wave functions at iteration $i+1$ ($\psi_n^{\text{QP}(i+1)}(\mathbf{r})$) are constructed via eq 9. The orbitals become orthonormal by construction due to the hermiticity of the operators in eq 10.

qsGW is closely related to G_0W_0 in the sense that in each cycle of the self-consistent solution the Green's function is a noninteracting G_0 . The final result was shown to be independent of the starting point,¹⁹ but both the stability of the iterative cycle and the rate of convergence can be greatly improved by using an optimal starting point. In addition, it was found that a simple iteration scheme may not always converge. In practice a linear mixing scheme is applied. In qsGW the orbital energies are directly available via eq 10.

Besides scGW, scGW₀, and qsGW, other approximate self-consistent GW approaches have been investigated in the past, such as eigenvalue self-consistent GW^{11,14,54,55} and GW+COHSEX.^{13,56} These will not be discussed in this article.

Among the different flavors of GW calculations, the starting-point dependence is most pronounced in G_0W_0 , since both G_0 and W_0 depend explicitly on the initial set of orbitals and eigenvalues. Yet, this ambiguity also provides a means to improve the accuracy of G_0W_0 , by seeking the optimal starting point that leads to the satisfaction of exact physical constraints. A prominent example is the piecewise linearity of the total energy.⁵⁷ Usually approximate theories do not automatically exhibit a linearly changing total energy under fractional electron removal (or addition) but instead produce a DSLE. If the total energy were a linear function of the fractional particle number, the ionization energy of the neutral system would be equal to

the electron affinity of the cation (EA_c).^{40,58} Identifying the ionization energy with the G_0W_0 quasiparticle HOMO and EA_c with the lowest unoccupied molecular orbital (LUMO) of the cationic system, one may thus define the DSLE as⁴¹

$$\Delta_{\text{DSLE}} \equiv \epsilon_{\text{HOMO}}^{\text{QP}} - \epsilon_{\text{LUMO},c}^{\text{QP}} \quad (12)$$

This definition can be applied to approximately quantify the DSLE in the GW method without explicitly invoking the total energy at fractional particle numbers. Furthermore, the minimization of Δ_{DSLE} in G_0W_0 calculations allows one to find a starting point that minimizes or completely eliminates the DSLE. We here adopt the DSLE-min GW approach proposed in ref 41 which is based on these concepts. For the DSLE-min procedure we utilize starting points from PBE-based hybrid (PBEh) functionals⁵⁹ with an adjustable fraction α of Hartree–Fock exchange and evaluate eq 12 with the $G_0W_0@PBEh(\alpha)$ quasiparticle energies. We then identify the optimal starting point with the very α that leads to a minimization of Δ_{DSLE} .

The coupled cluster singles, doubles, and perturbative triples [CCSD(T)]^{34–36} approach is often regarded as the *gold standard* among the quantum chemistry methods as it yields results that approach chemical accuracy for a variety of physical/chemical properties, such as binding energies and atomization energies. CCSD(T) values are thus particularly suitable to unambiguously establish the accuracy of GW approaches for the ionization energies. In the following, our calculated ionization energies are compared to reference values from CCSD(T),³⁷ whereby the ionization energy has been obtained as a total energy difference between the ionized and neutral molecules. The comparison to CCSD(T) is here preferred to experimental data as it allows us to focus on the effects of exchange and correlation. We can therefore safely ignore the effects of temperature, nuclear vibrations, and interaction with the environment, which affect experimental ionization energies.⁶⁰ The CCSD(T) calculations of ref 37 used the molecular geometries of the GW100 test set³³ and are therefore suitable to be compared with our calculations, in which the same geometries were employed. Additional details on the CCSD(T) calculations may be found in ref 37.

3. COMPUTATIONAL DETAILS

Our G_0W_0 , DSLE-min GW, and scGW calculations have been performed with the FHI-aims code,^{61–63} whereas qsGW calculations have been performed using a local version of the TURBOMOLE⁶⁴ code. For G_0W_0 , DSLE-min GW, and scGW the frequency dependence is treated on the imaginary frequency axis, and the quasiparticle energies are extracted by performing an analytic continuation based on Padé approximants. Similarly to ref 33, for G_0W_0 and DSLE-min GW the parametrization of the analytic continuation employed 200 imaginary frequency points on a Gauss-Legendre grid and 16 poles for the Padé approximant method. The qsGW calculations were performed directly in real frequency by exploiting the full analytic structure of G and W as described in refs 19 and 65. Our scGW calculations used the same computational parameters as refs 15 and 16 for the frequency dependence. At variance with ref 33, no basis set extrapolation scheme has been employed in this work. Additional details on the numerical implementations of G_0W_0 , scGW, and scGW₀ in FHI-aims^{15,16,63} and the qsGW implementation in TURBOMOLE^{19,65} can be found elsewhere. All calculations use the

Table 1. Vertical Ionization Energies for the GW100 Test Set Calculated with qsGW, scGW, scGW₀@HF, scGW₀@PBE, and DSLE-Minimized G₀W₀ (DSLE-min) and def2-TZVPP Basis Sets

	name	formula	qsGW	scGW	scGW ₀ @HF	scGW ₀ @PBE	DSLE-min	DSLE-min (T4+)	CCSD(T)
1	helium	He	-24.43	-24.44	-24.47	-24.01			-24.51
2	neon	Ne	-21.62	-21.40	-21.49	-20.84	-20.82	-20.22	-21.32
3	argon	Ar	-15.53	-15.26	-15.50	-15.18	-15.34	-15.27	-15.54
4	krypton	Kr	-13.74	-13.65	-13.88	-13.62	-13.62	-13.75	-13.94
6	hydrogen	H ₂	-16.22	-16.18	-16.27	-15.98			-16.40
7	lithium dimer	Li ₂	-5.34	-4.96	-5.15	-5.02	-5.00	-5.05	-5.27
8	sodium dimer	Na ₂	-5.02	-4.63	-4.80	-4.74	-4.87	-4.93	-4.95
9	sodium tetramer	Na ₄	-4.25	-3.85	-4.09	-3.99	-4.18	-4.27	-4.23
10	sodium hexamer	Na ₆	-4.41	-3.94	-4.25	-4.16	-4.31	-4.40	-4.35
11	dipotassium	K ₂	-4.08	-3.73	-3.90	-3.86	-3.96	-4.10	-4.06
13	nitrogen	N ₂	-16.01	-15.44	-15.84	-15.32	-15.49	-15.75	-15.57
14	phosphorus dimer	P ₂	-10.40	-9.73	-10.20	-10.01	-10.30	-10.52	-10.47
15	arsenic dimer	As ₂	-9.62	-9.00	-9.48	-9.34	-9.52	-9.82	-9.78
16	fluorine	F ₂	-16.33	-15.78	-16.17	-15.50	-15.56	-15.76	-15.71
17	chlorine	Cl ₂	-11.52	-11.07	-11.47	-11.13	-11.36	-11.55	-11.41
18	bromine	Br ₂	-10.54	-10.23	-10.58	-10.30	-10.31	-10.77	-10.54
20	methane	CH ₄	-14.56	-14.28	-14.50	-14.14	-14.20	-14.35	-14.37
21	ethane	C ₂ H ₆	-12.99	-12.62	-12.92	-12.55	-12.60	-12.75	-13.04
22	propane	C ₃ H ₈	-12.35	-11.95	-12.30	-11.92	-12.03	-12.18	-12.05
23	butane	C ₄ H ₁₀	-11.89	-11.46	-11.85	-11.46	-11.73	-11.88	-11.57
24	ethylene	C ₂ H ₄	-10.63	-10.14	-10.45	-10.24	-10.40	-10.60	-10.67
25	acetylene	C ₂ H ₂	-11.53	-10.89	-11.23	-10.98	-11.17	-11.43	-11.42
26	tetracarbon	C ₄	-11.45	-10.68	-11.21	-10.87	-10.87	-11.07	-11.26
27	cyclopropane	C ₃ H ₆	-11.13	-10.62	-10.98	-10.66	-10.77	-11.00	-10.87
28	benzene	C ₆ H ₆	-9.38	-8.73	-9.20	-8.97	-9.12	-9.34	-9.29
29	cyclooctatetraene	C ₈ H ₈	-9.30	-7.81	-8.33	-8.04	-8.21	-8.44	-8.35
30	cyclopentadiene	C ₅ H ₆	-8.73	-8.10	-8.54	-8.29	-8.47	-8.69	-8.68
31	vinyl fluoride	C ₂ H ₃ F	-10.64	-10.11	-10.46	-10.16	-10.36	-10.59	-10.55
32	vinyl chloride	C ₂ H ₃ Cl	-10.09	-9.63	-10.02	-9.72	-9.92	-10.14	-10.09
33	vinyl bromide	C ₂ H ₃ Br	-9.33	-8.82	-9.19	-8.94	-9.06	-9.32	-9.27
35	carbon tetrafluoride	CF ₄	-16.77	-16.34	-16.75	-15.89	-15.84	-15.78	-16.30
36	carbon tetrachloride	CCl ₄	-11.63	-11.16	-11.69	-11.18	-11.46	-11.57	-11.56
37	carbon tetrabromide	CBBr ₄	-10.57	-10.10	-10.59	-10.16	-10.33	-10.59	-10.46
39	silane	SiH ₄	-13.04	-12.74	-13.00	-12.55	-12.66	-12.88	-12.80
40	germane	GeH ₄	-12.81	-12.40	-12.67	-12.28	-12.41	-12.55	-12.50
41	disilane	Si ₂ H ₆	-10.88	-10.46	-10.82	-10.45	-10.48	-10.75	-10.65
42	pentasilane	Si ₅ H ₁₂	-9.56	-9.04	-9.50	-9.10	-9.18	-9.32	-9.27
43	lithium hydride	LiH	-8.00	-7.88	-7.97	-7.45	-6.48	-6.71	-7.96
44	potassium hydride	KH	-6.17	-6.02	-6.17	-5.52	-5.65	-5.63	-6.13
45	borane	BH ₃	-13.52	-13.22	-13.42	-13.05	-13.17	-13.30	-13.28
46	diborane(6)	B ₂ H ₆	-12.58	-12.23	-12.54	-12.09	-12.17	-12.30	-12.26
47	ammonia	NH ₃	-11.08	-10.76	-10.97	-10.59	-10.59	-10.78	-10.81
48	hydrogen azide	HN ₃	-10.91	-10.24	-10.69	-10.38	-10.61	-10.89	-10.68
49	phosphine	PH ₃	-10.65	-10.24	-10.53	-10.28	-10.39	-10.60	-10.52
50	arsine	AsH ₃	-10.50	-10.10	-10.39	-10.17	-10.24	-10.49	-10.40
51	hydrogen sulfide	SH ₂	-10.39	-9.97	-10.26	-10.02	-10.15	-10.38	-10.31
52	hydrogen fluoride	FH	-16.33	-16.11	-16.26	-15.71	-15.63	-15.64	-16.03
53	hydrogen chloride	ClH	-12.65	-12.28	-12.55	-12.27	-12.41	-12.57	-12.59
54	lithium fluoride	LiF	-11.52	-11.34	-11.50	-10.59	-10.66	-10.85	-11.32
55	magnesium fluoride	F ₂ Mg	-13.99	-13.77	-13.97	-13.05	-12.87	-13.00	-13.71
56	titanium fluoride	TiF ₄	-15.75	-15.55	-16.15	-14.98	-14.80	-15.19	-15.48
57	aluminum fluoride	AlF ₃	-15.69	-15.40	-15.68	-14.83	-14.59	-14.75	-15.46
58	fluoroborane	BF	-11.13	-10.64	-10.94	-10.56	-10.82	-10.98	-11.09
59	sulfur tetrafluoride	SF ₄	-12.98	-12.47	-12.95	-12.36	-12.51	-12.73	-12.59
60	potassium bromide	BrK	-8.15	-7.88	-8.12	-7.72	-7.84	-8.25	-8.13
61	gallium monochloride	GaCl	-9.80	-9.35	-9.69	-9.49	-9.62	-9.93	-9.77
62	sodium chloride	NaCl	-9.07	-8.79	-9.03	-8.51	-8.79	-9.03	-9.03
63	magnesium chloride	MgCl ₂	-11.64	-11.39	-11.70	-11.24	-11.22	-11.39	-11.67
65	boron nitride	BN	-11.79	-11.06	-11.58	-11.27	-11.19	-11.81	-11.89
66	hydrogen cyanide	NCH	-13.65	-13.15	-13.51	-13.20	-13.47	-13.72	-13.87

Table 1. continued

	name	formula	qsGW	scGW	scGW ₀ @HF	scGW ₀ @PBE	DSLE-min	DSLE-min (T4+)	CCSD(T)
67	phosphorus mononitride	PN	-11.93	-11.56	-12.03	-11.60	-11.60	-11.84	-11.74
68	hydrazine	H ₂ NNH ₂	-10.08	-9.63	-9.93	-9.52	-9.53	-9.75	-9.72
69	formaldehyde	H ₂ CO	-11.22	-10.82	-11.15	-10.67	-10.77	-11.02	-10.84
70	methanol	CH ₄ O	-11.46	-11.07	-11.36	-10.86	-10.94	-11.19	-11.04
71	ethanol	C ₂ H ₆ O	-11.07	-10.69	-11.05	-10.51	-10.59	-10.84	-10.69
72	acetaldehyde	C ₂ H ₄ O	-10.62	-10.20	-10.59	-10.03	-10.10	-10.36	-10.21
73	ethoxy ethane	C ₄ H ₁₀ O	-10.23	-9.81	-10.27	-9.67	-9.77	-10.02	-9.82
74	formic acid	CH ₂ O ₂	-11.78	-11.42	-11.80	-11.19	-11.29	-11.57	-11.42
75	hydrogen peroxide	HOOH	-11.98	-11.55	-11.90	-11.38	-11.42	-11.69	-11.59
76	water	H ₂ O	-12.91	-12.59	-12.78	-12.32	-12.26	-12.45	-12.57
77	carbon dioxide	CO ₂	-14.07	-13.55	-13.95	-13.45	-13.61	-13.91	-13.71
78	carbon disulfide	CS ₂	-10.04	-9.45	-9.95	-9.69	-9.89	-10.14	-9.98
79	carbon oxysulfide	OCS	-11.33	-10.72	-11.17	-10.88	-11.08	-11.35	-11.17
80	carbon oxyselelide	OCS _e	-10.60	-10.00	-10.42	-10.19	-10.29	-10.62	-10.79
81	carbon monoxide	CO	-14.55	-13.95	-14.43	-13.90	-14.21	-14.44	-14.21
82	ozone	O ₃	-13.21	-12.54	-13.16	-12.57	-12.24	-12.49	-12.55
83	sulfur dioxide	SO ₂	-12.54	-12.05	-12.54	-12.06	-12.21	-12.55	-13.49
84	beryllium monoxide	BeO	-10.11	-9.77	-10.01	-9.58	-9.40	-9.68	-9.94
85	magnesium monoxide	MgO	-8.30	-7.97	-8.27	-7.72	-7.48	-7.60	-7.49
86	toluene	C ₇ H ₈	-9.00	-8.35	-8.83	-8.60	-8.74	-8.96	-8.90
87	ethylbenzene	C ₈ H ₁₀	-8.97	-8.30	-8.80	-8.55	-8.68	-8.91	-8.85
88	hexafluorobenzene	C ₆ F ₆	-9.91	-9.48	-10.08	-9.66	-9.96	-10.23	-9.93
89	phenol	C ₆ H ₅ OH	-8.82	-8.19	-8.67	-8.39	-8.52	-8.78	-8.70
90	aniline	C ₆ H ₅ NH ₂	-8.12	-7.51	-7.99	-7.69	-7.83	-8.09	-7.99
91	pyridine	C ₅ H ₅ N	-9.76	-9.11	-9.58	-9.37	-9.53	-9.76	-9.66
92	guanine	C ₅ H ₅ N ₃ O	-7.95	-7.49	-8.06	-7.71	-7.88	-8.18	-8.03
93	adenine	C ₅ H ₅ N ₅ O	-8.41	-7.77	-8.33	-8.00	-8.16	-8.45	-8.33
94	cytosine	C ₄ H ₅ N ₃ O	-8.99	-8.38	-8.93	-8.47	-8.63	-8.92	-9.51
95	thymine	C ₅ H ₆ N ₂ O ₂	-9.30	-8.69	-9.25	-8.83	-9.01	-9.28	-9.08
96	uracil	C ₄ H ₄ N ₂ O ₂	-9.74	-9.12	-9.66	-9.22	-9.41	-9.69	-10.13
97	urea	CH ₄ N ₂ O	-10.45	-10.02	-10.45	-9.81	-10.13	-10.44	-10.05
99	copper dimer	Cu ₂	-7.52	-6.98	-7.23	-7.29	-7.15	-7.57	-7.57
100	copper cyanide	NCCu	-10.97	-10.54	-11.13	-10.26	-10.38	-10.50	-10.85

^aBasis set converged DSLE-minimized G_0W_0 calculations employ Tier 4 basis sets augmented by Gaussian aug-cc-pV5Z basis functions, denoted as DSLE-min (T4+). For comparison, we also report CCSD(T) values from ref 37. All values are in eV.

same parameters reported in ref 33 for the resolution-of-identity and the real-space grids. To enable the direct comparison with reference values from CCSD(T), we used the Gaussian def2-TZVPP basis sets.⁵² In FHI-aims the Gaussian basis functions are numerically tabulated and are treated as numerical orbitals. We refer to ref 33 for detailed convergence tests for this procedure. For the DSLE-min method, basis set converged calculations for the quasiparticle energies have been performed using the Tier 4 basis sets augmented by Gaussian aug-cc-pV5Z basis functions (Tier 4+).⁶³ To facilitate the comparison with CCSD(T), we also report DSLE-min quasiparticle energies obtained with def2-TZVPP basis sets.

We use the same geometries as in ref 33. [Experimental geometries have been employed whenever available, otherwise molecular geometries are optimized within the PBE approximation for the exchange-correlation functional using the def2-QZVP basis set. More details on the strategy adopted for selecting the compounds of the GW100 set and their geometries are given in ref 33.] We assume zero electronic temperature, and the effects of nuclear vibrations are ignored. All ionization energies are vertical and do not include any relativistic corrections.

4. IONIZATION ENERGIES FOR THE GW100 SET

The GW100 test set consists of 100 atoms and molecules which have been selected to span a broad range of chemical bonding situations, chemical compositions, and ionization energies. Due to the absence of all-electron def2-TZVPP basis sets for fifth-row elements, we exclude Xe, Rb₂, Ag₂, and the iodine-containing compounds (I₂, C₂H₃I, Cl₄, and All₃). For the remaining 93 members of GW100 we can then conduct a meaningful comparison with CCSD(T) reference data.

As discussed in ref 33, many molecules of the GW100 test set have positive LUMO energies (that is, negative electron affinities), which makes them unsuitable for a systematic assessment of electron affinities since experimental data for such compounds is difficult to obtain. Moreover, CCSD(T) reference data is presently also not available for the LUMOs in the GW100 test set.³⁷ For these reasons, we focus here on the first vertical ionization energy, for which experimental and CCSD(T) reference data are available. An assessment of GW methods for electron affinities may be found in ref 13. In Table 1, we report the ionization energies for this subset of GW100 calculated with qsGW, scGW, scGW₀@HF, and scGW₀@PBE and def2-TZVPP basis sets. For comparison, we also report the CCSD(T) ionization energies from ref 37.

5. COMPARISON OF GW METHODS

To quantify the deviation from CCSD(T) calculations, we analyze the error $\Delta \equiv \epsilon_{\text{CCSD(T)}}^{\text{HOMO}} - \epsilon_{\text{QP}}^{\text{HOMO}}$ and the absolute error $\Delta_{\text{abs}} \equiv |\epsilon_{\text{CCSD(T)}}^{\text{HOMO}} - \epsilon_{\text{QP}}^{\text{HOMO}}|$. In Figure 2, we report the error distribution for the molecules of the GW100 test set, whereas the absolute error is reported in Figure 3.

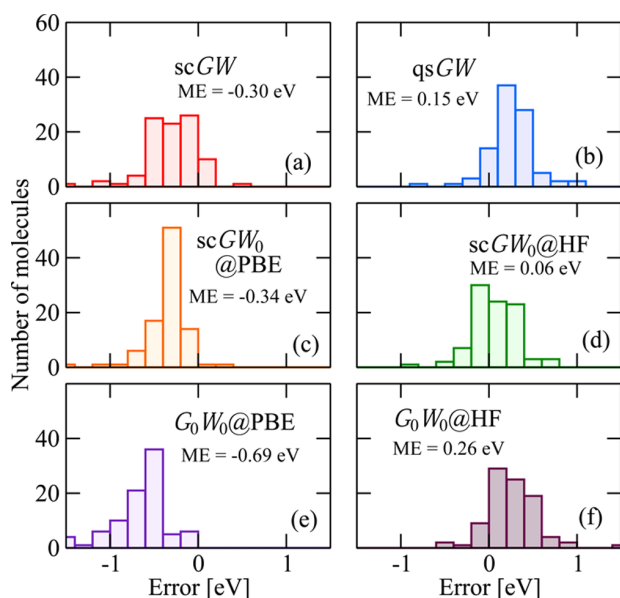


Figure 2. Error distribution [defined as the difference to CCSD(T) reference energies from ref 37] for the ionization energies of the GW100 test set evaluated using (a) scGW, (b) qsGW, (c) scGW₀@PBE, (d) scGW₀@HF, (e) G₀W₀@PBE, and (f) G₀W₀@HF and def2-TZVPP basis sets. The mean error (ME) for each method is listed in the corresponding panel.

5.1. scGW vs qsGW. We start by considering the scGW and qsGW approaches. At variance with G₀W₀ and scGW₀, the scGW ionization energies are independent of the starting point.^{15,16} Any deviations between scGW and CCSD(T) can then be attributed to intrinsic limitations of the GW approximation (i.e., missing vertex corrections) rather than the artificial starting-point dependence introduced by perturbation theory or approximate self-consistent procedures. The qsGW ionization energies of molecules have also been reported to be independent of the starting point.¹⁹ However, for some solids, a dependence on the starting point has been observed.⁶⁶

Our calculations reveal that qsGW overestimates the ionization potentials in our test set by 0.15 eV on average [Figure 2 (b)], whereas scGW underestimates them by 0.3 eV [Figure 2 (a)]. qsGW exhibits a MAE of ~0.22 eV [Figure 3 (b)], and it thus yields quasiparticle energies in slightly better agreement with CCSD(T) than scGW [MAE = 0.32 eV, Figure 3 (a)]. Overall, scGW and qsGW ionization energies differ on average by 0.45 eV, revealing that different forms of self-consistency may significantly affect the value of the quasiparticle energies and the corresponding agreement with experiment. In the following we explore four different potential explanations.

5.1.1. Screening Properties. While it is expected that different forms of self-consistency lead to different results, the magnitude of the difference is surprising. At first glance, scGW and qsGW should be similar since in both approaches the

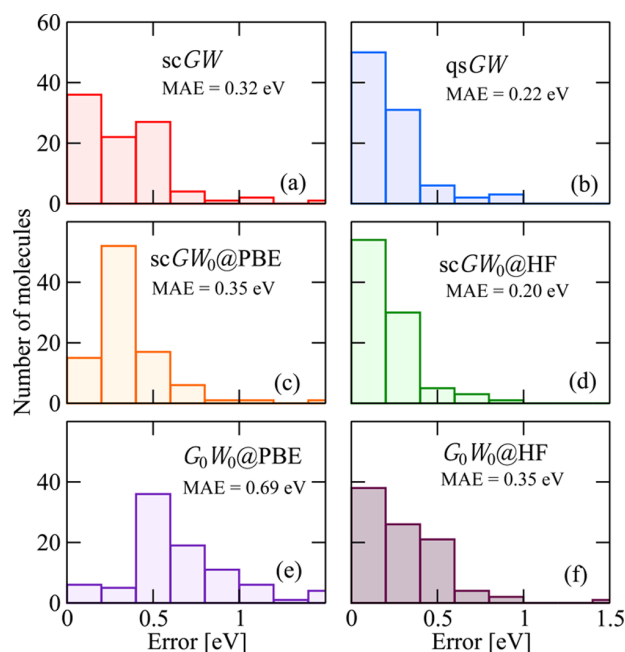


Figure 3. Absolute error distribution (defined similarly to Figure 2) for the ionization energies of the GW100 test set evaluated using (a) scGW, (b) qsGW, (c) scGW₀@PBE, (d) scGW₀@HF, (e) G₀W₀@PBE, and (f) G₀W₀@HF and def2-TZVPP basis sets. The mean absolute error (MAE) for each method is listed in the corresponding panel.

quasiparticle energies enter the denominator of the Green's function. For both approaches we would therefore expect underscreening, due to the inverse dependence of the magnitude of screening on the energy difference between the lowest unoccupied and the highest occupied state in GW. In a beyond-GW treatment this underscreening due to the large quasiparticle gap would be compensated by vertex corrections, such as ladder diagrams.^{30,67} Without this compensation, the underscreening due to the too large quasiparticle gap in *W* would lead to an overestimation of ionization energies and quasiparticle energies that resemble those of G₀W₀@HF, which is also based on an underscreened *W*₀ due to the large HOMO–LUMO gap in HF. For qsGW we indeed observe this resemblance with G₀W₀@HF in Figures 2 and 3, which results in the aforementioned slight average overestimation of ionization energies compared to CCSD(T). The small reduction of the ionization energies by 0.09 eV in going from G₀W₀@HF to qsGW can therefore be attributed to a reduction of the underscreening due to the fact that the qsGW gap is smaller than the HF gap and to density changes that we will discuss in the following.

The corresponding ionization-energy histogram for scGW is closer to scGW₀@PBE and G₀W₀@PBE than to G₀W₀@HF, with a concomitant underestimation of the CCSD(T) reference data. This observation is consistent with previous scGW calculations for molecules^{11,13,15,16,25,51,68} that observed a similar underestimation of the ionization potential. Also in scGW the HOMO–LUMO gaps are smaller than in G₀W₀@HF and smaller than in qsGW. scGW therefore underscreens less than qsGW, and we attribute part of the 0.45 eV average deviation between qsGW and scGW to this difference in screening.

5.1.2. Spectral-Weight Transfer. For solids, a spectral-weight transfer from the main quasiparticle peaks to satellites has been reported for scGW calculations of the homogeneous electron gas.⁶⁹ Schematically, the self-consistent Green's function can be written as $G = ZG_{qp} + \bar{G}$, where Z is the spectral weight of the quasiparticle peak G_{qp} , and \bar{G} is the incoherent part of the spectral function. In qsGW Z is equal to one and \bar{G} is zero.^{19,70} Conversely, for scGW Z is smaller than one, and \bar{G} is larger than zero, as spectral weight is transferred from G_{qp} to \bar{G} . This spectral weight transfer leads to an additional underscreening and an overestimation of band gaps in solids.^{22,27,71}

For small molecules there are no continuum states or collective excitations that could be excited at valence energies.⁴⁹ The scGW spectral functions therefore are sharply peaked around the quasiparticle energies, and the spectrum exhibits no signature of an incoherent background in the valence energy region⁴⁹ as shown in Figure 1. We would thus not expect any additional underscreening due to spectral-weight transfer, because Z is equal to one and G^- is zero, just as for qsGW. The spectral-weight transfer concept can therefore not explain the consistent underestimation observed for molecules in scGW.^{11,13,15,16,51,68}

5.1.3. Self-Consistent Density. Further insight into the effects of different GW approaches on electron correlation may be gained from the study of the self-consistent electron density. To focus on the effects of correlation, we consider in the following differences of the PBE, scGW, scGW₀, and qsGW electron density to the density of a Hartree–Fock calculation using the same computational parameters. Figure 5 illustrates isosurfaces of these density differences for F₂ (upper panel) and BF (lower panel) with isovalues of 0.05 and 0.01 Å⁻³, respectively. To quantify the difference between the GW and the HF densities, we introduce a density difference parameter D defined as

$$D = \int d\mathbf{r} |n^{\text{GW}}(\mathbf{r}) - n^{\text{HF}}(\mathbf{r})| \quad (13)$$

for which the values for BF and F₂ are also reported in Figure 5.

For both BF and F₂, scGW and scGW₀ induce qualitatively similar modifications of the electron density as compared to the Hartree–Fock reference both in shape and magnitude (as quantified by D). In particular, both scGW and scGW₀@HF yield $D = 0.20$ for BF and F₂, whereas scGW₀@PBE yields a slightly larger modification of the electron density, indicated by the larger D value, which we attribute to overscreening induced by the PBE starting point. In qsGW the change of electron density is more pronounced with respect to scGW and, for the BF dimer, exhibits a considerably different charge redistribution pattern.

Overall, these results indicate that electron densities resulting from scGW and qsGW calculation may exhibit quantitative and qualitative differences. In self-consistent treatments, such a density difference affects the external and the Hartree potential as well as the kinetic and the self-energy and thus contributes to the quasiparticle energy difference observed in this work. However, the small example shown in Figure 5 illustrates that the density difference between qsGW and scGW is neither systematic in shape nor in magnitude and can probably not explain the systematic shift of ~ 0.45 eV observed between our qsGW and scGW data.

5.1.4. Kinetic Energy. Another aspect in which scGW and qsGW differ is the treatment of the kinetic energy. In the G_0W_0

approach, the quasiparticles are subject to the noninteracting kinetic energy. If the noninteracting Green's function G_0 derives, for example, from a Kohn–Sham DFT calculation, the kinetic energy contribution to the total energy would be that of the *fictitious* noninteracting system of Kohn–Sham particles (T_s). In Kohn–Sham theory, the difference between T_s and the kinetic energy of the interacting system T – as obtained for instance from a self-consistent Green's function calculation – is included through the exchange–correlation energy functional. In the following, we analyze how the kinetic energy is handled in qsGW, a hybrid approach which combines elements of Green's theory and Kohn–Sham theory. In particular, we discuss whether the differences in the scGW and qsGW quasiparticle energies may be ascribed to a different treatment of the kinetic energy in the two methods.

The difference between the noninteracting and the interacting kinetic energy of a GW calculation may be quantified by invoking the analogy with the random-phase approximation (RPA).^{72,73} The total energy in scGW, G_0W_0 , and RPA can be separated into different contributions^{49,50}

$$E^{\text{GW}}[G] = T[G] + E_{\text{ext}}[G] + E_{\text{H}}[G] + E_{\text{x}}[G] + U_{\text{c}}^{\text{GW}}[G] \quad (14)$$

$$E^{G_0W_0}[G_0] = T_s[G_0] + E_{\text{ext}}[G_0] + E_{\text{H}}[G_0] + E_{\text{x}}[G_0] + U_{\text{c}}^{\text{GW}}[G_0] \quad (15)$$

$$E^{\text{RPA}}[G_0] = T_s[G_0] + E_{\text{ext}}[G_0] + E_{\text{H}}[G_0] + E_{\text{xc}}^{\text{RPA}}[G_0] \quad (16)$$

$$= T_s[G_0] + E_{\text{ext}}[G_0] + E_{\text{H}}[G_0] + E_{\text{x}}[G_0] + E_{\text{c}}^{\text{RPA}}[G_0] + T_{\text{c}}^{\text{RPA}}[G_0] \quad (17)$$

where T is the fully interacting kinetic energy, T_s is the noninteracting kinetic energy, E_{ext} is the external energy, E_{H} is the Hartree energy, and E_{x} is the exchange energy evaluated for the fully interacting Green's function G or the noninteracting reference calculation G_0 . Following refs 49 and 50, we defined U_{c}^{GW} and $E_{\text{c}}^{\text{RPA}}$ as the correlation energy functionals in the GW and RPA approximation, respectively

$$U_{\text{c}}^{\text{GW}} = \int_0^\infty \frac{d\omega}{2\pi} \text{Tr}\{v[\chi(i\omega) - \chi_0(i\omega)]\} \quad (18)$$

$$E_{\text{c}}^{\text{RPA}} = \int_0^\infty \frac{d\omega}{2\pi} \int_0^1 d\lambda \text{Tr}\{v[\chi_\lambda(i\omega) - \chi_0(i\omega)]\} \quad (19)$$

where χ_λ is the reducible polarizability

$$\chi_\lambda = \chi_0 + \chi_0 v \chi_\lambda \quad (20)$$

at coupling strength λ that follows from the irreducible polarizability χ_0 defined in eq 5. In GW there is no coupling strength integration and $\chi = \chi_{\lambda=1}$. RPA contains a coupling strength integration over fictitious systems with coupling strength λ that varies between zero (noninteracting) and one (fully interacting). The comparison between eqs 18 and 19 reveals that U_{c}^{GW} contains only electronic correlation (that is, arising from the Coulomb interaction), whereas $E_{\text{c}}^{\text{RPA}}$ recaptures an interacting kinetic energy contribution through the coupling constant integration for the same starting point G_0 .⁴⁹ We can then define the kinetic energy contribution of the correlation energy as

$$T_{\text{c}}^{\text{RPA}}[G_0] \equiv E_{\text{c}}^{\text{RPA}}[G_0] - U_{\text{c}}^{\text{GW}}[G_0] \quad (21)$$

Equations 15–21 illustrate that both the full Green's function framework (scGW) and DFT (e.g., RPA) incorporate the

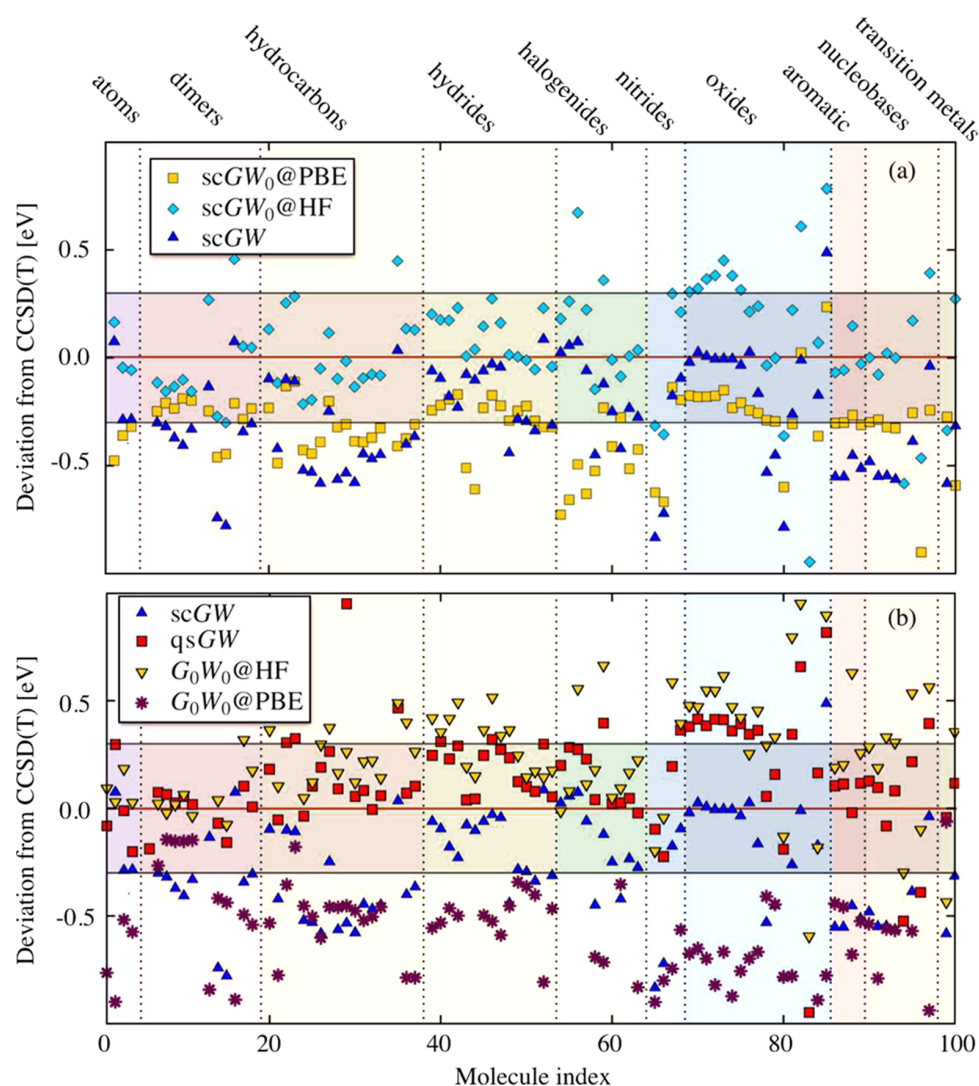


Figure 4. Deviation between the CCSD(T) reference ionization energies and our first-principles calculations obtained using (a) scGW, scGW₀@PBE, and scGW₀@HF and (b) scGW, qsGW, G₀W₀@PBE, and G₀W₀@HF, and def2-TZVPP basis sets. Only compounds with ionization energies that differ from CCSD(T) by less than 1 eV are included. Vertical dotted lines denote the separation between different subgroups of the GW100 test set and coincide with the horizontal separation lines of Table 1. The separation in subgroups (as well as the name attributed to each subgroup) is a guide to the eye but not necessarily representative of the chemical compositions of each compound. Points falling within the horizontal shaded area differ by less than 0.3 eV from CCSD(T).

interacting kinetic energy. In the perturbative G₀W₀ framework, however, this contribution is absent.

In scGW the quasiparticle energies are extracted directly from the imaginary part of the Green's function, i.e. the spectral function, as illustrated in Section 2, and therefore contain a contribution from the interacting kinetic energy. In DFT, the Kohn–Sham eigenvalues are obtained from the solution of the Kohn–Sham equation. The effective Kohn–Sham potential includes the exchange–correlation potential, that is defined as the functional derivative of the exchange–correlation energy $\frac{\delta E_{xc}}{\delta n}$ and therefore includes the difference between the interacting and the noninteracting kinetic energy in the correlation potential via the derivative of T_c .

Conversely, in the G₀W₀ approach, the quasiparticle energies ϵ^{QP} are evaluated as a first-order perturbative correction to the single-particle eigenvalues ϵ^{SP} as shown in eq 7, which we repeat here for clarity

$$\epsilon_{n\sigma}^{QP} = \epsilon_{n\sigma}^{SP} + \langle \psi_n^\sigma | \Sigma^{G_0W_0}(\epsilon_{n\sigma}^{QP}) - v_{xc} | \psi_n^\sigma \rangle \quad (22)$$

For DFT starting points, the matrix element of the exchange–correlation potential v_{xc} subtracts the aforementioned T_c contribution from the eigenvalue $\epsilon_{n\sigma}^{SP}$. Since $\Sigma^{G_0W_0}$ is purely an exchange and Coulomb correlation self-energy, it does not add an interacting kinetic energy contribution back in, which is thus absent from the G₀W₀ quasiparticle energies.

In qsGW the situation is similar to G₀W₀. Equation 22 is also solved for the qsGW quasiparticle energies. However, v_{xc} is replaced by $\tilde{\Sigma}$, the self-consistently determined, optimal, nonlocal, static potential that best represents the G₀W₀ self-energy. Since $\tilde{\Sigma}$ derives from $\Sigma^{G_0W_0}$ it also does not contain an interacting kinetic energy contribution and neither does $\epsilon_{n\sigma}^{SP}$. The kinetic energy contribution is therefore also absent from the quasiparticle energies in the qsGW framework.

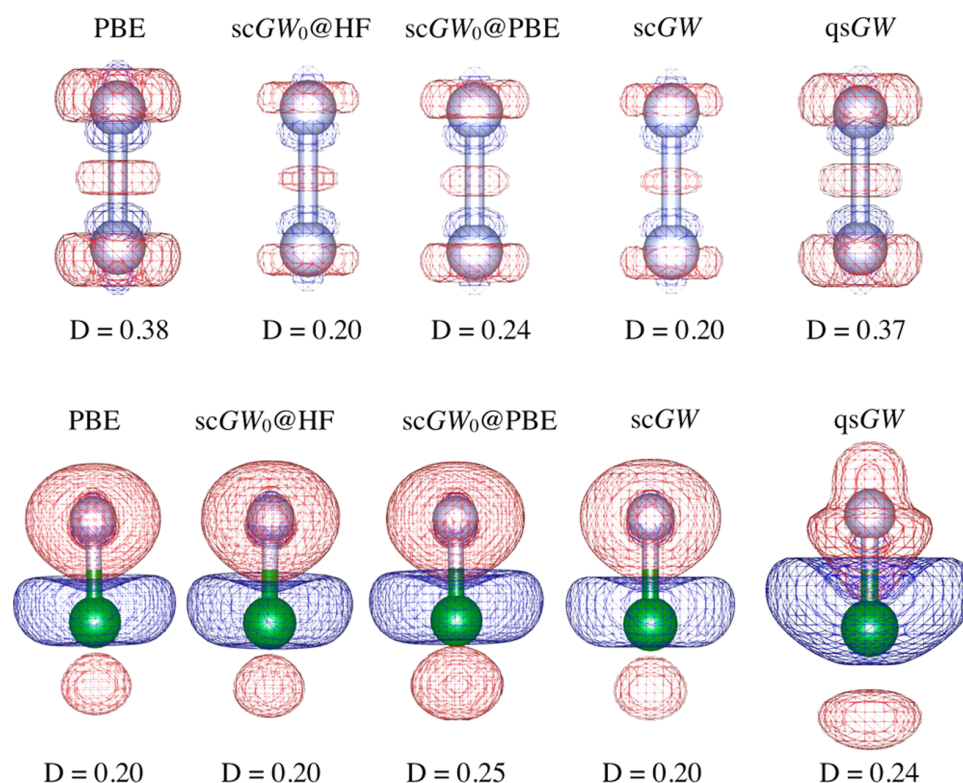


Figure 5. Isosurfaces of the density difference to Hartree–Fock for PBE, $scGW_0@HF$, $scGW_0@PBE$, $scGW$, and $qsGW$. We used an isovalue of 0.05 and 0.01 \AA^{-3} for F_2 (upper panel) and BF (lower panel), respectively.

We therefore conclude that although $scGW$ and $qsGW$ at first glance appear to be similar GW self-consistency schemes, they differ quite considerably in their treatment of the kinetic energy. We attribute the observed, average deviation of ~ 0.45 eV between these two schemes to the difference in the kinetic energy treatment, the difference in the electron density and the screening properties.

5.2. Partially Self-Consistent GW . We now turn to the partially self-consistent GW_0 scheme. Unlike $scGW$ and $qsGW$, the ionization energies of this partially self-consistent scheme still exhibit a dependence on the starting point, owing to the nonself-consistent treatment of W .¹¹ To account for this dependence, we based our $scGW_0$ calculations on two different starting points: PBE and HF. Our calculations for the GW100 set indicate that $scGW_0@PBE$ underestimates the ionization energies by 0.34 eV [Figure 2 (c)], whereas $scGW_0@HF$ overestimates them by 0.06 eV [Figure 2 (d)]. This trend reflects the over- and underscreening of the screened Coulomb interaction induced by the evaluation of W with PBE or HF orbitals, respectively. In practice, owing to the band gap problem of Kohn–Sham DFT⁷⁴ PBE calculations typically underestimate the HOMO–LUMO gap by as much as 50% as compared to quantum-chemical calculations or reference experimental values. The small HOMO–LUMO gap, in turn, leads to an overestimation of the polarizability [eq 5] and, correspondingly, of the correlation part of the G_0W_0 self-energy, as alluded to in the previous Section. Conversely, HOMO–LUMO gaps are typically overestimated in Hartree–Fock owing to the lack of electronic correlation which leads, following similar arguments, to an underscreening of the polarizability and a corresponding overestimation of the quasiparticle energies.

The $scGW_0@HF$ and $scGW_0@PBE$ ionization energies differ from each other by 0.4 eV on average, with a maximum deviation of 1.0 eV (e.g., for F_2Mg). $scGW_0@HF$ exhibits the lowest MAE (0.2 eV) relative to CCSD(T) among the GW methods considered in this work [Figure 3 (d)]. It gives larger ionization energies than $scGW$ on average. Since also the partial self-consistency scheme incorporates the interacting kinetic energy through the self-consistent Green’s function, we attribute the larger ionization energies in $scGW_0@HF$ to a more pronounced underscreening due to the fact that the HF HOMO–LUMO gap that determines the screening strength of $W@HF$ is larger than that of $scGW$. Conversely, the underscreening in $scGW_0@PBE$ indicates that PBE-based screening ($W@PBE$) is not as suitable for the GW100 set as Hartree–Fock based screening ($W@HF$), although for larger molecules or solids, the situation may differ.

5.3. The Perturbative G_0W_0 Scheme. For comparison, we report in Figures 2 and 3 the ME and MAE of $G_0W_0@HF$ and $G_0W_0@PBE$. Other G_0 starting points will be discussed in connection to the DSLE-scheme in Section 6. $G_0W_0@PBE$ underestimates the ionization energies by 0.7 eV [Figure 2 (e)], whereas $G_0W_0@HF$ overestimates by 0.3 eV [Figure 2 (f)]. G_0W_0 calculations exhibit a more pronounced dependence on the starting point as compared to $scGW_0$, since neither G and W are treated self-consistently. The average discrepancy between $G_0W_0@PBE$ and $G_0W_0@HF$ ionization energies is approximately 1 eV and can be as large as 2 eV. For G_0W_0 , in particular, HF provides a better starting point as it leads to a mean absolute error a factor of 2 smaller as compared to PBE [Figure 3 (e)-(f)]. A similar observation was also made for the ionization energies and electron affinities of organic acceptor molecules.¹³

As alluded to in Section 5.1, $G_0W_0@HF$ gives results that are comparable to $qsGW$. However, $scGW$ differs appreciably. Looking at the progression from $G_0W_0@HF$ to $scGW_0@HF$ to $scGW$ we can now understand the reduction of the ionization energies in terms of changes to the electronic screening, the electron density, and the kinetic energy. Going from $G_0W_0@HF$ to $scGW_0@HF$ incurs a density change as illustrated in Figure 5 and a change from the noninteracting to the interacting kinetic energy (albeit without possible kinetic energy changes due to changes in W). Both effects together reduce the ionization energies on average. Going from $scGW_0@HF$ to $scGW$ does not change the density appreciably anymore according to Figure 5. The additional reduction of the ionization energies in $scGW$ therefore results from a reduction of the underscreening in W in going from $W@HF$ to the self-consistent W and a concomitant change in the kinetic energy.

5.4. Trends across the GW100 Set. For all molecules of the GW100 set, the deviation from the CCSD(T) ionization energies is illustrated in Figure 4. The horizontal shaded area marks points differing by less than 0.3 eV from CCSD(T). As a guide through the chemical composition of the different compounds, we divided the GW100 set into ten subgroups: atoms, dimers, hydrocarbons, hydrides, halogenides, nitrides, oxides, aromatic molecules, nucleobases, and transition metals compounds. These categories are intended as an approximate indication of the chemical compositions of the GW100 subsets. Different categories are color-coded and separated by vertical dotted lines.

Figure 4 (b) shows that $scGW$ provides accurate ionization energies for molecules of the hydride, halogenide, and oxide groups. The MAE reduces to ~ 0.15 eV if we consider only molecules of the oxide group. A common element of these compounds is the presence of highly electronegative atoms (O, F, Cl) and, correspondingly, the formation of covalent bonds with a strong ionic character. The largest discrepancies among the $scGW$ ionization energies are observed for systems characterized predominantly by delocalized π -type orbitals such as, e.g., compounds of the hydrocarbon and nucleobase groups. At variance with $scGW$, $scGW_0@HF$ [Figure 4 (a)] and $G_0W_0@HF$ [Figure 4 (b)] exhibit the largest deviation from CCSD(T) for ionic compounds (hydrides, halogenides, and oxides), whereas the discrepancy is small for π -orbital compounds. Figure 4 further reveals that $scGW_0@PBE$ deviates rather homogeneously from the CCSD(T) reference data.

6. DSLE-MIN GW IONIZATION ENERGIES

We now turn to the discussion of the accuracy of basis-set converged (T4+) DSLE-min GW calculations. In Figure 6, we report the DSLE for two representative molecules of the GW100 test set, sodium chloride (left) and the adenine nucleobase (right). In practice, the DSLE is estimated by evaluation of eq 12 with the QP energies from $G_0W_0@PBEh(\alpha)$ for α between 0 (pure PBE exchange) and 1 (pure Hartree–Fock exchange). In addition, we show the deviation of the quasiparticle energy for the HOMO from the CCSD(T) reference ($\epsilon_{CCSD(T)}^{HOMO} - \epsilon_{QP}^{HOMO}$). Both molecules exhibit a clear correlation between the DSLE and the accuracy of the ionization energy. Figure 6 reveals that α values smaller than 0.4 typically result in a positive Δ_{DSLE} and a corresponding underestimation of the ionization energy, whereas the opposite trend is observed for larger α values. At $\alpha \approx 0.4$ for NaCl and $\alpha \approx 0.45$ for adenine we find $\Delta_{DSLE} = 0$. For NaCl, the DSLE-minimized starting point yields an ionization energy that

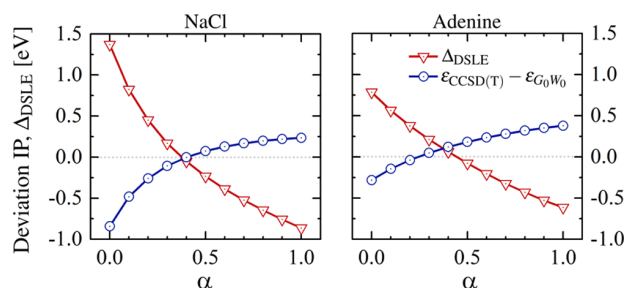


Figure 6. Correlation between DSLE and accuracy of the ionization energy for the NaCl (left) and the adenine (right) molecules. The deviation of the $G_0W_0@PBEh(\alpha)$ HOMO energies from the reference CCSD(T) ionization energies, $\epsilon_{CCSD(T)} - \epsilon_{G_0W_0}$ is displayed in blue for different amounts of Hartree–Fock exchange α used in the PBE hybrid starting point. The Δ_{DSLE} values are depicted in red as a function of α . We use Tier 4⁺ basis sets for our DSLE-min G_0W_0 calculations.

coincides with the CCSD(T) result, whereas for adenine it is slightly overestimated. More generally, we find for all the systems in the GW100 set that the deviation from CCSD(T) is strongly reduced when the DSLE is minimized.

More generally, we find that also for other systems of the GW100 set the deviation from CCSD(T) is strongly reduced whenever the DSLE is minimized. In Figure 7, we illustrate the

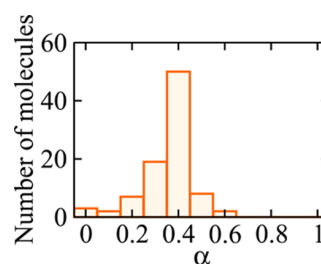


Figure 7. Distribution of the optimal α values obtained from the DSLE-min G_0W_0 approach for the GW100 test set with the Tier 4⁺ basis set.

distribution of optimal α values across the systems of the GW100 test set computed with the Tier 4⁺ basis set. The optimal α determined from the DSLE-min G_0W_0 approach is almost unaffected by finite basis set errors owing to cancellation effects in eq 12. Only three molecules of the GW100 test set minimize the DSLE already for $\alpha = 0$ (that is, for pure PBE exchange): LiH, Li₂, and Na₂. The average over all α values amounts to 0.35. This substantiates the results of previous starting-point benchmarks,^{75–78} which find a similar fraction of Fock exchange to provide the most accurate vertical ionization energies. Figure 8 explicitly shows the MAE for the ionization energies of the GW100 set obtained from $G_0W_0@PBE(\alpha)$ as a function of α and, marked by a horizontal red line, the MAE of DSLE-min GW .

Finally, in Figure 8 we report the MAE for the ionization energies of the GW100 set obtained from $G_0W_0@PBE(\alpha)$ as a function of α and, marked by a horizontal red line, the MAE of DSLE-min GW . Figure 8 reveals that, among all possible choices of $PBEh(\alpha)$ starting points, the DSLE-minimization procedure yields a gratifying MAE and, thus, is a reliable choice for ionization energy predictions.

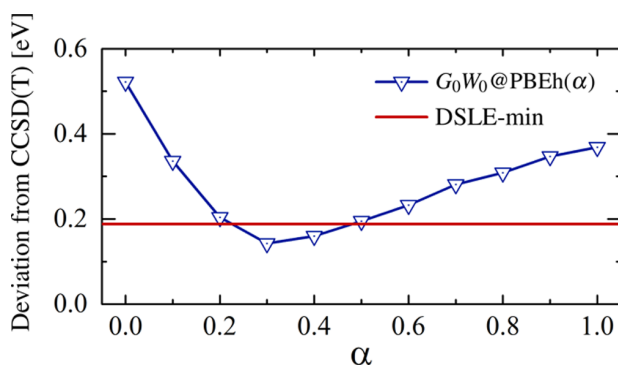


Figure 8. Mean absolute error of the deviation from CCSD(T) for the $G_0W_0@PBE(\alpha)$ ionization energies of the GW100 benchmark set as a function of α . The MAE of DSLE-min GW is reported as a red solid line. We use Tier 4⁺ basis sets for our DSLE-min G_0W_0 calculations.

7. CONCLUSIONS

In summary, we have studied the accuracy of state-of-the-art techniques based on many-body perturbation theory for the description of (charged) electronic excitations in molecules. For compounds of the GW100 benchmark set, we have computed the ionization energies as obtained from perturbative (G_0W_0) and self-consistent GW approaches (scGW, qsGW, and scGW₀), as well from the recently developed DSLE-min GW approach. Based on the comparison with CCSD(T) reference data, the results presented here quantify the overall accuracy of different flavors of GW calculations for molecular compounds of diverse chemical composition. Overall, our scGW calculations suggest that the effect of vertex correction may become important for compounds characterized by chemical bonds with a pronounced ionic character (as, for instance, halogenides) or by nitrogen-lone pair orbital types, as these compounds exhibit the largest deviation from CCSD(T). Conversely, scGW ionization energies lie typically within 0.3 eV from CCSD(T) for covalently bonded compounds. The comparison between scGW, scGW₀, and qsGW further reveals that different forms of self-consistency may influence the ionization energies and its agreement with the reference data considerably. We have identified underscreening, density changes, and the treatment of the kinetic energy as reasons for the difference in the different self-consistent GW schemes. Finally, we have shown that the deviation from CCSD(T) may in part be attributed to the DSLE, and, correspondingly, the DSLE-minimization procedure recently proposed by some of the authors emerges as a promising way to optimize the starting point of G_0W_0 calculations to improve the prediction of ionization energies.

AUTHOR INFORMATION

Corresponding Author

*E-mail: patrick.rinke@aalto.fi

Notes

The authors declare no competing financial interest.

ACKNOWLEDGMENTS

We thank Xinguo Ren and Stephan Kümmel for fruitful discussions. This work was supported by the Academy of Finland through its Centres of Excellence Programme under project numbers 251748 and 284621. M.D. acknowledges support by Deutsche Forschungsgemeinschaft Graduiertenkol-

leg 1640 and the Bavarian State Ministry of Science, Research, and the Arts for the Collaborative Research Network Soltech.

REFERENCES

- (1) Fetter, A. L.; Walecka, J. D. *Quantum Theory of Many-Particle Systems*; Dover Publications: 2003.
- (2) Hohenberg, P.; Kohn, W. *Phys. Rev.* **1964**, *136*, B864–B871.
- (3) Kohn, W.; Sham, L. J. *Phys. Rev.* **1965**, *140*, A1133–A1138.
- (4) Aulbur, W. G.; Jönsson, L.; Wilkins, J. W. *Solid State Phys.* **2000**, *54*, 1.
- (5) Onida, G.; Reining, L.; Rubio, A. *Rev. Mod. Phys.* **2002**, *74*, 601–659.
- (6) Rinke, P.; Qteish, A.; Neugebauer, J.; Freysoldt, C.; Scheffler, M. *New J. Phys.* **2005**, *7*, 126.
- (7) Faber, C.; Boulanger, P.; Attacalite, C.; Duchemin, I.; Blase, X. *Philos. Trans. R. Soc., A* **2014**, *372*, 20130271.
- (8) Hedin, L. *Phys. Rev.* **1965**, *139*, A796–A823.
- (9) Hybertsen, M. S.; Louie, S. G. *Phys. Rev. B: Condens. Matter Mater. Phys.* **1986**, *34*, 5390–5413.
- (10) Fuchs, F.; Furthmüller, J.; Bechstedt, F.; Shishkin, M.; Kresse, G. *Phys. Rev. B: Condens. Matter Mater. Phys.* **2007**, *76*, 115109.
- (11) Marom, N.; Caruso, F.; Ren, X.; Hofmann, O. T.; Körzdörfer, T.; Chelikowsky, J. R.; Rubio, A.; Scheffler, M.; Rinke, P. *Phys. Rev. B: Condens. Matter Mater. Phys.* **2012**, *86*, 245127.
- (12) Gallandi, L.; Marom, N.; Rinke, P.; Körzdörfer, T. *J. Chem. Theory Comput.* **2016**, *12*, 605–614.
- (13) Knight, J. W.; Wang, X.; Gallandi, L.; Dolgounitcheva, O.; Ren, X.; Ortiz, J. V.; Rinke, P.; Körzdörfer, T.; Marom, N. *J. Chem. Theory Comput.* **2016**, *12*, 615–626.
- (14) Kaplan, F.; Weigend, F.; Evers, F.; van Setten, M. J. *J. Chem. Theory Comput.* **2015**, *11*, 5152–5160.
- (15) Caruso, F.; Rinke, P.; Ren, X.; Scheffler, M.; Rubio, A. *Phys. Rev. B: Condens. Matter Mater. Phys.* **2012**, *86*, 081102.
- (16) Caruso, F.; Rinke, P.; Ren, X.; Rubio, A.; Scheffler, M. *Phys. Rev. B: Condens. Matter Mater. Phys.* **2013**, *88*, 075105.
- (17) Faleev, S. V.; van Schilfhaarde, M.; Kotani, T. *Phys. Rev. Lett.* **2004**, *93*, 126406.
- (18) van Schilfhaarde, M.; Kotani, T.; Faleev, S. *Phys. Rev. Lett.* **2006**, *96*, 226402.
- (19) Kaplan, F.; Harding, M. E.; Seiler, C.; Weigend, F.; Evers, F.; van Setten, M. J. *J. Chem. Theory Comput.* **2016**, *12*, 2528–2541.
- (20) Stan, A.; Dahlen, N. E.; van Leeuwen, R. *Europhys. Lett.* **2006**, *76*, 298.
- (21) Stan, A.; Dahlen, N. E.; van Leeuwen, R. *J. Chem. Phys.* **2009**, *130*, 224101.
- (22) Kutepov, A.; Savrasov, S. Y.; Kotliar, G. *Phys. Rev. B: Condens. Matter Mater. Phys.* **2009**, *80*, 041103.
- (23) Rostgaard, C.; Jacobsen, K. W.; Thygesen, K. S. *Phys. Rev. B: Condens. Matter Mater. Phys.* **2010**, *81*, 085103.
- (24) Kutepov, A.; Haule, K.; Savrasov, S. Y.; Kotliar, G. *Phys. Rev. B: Condens. Matter Mater. Phys.* **2012**, *85*, 155129.
- (25) Koval, P.; Foerster, D.; Sánchez-Portal, D. *Phys. Rev. B: Condens. Matter Mater. Phys.* **2014**, *89*, 155417.
- (26) Wang, L.-W. *Phys. Rev. B: Condens. Matter Mater. Phys.* **2015**, *91*, 125135.
- (27) Chu, I.-H.; Trinastic, J. P.; Wang, Y.-P.; Eguluz, A. G.; Kozhevnikov, A.; Schulthess, T. C.; Cheng, H.-P. *Phys. Rev. B: Condens. Matter Mater. Phys.* **2016**, *93*, 125210.
- (28) Kotani, T.; van Schilfhaarde, M.; Faleev, S. V. *Phys. Rev. B: Condens. Matter Mater. Phys.* **2007**, *76*, 165106.
- (29) Kotani, T.; van Schilfhaarde, M.; Faleev, S. V.; Chantis, A. J. *Phys.: Condens. Matter* **2007**, *19*, 365236.
- (30) Shishkin, M.; Marsman, M.; Kresse, G. *Phys. Rev. Lett.* **2007**, *99*, 246403.
- (31) Bruneval, F.; Gatti, M. In *First Principles Approaches to Spectroscopic Properties of Complex Materials*; Di Valentin, C., Botti, S., Cococcioni, M., Eds.; Springer Berlin, Heidelberg: Berlin, Heidelberg, 2014; pp 99–135.

- (32) Bechstedt, F. In *Many-Body Approach to Electronic Excitations*; von Klitzing, K., Merlin, R., Queisser, H.-J., Keimer, B., Eds.; Springer Series in Solid-State Sciences; Springer: 2015; Vol. 181.
- (33) van Setten, M. J.; Caruso, F.; Sharifzadeh, S.; Ren, X.; Scheffler, M.; Liu, F.; Lischner, J.; Lin, L.; Deslippe, J. R.; Louie, S. G.; Yang, C.; Weigend, F.; Neaton, J. B.; Evers, F.; Rinke, P. *J. Chem. Theory Comput.* **2015**, *11*, 5665–5687.
- (34) Purvis, G. D., III; Bartlett, R. J. *J. Chem. Phys.* **1982**, *76*, 1910.
- (35) Raghavachari, K.; Trucks, G. W.; Pople, J. A.; Head-Gordon, M. *Chem. Phys. Lett.* **1989**, *157*, 479.
- (36) Szabo, A.; Ostlund, N. S. *Modern Quantum Chemistry: Introduction to Advanced Electronic Structure Theory*; McGraw-Hill: New York, 1989.
- (37) Krause, K.; Harding, M. E.; Klopper, W. *Mol. Phys.* **2015**, *113*, 1952–1960.
- (38) Perdew, J. P.; Parr, R. G.; Levy, M.; Balduz, J. L. *Phys. Rev. Lett.* **1982**, *49*, 1691–1694.
- (39) Cohen, A. J.; Mori-Sánchez, P.; Yang, W. *Science* **2008**, *321*, 792–794.
- (40) Atalla, V.; Zhang, I. Y.; Hofmann, O. T.; Ren, X.; Rinke, P.; Scheffler, M. *Phys. Rev. B: Condens. Matter Mater. Phys.* **2016**, *94*, 035140.
- (41) Dauth, M.; Caruso, F.; Kümmel, S.; Rinke, P. *Phys. Rev. B: Condens. Matter Mater. Phys.* **2016**, *93*, 121115.
- (42) Lani, G.; Romaniello, P.; Reining, L. *New J. Phys.* **2012**, *14*, 013056.
- (43) Lischner, J.; Deslippe, J.; Jain, M.; Louie, S. G. *Phys. Rev. Lett.* **2012**, *109*, 036406.
- (44) Berger, J. A.; Romaniello, P.; Tandetzky, F.; Mendoza, B. S.; Brouder, C.; Reining, L. *New J. Phys.* **2014**, *16*, 113025.
- (45) Tandetzky, F.; Dewhurst, J. K.; Sharma, S.; Gross, E. K. U. *Phys. Rev. B: Condens. Matter Mater. Phys.* **2015**, *92*, 115125.
- (46) Stan, A.; Romaniello, P.; Rigamonti, S.; Reining, L.; Berger, J. A. *New J. Phys.* **2015**, *17*, 093045.
- (47) Scherpelz, P.; Govoni, M.; Hamada, I.; Galli, G. *J. Chem. Theory Comput.* **2016**, *12*, 3523–3544.
- (48) Dahlen, N. E.; van Leeuwen, R.; von Barth, U. *Phys. Rev. A: At, Mol., Opt. Phys.* **2006**, *73*, 012511.
- (49) Caruso, F.; Rohr, D. R.; Hellgren, M.; Ren, X.; Rinke, P.; Rubio, A.; Scheffler, M. *Phys. Rev. Lett.* **2013**, *110*, 146403.
- (50) Hellgren, M.; Caruso, F.; Rohr, D. R.; Ren, X.; Rubio, A.; Scheffler, M.; Rinke, P. *Phys. Rev. B: Condens. Matter Mater. Phys.* **2015**, *91*, 165110.
- (51) Caruso, F.; Atalla, V.; Ren, X.; Rubio, A.; Scheffler, M.; Rinke, P. *Phys. Rev. B: Condens. Matter Mater. Phys.* **2014**, *90*, 085141.
- (52) Weigend, F.; Ahlrichs, R. *Phys. Chem. Chem. Phys.* **2005**, *7*, 3297–3305.
- (53) Perdew, J. P.; Burke, K.; Ernzerhof, M. *Phys. Rev. Lett.* **1996**, *77*, 3865–3868.
- (54) Blase, X.; Attaccalite, C.; Olevano, V. *Phys. Rev. B: Condens. Matter Mater. Phys.* **2011**, *83*, 115103.
- (55) Faber, C.; Attaccalite, C.; Olevano, V.; Runge, E.; Blase, X. *Phys. Rev. B: Condens. Matter Mater. Phys.* **2011**, *83*, 115123.
- (56) Bruneval, F.; Vast, N.; Reining, L. *Phys. Rev. B: Condens. Matter Mater. Phys.* **2006**, *74*, 045102.
- (57) Perdew, J. P.; Parr, R. G.; Levy, M.; Balduz, J. L., Jr *Phys. Rev. Lett.* **1982**, *49*, 1691–1694.
- (58) Yang, W.; Cohen, A. J.; Mori-Sánchez, P. *J. Chem. Phys.* **2012**, *136*, 204111.
- (59) Adamo, C.; Barone, V. *J. Chem. Phys.* **1999**, *110*, 6158–6170.
- (60) Gallandi, L.; Kördörfer, T. *J. Chem. Theory Comput.* **2015**, *11*, 5391–5400.
- (61) Blum, V.; Gehrke, R.; Hanke, F.; Havu, P.; Havu, V.; Ren, X.; Reuter, K.; Scheffler, M. *Comput. Phys. Commun.* **2009**, *180*, 2175–2196.
- (62) Havu, V.; Blum, V.; Havu, P.; Scheffler, M. *J. Comput. Phys.* **2009**, *228*, 8367.
- (63) Ren, X.; Rinke, P.; Blum, V.; Wieferink, J.; Tkatchenko, A.; Sanfilippo, A.; Reuter, K.; Blum, V.; Scheffler, M. *New J. Phys.* **2012**, *14*, 053020.
- (64) TURBOMOLE V7.0 2015, a development of University of Karlsruhe and Forschungszentrum Karlsruhe GmbH, 1989–2007, TURBOMOLE GmbH, since 2007. Available from <http://www.turbomole.com> (accessed Sept 22, 2016).
- (65) van Setten, M. J.; Weigend, F.; Evers, F. *J. Chem. Theory Comput.* **2013**, *9*, 232–246.
- (66) Liao, P.; Carter, E. A. *Phys. Chem. Chem. Phys.* **2011**, *13*, 15189–15199.
- (67) Bruneval, F.; Sottile, F.; Olevano, V.; Del Sole, R.; Reining, L. *Phys. Rev. Lett.* **2005**, *94*, 186402.
- (68) Pinheiro, M.; Caldas, M. J.; Rinke, P.; Blum, V.; Scheffler, M. *Phys. Rev. B: Condens. Matter Mater. Phys.* **2015**, *92*, 195134.
- (69) Holm, B.; von Barth, U. *Phys. Rev. B: Condens. Matter Mater. Phys.* **1998**, *57*, 2108–2117.
- (70) Kotani, T.; van Schilfgaarde, M.; Faleev, S. V. *Phys. Rev. B: Condens. Matter Mater. Phys.* **2007**, *76*, 165106.
- (71) Schöne, W.-D.; Eguiluz, A. G. *Phys. Rev. Lett.* **1998**, *81*, 1662–1665.
- (72) Langreth, D. C.; Perdew, J. P. *Phys. Rev. B* **1977**, *15*, 2884–2901.
- (73) Ren, X.; Rinke, P.; Joas, C.; Scheffler, M. *J. Mater. Sci.* **2012**, *47*, 7447–7471.
- (74) Perdew, J. P.; Levy, M. *Phys. Rev. Lett.* **1983**, *51*, 1884–1887.
- (75) Bruneval, F.; Marques, M. A. J. *J. Chem. Theory Comput.* **2013**, *9*, 324.
- (76) Kördörfer, T.; Marom, N. *Phys. Rev. B: Condens. Matter Mater. Phys.* **2012**, *86*, 041110.
- (77) Körbel, S.; Boulanger, P.; Duchemin, I.; Blase, X.; Marques, M. A. L.; Botti, S. *J. Chem. Theory Comput.* **2014**, *10*, 3934.
- (78) Govoni, M.; Galli, G. *J. Chem. Theory Comput.* **2015**, *11*, 2680–2696.